Energy Conversion between CO and Porphyrins on Surfaces Studied by Ultrafast Vibrational and Scanning Tunneling Spectroscopies

Thesis submitted in accordance with the requirements of the University of Liverpool for the degree of Doctor in Philosophy by

Takuma Omiya

September, 2015

Surface Science Research Centre
Department of Chemistry
University of Liverpool

Abstract

Energy conversion between carbon monoxide (CO) and ruthenium tetraphenyl porphyrin (RuTPP) on Cu(110) surface has been investigated by means of vibrational sum frequency generation spectroscopy (SFG) and scanning tunneling microscopy (STM) in order to understand vibrational and chemical dynamics at surfaces. The study revealed that introducing porphyrins has considerable effect on the energy conversion between CO and copper, and also on the adsorbate dynamics, i.e. desorption of CO.

CO/Cu(110), was first studied, showing that energy conversion between CO and copper becomes faster with increasing coverage of CO. This coverage dependence can be explained by the modification of the potential energy surface (PES) and gradual filling of density of states (DOS) around the Fermi level (E_F). The results also indicate that the frustrated translation mode cannot be the dominant vibrational mode for electron coupling.

For the study of the energy conversion between CO and porphyrin on Cu(110), the adsorption structure of RuTPP is first investigated using an STM, revealing that the ruthenium atom occupies the short bridge site of Cu(110). With increasing coverage of RuTPP molecules, surface supramolecular organization was formed and it was compared to theoretically calculated structures. The calculated structures are used for the modeling of the PES and DOS.

The first discovery from CO-RuTPP/Cu(110) is the modification of the PES for the C-O stretch mode, showing a larger Morse anharmonicity χ_e and lower dissociation energy D_e than on a bare copper. The anharmonic constants are compared for various surfaces, which suggest the importance of considering local electric fields and the vibrational Stark effect to explain the large anharmonicity of oxidized and porphyrin covered surfaces.

Inserting RuTPP also changes the desorption mechanism of CO by inelastic tunneling process from a one-carrier to a two-carrier process with lower threshold bias voltage. The resonant electron tunneling from occupied states of CO-RuTPP to an STM tip triggers CO desorption. The two-carrier process can be explained by tunneling of a second hole into an excited state, which was created by a hole tunneling into an adsorbate HOMO.

On the other hand, facile laser-induced-desorption of CO was observed from CO-RuTPP/Cu(110), although, it shows a larger desorption energy of CO than on bare Cu(110). This can be explained by the enhancement of hot electron coupling via the DOS around E_F. The coupling between the C-O stretch mode and hot electrons is also changed from a frequency redshift to a blueshift, indicating that the CO-Ru bond weakens, which can be caused by excitation of the CO-Ru stretch or bending of CO.

Publications

1. Coverage dependent non-adiabaticity of CO on a copper surface, **Takuma Omiya** and Heike Arnolds, The Journal of Chemical Physics 141, 214705 (2014).

2. Desorption of CO from individual single ruthenium porphyrin molecules on a copper surface by inelastic tunneling process, **Takuma Omiya**, Heike Arnolds, Rasmita Raval and Yousoo Kim, in preparation.

3. Adsorption structure and supramolecular growth of RuTPP on Cu(110), **Takuma Omiya**, Paolo Poli, Mats Persson, Heike Arnolds, Yousoo Kim, and Rasmita Raval, in preparation.

4. Vibrational anharmonicity of carbon monoxide on metal surfaces –backdonation and Stark effects, **Takuma Omiya,** Paolo Poli, Mats Persson, Yousoo Kim, Rasmita Raval and Heike Arnolds, in preparation.

5. Femtosecond laser induced desorption and electron-vibration coupling of CO from surface confined ruthenium porphyrin, **Takuma Omiya,** Paolo Poli, Mats Persson, Yousoo Kim, Rasmita Raval and Heike Arnolds, in preparation.

Acknowledgement

In the 42 months of my PhD, I received the privilege to work in a collaboration project in the Surface Science Research Centre (SSRC), University of Liverpool, UK and Surface and Interface Science Laboratory (SISL), RIKEN, Japan, under the supervision of three distinguished scientists: Prof.Rasmita Raval, Dr.Heike Arnolds, and Dr.Yousoo Kim. I deeply acknowledge all three for precious support to all aspects of my life in UoL and RIKEN.

I would like to acknowledge Prof.Mats Persson and Paolo Poli for their collaboration and DFT calculations. I also thank all members in our laboratory for their technical and mental support, in particular to Dr.Sam Haq, Dr. Sergio Mauri, Dr.Junepyo Oh, Dr.Hyunjin Yang and Dr.Emiko Kazuma and Kan Ueji for their help to my project.

For the financial support during my PhD, I would like to thank from the studentship, University of Liverpool and international program associate, RIKEN.

I like to thank to my friends for all the good times shared, to many researchers who discussed science with me in the laboratory and at conferences. Special thanks to my parents, sister and grandma for all of their help over the years.

Outline

1. Introduction

2. Experimental

3. Coverage dependent non-adiabaticity of CO on a copper surface

4. Adsorption structure and supramolecular growth of RuTPP on Cu(110)

4.3 Results and discussion

4.3.2 Room temperature STM

5. Vibrational hot band of CO on bare and RuTPP covered Cu(110)

5.3 Results

6. Desorption of CO from single ruthenium porphyrin on Cu(110) with STM

6.3 Results

List of abbreviation

2PPE	Two-photon photoemission
Γ	Linewidth
AS	Action spectroscopy
BBO	β-barium borate
BB-SFG	Broadband SFG
CO	Carbon monoxide
CO-RuTPP	Ruthenium tetraphenyl porphyrin carbonyl
CoTPP	Cobalt tetraphenyl porphyrin
CPA	Chirp pulse amplification
DFG	Difference frequency generation
DFT	Density functional theory
DOS	Density of states
E_F	Fermi energy
ESDIAD	Electron stimulated desorption ion angular distributions
FR	Frustrated rotation
FROG	Frequency resolved optical gating
FTIR	Fourier transform infrared spectroscopy
FT	Frustrated translational
FWHM	Full width half maximum
HAS	Helium atom scattering
HeNe	Helium-neon
HOMO	Highest occupied molecular state
HREELS	High resolution electron energy loss spectroscopy
ICCD	Intensified charge coupled device
IET	Inelastic electron tunneling
IETS	Inelastic electron tunneling spectroscopy
IIV-SFG	IR-IR-Visible SFG
IS	Internal stretch
JDOS	Joint density of states
LASER	Light amplification by stimulated emission of radiation
LDOS	Local density of states
LEED	Low-energy electron diffraction
LT	Low temperature
LUMO	Lowest unoccupied molecular orbital
M	Metal-molecule stretch
ML	Monolayer

Nd:YAG	Neodymium yttrium aluminum garnet
NEXAFS	Near edge X-ray absorption fine structure
NO	Nitrogen monoxide
NR-SFG	non-resonant SFG
OPA	Optical parametric amplification
QMS	Quadrupole mass spectroscopy
RAIRS	Reflection-absorption infrared spectroscopy
RT	Room temperature
RuTPP	Ruthenium tetraphenyl porphyrin
SFG	Sum frequency generation
SHG	Second harmonic generation
STM	Scanning tunneling microscopy
STS	Scanning tunneling spectroscopy
T_{ads}	Adsorbate temperature
T_{el}	Electronic temperature
T_{lat}	Lattice temperature
THG	Third harmonic generation
Ti:S	Ti:sapphire
TMP	Turbo molecular pump
TOPAS	Traveling-wave optical parametric amplifier of superfluorescence
TPD	Temperature programmed desorption
TSA	Ti:Sapphire amplifier
TSP	Ti-sublimation pump
UHV	Ultra high vacuum
UPS	UV photoelectron spectroscopy
XAS	X-ray absorption spectroscopy
XES	X-ray emission spectroscopy
XPS	X-ray photoelectron spectroscopy

Chapter 1

Introduction

1.1 Energy conversion at surfaces

The basis of chemistry is the conversion of energy from one form to another form within a molecule. In particular the harvesting of solar energy is one of the great chemistry challenges of this century, because our sun is a free energy source which will last another 5 billion years. In order to understand and improve light harvesting, we need to understand how the energy of a photon is transferred into other forms of energy within a molecule. For example, photon energy changes to chemical or vibrational energy in a gas phase molecule. Figure 1.1(a) illustrates how a photon with a frequency in the visible region transfers its energy to an isolated molecule in the gas phase. The molecule can absorb the energy of the photon to create an electronically excited state or emit a photon immediately in the form of Rayleigh or Raman scattering. The energy in electronically excited states may transfer to specific molecular motion, leading to dissociation or simply dissipate to vibrations.

A femtosecond laser is a powerful tool used to investigate such energy conversion mechanisms at the molecular level[1,2]. A famous example of the study with a femtosecond laser is the dissociation of sodium halides (NaX)[3]. The pump pulse excites NaX to an activated form [NaX]*, and its property changes by molecular vibration. When Na and a halogen atom are at their outer turning points, the electron structure becomes ionic, while it is covalent at short distances. In addition, a certain point of vibration cycle leads to a great probability of de-excitation. Another example is the photoisomerization of stilbene. It is found that the isomerization process occurs within 200 fs, and suggests that the adsorbed energy is localized to the target double bond inducing such a fast photochemical process[4]. In addition, a gradual frequency shift of a low-frequency spectator vibration in the photoisomerization process of stilbene was also observed, reflecting changes in the restoring force along this coordinate throughout the isomerization[5]. These studies revealed that photon-induced-chemical-reactions are highly conjugated to the energy conversion, in particular with the molecular vibration.

In comparison with the gas phase, energy conversion mechanisms are more complex at the surface, because the substrate also plays a major role in addition to the molecule, as summarized in figure 1.1(b)[6]. The metal substrate can absorb the energy of the photon, by creating electron-hole pairs, which are usually referred to as hot electrons. Hot electrons dissipate their energy to adsorbate molecules and substrate phonons. Phonons also transfer their energy to adsorbates. Thus, there are three energy channels available to the adsorbate; photons, electrons and phonons. These multiple energy channels are the cause of complex surface dynamics. Surfaces do not merely provide a passive support for photochemical processes, but can form an active part. For example, azobenzene is model used as a study of isomerization, but its photoisomerization ability quenches upon adsorption on metal surfaces[7]. Inserting tert-methyl groups restores the isomerization property of azobenzene on Au(111) surface. This is caused by the decoupling from the surface by a spacer functional group[7,8]. The isomerization is not induced by direct light absorption by adsorbates, but by hole formation in the Au d-band followed by a hole transfer to the highest occupied molecular orbital (HOMO) of the adsorbate, emphasizing the importance of substrate mediated processes[9]. The goal of this thesis is to investigate these energy transfer processes within light harvesting molecules on metal surfaces.

Energy transfer from electrons in the substrate to adsorbates has been widely studied in the last 25 years due to the availability of ultrahigh vacuum and femtosecond lasers to study well-defined surfaces on the time scale of electron energy dissipation, which can be separated into three stages as shown in figure 1.2[10,11]. In the first tens of femtoseconds, the hot electron retains the memory of the incoming photon; the energy distribution reflects the absorbed photon. After hundreds of femtoseconds, the energy distribution follows a Fermi-Dirac distribution. Finally, the electron equilibrates with the substrate phonons within a picosecond or shorter, depending on the metal substrate[12,13]. Molecules can receive energy from electrons in the substrate at any of the three stages. The adsorbate can directly absorb the photon to become electronically excited, however, this energy dissipates into the metal substrate by creating electron-hole pairs on the femtosecond time scale[14,15].

The energy transfer from substrate to adsorbate can be probed by vibrational spectroscopy. The first time-resolved experiments were conducted on CO on Pt(111)[16,17], Cu(111)[18] and (100)[19] surfaces, through monitoring the frequency shift of the C-O stretch mode. The C-O stretch mode is known to show the temperature dependence frequency shift, resulting from anharmonic coupling between the C-O stretch and low-frequency modes such as the frustrated translation or rotation modes. By comparing the static temperature dependence of the frequency shift and hot electron temperature profile, the coupling strength between the adsorbate vibration and electrons in substrates can be studied. On copper, electron coupling constant τ_{el} of 6 ps/5.1 ps and lattice constant τ_{lat} of 7 ps/4.2 ps were found for the (111) and (100) surfaces, respectively. Other metal surfaces, including platinum[16,17,20], ruthenium[21-23] and iridium[24] show stronger electron-phonon coupling, resulting in less pronounce electron-adsorbate coupling than on copper surfaces.

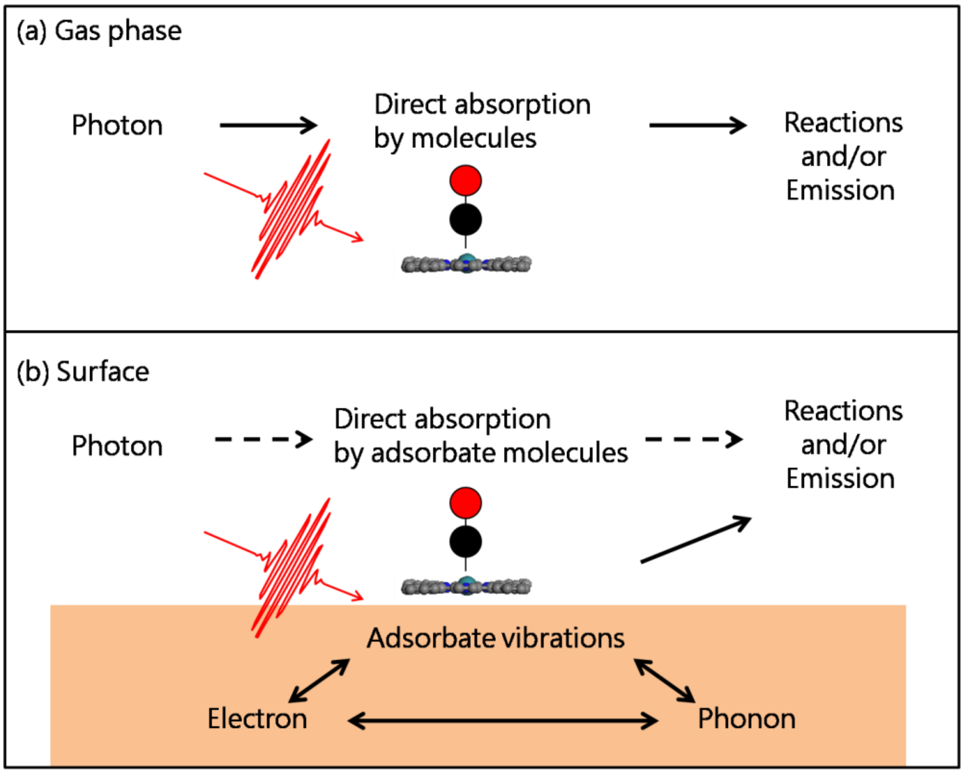

Figure 1.1 Schematics of energy conversion (a) in the gas phase and (b) on surfaces.

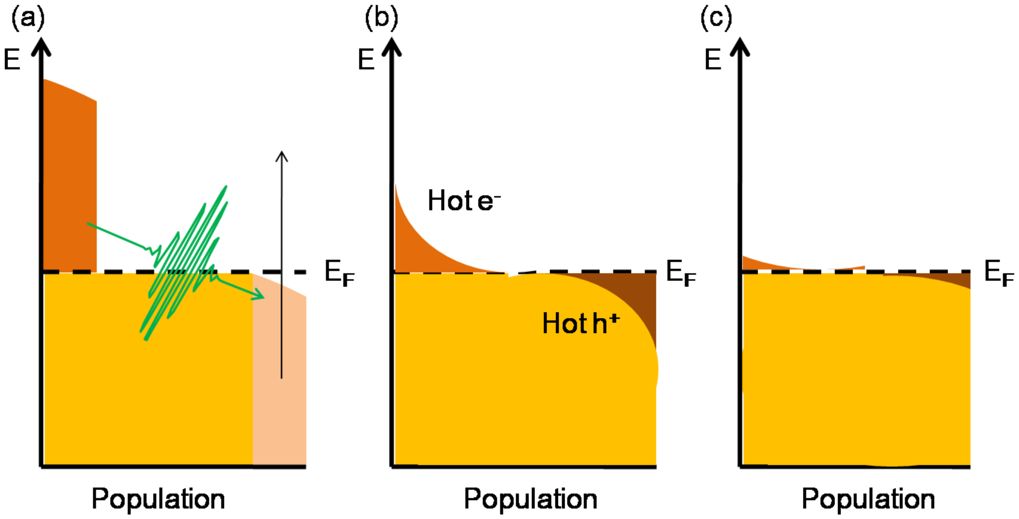

Figure 1.2 Photoexcitation and subsequent relaxation processes of electrons in a metal substrate over characteristic time scales. (a) Tens of femtoseconds after excitation, (b) ~100 fs (c) >1 ps.

On the other hand, NO on Ir(111) exhibits a stronger coupling between the internal vibration and hot electrons due to a larger local density of states (LDOS) near the Fermi level than CO[24,25]. Photodesorption of NO from Pt(111) step sites were also enhanced compared to terrace sites due to more efficient electron-vibration coupling through the large LDOS around the Fermi level[26]. These studies suggest that electron-adsorbate coupling is governed by the LDOS at the surface. A large LDOS near the Fermi level also enhances the excitation of molecular vibrations[27,28], in particular if the corresponding orbital spatially overlaps with the vibrating bond[29,30].

Despite this wealth of knowledge about the importance of LDOS for energy conversion at surfaces, it has rarely been explored to control energy conversion by adjusting LDOS. The difficulty arises from experimental limitations to obtain all the necessary information (i.e. LDOS, the relationship of LDOS and surface dynamics, and vibrational dynamics) from a single technique. Femtosecond laser spectroscopy is a powerful tool to investigate motions of adsorbates with sub-picosecond time resolution, which is the time scale of vibrational energy dissipation. In particular, vibrational sum frequency generation spectroscopy (SFG) allows studying vibrational dynamics and its relationship with surface dynamics following femtosecond laser excitation. However, the optical excitation corresponds to the joint density of occupied and unoccupied states, and it is not easy to link this to the surface electronic structure[31]. By comparison, scanning tunneling microscopy (STM) based techniques can measure LDOS through dI/dV spectroscopy. The submolecular resolution of STM induces adsorbate motion through transferring electrons into/from a particular site within the molecule and the responsible electronic or vibrational states for the motions can be detected by action spectroscopy with STM (STM-AS). The limitation of the STM based technique is its poor time resolution and difficulty to obtain vibrational spectra, making it practically impossible to study kinetics and dynamics of adsorbate vibrations. The combination of these two techniques should provide a more comprehensive picture of surface energy conversion.

The electron-adsorbate energy conversion in the sub-picosecond time scale has been studied mostly for CO on metal surfaces[32] with a few exceptions.[18,19,33] Most studies focus on substrate mediated process (i.e. hot electrons and phonons) and the direct absorption of photons by CO has rarely been reported[34], due to excited states being far from E_F and a short excitation lifetime. The central idea of this thesis is to enhance adsorbate mediated processes by combining CO with a dye molecule which shows strong visible light absorption and a long excited state lifetime. This combination allows testing the control of LDOS for energy conversion at surfaces, and the utilization of two techniques i.e. SFG and STM-AS. This thesis focuses on CO on well defined molecular layers for adjusting LDOS to control energy conversion at surfaces, in particular to control the degree of coupling to excited electrons and desorption yield of CO from a Cu(110) surface through inserting a ruthenium tetraphenyl porphyrin (RuTPP) layer. RuTPP is chosen for this study because it strongly binds to CO and forms a well ordered self-assembled layer on metal surfaces. The following two outcomes are expected from this study.

1. Direct absorption of visible light by CO-RuTPP may induce photolysis[35] if an adsorbate mediated photochemical reaction occurs.
2. Hot electron transfer and/or inelastic tunneling electron process may be enhanced through the LDOS of CO-RuTPP/Cu(110).

This thesis aims to elucidate the above two assumptions by visible pump- SF probe spectroscopy and STM-AS, and understand the effect of the porphyrin layer on the energy conversion between CO and metal substrates. Since both of the techniques and the sample are complex, this thesis is organized to help the reader understand the system step by step. After the introduction of experimental techniques in the next chapter, the vibrational dynamics of CO on Cu(110) are presented in chapter 3, showing a simple example of how adsorbate coverage can modify LDOS and thus adsorbate dynamics. Chapter 4 describes STM studies of RuTPP on Cu(110) to determine the structure and supramolecular growth on the surface. This used for the modeling of the potential energy surface and LDOS in later chapters. Chapter 5 focuses on static studies of SF spectra, in particular, vibrational hot band transitions of the C-O stretch mode, showing the complexity of the anharmonic potential at surfaces. Based on the knowledge from chapters 3 to 5, the role of LDOS and vibrational dynamics in desorption of CO have been investigated with STM-AS (chapter 6) and SFG (chapter 7), showing an unusual desorption of CO which relates to the modification of energy conversion by inserting RuTPP layer. In the rest of chapter 1, surface dynamics of carbon monoxide are presented to provide an overview of our current understanding of energy conversion at the surface, in particular, how vibrations, hot electrons and surface dynamics are correlated to each other.

1.2 Surface dynamics of carbon monoxide

Most previous studies in ultrafast surface dynamics have been conducted with CO on metal surfaces, which will be reviewed in this section. CO is a poisonous gas molecule and is a byproduct which is generated during incomplete combustions of hydrocarbons from exhaust gases of automobiles and factories. The conversion of CO to benign gases can be achieved by heterogeneous catalysis, and this is a reason why CO on metal surfaces has been widely studied. Surface electronic structure and dynamics are key to understanding CO conversion by heterogeneous catalysis. Adsorption of CO onto metal surfaces alters reaction activation energies, which strongly relates to the charge transfer between CO and metal surfaces. Charge transfer creates chemisorption of CO onto a metal surface, governed by electron donation and backdonation as proposed by Blyholder[36]. Blyholder applied the Dewar–Chatt–Duncanson model[37,38] of organometallic chemistry to surface science; electrons are donated from the CO 5σ orbital to the metal d orbital, while electron backdonation is from the metal into the CO 2π* antibonding orbital, as shown in figure 1.3(a). This hybridization creates four surface electronic states as shown in figure 1.3(b). The backdonation into the CO 2π* antibonding orbital weakens the C-O bond creating a lower activation barrier. The properties of the chemical bond can be studied by vibrational spectroscopy, in particular the frequency of the C-O internal stretch (IS) mode.

CO in the gas phase exhibits a single vibrational state, the C-O stretch mode at 2143 cm^{-1}, however, additional modes appear upon adsorption, including the metal-CO stretch (M) (or external stretch) mode, the frustrated rotational (FR), and the frustrated translational (FT) modes as shown in figure 1.4. The dynamic dipole moment of the C-O stretch increases from 0.1 D in the gas phase to 0.25 D on copper due to the charge transfer between surface and molecule[39]. The vibrational energies of these four modes are summarized in table 1.1.

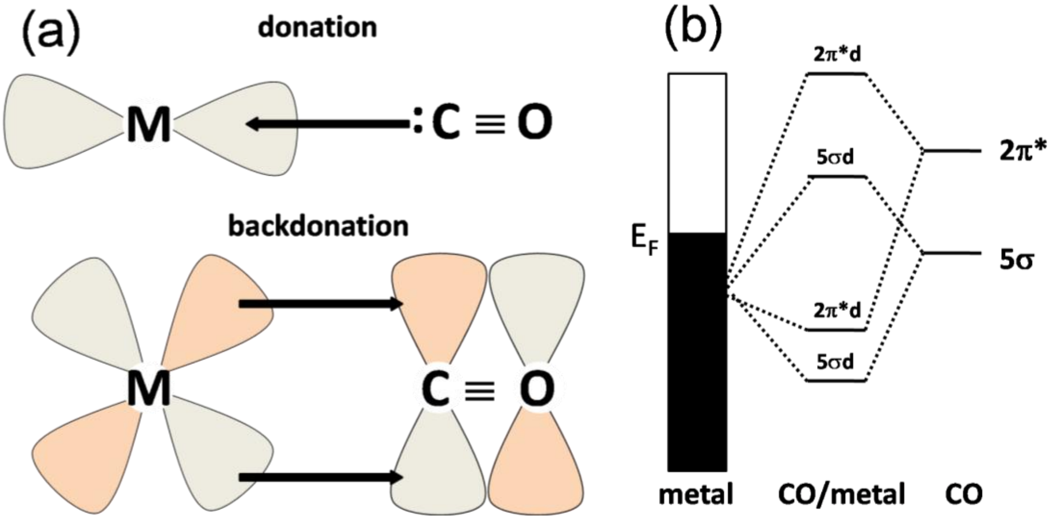

Figure 1.3 (a) Schematic representation of Blyholder model. (b) Energy diagram of metal-CO electronic hybridization.

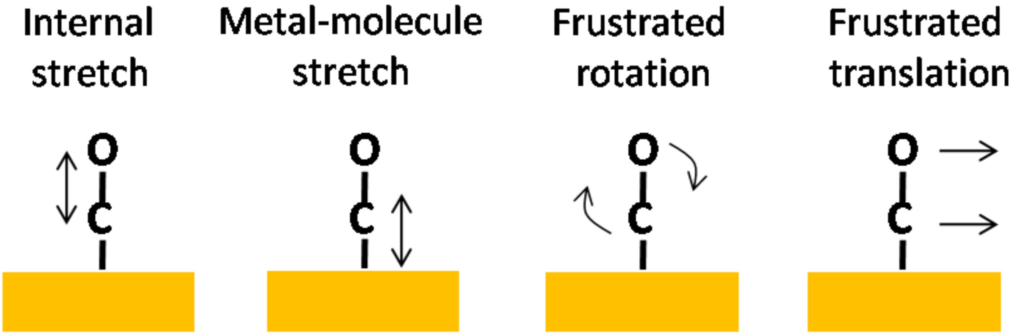

Figure 1.4 Schematics of vibrational modes of CO on a metal surface

Table 1.1 Vibrational energy of CO on copper surfaces [meV(cm^{-1})]

	RAIRS[40,41] CO/Cu(100)	HAS[42] CO/Cu(110)	IETS[43] CO/Cu(110)	ESDIAD[44] CO/Cu(110)	Calculation[45] CO/Cu(110)
IS	259 (2089)	-	257 (2073)	-	260.9 (2104)
M	43 (347)	-	-	-	49.5 (399)
FR	35.6 (287)	-	36.3 (293)	-	35.6, 38.0 (287, 306)
FT	-	3.2, 3.6 (25.8, 29.0)	-	3.1,4.9 (25.0, 39.5)	7.7, 7.1 (62.1, 57.3)

Table 1.1 IS: Internal stretch mode, M: Metal-molecule stretch, FR: Frustrated rotation, FT: Frustrated translation, RAIRS: Reflection absorption infrared spectroscopy, HAS: Helium atom scattering, IETS: Inelastic electron tunneling spectroscopy, ESDIAD: Electron stimulated desorption ion angular distributions.

Vibrational dynamics of CO on metal surfaces have been widely studied as a model system of energy dispersion from the adsorbate to the surface[32]. Vibrational energy can transfer to other vibrational modes or decay via creation of electron-hole pairs. Due to the large frequency mismatch between the C-O stretch (~2000 cm^{-1}) and lower frequency modes (~300 cm^{-1}) or phonons of metal substrates (~100 cm^{-1}), the internal stretch predominantly decays via electron-hole pairs. This can be understood as a charge flow between surface and molecule caused by the vibration as illustrated in figure 1.5[6,46]: as the C–O bond stretches during vibration, the anti-bonding $2\pi^*$ level is lowered towards the metal surface and charge flows from the metal surface to the unoccupied orbital of CO[47,48]. This is also known as damping via electronic friction[49,50]. Phrased differently, the adsorbate vibration is too rapid for the electrons to follow adiabatically, causing the generation of electron–hole pairs as a form of non-adiabatic chemistry[51,52]. Persson *et al.* calculated the vibrational lifetime of the C-O stretch mode for CO on Cu(100) by calculating the amount of charge transfer per vibrational cycle, giving a vibrational lifetime of 1.8 ps[53], which is close to the experimentally measured value of 2.0 ± 1.0 ps[54]. Thus, it is accepted that electron friction process plays a major role in vibrational deexcitation for high frequency vibrational modes on metal surfaces.

Lower frequency modes, in particular the FT mode, can relax adiabatically by coupling with substrate phonons[47]. However, both FT and FR modes can in addition relax non-adiabatically via electron-hole pair creation. The efficiency of the non-adiabatic vibrational deexcitation depends on the spatial overlap between HOMOs and LUMOs[32,47]. Since FT and FR modes break the symmetry of the chemisorbed CO, they can cause non-adiabatic transitions between HOMOs and LUMOs of different symmetry. In the language of electronic friction, both frustrated modes can be dampened via an electron density shift in the surface plane. This damping is more efficient for the frustrated rotation than the frustrated translation mode, because the frustrated rotation moves the carbon more than the oxygen. Vibrational damping by electronic friction is most efficient for the internal stretch mode because of the larger charge fluctuation and better overlap with low-lying unoccupied orbitals. Krishna *et al.* calculated vibrational lifetimes for CO/Cu(100): 3.3 ps for IS, 13.7 ps for M, 3.8 ps for FR, and 19.5 ps for FT modes[55].

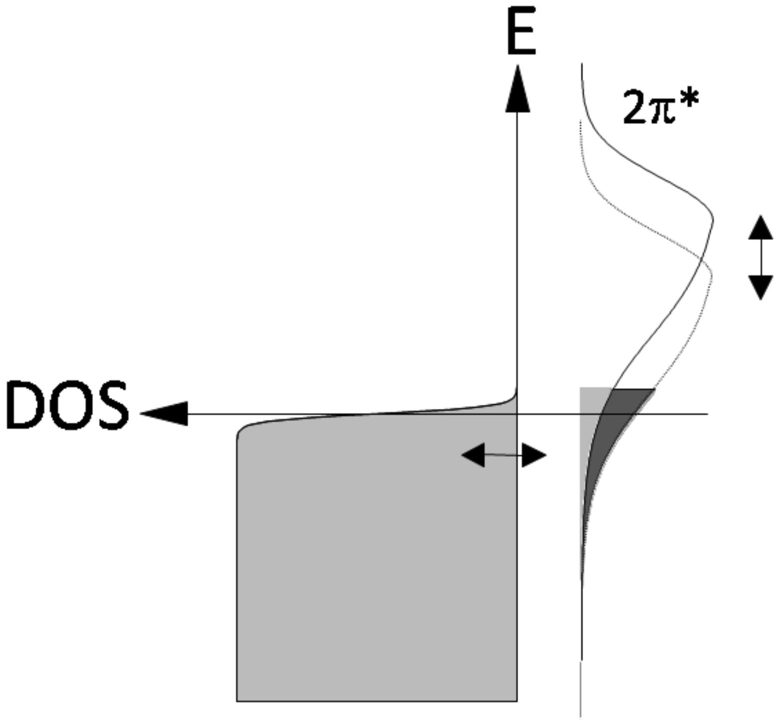

Figure 1.5 Vibration of the C-O stretch mode causes a 2π* orbital to move into and out of the Fermi sea of a metal surface, inducing nonadiabatic charge flow between adsorbate and surface, which causes the damping of the vibrational resonance.

Surface vibrational dynamics are strongly coupled to surface motions such as diffusion and desorption, which have been well documented in the literature. For example, surface diffusion correlates with a combined FT and FR motion. This was demonstrated by Backus *et al.* using visible pump-SF probe spectroscopy of CO on Pt(533) to reveal the diffusion dynamics of CO from the step site to the terrace site in 500 fs[56]. In another example, excitation of the high frequency mode by electron tunneling also induced diffusion by anharmonic coupling[57]. Diffusion dynamics can also be controlled by switching excitation source. Bartels *et al.* performed combined experiments of STM with a femtosecond laser to reveal that the hot carriers created by the laser irradiation induce CO diffusion in both [001] and [1-10] direction on the Cu(110) surface, while thermally induced diffusion to [001] is unfavorable[58]. This observation was later explained by Ueba *et al.* as intermolecular vibrational coupling in which the FR mode is first excited by hot electrons, following energy transfer to the FT mode[59].

The desorption dynamics of CO has been investigated over the last 50 years. Initially, two pulse correlation measurements were widely used, where the photodesorption yield is measured as a function of time delay between two pulses of equal intensity. These studies built a generally accepted model for photodesorption called desorption induced by (multiple) electronic transitions (DI(M)ET)[60-62], which explains laser induced desorption via multiple excitations to an electronically excited state as gradual vibrational ladder climbing in the ground state[63]. Later, the correlation between vibrational and desorption dynamics was studied by pump-probe vibrational and electronic spectroscopy which lead to the conclusion that the excitation of the FR mode is likely involved in the desorption process. Bonn *et al.* observed a sub-picosecond large frequency redshift and significant SF intensity reduction of the C-O stretch mode under desorption conditions, suggesting a contribution of the FR mode to desorption[21]. A similar conclusion was reached for CO on Pt(111)[86, 87]. Recently, ultrafast X-ray spectroscopy with a free electron laser allowed observing changes in the adsorbate electronic structure on a sub-picosecond timescale to reveal the weakening of the CO-substrate interaction during desorption. A large fraction of CO molecules (30 %) was trapped in a transient precursor state prior to desorption 2 ps after the pump pulse arrived[64], while the first picosecond showed the coupling between adsorbate and hot electrons, suggesting that the excitation of the FR mode plays a crucial role in desorption[65]. Tunneling electrons from the tip of an STM can also induce CO desorption as demonstrated by Bartels *et al.* with a threshold of the sample bias voltage at V_s=2.4 V, which was explained by the fact that the motion of a CO molecule is caused by a single electronic transition through electron injection into the CO $2\pi^*$ state[58] in analogy to the DIET mechanism[61,66].

The common theme of all these studies is that molecular orbitals of the adsorbate play an important role in surface dynamics. This thesis will now explore this theme for CO adsorbed on Cu(110) and RuTPP/Cu(110).

Chapter 2

Experimental

Experiments in this thesis were performed in two places, Surface Science Research Centre, University of Liverpool, and Surface and Interface Science Laboratory, RIKEN, Japan. In my PhD, I have spent 20 months (Oct 2013-May2015) in RIKEN, to perform STM experiments at cryogenetic temperature, which are presented in chapters 4 and 6. All experiments in this thesis have been exclusively conducted under UHV condition, with variety of surface science techniques. Here, the experimental setups and theoretical backgrounds are described.

2.1 Surface science in ultra high vacuum

2.1.1 Ultra high vacuum

The fundamental study of solid surfaces with an adsorbate molecule requires an atomically clean surface. Therefore, the ultrahigh vacuum condition is fundamentally important to create and maintain a well-defined surface during the experiments. A surface never remains atomically clean at atmospheric pressure because of contaminations from the ambient environment. From the state equation of the ideal gas, the rate of adsorption Z [cm^{-2} s^{-1}] at pressure P [N m^{-2}] can be written as[67],

$$Z = \frac{\alpha P}{\sqrt{2\pi m k T}} \quad [\mathrm{m}^{-2}\ \mathrm{s}^{-1}] \qquad (2.1)$$

where α is the sticking probability, m molecular mass, k Boltzmann constant [JK^{-1}], and T the gas temperature [K]. If gas molecules at 0.1 Torr collide with the surface at 300 K, with an average molecular mass of 28 and the surface has an atomic density of 10^{15} cm^{-2}, the surface is fully contaminated in 27 μs, assuming a sticking probability of 1, but experiments often take several hours. Thus, experiments have to be performed in ultrahigh vacuum (UHV) chambers with a base pressure better than 2×10^{-10} mbar (1 mbar = 100 Pa = 0.75 torr), to minimize the effect of contamination. UHV condition is achieved by using a combination of vacuum pumps including a rotary pump, a turbo molecular pump (TMP), an ion getter pump, and a Ti-sublimation pump (TSP). Rotary pump is first used for rough pumping to 10^{-3}-10^{-4} mbar, followed by TMP pumping down to 10^{-9}-10^{-10} mbar. An ion pump further improves the vacuum down to 10^{-10}-10^{-11} mbar. A TSP is used to pump hydrogen gases. The vacuum condition is monitored by an Bayard-Alpert hot thoria coated iridium filament ionization gauge (often called a B-A gauge or ion gauge) and also a quadrupole mass spectrometer (QMS) for the composition of the residual gas. If the vacuum needs to be broken, for repairing, changing the substrate, or attaching a new tool etc, the vacuum chamber is first filled with an inert gas such as nitrogen before release to atmospheric pressure to prevent reactive gases covering the chamber wall. After the required work at ambient condition, the chamber is pumped down but it does not achieve UHV within a reasonable time because of continuous degassing from chamber walls. To enhance degassing for faster pumping, baking is required to heat up the whole vacuum chamber. Typically baking is done over 2-3 days at a maximum temperature of 100-120 °C.

2.1.2 Cu(110) single crystal

The single crystal surface is a well defined system which is suitable to study the surface-adsorbate interaction at the molecular scale. In this thesis, a Cu(110) surface is used, with the copper fcc lattice and the surface structure shown in figure 2.1. The surface unit cell has dimensions of 2.56 Å×3.62 Å. Copper is a coinage metal which exhibits a higher reactivity to CO than gold or silver, but lower than ruthenium and platinum. An important feature of the copper substrate is its weak phonon-electron coupling[12,68], resulting in a longer lifetime of hot electrons, which enables to observe electron-vibration coupling with 200 fs laser pulses.

The sample mount of the copper substrate is shown in figure 2.2. This schematic is for the RAIRS setup, but it is almost identical for SFG except for the size and shape of the copper crystal. For RAIRS/SFG experiments, a Cu(110) single crystal (15 mm × 9 mm and 2 mm thick rectangular crystal for RAIRS, 10 mm diameter and 2 mm thick crystal for SFG) was mounted to an x-y-z- manipulator via tungsten wire, and differentially pumped by a roughing pump. A type-K thermocouple is inserted into the side of the copper crystal to monitor substrate temperature. A base temperature of 97 K (SFG) and 83 K (RAIRS) is achieved by contact to a liquid nitrogen reservoir. For STM experiments, a similar Cu(110) single crystal (10 mm diameter and 1.5 mm thickness) is attached to a tantalum plate and inserted into the STM scanning head.

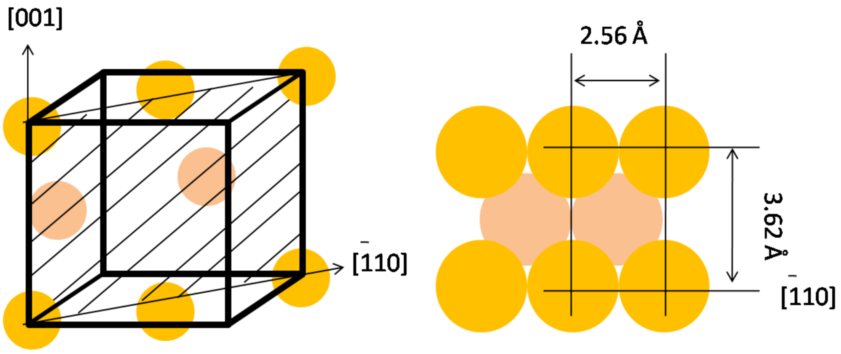

Figure 2.1Schematics of Cu(110) surface and the surface unit cell. Orange and pink circles represent the top and the second layer atoms, respectively.

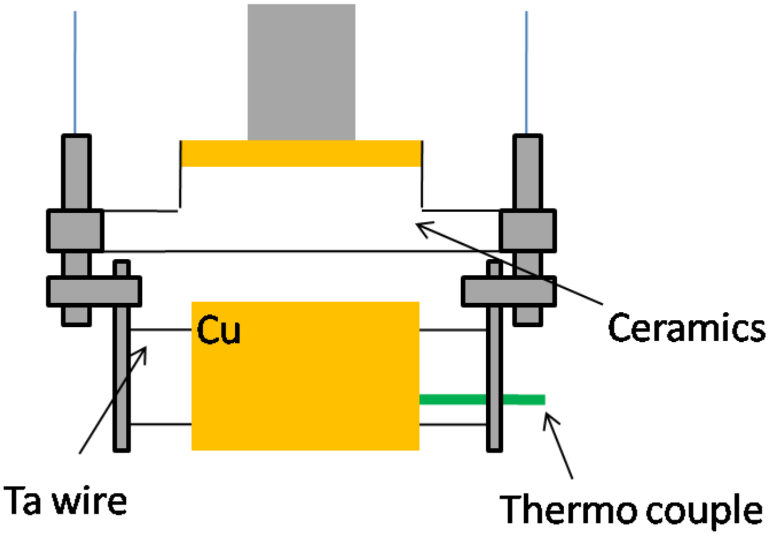

Figure 2.2 Schematics of copper crystal mounting onto the manipulator. A tantalum/copper block is attached to flow the current for resistive heating. A thermocouple (green line) is directly attached to the copper crystal. Ceramics (white block) are used to insulate the crystal for resistive heating. Thermal contact is achieved by a copper block attached to a liquid nitrogen reservoir, cooling down to 83 K/97 K for RAIRS/SFG.

The Cu(110) single crystal is cleaned *in situ* by multiple cycles of Ar^+ sputtering and annealing. The sputtering can remove the contamination from the surface by bombardment with high energy argon ions, but also damages the copper substrate. Annealing smoothes the surface by enhancing the diffusion rate, but also introduces contamination from the bulk. Repeating the sputtering/annealing cycles, the surface becomes eventually clean. Ar^+ ions are created by electron bombardment followed by acceleration by the electric field. Typically, an argon pressure of 1×10^{-4} torr and 1.0 keV is used for Ar^+ sputtering. The alignment is monitored by the ion current at the copper sample. Annealing is performed either by resistive heating (SFG/RAIRS/TPD) or electron bombardment (LT-STM). During annealing, the sample temperature is monitored by thermocouple (SFG/RAIRS/TPD) or IR thermometer (LT-STM). The annealing temperature is kept at 600-700 K. The surface cleanliness was confirmed by a sharp 1×1 low energy electron diffraction (LEED) pattern, temperature programmed desorption, or STM imaging.

2.1.3 Temperature programmed desorption

Temperature programmed desorption (TPD) is a simple technique to study the energetic and surface stoichiometry, first described by Apker[69]. The desorption activation energy E_{des} is approximately equal to the differential heat of adsorption, which makes TPD the simplest experiment to measure the bond energy of an adsorbed species. If the observed desorption peak is a single peak, the desorption rate per unit area can be calculated with the following equation[70]

$$\frac{\mathrm{d}N}{\mathrm{d}t} = \frac{V}{AkT_g}\left(\frac{\mathrm{d}P}{\mathrm{d}t} + \frac{S}{V}P\right) \qquad (2.2)$$

where N is the surface coverage [molecule cm^{-2}], V is the vacuum chamber volume [m^3], A is surface area [m^2], T_g is the gas phase temperature [K], P is the pressure increase above the background [Pa], and S is the pumping speed [m^3/s]. If no re-adsorption occurs during desorption, and a large pumping speed or low heating rate leads to $\frac{\mathrm{d}P}{\mathrm{d}t} = \frac{S}{V}P$, then the desorption rate is simply proportional to the pressure increase P. The desorption energy E_{des} can be estimated from the desorption peak temperature T_{max}, using the Redhead equation[71],

$$E_{des} = RT_{max}[\ln(\nu_i\frac{T_{max}}{\beta} \; -3.46)] \qquad (2.3)$$

where β is the heating rate dT/dt. This equation is valid for first order desorption and a linear variation of the sample temperature with time and the correct guess of frequency factor ν_i. Frequency factor ν_i is assumed to be 10^{13} [s^{-1}] from reference[72]. More accurate values can be derived by line shape analysis, but this requires multiple TPD data from different coverages[73] or different heating rates[71,74].

The crystal surface is heated with a constant heating rate (2 K/s in the experiments presented in the thesis) and the desorbed molecules from the surface are monitored by quadrupole mass spectroscopy (QMS). From the temperature desorption spectra, desorption energies for each adsorbate can be derived from the Redhead equation[71]. TPD is often used to confirm the sample cleanliness before/after experiments, to measure adsorbate coverage, and estimate desorption energies.

2.1.4 Deposition of molecules

- Carbon monoxide

For LT-STM experiments, CO molecules were introduced into the UHV chamber through a small tube connected to a leak valve. First, the vacuum line of gas dosing is pumped by a TMP, then it is filled by CO gas after flushing twice. The purity of CO is confirmed by QMS. A small box made of Ta foil is attached at the end of the tube to increase the local pressure for achieving efficient adsorption. Since the substrate is taken out from cryostat to adsorb CO, the crystal temperature raises. The temperature of the substrate is estimated to be at ~30-50 K during CO adsorption from the previously measured temporal evolution of the substrate temperature[75]. For SFG, RAIRS and TDS, CO gas was simply introduced from the background pressure.

- RuTPP

Deposition of the RuTPP molecules is performed by the sublimation of its powdered form onto the Cu(110) surface at room temperature. A solid sublimation doser consists of an electrical feed-through flange containing a Ta foil with a filament wire (for LT-STM), two copper rods and a K-type thermocouple, as shown in figure 2.3. A glass tube was also used instead of Ta foil in SFG/RT-STM, but the principle remains the same. RuTPP is used as purchased from Sigma Aldrich. Before the deposition onto the Cu(110) surface, the RuTPP doser was degassed over 24 hours ~50 °C lower than deposition temperature to remove residual impurity. The presence and removal of impurity (water and solvent) was monitored by mass spectroscopy. In Liverpool, the doser was heated by applying a current of 1.4 A, which is estimated to produce ~200 °C from a previously measured temperature calibration. In RIKEN, the attached thermocouple shows ~280 °C while dosing RuTPP, but the thermocouple is attached to the Ta foil which is a few millimeters away from the molecular doser.

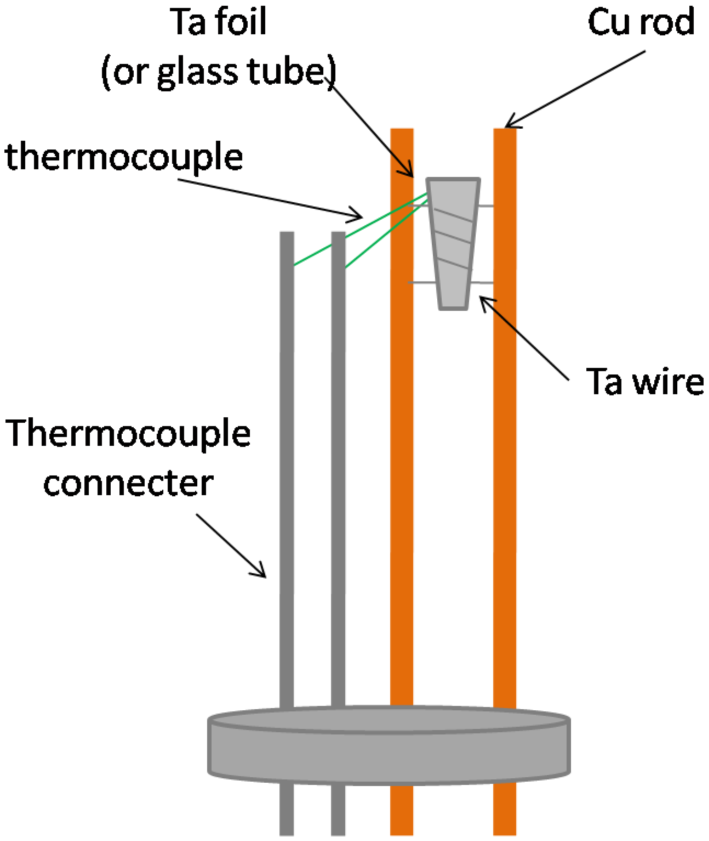

Figure 2.3 Schematics of molecular doser for RuTPP

2.1.5 Reflection absorption infrared spectroscopy

Infrared (IR) absorption spectroscopy is a classical tool to study chemical species and is routinely used in general organic and physical chemistry to identify chemical bonds. An IR electromagnetic field interacts with molecular vibrations by resonant absorption. The electromagnetic field E_{IR} induces a change in the transition dipole moment along a vibrational coordinate Q. Thus, an IR active molecule must have a dipole moment which changes during the vibration. The absorption intensity I_{IR} depends on the change in dipole moment; $I_{IR} \propto (\partial \mu / \partial Q)^2 |E_{IR}|^2$. In a vibrational state picture, this corresponds to a transition from the fundamental vibrational state ν=0 to the first excited state ν=1.

Reflection absorption infrared spectroscopy (RAIRS) is a surface sensitive IR spectroscopy[76]. RAIRS has two selection rules, 1) the molecule must have a transition dipole moment 2) the vibrational coordinate must contain the surface normal. The former rule is common for any IR spectroscopy, but the latter is unique for RAIRS at metal surfaces created by the adsorbate image dipole in the metal substrate as shown in figure 2.4. For example, flat-lying CO is IR inactive because its dipole is canceled by the image dipole while upright CO has IR active internal and external stretch modes. Tilted CO is also IR active, but the signal is lower than in the upright configuration. To maximize the signal, RAIRS is carried out at grazing incidence, to enhance the absorption of p-polarized light by the adsorbate.

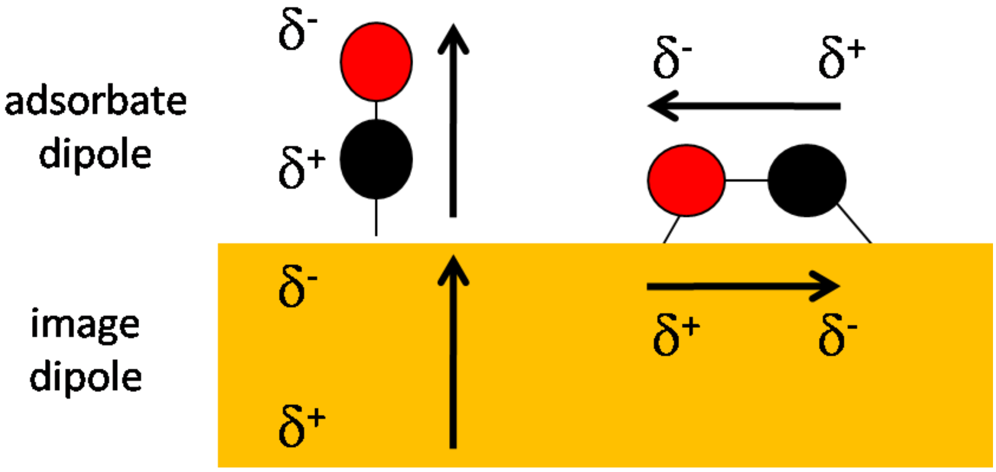

Figure 2.4 Schematic representation of the surface selection rule of IR spectroscopy on a metal surface. A perpendicular CO is IR active, but a flat lying CO is not.

As a simple example, RAIR spectra of the coverage dependent C-O frequency shift from CO on Cu(110) are shown in figure 2.5. Typically, the frequency of the C-O stretch (IS) mode identifies the adsorption site of CO, either atop (2000-2130 cm^{-1}), bridge (1800-2000 cm^{-1}) or multi-coordinated sites (1650-1800 cm^{-1})[77]. In case of CO on Cu(110), the C-O stretch mode appears at ~2090 cm^{-1}. STM studies revealed that CO occupies the atop site of Cu(110)[78], which agrees with the prediction from its frequency. The frequency shifts to higher wavenumbers (called blueshift) by dipole-dipole coupling. The observed frequency shift is much smaller than the excepted value from a pure dipole effect. This is caused by a modification of the surface electronic structure, a broadening of the $2\pi^*$ LUMO upon delocalization[79-81] increasing backdonation from the metal d orbital. This effect (known as chemical shift) cancels most but not all of the blueshift from dipole-dipole coupling[82]. This will be further discussed in chapter 5.

RAIRS has been widely applied to CO on metal surfaces, detecting low frequency modes[40,41], vibrational overtones[83], hot bands[84] and combination bands[83]. It is not limited to metal surfaces, but nano-particles[85-87] and oxide surfaces[88] have also been studied by RAIRS. The advantage of RAIRS over SFG is the availability of turn-key instrumentation and an easier correlation between intensity and coverage. Broadband SFG has the advantage of providing time-resolution down to 100’s of femtoseconds.

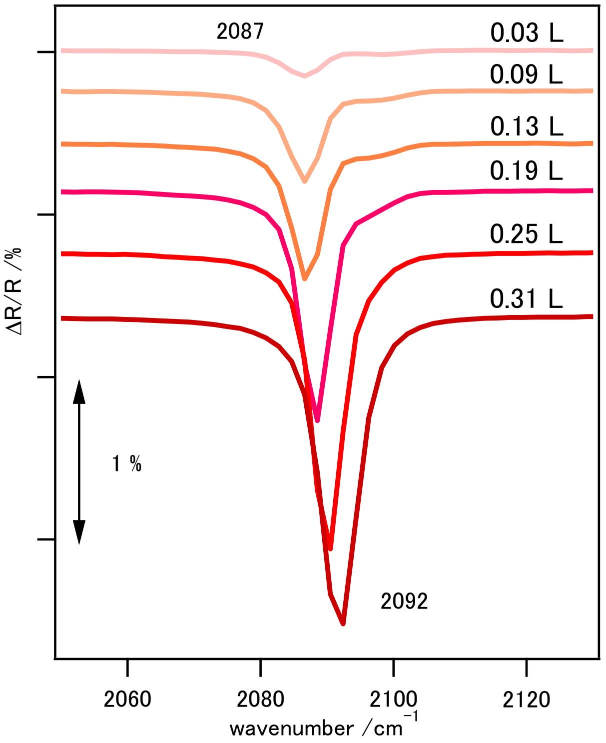

Figure 2.5 RAIR spectra of CO on Cu(110) at 83 K as a function of CO coverage. CO dosage increases from top to bottom.

RAIRS experiments were carried out using a UHV chamber (base pressure 1×10^{-10} mbar) interfaced with a Nicolet 860 Magnon FTIR spectrometer via ancillary optics and KBr windows[89]. A nitrogen cooled HgCdTe MCT detector allowed the spectral range from 550-4000 cm^{-1} to be accessed. The spectrometer was operated with a resolution of 4 cm^{-1} with the addition of 256 scans for each spectrum. The RAIRS chamber is equipped with LEED, QMS and Ar^+ sputter gun. The optical path is purged by CO_2 free dry air to reduce the absorption by H_2O and CO_2. The polarization is not controlled in the present experiments. RuTPP was first deposited at room temperature, subsequently cooled down to 87 K while CO exposure and data acquisition were carried out. A reference background spectrum of clean or RuTPP covered Cu(110) was subtracted from subsequent spectra.

2.2 Sum frequency generation spectroscopy

Our main motivation to perform SFG experiments is for time-resolved studies. The molecular time scale on a surface can be defined as the time it takes for a molecule to move to an adjacent surface site, which typically takes 100 fs[90]. To date, a laser pulse is the only experimental tool to access such a short time scale[91]. There are several experimental techniques to investigate the surface by short laser pulses. Surface electron dynamics can be probed by two photon photoelectron spectroscopy[92-96]. Time resolved study with X-ray emission spectroscopy (XES) and X-ray absorption spectroscopy (XAS) are also possible using a free electron X-ray laser[64,97]. STM can be combined with a femtosecond laser system to follow surface diffusion[98] and ultrafast carrier dynamics[99]. Surface enhanced Raman spectroscopy (SERS)[100] and IR spectroscopy[19,54] have also been used for ultrafast surface vibrational spectroscopy.

SFG has three advantages compared with other techniques. Firstly, the SF resonant signal contribution is dominated by the surface. Secondly, SF spectroscopy is an emission spectroscopy in the visible range, which allows us to use a charge coupled device (CCD), the most commonly used high sensitivity detector. Thirdly, broadband SF spectra cover a wide frequency range with femtosecond time resolution and <10 cm^{-1} energy resolution. These three advantages allow us to study the dynamics of vibration[101], diffusion[56] and desorption[20,21] with sub-picosecond time resolution.

2.2.1 Theory

The theoretical basis of SFG was described in 1962[102], and the first SFG spectra were obtained in the 1980s[103-105]. Recent review papers have described the details of the theoretical background[106-108] and current development[32,90,109-112]. This section describes the basic theory of SFG to interpret SF spectra, based on the two review papers[90,106]. The incorporation of perturbation theory is required for a more precise description[113,114].

Sum frequency generation requires the mixing of two incoming photons. For vibrational SFG, a fixed visible frequency and a tunable IR frequency beam overlap in time and space to generate SFG. Figure 2.6 compares IR absorption, Raman scattering and SFG from the vibrational excitation point of view. IR detects the change in dipole moment μ as described in the RAIRS section, while the Raman spectroscopy response is due to the change in molecular polarizability α. In Stokes scattering, the adsorbate gains energy from the incident photon, while in anti-Stokes scattering, the molecule loses vibrational energy. SFG is an anti-Stokes Raman process following vibrational excitation by an IR pulse. This coherent combination of IR and Raman transitions means the sample has to be both IR and Raman active.

In linear IR spectroscopy, the induced electric dipole μ is given by

$$\mu=\mu_0+\alpha E \tag{2.4}$$

where μ_0 is the permanent dipole, α is the polarizability of molecular electrons and αE corresponds to $\partial \mu / \partial Q$ in this simple approximation. From a macroscopic point of view, the dipole moment per unit volume, which is equal to the bulk polarization P, is used and equation (2.4) can be rewritten as

$$P=\varepsilon_0\chi^{(1)} E \tag{2.5}$$

where ε_0 is the electric permittivity in vacuum, $\chi^{(1)}$ is the macroscopic average of α, known as the first-order susceptibility. This term describes the light-material interaction, which can be detected by linear IR spectroscopy. In contrast, a short laser pulse provides a strong E field, which requires the incorporation of higher order terms to describe P accurately,

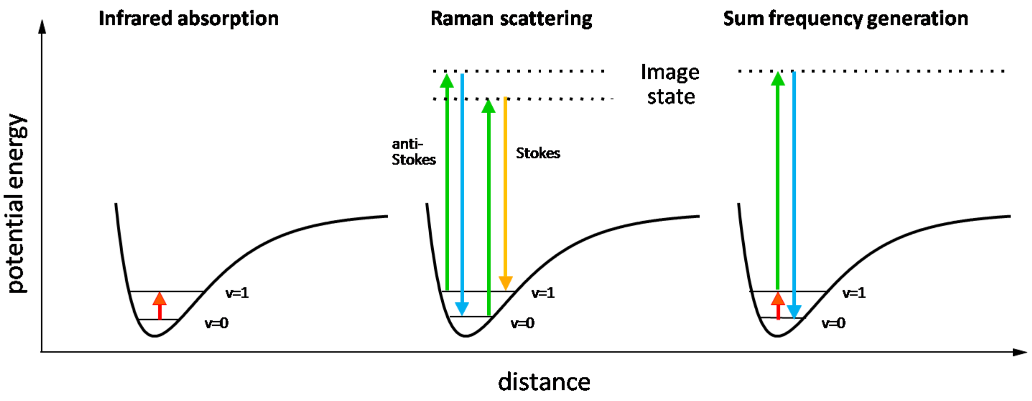

Figure 2.6 Schematic illustration of IR, Raman and SF transitions[32]

$$\mu=\mu_0+\alpha E+\beta E^2+\gamma E^3+\cdots \qquad (2.6)$$

$$P=\varepsilon_0(\chi^{(1)} E+\chi^{(2)} E^2+\chi^{(3)} E^3\cdots) \qquad (2.7)$$

where β and γ are first- and second- order hyperpolarisabilities, and $\chi^{(2)}$ and $\chi^{(3)}$ are the second- and third order non-linear susceptibilities, respectively. In these equations, the electric dipole approximation is used, in which the effects of magnetic fields and multipoles are ignored.

The electric field E is generated by an electromagnetic wave, which can be expressed in the form of a cosine,

$$E=E_1\cos \omega t \qquad (2.8)$$

where ω is the frequency. The induced polarization can be rewritten as

$$\begin{aligned} P&=\varepsilon_0(\chi^{(1)} E_1\cos \omega t+\chi^{(2)} (E_1\cos \omega t)^2+\chi^{(3)} (E_1\cos \omega t)^3+\cdots) \\ &=\varepsilon_0(\chi^{(1)} E_1\cos \omega t+\chi^{(2)}\, 1/2\, E_1^2(1+\cos 2\omega t) \\ &\quad +1/4\, \chi^{(3)} E_1^3(3\cos\omega t+\cos 3\omega t)^3+\cdots) \end{aligned} \qquad (2.9)$$

Equation (2.9) contains second and third order terms showing the doubling and tripling of the incident E field frequency. This is the origin of second harmonic generation (SHG) and third harmonic generation. If two incident electric fields with different frequencies ω_1 and ω_2 are used instead, the surface electric field can be written as,

$$E=E_1\cos \omega_1 t+E_2\cos \omega_2 t \qquad (2.10)$$

Then the second order term of induced polarization is given by

$$P^{(2)}=\varepsilon_0\chi^{(2)} (E_1\cos \omega_1 t+E_2\cos \omega_2 t)^2 \qquad (2.11)$$

Equation (2.11) contains the electric fields at four different frequencies, $2\omega_1$, $2\omega_2$ (SHG) $\omega_1+\omega_2$ (SFG) and $\omega_1-\omega_2$ (difference frequency generation; DFG). If the incoming beams are in the visible and in the IR with frequencies of ω_{VIS}, ω_{IR} and electric fields of E_{VIS} and E_{IR}, the sum frequency component can be written as,

$$\omega_{SF}=\omega_{VIS}+\omega_{IR} \qquad (2.12)$$

$$P_{SF}^{(2)}=\varepsilon_0\chi^{(2)} E_{VIS} E_{IR} \qquad (2.13)$$

Equation(2.12) shows the emitted light oscillates at the sum of two incoming frequencies. This also means the momentum k must follow $k_{SF}=k_{vis}+k_{IR}$, To illustrate the surface specificity of this even-order non-linear optical process, axis reversal **r→-r** is considered. This accompanies the inversion of the sign of polarization and field vectors.

$$\begin{aligned}\mathbf{P}^{(2)}(-\mathbf{r}) &= -\ \mathbf{P}^{(2)}(\mathbf{r}) \\ &= \varepsilon_0\chi^{(2)}\ \mathbf{E}(-\mathbf{r})\ \mathbf{E}(-\mathbf{r}) \\ &= \varepsilon_0\chi^{(2)}\ (-\mathbf{E}(\mathbf{r}))\ (-\ \mathbf{E}(\mathbf{r})) \\ &= \varepsilon_0\chi^{(2)}\ \mathbf{E}^2 \\ &= \mathbf{P}^{(2)}(\mathbf{r}) \qquad (2.14)\end{aligned}$$

In a medium with inversion symmetry, equation (2.14) can be fulfilled only for $\chi^{(2)} = 0$, meaning SFG is forbidden. In contrast, a surface breaks the inversion symmetry, $\chi^{(2)}$ has a non-zero value and therefore SFG is allowed. In addition to the macroscopic asymmetry, molecular level asymmetry is required to be SF active. For example, the alkane chain of a self-assembled monolayer often contains two CH_2 groups in mirror positions, which are SF inactive because the sum of their individual electric polarizations is zero. A disordered adsorbate also becomes SF inactive for the same reason.

SFG allows us to resolve the vibrational resonance with an energy resolution of a few wavenumbers. Initially, SFG was developed with a scanning picosecond laser system because a femtosecond laser pulse must contain a large bandwidth due to the uncertainty principle. Later, broadband multiplex SFG (BB-SFG) with a femtosecond laser system was demonstrated[115,116]. Instead of a picosecond laser system, BB-SFG requires a femtosecond IR pulse and picosecond visible pulses to realize time and energy resolution simultaneously. Figure 2.7 shows a schematic illustration of BB-SFG. The femtosecond IR pulse covers a wide frequency range in a single shot but the resonant IR absorption is governed by the intrinsic linewidth of the molecule, which is determined by its vibrational lifetime. Spectrally narrow picosecond visible light induces the Raman transition from the vibrationally excited state to a virtual state, which is called upconversion. Then, the SF photon is emitted with a linewidth that corresponds to a convolution of the molecular linewidth Γ_{01} and the upconversion width Γ_{vis}.

BB-SFG requires two laser pulses of different frequency and linewidth. A femtosecond visible laser pulse is first created, then the IR pulse is generated by optical parametric amplification. To spectrally narrow visible light, an etalon is used as described in the next section.

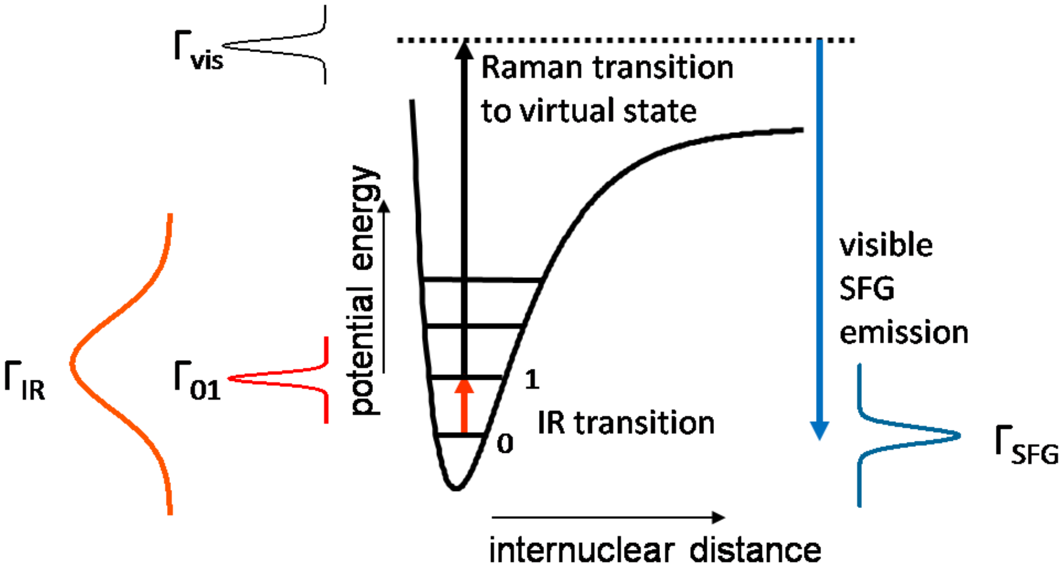

Figure 2.7 Schematic diagram of the sum frequency process in broadband SFG

2.2.2 Nonresonant background suppression

The SFG spectrum reflects the vibrational resonance at the interface, but it does not provide direct information on the molecular hyperpolarisability. This is because the surface electrons also respond to the incoming fields and generate so-called non-resonant SFG, which interferes with the light emitted resonantly by the adsorbate. The phase between the resonant and nonresonant contribution cannot be determined *a priori*, which makes the analysis of SFG spectra complex (see 2.2.3). Moreover, the SF signal reflects $|\chi^{(2)}|^2$, not $\chi^{(2)}$, which loses information of the sign. The accurate determination of $\chi^{(2)}$ requires an introduction of a local oscillator with known phase[117-119]. SFG spectroscopy with a local oscillator is known as heterodyne SFG and can provide the sign of $\chi^{(2)}$ which can reveal the absolute orientation of molecules at the interface[120,121].

The main origin of NR-SFG on metals is the surface dipole while dielectric media show a dominant bulk quadrupole contribution[122,123]. On a metal surface, NR-SFG depends on the frequency of the visible light and the substrate[124] which indicates that NR-SFG reflects the surface electronic structure in analogy to SHG. NR-SFG changes its intensity and relative phase by introducing adsorbates, because they can alter the surface electronic structure. Guyot-Sionnest *et al.* reported the reduction of the NR-SFG signal by CO adsorption onto a W(100) surface[125], the Somorjai group reported that the NR-SFG intensity and phase from Fe(111) surface depends on adsorbates[126]. For example, the relative phase between resonant and NR signals is inverted after oxidation of an iron surface. This change in phase by oxidation is observed on copper surfaces, during methanol synthesis[127] and initial oxidation of SAM[128-130]. It should be noted that oxidation does not always produce a phase shift, for example in the case of a Ru(001) surface, the phase is nearly constant before and after oxygen adsorption[131].

However, extracting information from NR-SFG is not easy and makes it more difficult to assign the resonant contribution. The Dlott group introduced a clever method to reduce the intensity of NR-SFG using an etalon[132,133]. The etalon allows us to change the shape of the visible pulse to upconvert specifically only the vibrationally resonant response. The idea of this scheme is shown in figure 2.8. At the time zero, an IR pulse generates a nonresonant and a resonant polarization. The latter decays over a few ps, the vibrational lifetime of the molecule, while the nonresonant polarization decays within a few fs. The etalon generates an asymmetric temporal profile as shown in figure 2.7. A Gaussian pulse can be also used as reported by Ishibashi *et al.*[134] and Stiopkin *et al.*[135], but is less efficient when compared with the use of etalon. It should be noted that Weeraman *et al.* proposed an inverted etalon pulse to suppress the nonresonant background[136].

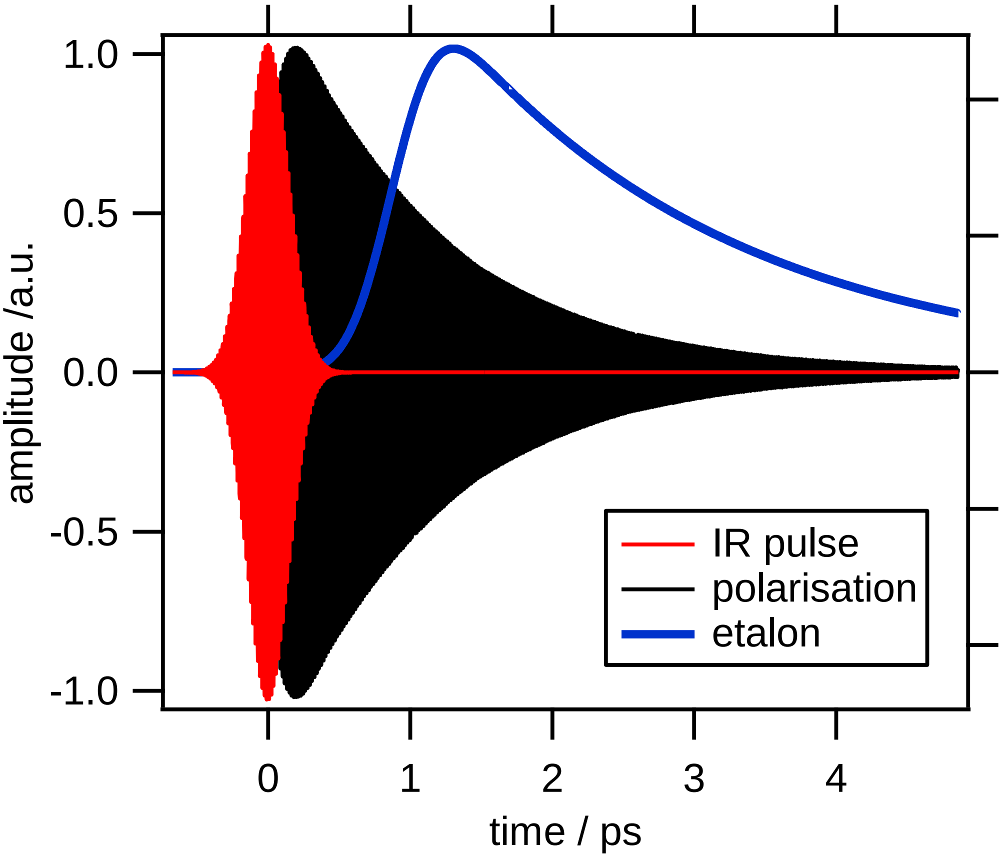

Figure 2.8 A temporal evolution of IR pulse, induced polarization and etalon pulse.

The construction of an etalon is very simple; two glasses are separated by an air gap *d* which is about 10 μm wide. These glasses give multiple reflections, to generate a pulse train. If the pulse train is shorter than the pulse width, a continuous pulse is achieved. The pulse train interval is $\tau_{RT} = 2d/c$ which is called the free spectral range (FSR). The phase difference δ between reflections depends on the incident wavelength λ_0 and the refractive index n between the two glasses, the incident angle θ and the thickness d [137],

$$\delta=\frac{4\pi}{\lambda_0}\cdot n\cdot d\cdot\cos(\theta). \qquad (2.15)$$

Constructive interference between pulses in the train leads to an exponentially decaying pulse shape with a decay time for the intensity of

$$\tau = -\frac{d\cos\theta}{c\ln R}. \qquad (2.16)$$

Here, R is the reflectivity of the glass. Our etalon characteristics are R=95.5 % and d=10.77 μm[138] resulting in τ=780 fs which corresponds to a spectral resolution of 6.9 cm^{-1}. The measured spectral resolution is 7.2 cm^{-1}. A more detailed discussion of pulse shape effects can be found in reference[135,138]. If this pulse is delayed sufficiently, then only resonant polarization is upconverted.

As an example of NR-SFG suppression, SF spectra of CO on the Cu(110)-(2×1)O surface are shown in figure 2.9. The resonant C-O stretch peak interferes with the NR background, resulting in a dip in the spectra. This resonant contribution is small compared to the nonresonant background making the analysis harder. If a time delay of 1.3 ps between IR and visible pulse is introduced to reduce the nonresonant background, the peaks appear at almost the same position of the dip. The centre frequency of the main peak is 2112.1 cm^{-1}, which is assigned to the C-O stretch mode of CO on Cu(110)-(6×2)O surface[139], rather than CO on Cu(110)-(2×1)O surface where the frequency of the C-O stretch mode should be 2105 cm^{-1}. We initially attempt to study CO on Cu(110)-(2×1)O, however, the sudden transition from 2093 cm^{-1} for CO on a bare Cu(110), to 2112 cm^{-1} for CO on Cu(110)-(6×2)O was observed. This can be explained by different Raman tensor or adsorption energy to oxidized surfaces. A second peak at 2083 cm^{-1} is also resolved in addition to the main peak at 2112,1 cm^{-1}. This peak is further characterized as a vibrational hot band by measuring the fluence dependence as shown in figure 2.9(b).

A hot band is a vibrational transition from an excited vibrational state as schematically shown in figure 2.10(a). If an incoming IR pulse is intense, the adsorbate interacts with the IR pulse more than once. The adsorbate absorbs the energy of the IR pulse to induce a vibrational transition. This transition populates the vibrational excited state, as shown in figure 2.10(b). If the adsorbate absorbs a second IR photon after the creation of the vibrational excited state, the vibrational transition from the first excited state to the second excited state (ν=1→2) becomes possible. This emits a SF photon with the sum frequency of visible and $\nu_{1\text{-}2}$. This transition is called hot band transition. The first observation of a hot band transition was from hydrogen on silicon surfaces[140,141], and then extended to metal surfaces. The ν= 1→2 vibrational hot band of the C-O stretch mode on Ru(001)[142] and Ir(111)[143] has also been reported.

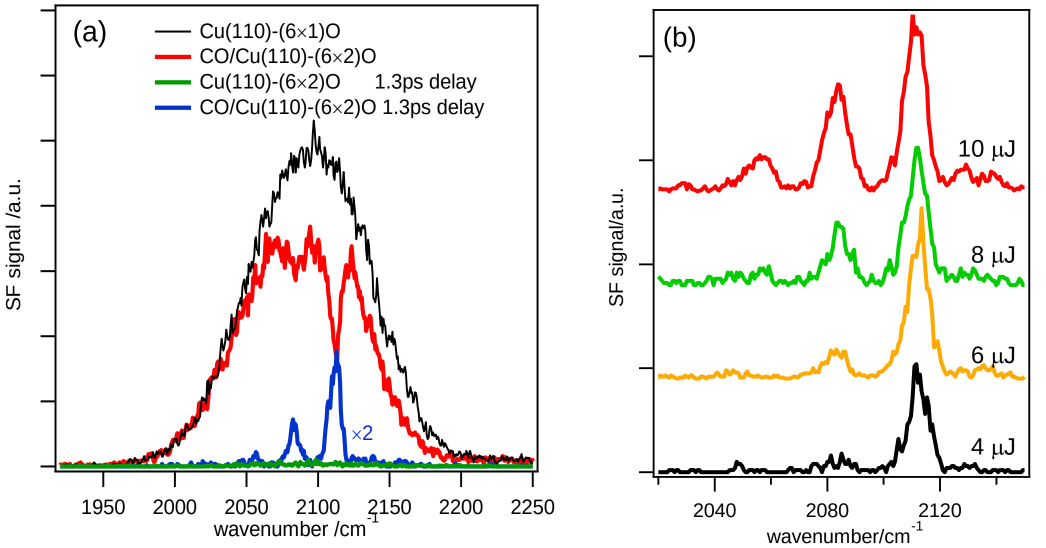

Figure 2.9 SF spectra from CO/Cu(110)-(6×2)O, (a) with different visible-IR time delays (b) as a function of IR fluence.

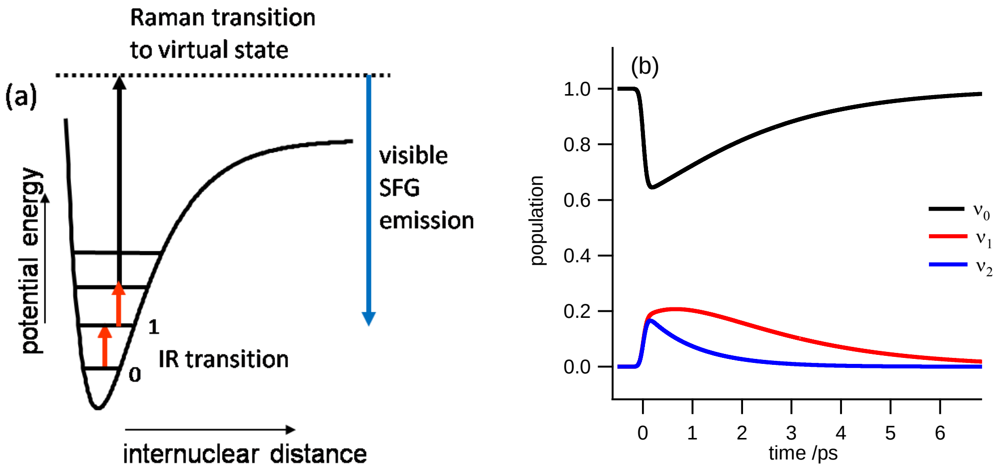

Figure 2.10 (a) Schematic diagram of the hot band transition. (b) A simulated population change of the vibrational states. The intense IR pulse arrives at time zero.

2.2.3 Fitting SFG spectra

The SF intensity is the square of the induced polarization from equation (2.13)

$$I_{SFG}(\omega)=|P^{(2)}(\omega)|^2 \qquad (2.17)$$

$\chi^{(2)}$ is written as a sum of a constant nonresonant term (if the visible SF frequency is far from electronic resonance) and Lorentzian term for the vibration[106]:

$$\chi^{(2)} = \chi_{Res}^{(2)} + \chi_{NR}^{(2)} = A_{NR}\, e^{i\phi_{NR}} + \sum_n \frac{A_n}{\omega_R - \omega_{IR} - i\Gamma_n} \qquad (2.18)$$

where A_{NR} and A_n are the amplitude of nonresonant and nth resonant susceptibility, ϕ_{NR} is phase of nonresonant susceptibility, ω_R is the resonance frequency and Γ is the linewidth. An inhomogeneous Gaussian contribution can be incorporated in the form of a Voigt function.

Fitting a single peak of the C-O stretch mode is trivial, as there are only two components: resonant and nonresonant, and the resonant contribution is much larger than NR-SFG. The centre frequency and linewidth of NR-SFG can be separately determined from a bare metal surface spectrum. The variable parameters for fitting are resonant frequency, linewidth, and height for resonant and nonresonant contributions. For our experiment, the etalon delay technique can almost completely remove the NR contribution.

2.2.4 Laser system for pump-probe experiments

The sub-picosecond pulse width of the laser allows us to perform pump-probe spectroscopy to reveal ultrafast phenomena. In pump-probe spectroscopy, two laser pulses are separated in time. The first pulse, called the pump pulse, induces a change in the system e.g. excites a vibration, increases electron temperature or induces desorption. The second pulse is called the probe pulse and measures the time evolution of the system. SFG spectroscopy is used as probe, which requires two laser pulses in the IR and visible region. The time delay between the three beams can be adjusted by changing the travel distance using translational delay stages. The rest of this section is devoted to explaining how to make femtosecond pulses with three different frequencies: IR, upconversion visible, and visible for pump beam. The details of the laser system and associated theory are well documented in Symonds' PhD thesis[22].

A temporally short laser pulse must contain the wide range of frequencies known from the inverse Fourier transform relationship. This can be achieved by the constructive overlap of different frequency pulses in the laser cavity. This process is called mode locking, and is done in the Ti:Sapphire (Ti:S) oscillator. The Ti:S oscillator produces femtosecond laser pulses with nJ fluence. These pulses have to be amplified to mJ by chirped pulse amplification (CPA). The laser pulse is first stretched in the time domain by a grating to induce different frequencies to travel different path lengths. This avoids damage to the optics in the amplification process and pulse distortion by higher order effects by stretching the pulse to 200 ps, thus lowering its intensity. This chirped pulse is amplified in a Ti:S crystal pumped by Nd:YAG laser. Finally, the chirped pulse is compressed in time. The beam shape, pulse width and pulse front tilt can be measured by frequency resolved optical gating (FROG)[144].

A 150 fs femtosecond 800 nm pulse is amplified to about 10 mJ. This beam is split into three parts. Two of them travel to the two TOPAS (traveling-wave optical parametric amplifier of superfluorescence). TOPAS has two stages to create tunable pulses. In the first stage, optical parametric amplification creates tunable visible pulses, called signal and idler, with photon energies which add up to the photon energy of the 800 nm beam, for example:

$$\frac{1}{800\ \mathrm{nm}} = \frac{1}{1380\ \mathrm{nm}} + \frac{1}{1900\ \mathrm{nm}}$$

Next, the signal and idler pass into a second section which generates their difference frequency in an $AgGaS_2$ crystal. This process creates the tunable IR pulse.

$$\frac{1}{1380\ \mathrm{nm}} - \frac{1}{1900\ \mathrm{nm}} = \frac{1}{5000\ \mathrm{nm}}$$

In this example, signal and idler produce light at 5 μm = 2000 cm^{-1}, which is suitable to observe the internal stretch mode of CO. A second TOPAS creates a tunable visible pulse. In the second stage, a BBO crystal produces SFG, DFG or SHG from a combination of signal, idler and residual 800 nm pump pulse to cover a range from 250 nm to 2400 nm.

2.2.5 Setup and alignment

Experiments were performed with an amplified 10 Hz femtosecond laser system combined with an ultra-high vacuum chamber[22,145] as shown in figure 2.11. A *Millennia Pro* diode-pumped laser (532 nm, 5.75 W) pumps the *Tsunami* Ti:sapphire (Ti:S) oscillator to generate 90 fs, 800 nm pulses at 82 MHz repetition rate. This pulse is amplified in a Ti:S amplifier (TSA-10) which is pumped by a frequency doubled Nd:YAG laser at a repetition rate of 10 Hz. The amplifier produces 150 fs pulses of 10 mJ, which enter the two TOPAS to produce tunable mid-IR and visible pulses. The mid-IR wavelength can be tuned from 3-11 μm with 200 fs pulse width, and visible to near IR wavelength from 200-2400 nm. In this thesis, 800 nm, 532 nm and 400 nm pump pulses are used. The remainder of the 800 nm pulse is passed through an etalon (SLS Optics) to produce an upconversion pulse of about 7 cm^{-1} spectral width, time-shifted by 1.3 ps to reduce the nonresonant sum frequency signal[133]. The reported delay time is the time between the pump pulse and the infrared pulse. All three beams are p polarized with an average incidence angle of 67° and 5° difference between the pump pulse and the collinear 800 nm and IR beams. The visible pulse may exceed the damage threshold of the sample. The intensity of visible pulses can be decreased by the combination of zero order half-waveplate and polarizing beam splitter. The IR and visible pulses pass through a dichroric mirror for collinear incidence on the crystal.

It is not trivial to align the laser into the UHV chamber. Firstly, an equivalent position to the sample crystal is needed to align the laser outside the chamber. This guides the laser pulse through a flipped mirror and lens to focus onto the sample crystal. Secondly, a pinhole is placed at the equivalent position. If all three beams go through the pinhole, spatial overlap is achieved. Thirdly, after obtaining spatial overlap, the pinhole is replaced with a non-linear crystal. Mechanical delay stages with mirrors permit adjustment of the temporal delay, which is optimized by maximizing SFG or DFG of the beams in the nonlinear crystal. Finally, this light is traced by a HeNe laser, which then traces the SFG path from the UHV chamber to the detector.

Further alignment in the UHV chamber is performed using the SF signal from a saturated CO/Cu(110) sample and nonresonant IR-IR-visible sum frequency signal. The mid-infrared and visible upconversion pulses generate a nonresonant $\chi^{(3)}$ signal at $2\omega_{IR}+\omega_{VIS}$, which can be detected at 600 nm. This infrared-infrared-visible (IIV) sum frequency signal is reduced by the pump pulse. Figure 2.12 shows the nonresonant IIV-SFG signal as a function of time delay between pump and SF probe signal, together with calculated electron temperature convoluted by the 200 fs width of the infrared pump pulse. The reduction in IIV-SFG follows the calculated electron temperature and is likely caused by a temperature-dependent $\chi^{(3)}$, similarly to the electron temperature dependent $\chi^{(2)}$ response observed for Cs/Ir(111)[24].

A narrow band pass filter is placed before the spectrograph to cut the residual visible pulse. The SF signal is detected by an intensified charge-coupled device (ICCD I-Star from Andor) on an Acton 0.3 m imaging spectrograph with a dispersion of 0.6 cm^{-1}/pixel.

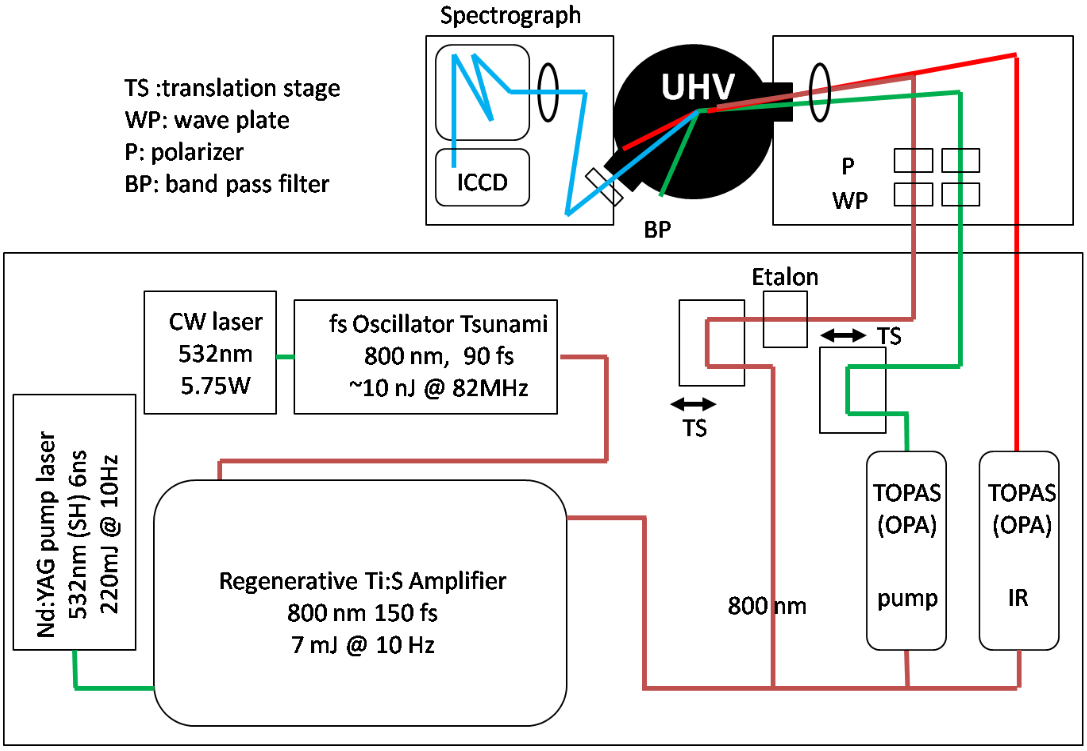

Figure 2.11 Schematic of setup for pump-probe SFG

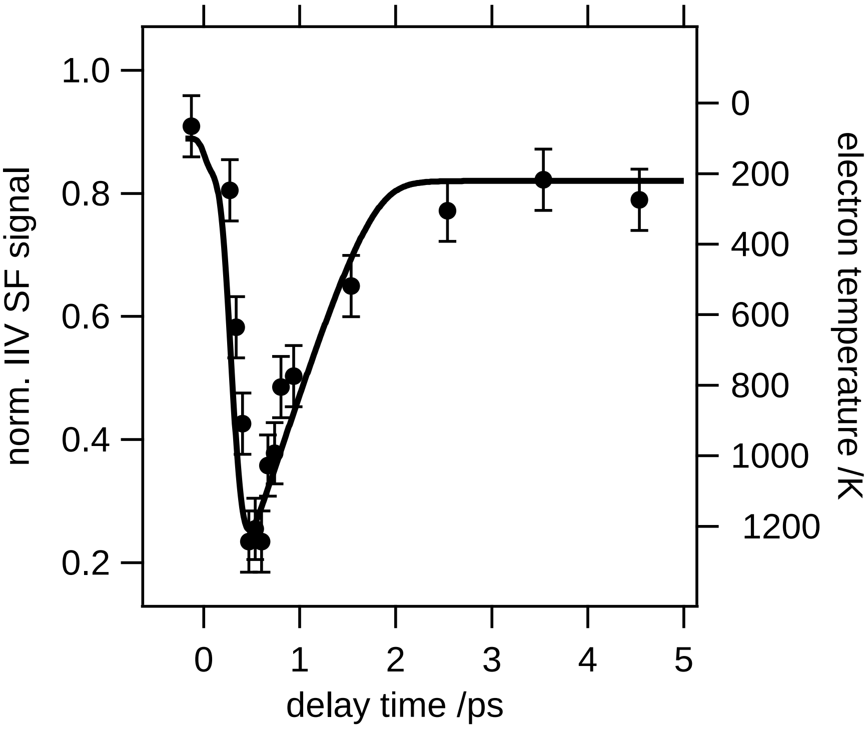

Figure 2.12 Nonresonant IR-IR-visible sum frequency signal as a function of time delay between a 400 nm pump pulse (absorbed 10 Jm^{-2}) and femtosecond SF probe pulses. The solid line is the scaled convolution of the electron temperature with a 200 fs probe pulse.

2.3 Scanning tunneling microscopy

After the invention of the STM by Binnig and Rohrer in the early 1980s[146,147], this atomic resolution microscope became a powerful tool to understand the structure, properties and chemical reactions at solid surfaces. A key component of STM is the tip. An atomically sharp metallic tip is brought close to a conductive sample. By applying a voltage to create a small potential difference between the tip and the sample, electrons tunnel between them. In the experiments of this thesis, the bias voltage V_s is applied to the sample. Alternatively, the voltage bias can be applied to the tip. The exponential decay of the wave functions from the tip/sample into the vacuum gap provides a sufficient overlap when their distance is about 1 nm apart; at this point a tunneling current (I_t) can be measured. The tip is scanned across the sample surface by using a piezo-electric tube, which typically expands/contracts by 0.1 nm per millivolt[67]. The tunneling current varies with tip-sample distance (z) which reflects the corrugation of the surface. The current decreases by approximately an order of magnitude with an increase of distance z by 1 Å.

2.3.1 Theory

Classically, the electrons in the solid require a minimum energy to escape into the vacuum which is known as the work function and is typically several eV. However, when the tip-sample distance becomes less than 1 nm, electrons are able to pass through the vacuum gap, known as electron tunneling. Electron tunneling was demonstrated in the 1960s by Giaver, and this work led to the demonstration of vacuum tunneling in the early 1970s[148]. Figure 2.13 displays an energy level diagram for an STM tip close to a conductive substrate. The grey shaded area shows the occupied states of the sample and tip. Without applied bias, the vacuum levels of tip and sample line up. A positive bias applied to the sample lowers its Fermi level and electrons can transfer from the tip into the unoccupied states of the sample as shown in figure 2.13(b).

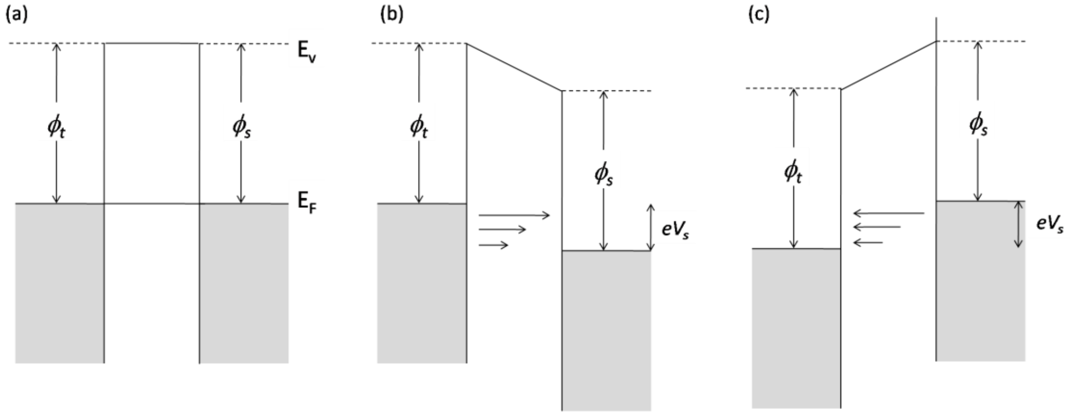

Figure 2.13 Energy diagram of a metallic tip and a metal substrate. (a) before applying voltage, (b) positive V_s is applied, (c) negative V_s is applied.

Quantitative understanding of tunneling current between the tip and the sample can be gained by quantum mechanics. Here, the basic theory of tunneling is described. For full description of the theory, the reader is guided to other references[75,148-150]. In quantum mechanics, an electron with energy E in a one dimensional rectangular barrier U satisfies the Schrödinger equation,

$$-\frac{\hbar^2}{2\mathrm{m}}\frac{\mathrm{d}^2}{\mathrm{d}^2\mathrm{z}}\varphi(z)+U(\mathrm{z})\varphi(\mathrm{z})=E\varphi(\mathrm{z}) \qquad (2.19)$$

where $\varphi(z)$ is the wavefunction of the electron. Equation (2.19) for the classically allowed region, E>U is:

$$\varphi(\mathrm{z})= \varphi(0)\ \exp(\pm\mathrm{ikz}) \qquad (2.20)$$

where the wave vector k can be written as

$$\mathrm{k}=\frac{\sqrt{2\mathrm{m}(\mathrm{E}-\mathrm{U})}}{\hbar}. \qquad (2.21)$$

On the other hand, in the classically forbidden region E<U, φ can be written as

$$\varphi(\mathrm{z})= \varphi(0)\ \exp(-\kappa\mathrm{z}) \qquad (2.22)$$

where κ is the decay constant given by,

$$\kappa=\frac{\sqrt{2\mathrm{m}(\mathrm{U}-\mathrm{E})}}{\hbar}. \qquad (2.23)$$

The above equation shows the electron can penetrate the potential barrier, and the probability density is proportional to $|\varphi(0)|^2\ \exp(-2\kappa z)$. The height of the barrier U is the average of the workfunctions of tip and sample: $\Phi=\frac{1}{2}(\Phi_t + \Phi_S)$. If the applied bias voltage V_S is much smaller than the workfunction, the decay constant κ can be approximated by:

$$\kappa = \frac{\sqrt{2\mathrm{m}\Phi}}{\hbar}. \qquad (2.24)$$

Using eV as the unit of the work function Φ and Å^{-1} as the unit of the decay constant, κ can be written as

$$\kappa = 0.5\sqrt{\Phi(eV)}\ \text{Å}^{-1}. \qquad (2.25)$$

Metal surfaces have a work function of typically 4-5 eV[151]. Thus, for every Angström increase in the tip-sample distance, the tunneling current will decrease by about one order of magnitude.

The tunneling current is proportional to the number of states in the sample in the energy range E_F-eV_s which can be written as,

$$I_t \propto \sum_{E_n=E_F-eV_s}^{E_F} |\varphi_n(0)|^2 \exp(-2\kappa a) \qquad (2.26)$$

where a is the tip-sample distance. If V_s is small enough for the density of states between E_F and E_F-eV_s to remain constant, the tunneling current can be expressed by using the local density of states (LDOS) at the Fermi level, $\rho_S(z, E_F)$, which is defined as the number of electrons per volume per energy, at a given point in space and at a given energy, as

$$\rho_S(z, E_F) = \frac{1}{eV_s} \sum_{E_n=E_F-eV_s}^{E_F} |\varphi_n(z)|^2. \qquad (2.27)$$

The tunneling current is then given by,

$$I_t \propto V\rho_S(0, E_F) \exp(-2\kappa a). \qquad (2.28)$$

Equation (2.28) shows that tunneling current I_t depends on the LDOS of the surface and shows exponential decay in distance. For a more accurate description, the effect of the tip LDOS needs to be considered which is achieved by Tersoff and Hamann[152,153] who applied the Bardeen approach[154] to the tip-vacuum-sample system.

2.3.2 **STM imaging**

There are two operation modes for STM imaging, constant-current or constant-height as shown in figure 2.14. In constant-current mode, the measured current I is compared to a preset current by a feedback circuit. Once the tunneling current changes due to a variation of topography or electronic structure at the surface, the feedback system reacts and changes the tunneling current back to the original value (set point). The feedback signal is recorded together with the x-y position of the tip while scanning the surface. An image obtained in the constant current mode reflects the variations of LDOS of the surface. In constant-height mode, the tip-sample distance z remains constant and the tunneling current is recorded during the scanning of the surface. Generally, the constant-current mode provides better resolution while the constant-height mode allows faster scanning. The STM images in this thesis were obtained using constant current mode.

An STM image can provide rich information on the adsorbate. For example, an STM image of CO on Cu(110) is shown in figure 2.15. CO molecules appear as darker circles showing their apparent relative height is lower than other areas of the copper surface. This does not mean CO dents the surface. As discussed in the previous section, tunneling current depends on the tip-sample distance and also on the DOS of tip and sample. The apparent lower height reflects a lower DOS around the Fermi level at the CO molecule. CO molecules do not form a molecular island structure due to repulsive interactions, but form dimer and longer molecular chains predominantly along the [001] direction[78]. The lower apparent height at the edge of chains indicates that DOS is localized in the centre of a chain.

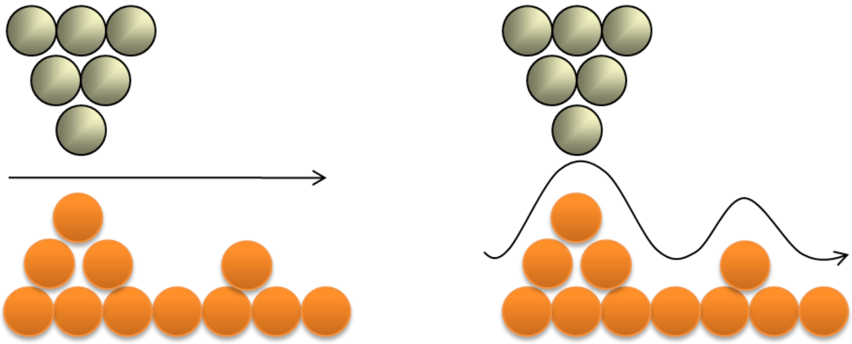

Figure 2.14 Schematic representation of (left) constant height, (right) constant current mode.

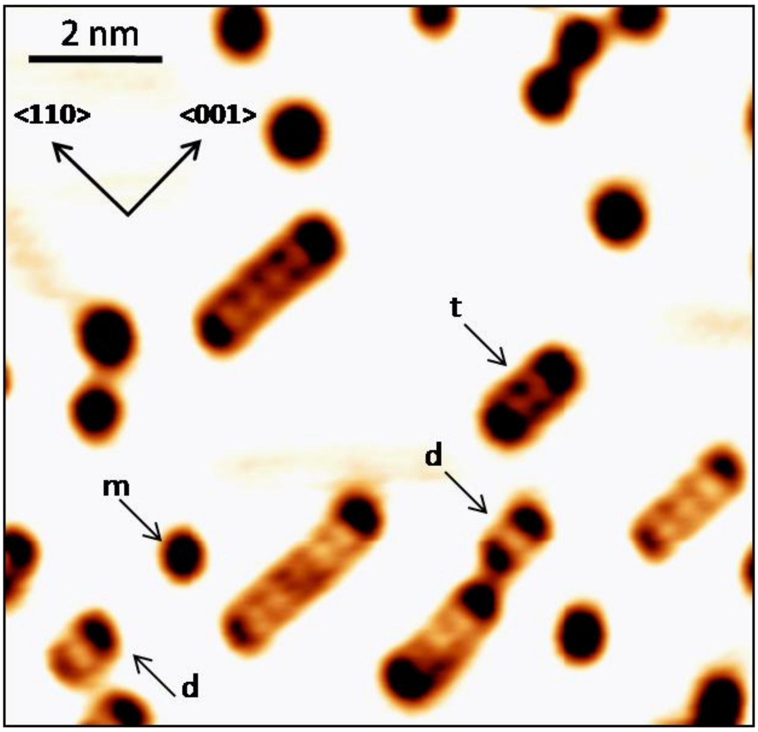

Figure 2.15 STM image of 0.03 ML CO on Cu(110) at 4.7 K, V_s=0.1 V, I_t=1 nA. Labels m,d,t corresponds to CO monomer, dimer and trimer, respectively.

2.3.3 Scanning tunneling spectroscopy

The tunneling current is proportional to the LDOS at the surface. Thus, applying a voltage ramp to the tunneling junction (with feedback loop off) can yield the LDOS. This is known as scanning tunneling spectroscopy (STS) or dI/dV spectroscopy. Since DOS is derived from the dispersion relationship between energy and the momentum of electrons, the amplitude of tunneling current reflects the DOS at each bias voltage. The spectroscopic signal dI/dV can be directly obtained by a lock-in amplifier technique[155,156]. For dI/dV measurement, the maximum applied bias should be smaller than the work function of tip and sample. If V_s becomes comparable to the work function of tip or sample, then the transmission coefficient depends on the sample bias in an exponential manner. An alternative method is dZ/dV measurement which measures tip-sample distance z against V_s for a work function measurement.

Experimentally, the STM tip is positioned over the target point, setting I and V_s, with feedback loop off, then a triangular wave is applied as DC offset using a function generator. The oscilloscope and the lock-in amplifier record I-V and dI/dV curves, respectively. Typical parameters for STS are modulation frequency 797 Hz, modulation amplitude 40 mV, initial current (I_0) 50-500 pA, and initial voltage (V_0) 0.1-1 V.

2.3.4 Action spectroscopy with STM

If DOS of tip and sample are constant over the measured energy range, the tunneling current depends linearly on the applied sample bias voltage in an elastic process. Inelastic electron tunneling occurs when electrons from the tip enter specific quantum states of atoms or molecules. This process can be used to detect vibrational or electronic excitations of molecules, known as STM inelastic tunneling spectroscopy (STM-IETS)[157]. The IET process occurs by electron trapping into a molecular orbital to form a tentative ion resulting in a change in potential energy surface, analogous to resonant scattering in HREELS[158,159].

The excitation of vibrational modes or electronic transitions can induce a motion of the atom or molecule. This motion occurs with a certain reaction probability at each applied bias voltage. If the reaction yield (Y) is measured as a function of applied bias, “action spectra” are obtained[120]. Action spectra reflect the active vibrational modes or electronic states that are responsible for the given motion. The yield Y is often described as the probability per electron to trigger adsorbate motion. The adsorbate motion can be detected by subsequent STM imaging. Quantitatively, it is possible to estimate the reaction yield per electron from the change in the conductance, as shown in the schematic of figure 2.16. The threshold obtained from a Y(V_s) curve reveals the energy required to activate the motion.

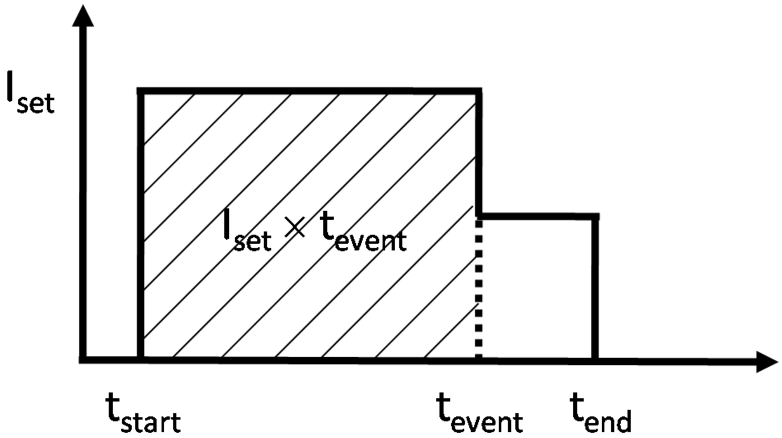

Figure 2.16 Schematic representation of I-V trace for a single pulse to detect an event. The shaded area corresponds to the total number of tunneling electrons before the reaction happens.

Molecular motion caused by STM-IET was first investigated by the Ho group[160,161]. The concept of STM action spectroscopy (STM-AS) was later introduced by Kawai *et al.*[162] and developed mainly for vibrational spectroscopy[27,28,160,161,163,164], but also used for electronic transitions[30,165,166]. As a microscopic vibrational spectroscopy, IET can also be utilized to detect the vibrational differential conductance known as STM-IETS[167,168], in contrast STM-AS can detect a vibrational signal from a vibration-mediated reaction. An advantage of STM-AS over STM-IETS is the higher intensity of reaction yield compared to conductance change, because the reaction yield reflects vibrational DOS at the responsible vibrational energy for the observed reaction[164,169] while STM-IETS detects d^2I/d^2V signal resulting from a few percent of differential conductance change.

STM-AS has been used to identify the mechanism of chemical bond breaking, such as the dissociation of trans-2-butene on Pd(110)[27] and $(CH_3S)_2$ on Cu(111)[28] by the excitation of C-H stretch mode, and the dehydration of $CNHCH_3$ on Pt(111) by electron attachment to the LUMO (π* orbital)[165]. The combination of STM-AS and dI/dV spectra allows us to experimentally reveal the correlation between the reaction mechanism and the local electronic structure, for example Henzel *et al.* proposed that the isomerization of an azobenzene derivative is caused by electron injection into the LUMO+1 state[166].

The experimental procedure is as follows. First, an STM image is collected and the STM tip fixed to the point of the measurement with the feedback loop off. Then, the bias voltage is set to zero for a few tens of milliseconds to stabilize the STM junction at zero current. Next, tunneling electrons are injected into the molecule at a certain V_s until a reaction or adsorbate motion appears as change in the tunneling current I_t, as shown in figure 2.17. The sudden change of I_t around 0.6 sec from 5 nA to 1 nA indicates the desorption of CO from

CO-RuTPP/Cu(110) in this case. The event is confirmed using the subsequent STM imaging. The time required for the single event *t* can be obtained directly from the current trace. The distribution of *t* for a number of events follows an exponential distribution because the reaction probability per time should be constant:

$$f(t) = \frac{1}{\tau}\exp\left(-\frac{1}{\tau}t\right) \tag{2.29}$$

where τ is the time constant which can be obtained from the experimentally measured distribution of *t* by fitting.

The number of injected tunneling electrons n_e to induce an event is calculated by $n_e = t \times I/e$, where e is the elementary charge (1.602×10^{-19} C). The reaction yield Y is then determined as $1/n_e$ [160]. The τ can be treated as simply an average of *t*, if *t* follows the exponential distribution[164,170]. A sufficient number of events should provide the averaged *t* close to the expected value of the exponential distribution given by

$$E_t = \int_0^{\infty} t\, f(t)dt \ = \tau. \tag{2.30}$$

The resulting E_t is identical to the time constant τ obtained by exponential fitting. Thus, τ and Y can be obtained by measuring the average of *t* if the reaction probability is constant and/or *t* follows the exponential distribution. The desorption yield Y was calculated from $Y = e/I_t$. The averaged values of Y(V) were obtained by repeating the aforementioned experiment, typically ten times for each V_s.

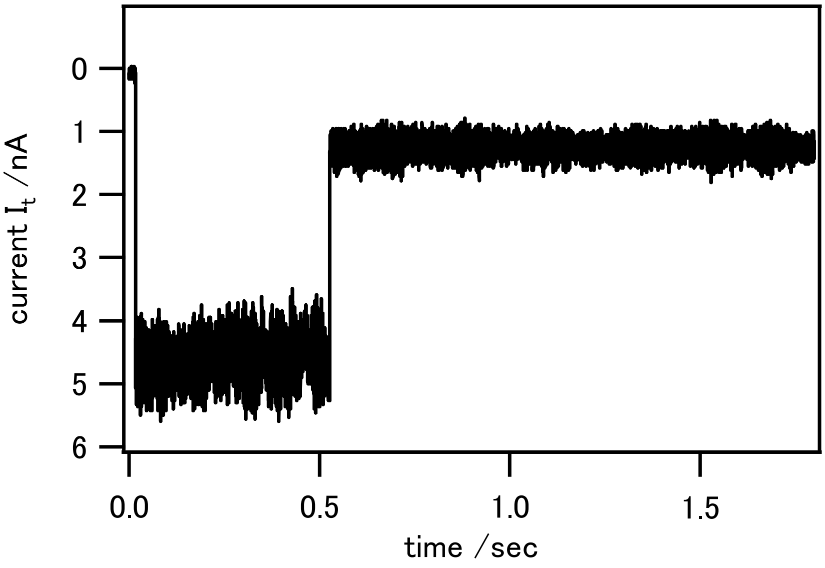

Figure 2.17 A typical current trace for desorption of CO from CO-RuTPP on Cu(110).

2.3.5 Setup

- **Omicron-LT STM**

All STM experiments at 4.7 K and 77 K have been performed in RIKEN, Japan, with Omicron-STM. The Omicron design of the STM scanner uses a single piezo tube, which was first reported by Binnig and Smith in 1986[171]. The single tube design has become popular due to its compact and simple structure. The sample is fixed in the Omicron LT-STM (and also SPEC-STM for room temperature experiments) and the tip is scanned. When a voltage is applied, the tip is moved by piezoelectrics which expand/shrink with sub-nano meter precision. In addition, the coarse motion of the scanner is also required to approach/retract the tip to/from the sample on a cm scale, to enable sample/tip exchange. The coarse motion is operated by X/Y- and Z- sliders, which use piezoelectric bars to control the movements.

- Topographic images

The topographic images were acquired with Omicron SCALA PRO software (or SPECS software for RT-STM) and were processed by the WxSM program provided by Nanotec[172]. Images presented in this thesis were acquired in constant current mode. The calibration of length and angle is performed with a reference clean Cu(110) surface image. The *plane* function is used to correct the slope of the scan. The *flatten* and the *smooth* function are also used for some of the images to improve the quality of image contrast. The typical scanning conditions were V_s=50-1500 mV, I_t=0.01-1.0 nA, and a scan speed of 3-5 Hz. An oscilloscope (Waverunner, NF) for current trace, function generator (Wavefactory WF1945, NF) for controlling current in STS and lock-in amplifiers for recording dI/dV signal were also installed in the system. The schematics of the whole STM measurement system are shown in figure 2.18.

- Cryostat and vibrational isolation

The room temperature STM image is often affected by thermal drift; the scanning position moves due to the temperature difference between the tip and the sample. To minimize the thermal drift, cryogenic temperatures are required. A double cryostat system was used in the Omicron STM chamber at RIKEN, where outer and inner cryostats are filled with liquid nitrogen and helium (^{4}He), respectively, to achieve 4.7 K for the STM head and tip. Copper cylindrical shields are mounted around the scanner head to reduce radiative heating. The temperature is monitored using a silicon diode sensor. The entire apparatus is held by vibration-isolators with constant nitrogen gas feed, which allows the system to be decoupled from the ground. For further vibration-isolation, the STM head is suspended by three wires from the top of the chamber during scanning.

- UHV system for STM

As with other UHV systems, the vacuum is maintained by a turbomolecular pump, an ion getter pump, and a Ti-sublimation pump. The turbomolecular pump is switched off during STM measurement to avoid interfering noise, and only an ion getter pump is used to maintain UHV. The STM chamber and the preparation chamber are separated by a gate valve and each chamber has its own pumping system, with which the base pressure is kept at 1×10^{-10} Torr (preparation chamber) and 3×10^{-11} Torr (STM chamber). A loadlock chamber was also attached for introducing samples into the UHV system. The samples and the STM tips can be transferred between the three chambers with a magnetically coupled transfer rod.

- Tip preparation

An electrochemically etched tungsten tip is used for STM measurement, due to its mechanical stiffness and flat DOS near E_F. A tungsten wire with a diameter of 0.15 mm is etched in NaOH solution using a commercial tip making device (TM59060, JEOL) in which a voltage is applied to the tip for etching, and automatically stopped when the edge of the tip falls apart. The sharpness of the tip apex is confirmed by an optical microscope prior to UHV installation. The tip apex is initially covered with oxide and impurities, which inhibit STM performance. Further treatment of the tip is required in UHV. There are two methods to change the tip condition. One is applying a high voltage pulse (10 V) for a large degree of change and another is a soft crash to a sample for a smaller degree of change. For STS or STM-AS, the linearity of the I-V curve is critical to obtain reliable spectra, which should be confirmed prior to measurement. A good tip provides linear and symmetric I-t and I-V curves.

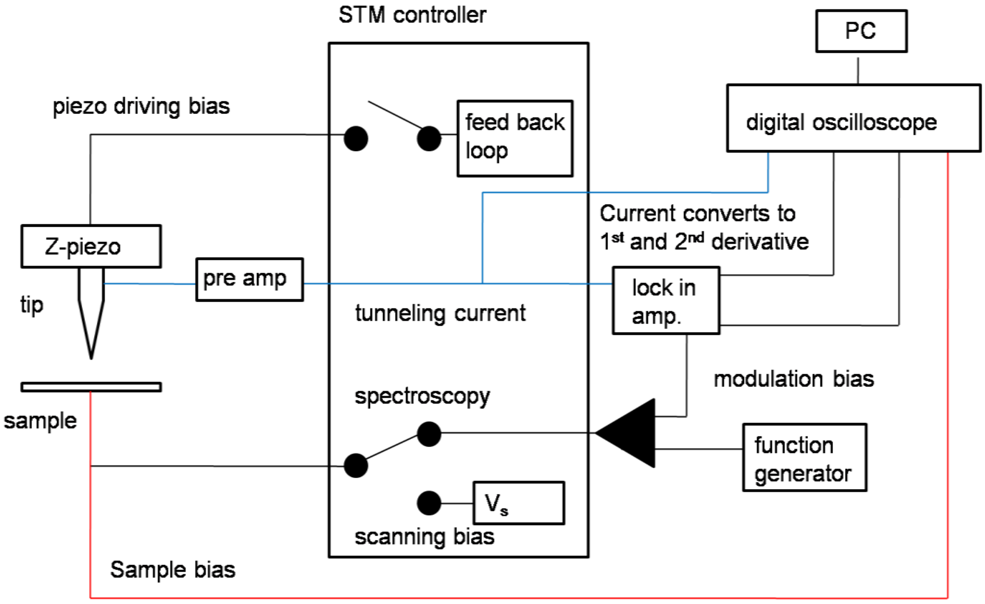

Figure 2.18 Schematic representation of STM imaging and spectroscopy measurement system.

Chapter 3

Coverage dependent non-adiabaticity of CO on a copper surface

In this chapter, SFG studies of CO/Cu(110) surface are presented together with relevant theoretical background. The coverage-dependent energy transfer dynamics between hot electrons and CO on Cu(110) were studied by femtosecond visible pump, sum frequency probe spectroscopy. Transients of the C-O stretch frequency display a red shift, which increases from 3 cm^{-1} at 0.1 ML to 9 cm^{-1} at 0.77 ML. Analysis of the transients reveals that the non-adiabatic coupling between the adsorbate vibrational motion and the electrons becomes stronger with increasing coverage. This trend requires the frustrated rotational mode to be the cause of the non-adiabatic behavior, even for relatively weak laser excitation of the adsorbate. The coverage dependence is attributed to both an increase in the adsorbate electronic density of states and an increasingly anharmonic potential energy surface caused by repulsive interactions between neighboring CO adsorbates. This work thus reveals adsorbate-adsorbate interactions as a new way to control adsorbate non-adiabaticity.

3.1 Introduction

An important part of current surface dynamics is concerned with energy transfer between substrate and adsorbate through non-adiabatic coupling between substrate electrons and adsorbate nuclear motion[52]. It occurs on timescales of femto- to picoseconds and is the focus of surface femtochemistry[6]. Of particular interest have been non-adiabatic reaction channels leading to thermally inaccessible pathways, such as hot electron induced CO_2 production[173] or CO diffusion[174]. Hot electrons are not the sole concern of surface femtochemistry, but also play a major role in plasmon-enhanced photochemistry[10,175].

Despite numerous studies establishing the presence of the phenomenon[6,90,176], it is still unclear why certain adsorbate/metal systems will behave more non-adiabatic than others and whether the degree of coupling can be predicted or even controlled. Only few studies have addressed this challenge and made a link to traditional surface reactivity concepts: adsorbates on step sites couple more strongly to hot electrons than adsorbates on terrace sites due to a higher adsorbate-projected density of states at the Fermi level, as shown for CO and NO on platinum[26]; NO exhibits faster coupling to hot electrons than CO on iridium since its unoccupied states are closer to the Fermi level[25]; the number of vibrational states participating in the hot-electron induced reaction strongly influences the reaction rate[177]; adsorbates with higher desorption energy couple more strongly to hot electrons[178]. A key concept in surface science presently without a surface femtochemistry equivalent is the use of adsorbate-adsorbate interactions to control reactivity[179]. Here it is demonstrated that non-adiabaticity can be controlled through adsorbate-adsorbate interactions by the relatively simple means of changing adsorbate coverage.

A widely studied model system in this field is CO on copper surface, because the internal stretching vibration shows a clear non-adiabatic response to femtosecond pulses well below the desorption threshold[18,19]. Femtosecond laser heating of metal surfaces disturbs the electron-phonon equilibrium and generates a hot electron bath with a temperature of around a thousand Kelvin for a few picoseconds (figure. 3.1). The faster the observed vibration changes frequency, the more non-adiabatic the observed process[90]. Copper is an ideal substrate to separate electron and phonon driven processes in the time domain due to a relatively small electron-lattice coupling constant[12]. The coupling between the C-O stretch and hot electrons is not direct, but instead is thought to occur via anharmonic coupling to a low frequency mode, the frustrated translation (FT), which in turn couples to both hot electrons and phonons on a time scale of a few picoseconds[18,19]. Coupling to hot electrons via other low frequency modes such as the frustrated rotation (FR) has only been inferred at higher excitation densities that cause diffusion or desorption[21,59]. Transients generally show a faster response when the FR is involved[56], due to more efficient coupling to electron-hole pairs[47]. Figure 3.1 shows a cartoon of the modes, coupling times and anharmonic couplings involved.

Both the frustrated translation and rotation experience characteristic changes with increasing CO coverage on copper which can potentially alter the degree of non-adiabatic coupling. The FT mode couples much more effectively to phonons at high coverages, as seen by a fourfold decrease in its lifetime measured by helium atom scattering (HAS)[180,181]. Increasing coverage also leads to an increasing coupling between FT and FR for CO/Cu(100)[182], as neighboring CO molecules restrain the vibrational motion, such that it becomes more wagging- than translation-like. This distance-dependent effect should be present on any of the copper surfaces with increasing coverage and would lead to faster coupling to hot electrons as the FR becomes involved.

In this chapter, the results of visible pump- SF probe spectroscopy reveals that the transients do indeed depend on adsorbate coverage, and that they are best described by more densely packed CO layers coupling more strongly to substrate hot electrons, not phonons. Therefore the coupling mode responsible for the non-adiabatic behavior has to involve the frustrated rotation, even at comparatively low excitation of the substrate electrons. The effect of lateral CO-CO interactions on CO orientation and the degree of backdonation into the CO 2π* level will be discussed in detail. Interactions between adsorbates emerge as a new way to control non-adiabaticity, in particular on noble metal surfaces.

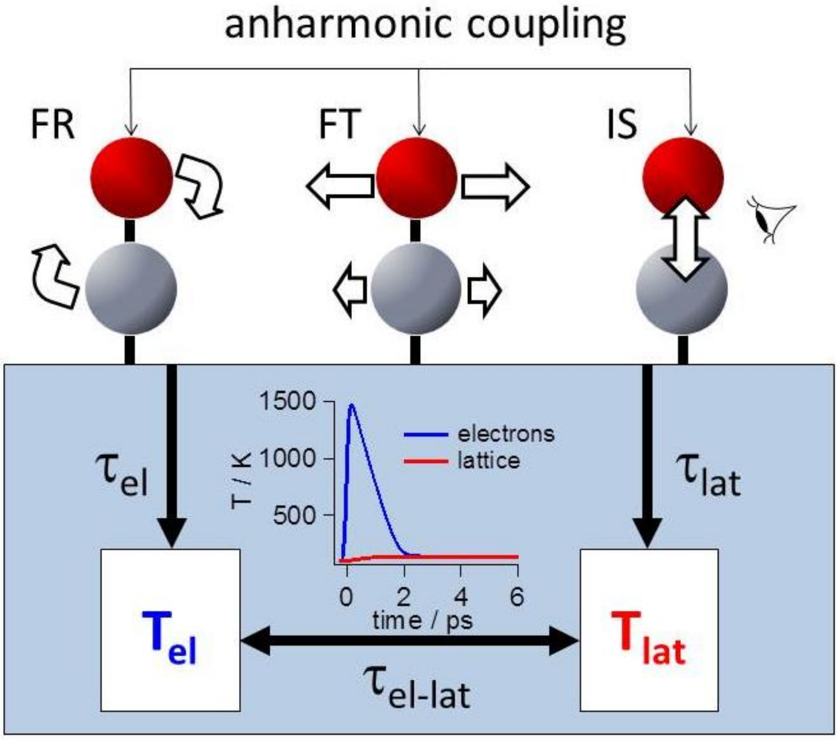

Figure. 3.1. Schematic diagram of the non-adiabatic behavior of CO on a metal surface. A femtosecond laser pulse creates a hot electron bath for a short time, as shown in the inset, with a time scale determined by electron-phonon coupling ($\tau_{el\text{-}lat}$). The adsorbed CO couples to hot electrons and hot phonons with two different coupling constants (τ_{el},τ_{lat}). In the experiment, the internal stretch (IS) was observed, which anharmonically couples to the frustrated translation (FT) and/or frustrated rotation (FR). A shorter coupling time to hot electrons means a higher degree of non-adiabaticity.

3.2 Experimental

Broadband infrared-visible sum frequency generation (SFG) is used to probe changes in the C-O stretch vibrational frequency and line width on sub picosecond time scales, as described in chapter 2. TOPAS optical parametric amplifier generates 200 fs mid-IR pulses and also creates a 150 fs 400nm pump beam from a β-BaB_2O_4 crystal. The remainder is passed through an etalon (SLS Optics) to produce an upconversion pulse of about 7 cm^{-1} spectral width, time-shifted by 1.3 ps to reduce the non-resonant sum frequency signal[133].

A Cu(110) single crystal was cleaned by Ar^+ bombardment at 1 keV, followed by annealing to 600 K. Surface cleanliness was confirmed by a sharp (1×1) low energy electron diffraction (LEED) pattern and temperature programmed desorption (TPD). CO coverage is determined through TPD and C-O frequency shift with reference to the saturation coverage of 0.77 ML[82,183]. The lowest coverage of 0.1 ML is prepared by annealing a saturated layer to 185 K. Annealing to 165 K produces a coverage of around 0.25 ML with a well-developed (2×1) LEED pattern due to formation of (2×1) islands below the nominal 0.5 ML coverage.

All sum frequency spectra shown were recorded at 100 K substrate temperature unless otherwise mentioned, with 200, 400 or 1000 shots at each delay time for saturated, 0.25 ML and 0.1 ML coverage, respectively. Unpumped sum frequency spectra were recorded every 10 minutes to confirm long term stability of the surface layer.

3.3 Results

3.3.1 Static temperature dependence

In order to analyze the measured transients, it is required to know how much the C-O frequency changes when the coupling mode is excited, which can be studied by simply measuring substrate temperature dependence frequency shift. For CO on Cu(100), the internal stretch couples to the frustrated translation, not the rotation, when electrons and phonons are in equilibrium, as shown by low temperature infrared spectroscopy[184]. The anharmonic coupling constant to the FT mode, Γ_{14}, can be derived from[19],

$$\nu_1 = \nu_1^0 - \Gamma_{14} < n_4(T) > \tag{3.1}$$

where ν_1 and ν_1^0 are the frequency of the C-O stretch mode at temperature T and 0 K, respectively and $<n_4(T)>$ is the population of the FT mode at temperature T. The equivalent anharmonic coupling constant is determined here for CO/Cu(110) from the frequency data shown in figure 3.2 (left).

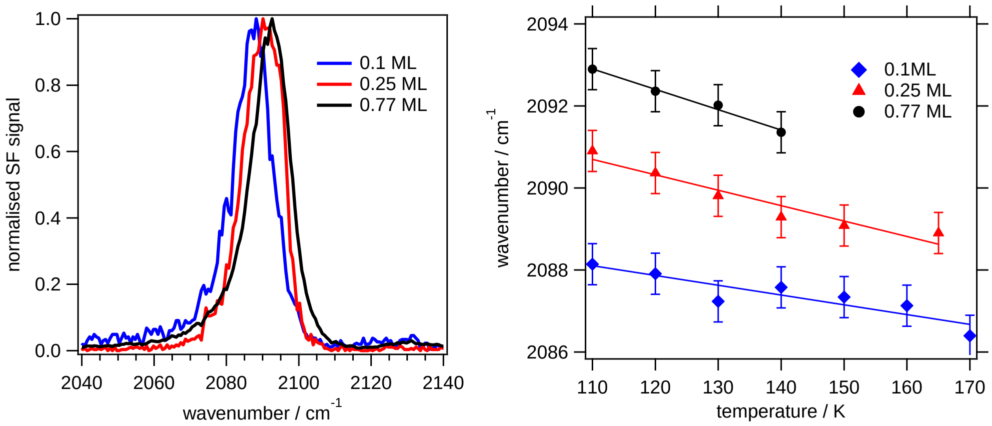

Figure. 3.2 Left: Normalized sum frequency spectra at 110 K for 0.1 ML, 0.25 ML and 0.77 ML. Right: Substrate temperature-dependent frequency shift of CO on Cu(110) for 0.77 ML (black circles), 0.25 ML (red triangles) and 0.1ML (blue rhombi). Solid lines are fits to the data using eqn.(3.1).

Figure 3.2 shows SF spectra of the C-O stretch mode for CO/Cu(110), and how the frequency shifts as a function of the substrate temperature. The substrate temperature provides the information of the FT mode population, simply dividing by the energy of the FT mode. It should be noted that heating effect from probe laser is negligible. CO/Cu(110) possesses two FT modes with values of 30.2 cm^{-1} and 27.4 cm^{-1} along the [1-10] and [001] direction at 110 K surface temperature[42]. If the average FT mode frequency of 28.8 cm^{-1} is used, then we obtain from equation (3.1) anharmonic coupling constants Γ_{14} of 2±0.2 cm^{-1} for 0.77 ML, 1.5±0.2 cm^{-1} for 0.25 ML coverage and 1.0±0.2 cm^{-1} for 0.1 ML coverage. For comparison, Germer *et al.* obtained 1.4 cm^{-1} for the c(2×2)-CO layer on Cu(100)[19]. An increase of anharmonicity with coverage implies that a lateral shift of CO away from the atop adsorption site causes a larger change in stretch frequency when there are CO molecules in neighboring adsorption sites[185]. This could be caused by repulsive lateral interactions.

3.3.2 Visible pump SF probe spectroscopy

The corresponding transients in frequency and line width of the C-O stretch following 400 nm pump pulses at a fluence of 10 J/m^2 are shown in figure 3.3. We also recorded pump-probe curves with 532 nm and 800 nm pump pulses, as shown in figure 3.4(a) and found no clear dependence on pump photon energy, similar to Germer *et al.*[19] The fast response in the transients is therefore caused by coupling to an equilibrated hot electron bath. The C-O stretch clearly exhibits a coverage-dependent transient redshift and broadening. At saturation coverage, the maximum frequency shift is 9 cm^{-1}, which is reduced to 3 cm^{-1} at 0.1 ML. The coverage dependence of the line width transients is more complex, with the smallest change detected for 0.25 ML coverage. At this coverage, ordered islands with (2×1) structure are seen in LEED and a free induction decay measurement[90] results in a significantly longer dephasing time T_2 of 1.4 ps, compared to 1.1 ps at 0.1 ML and 1.2 ps at 0.77 ML. These T_2 values correspond to line widths of 7.6 cm^{-1} at 0.25 ML, 9.6 cm^{-1} at 0.1 ML and 8.8 cm^{-1} at saturation coverage.

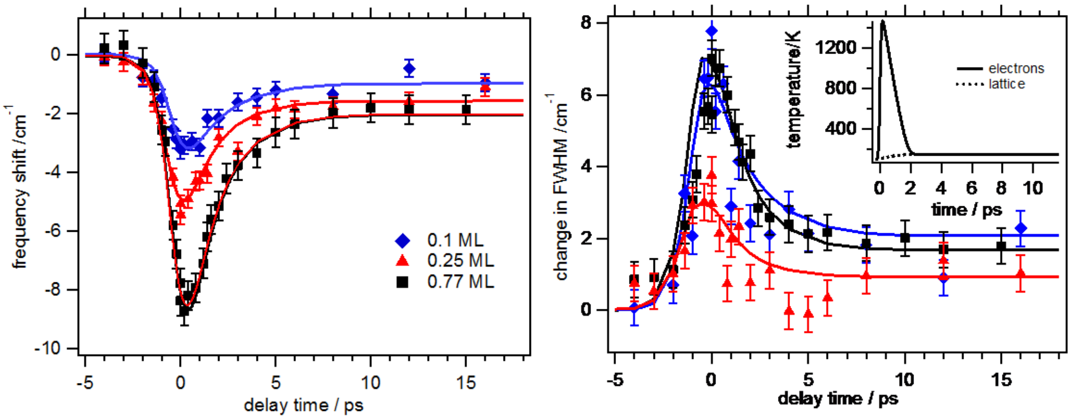

Figure 3.3 Transient pump induced changes in CO internal stretch frequency (left) and FWHM (right) for different CO coverages (0.1 ML, 0.25 ML, 0.77ML) at 100 K. Absorbed pump fluence at 400 nm was 10 Jm^{-2}. Solid lines are derived from calculated electron and lattice temperatures, as described in the text and shown in the inset.

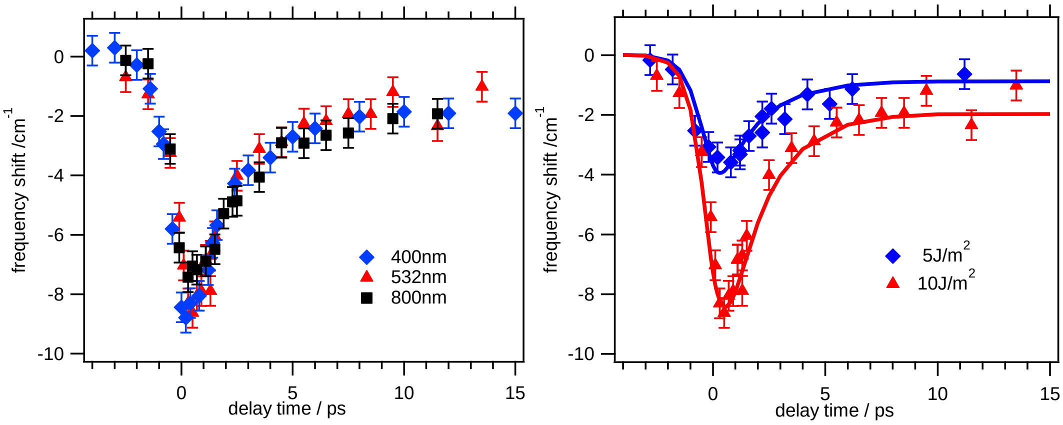

Figure 3.4 Transient pump induced changes in the C-O internal stretch frequency for (left) different pump wavelengths of 400 nm, 532 nm and 800 nm (absorbed fluence 10 J/m^2) and (right) different absorbed pump fluences of 5 J/m^2 and 10 J/m^2(pump wavelength 532 nm) at 100 K. Solid lines are derived from calculated electron and lattice temperatures and use the same coupling constants τ_{el} and τ_{lat}.

3.3.3 Modeling

In order to extract the coupling constants of this non-adiabatic process, we calculate hot electron and phonon temperatures using two-temperature model[186,187]. This approach was first proposed by Anisimov *et al.* in 1974[188,189]. A photon deposits its energy into the electron bath in the metal substrate, followed by heat transfer to the phonons baths. Electron and phonons equilibrate within a few ps, while the phonons relaxes over a timescale of hundreds of picoseconds[12]. The different timescales allow the experimental distinction between electron and phonon driven process in time. Electron, phonon and adsorbate temperatures can be described as

$$T_{el}\frac{\partial T_{el}}{\partial t} = \kappa\nabla^2 + g(T_{lat} - T_{el}) + S(z,t)$$

$$C_{lat}\frac{\partial T_{lat}}{\partial t} = -g(T_{lat} - T_{el}) \qquad (3.2)$$

where T_{el} and T_{lat} are electron and phonon temperature, respectively. τ_{el} and τ_{lat} are electron and phonon coupling constants, respectively. Shorter coupling constants mean stronger coupling. We used the experimentally determined electron-lattice coupling constant[12] $g=1\times10^{17}$ $Wm^{-3}K^{-1}$, and other parameters as cited by Germer *et al.*[19], as summarized in table 3.1. A more accurate version of the two temperature model is reported by Carpene[30], which incorporates the effect of the non-thermal electron distribution which is created immediately after the laser pulse arrives. This effect reduces the maximum electron temperature and is confirmed experimentally[31]. Carpene's modified two temperature model is used for the simulation here. S(z,t) describes incoming laser pulse, and is determined by the surface reflectivity and pulse fluence. This parameter is adjusted to match with the measured frequency shift of transient at long delay times (>5 ps) where phonon-vibration coupling dominates. The calculation of electron and phonon temperatures are performed with the Matlab program provided by Dr.Michael Higlett[187].

With the adsorbate temperature as input, we numerically solve the optical Bloch equations to obtain the time-dependent vibrational polarization[23], which is multiplied by the time-shifted envelope of the etalon-shaped upconversion pulse before Fourier transform to simulate the pump-induced frequency shift for each experimental conditions. We modify τ_{el} and τ_{lat} until we obtain a good overlap with experimental values as determined by a minimum in deviation (χ^2). The time resolution of the pump probe curves depends on the dephasing time T_2. A linear relationship between the time-dependent T_2 and the transient adsorbate temperature was assumed. Calculated frequency shifts and linewidths are overlaid with the data in figure 3.3 and 3.4, which also show that transients obtained with different pump fluences can be reproduced by the same τ_{el} and τ_{lat}.

The inset in figure 3.4 shows that under these experimental pump conditions, the electron temperature reaches over a thousand Kelvin within the first few picoseconds, while the phonon temperature increases by less than 40 K. The adsorbate temperature is calculated via the heat U_x=hν/exp(hν/kT_x) using τ_{el} and τ_{lat} as coupling constants to electron hole pairs and phonons:

$$\frac{dU_{ads}}{dt} = \frac{1}{\tau_{el}}(U_{el} - U_{ads}) + \frac{1}{\tau_{lat}}(U_{lat} - U_{ads}) \qquad (3.3)$$

Figure 3.5 illustrates how different electron and phonon coupling times in equation 3.2 affect the instantaneous adsorbate temperature (top graph) and the frequency shift calculated from the Bloch equations (zero delay between infrared and etalon-shaped upconversion pulse), assuming a gradient of 0.04 cm^{-1}/K. Calculation of electron temperature T_{el} and lattice temperature T_{lat} assumed an absorbed fluence of 10 J/m^2.

Analysis of the saturated CO transient results in coupling times of τ_{el}=4.6 ps and τ_{lat}=2.8 ps, which compares well to the transients on Cu(100), where values of τ_{el}=5.1 ps and τ_{lat}=4.2 ps were obtained at a lower time resolution. The electron coupling time increases to 6.2 ps for 0.25 ML and 6.7 ps for 0.1 ML coverage, while τ_{lat} only shows a minor variation with coverage. χ^2 analysis results in approximately 0.5 ps fitting error for all coupling times. These data are summarized in Table 3.2.

第1章 Table 3.1 Parameters for two temperature model of copper substrate

第2章 Electron-lattice coupling constant[12]	G	1×10^{-10}	W nm^{-3} K^{-1}
Electron thermal conductivity[19]	κ	4.28×10^{-7}	W nm^{-1} K^{-1}
Electron specific heat constant[19]	γ	0.966×10^{-10}	W nm^{-3} fs K^{-2}
Lattice heat capacity[19]	c_{lat}	3.5 ×10^{-6}	W nm^{-3} fs K^{-1}

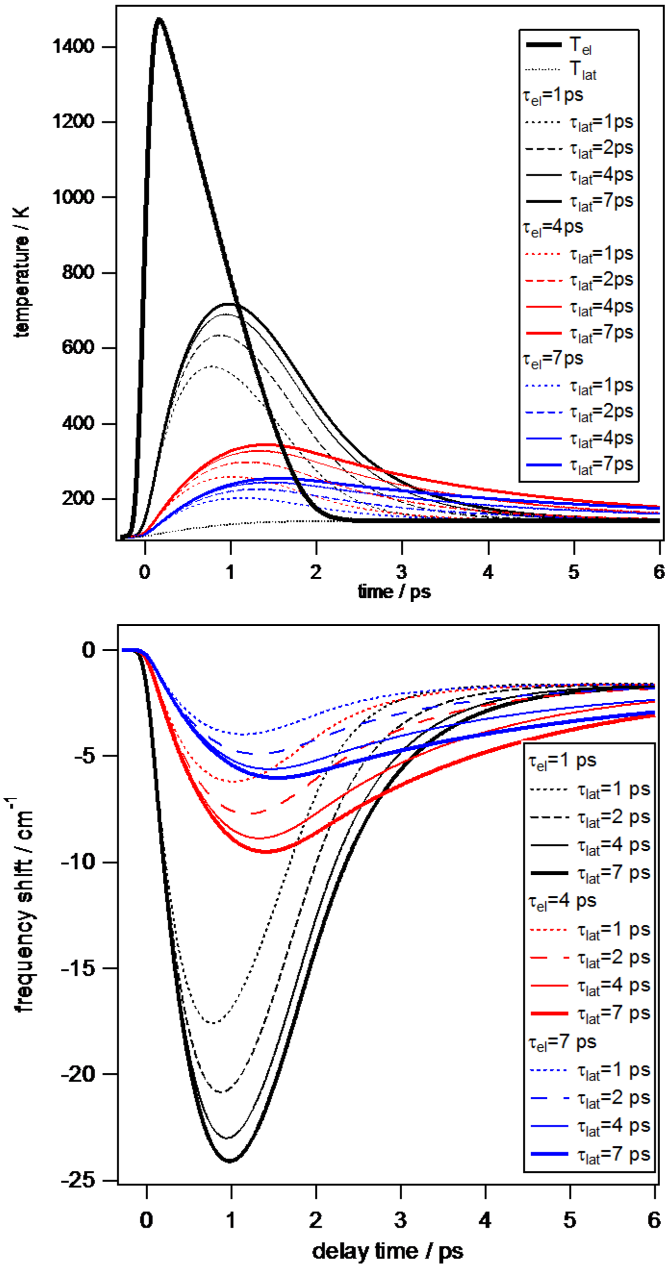

Figure. 3.5 Influence of electron and phonon coupling times. top: instantaneous adsorbate temperatures. bottom: frequency shift calculated from the Bloch equations.

Table 3.2: parameters for coverage dependence CO/Cu(110)

Coverage	T_2/ps	Γ/cm^{-1}	Frequency gradient /cm^{-1}K^{-1}	FWHM gradient /cm^{-1}K^{-1}	τ_{el}/ps	τ_{lat}/ps
0.1 ML	1.1	9.6	0.0239	0.08	6.7	3.1
0.25 ML	1.4	7.6	0.0375	0.04	6.2	2.4
0.77 ML	1.2	8.8	0.0490	0.07	4.6	2.8

Table 3.2 Values for T_2 are determined from free induction decays, Γ is calculated from T_2, the frequency gradient is derived from steady-state measurements, the FWHM gradient is chosen to

reproduce the maximum FWHM and τ_{el} and τ_{lat} are obtained from fitting frequency transients.

3.4 Discussion

3.4.1 Responsible vibrational modes

The transients exhibit a faster coupling to hot electrons with increasing coverage with hardly any change in phonon coupling. If the FT mode was indeed responsible for the non-adiabatic coupling, then we would expect much slower coupling to phonons at low coverage. Its lifetime τ_{FT} is related to the coupling times to hot electrons and phonons, τ_{el} and τ_{lat}, via $1/\tau_{FT} = 1/\tau_{el} + 1/\tau_{lat}$[19,190], which gives 2.3 ps for c(2×2)-CO on Cu(100) obtained by pump-probe spectroscopy[19].. Theoretical models of the phonon-induced damping of the frustrated translation and its coverage dependence give close agreement with the HAS values of 8 ps for isolated CO on Cu(100) and 2.1 ps for c(2×2)-CO on Cu(100)[180], respectively. The same theory would predict 5.7 ps for our lowest accessible coverage of 0.1 ML and 1.1 ps for our saturation coverage of 0.77 ML, where the change in τ_{FT} should be entirely caused by a reduction in τ_{lat}. Our pump probe results however determine FT lifetimes of 2.1 ps at 0.1 ML and 1.7 ps at saturation with the change almost entirely caused by τ_{el}. From this we can conclude that the mode responsible for the non-adiabaticity cannot be the frustrated translation, instead, it is most likely the frustrated rotation.

While this requires a reinterpretation of earlier experimental studies[18,19], it is actually the expected behavior from a theoretical viewpoint. The relaxation of both FT and FR modes is caused by excitation of electrons between orbitals of σ and π symmetry, as displacement along the FR and FT normal coordinates breaks the symmetry of the molecular orbitals of upright CO. This can be alternatively understood as both parallel modes coupling to electron-hole pairs via a delocalized electron density shift in the surface plane. The FR mode simply couples more strongly because the carbon atom moves further than in the FT mode. This leads to predicted vibrational mode lifetimes that are 30 to 50 times shorter for the FR than the FT for CO/Cu(100)[45,47]. The lack of coverage dependence in the phonon coupling time is consistent with the vibrational motion of the FR, which does not change the center-of-mass of the molecule. The FR, however, cannot directly change the frequency of the internal stretch via anharmonic coupling. With a frequency of 285 cm^{-1}, the highest electron temperatures reached here and in earlier works cannot populate it sufficiently[41]. Such direct coupling is only likely at very high pump fluences which cause desorption or diffusion[20,21,56,64,65,191]. Instead, the frustrated rotation indirectly excites the frustrated translation, as proposed in a recent series of papers by Ueba and Persson[59,192,193]. Fitting experimental transients to this FT-FR intermode coupling model is problematic, though, as the required anharmonicity parameters cannot be obtained from equilibrium experiments. Nonetheless, modeling our data with Ueba's indirect heating model would only change the absolute values of the coupling constants, but not their qualitative trend with coverage.

3.4.2 Coverage dependent non-adiabaticity

Coverage is therefore able to modify the adsorbate's non-adiabatic behavior. The lowest coverage transient at 0.1 ML can serve as a good approximation of an isolated CO adsorbate, since sum frequency spectra recorded at higher infrared pulse energies display a hot band well-separated from the fundamental[142,143] (more detail in chapter 5). Prior work has revealed possible sources for the increasing non-adiabatic coupling with coverage: the CO lateral potential energy surface becomes more anharmonic[182], and the occupation of the CO $2\pi^*$ level increases[82]. The latter leads to a weaker internal bond and in turn a lower stretching frequency, the so-called chemical shift, which for CO/Cu(110) has been determined as $-32\ \mathrm{cm}^{-1}$ across the full coverage range [82]. The origin of this chemical shift is a gradual overlap between the diffuse $2\pi^*$ LUMO orbitals of neighbouring CO molecules, which leads to a broadening of these states from 1.9 to 2.6 eV, which in turn increases their overlap with the d-band of copper, and therefore increases backdonation from the surface electrons[79-81]. This effectively increases the charge density around the carbon atom[194] and thereby enhances the non-adiabatic coupling of the frustrated rotation[47]. This is similar to the enhancement of non-adiabaticity of adsorbates at step sites[26], only caused by coverage in our case, rather than adsorption site. The chemical shift may be used as a measure for the electron density involved in the chemisorption bond, then coupling to hot electrons becomes faster as the chemisorption bond becomes stronger, as shown in figure 3.6.

How adsorbate-adsorbate interactions influence the shape of the CO potential energy surface and thereby the coupling of vibrational modes to hot electrons is more difficult to predict. An increasingly anharmonic coupling between the stretch and the frustrated translation at higher coverage was seen in the static temperature dependence in figure 3.2, which is likely caused by lateral interactions between CO molecules. Long-range interactions between CO molecules can change the curvature of the PES at the transition state for diffusion[195]. They are mediated by adsorbate-induced modification of the local electron density[196,197] or by dipole-dipole interactions[198]. Recent theoretical work, using improved potential energy surfaces, revealed that the angular degrees of freedom of CO on copper play an important role in energy redistribution between vibrational states[199]. Nearby adsorbates could easily influence these angular states. In fact, the electron-stimulated desorption ion angular distribution (ESDIAD) of CO on Cu(110) reveals that repulsive interactions between adsorbed molecules lead to an increasing tilt angle[200]. Tilting CO leads to a hybridization between σ and π orbitals, just like the frustrated rotational motion[47]. Electronic friction calculations of CO/Cu(100) accordingly confirm that coupling to electron-hole pairs generally becomes stronger with increasing tilt angle[201]. A progressively tilted CO was probably also the reason behind an earlier observation of an enhanced non-adiabaticity of CO/Ir(111) in the presence of NO coadsorbates, which is originally attributed more to a spectator effect[202].

How does this then relate to non-adiabatic chemistry of CO on other transition metals? The roughly three times stronger chemisorption bond and the d-band straddling the Fermi level should in principle increase the adsorbate density-of-states compared to copper and lead to stronger coupling to electron-hole pairs. Instead, previous studies have found little evidence for coupling to electrons in C-O stretch transients at low pump fluence[90]. The reason is very likely the much faster equilibration between hot electrons and phonons, which typically occurs in less than a picosecond, and thereby on the same timescale as coupling between hot electrons and the frustrated rotation. The influence of the FR mode can therefore only be clearly seen, when the adsorbate reaches the vicinity of the transition state to diffuse or desorb[56,64,65], and one would generally expect a more anharmonic potential and therefore stronger intermode coupling. The problem is compounded by the positive chemical shift on non-noble transition metals, which will tend to reduce backdonation into the CO LUMO, and thereby non-adiabaticity, at the high coverages typically used in pump-probe studies.

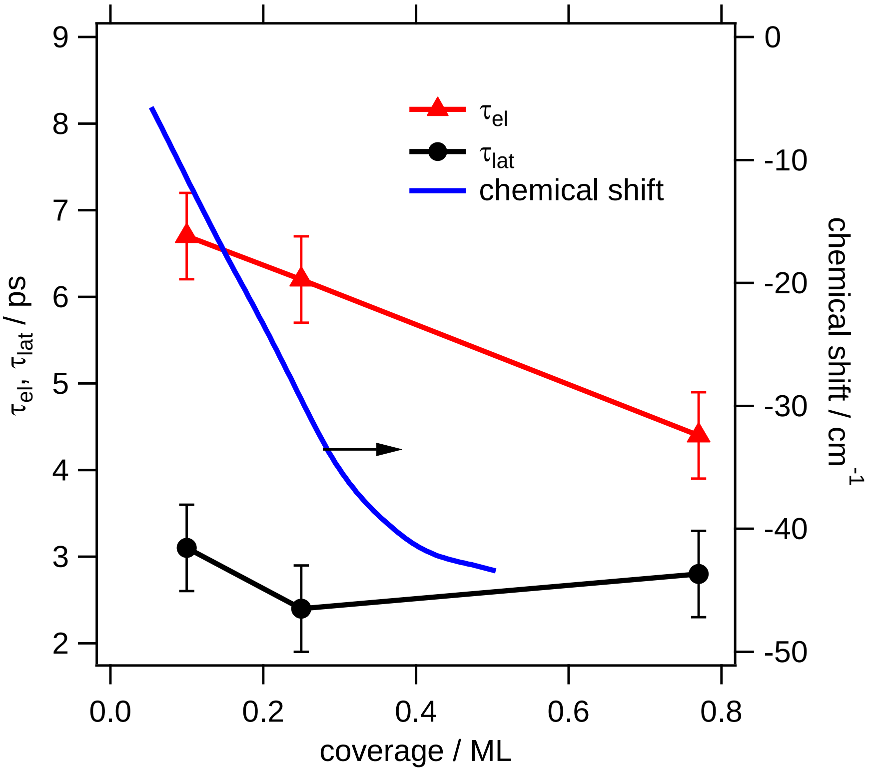

Figure 3.6 Electron and phonon coupling times (left axis) as a function of CO coverage. The chemical shift plotted on the right axis (arrow) was extracted from reference[82].

3.5 Conclusions

The origin of the coverage dependence of hot electron coupling time of adsorbates on metal surfaces has been studied through pump-probe SFG of CO on Cu(110). The higher the coverage, the faster the energy transfer between substrate electrons and adsorbate, which identifies the frustrated rotation as the responsible mode. This demonstrates that interactions between CO adsorbates can control non-adiabaticity and we argue that the underlying reason is a combination of adsorbate density-of-states and shape of the potential energy surface. The scope for modifying non-adiabatic coupling rates to hot electrons through adsorbate interactions is likely to be largest on noble metals with long electron-phonon coupling times.

This chapter provided necessary information to understand the following chapters, by identifying the FR mode and its coupling to hot electrons as the responsible vibrational mode for the observed transient redshift. We will investigate the more complicated system, namely CO on RuTPP covered Cu(110) in chapter 5-7, after the discussing the detailed adsorption structure of RuTPP on Cu(110) in the next chapter.

Chapter 4

Adsorption structure and supramolecular growth of RuTPP on Cu(110)

Porphyrins on metal surfaces have been widely studied as a model system of the π conjugated organic molecule-metal interface and for the uniqueness of their self-assembled structures. Here, RuTPP on Cu(110) has been studied by STM to provide a structural basis for the deeper under standing of vibrational and desorption dynamics, which will be presented in later chapters. It is experimentally shown that the ruthenium atom occupies the short bridge site. CO molecules adsorb atop of the ruthenium atom to form a monocarbonyl complex. The major supramolecular structure at 4.7 K shows an equivalent unit cell to previously reported cobalt TPP (CoTPP) on Cu(110), but there is also an antiboundary phase which has a unit cell of one copper atom larger in [1-10] direction. This larger unit cell structure is observed as a major phase at room temperature at low coverage implying the existence of two stable supramolecular structures.

4.1 Introduction

Porphyrins are an important molecular component in a variety of technologies including heterogeneous catalysis[203,204], gas sensors[205], light harvesting[206,207], molecular switches[208,209], and field effect transistors[210,211]. For these devices, porphyrin molecules have to be bound onto the surfaces for immobilization and/or electronic contact requiring a study of their morphological and electronic structures. Relevant surface science studies from last 15 years can be found in review papers[212-220].

Porphyrins are a class of molecules composed of a planar tetrapyrrole macrocycle structure which can be functionalized by inserting a metal atom into the core and/or by changing the substituted group, as shown in figure 4.1. These three components each have a unique role. The tetrapyrrole macrocycle possesses a π conjugated electronic structure, which can play the role of light harvesting in the photosynthesis system of chlorophyll. This tetrapyrrole macrocycle is called the *porphine,* and *porphyrin* is a porphine with peripheral substituents. The substituted groups can increase conformational flexibility and stability to adapt to the local environment. The central metal core can be a binding site for axial ligand molecules e.g. oxygen binds to the iron of hemoglobin.

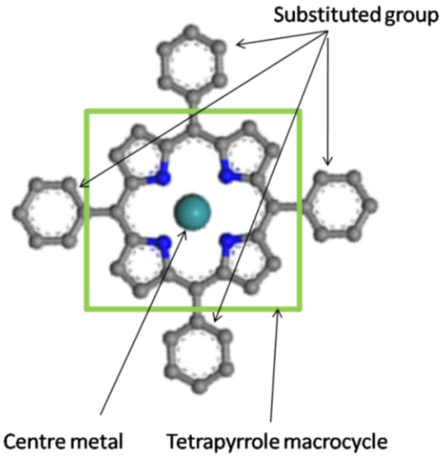

Figure 4.1 Molecular structure of a porphyrin (RuTPP)

From the planar structure of porphyrin in the gas-phase, it was expected that the macrocycle of porphyrins remains in a planar configuration on metal surfaces to maximize the electronic hybridization, which increases with closer macrocycle-substrate distance. Indeed, Jung *et al.* have shown that adsorption of porphyrin onto metal surfaces induces a structural deformation of substituted groups to the molecular plane to increase macrocycle-substrate and adsorbate-adsorbate attractive interactions which induce the different phases on different metal substrates[221]. The authors have investigated Cu-tetra[3,5 di-*t*-butylphenyl]porphyrin (CuTBPP) on Cu(100), Au(110) and Ag(110) by STM revealing the flexibility of the substituted groups adopting to the local environment. This study suggests that the adsorption structures of porphyrins are not simple, and also indicates that designed porphyrin molecules can be used to control the adsorbate geometry. For example this can be achieved by carefully choosing substituted groups to form a self-assembled 1D structure[222]. 5,10,15,20-tetrakis- (3,5-di-tertiarybutylphenyl) porphyrin (2HTBPP) and its derivative molecules, where one or two 3,5-di-tertiarybutylphenyl are replaced with cyanophenyl, have been studied by STM showing that the cyanophenyl groups predominantly interact with each other to form the controlled self-assembled structure.

The distortion of the molecular conformation has been studied in detail on metal surfaces with a model porphyrin molecule, tetraphenyl porphyrin (TPP), by combination of STM, density functional theory (DFT) and near edge X-ray absorption fine structure (NEXAFS)[215,223]. A typical adsorption structure of TPP is a saddle shaped structure where opposite pairs of pyrrole rings tilt either upwards or downwards inducing a symmetry reduction from D_{4h} to C_{2v}. This saddle shape is common for Co, Fe, Cu and free base TPP on Ag(111) and Cu(111) surfaces[215,223]. Similar structural distortion was observed for an isolated single CoTPP molecule on the Cu(110) surface, but not for the supramolecular structure of CoTPP on Cu(110). Planar and saddle shaped structures can coexist and even interconvert[224].

The metal substrate also affects the self-assembly of porphyrins. For example, a repulsive intermolecular interaction of 2HTPP leads to disordered structure on Cu(111)[225-228], while an attractive intermolecular interaction triggers an ordered self-assembled structure on Ag(111)[227-230]. An STM study of CoTPP on Ag(111) displays electronic hybridization between the cobalt atom and silver surface which dominates strong surface-adsorbate interactions inducing a disordered surface structure without forming a self-assembled molecular island, while 2HTPP forms a well ordered self-assembled structure on silver due to its high mobility, which indicates the adsorbate-substrate interaction is relatively weak. In contrast, the Cu(111) surface induces a stronger interaction with the nitrogen atoms of the macrocycle than the centre metal atom, which results in the opposite behavior to the silver surface; CoTPP on Cu(111) exhibits an ordered structure with high diffusivity, but 2HTPP is anchored onto the surface preventing the formation of the ordered layer[227,228].

Despite the long history of porphyrin surface science, most studies were performed on non-reactive metal surfaces including low index gold, silver and copper. Reactive metal surfaces may provide a stronger surface contribution to induce a conformational deformation and/or unique self-assembled structure which could pave a new route to tune functionality as well as increase versatility for device applications[231-233]. A first step to study reactive metal surfaces is the Cu(110) surface, which is non-reactive metal surface, but the most reactive surface amongst the non-reactive metal surfaces. Previous STM studies of porphyrins on Cu(110) revealed creation of molecular building blocks by reaction with copper adatoms[234-238], and unexpected deformation of the porphyrin macrocycle[89] due to the strong interaction with the surface. DFT studies also revealed strong coupling between the porphyrin and the copper substrate which induces chemisorption[89]. The average adsorbate-surface distance on Cu(110) is shorter than on other substrates; e.g CoTPP (2.1-2.4 Å)[89], simple porphyrin (1.9-2.65 Å)[239], and copper porphyrin (2 Å)[238], compared with e.g. CoTPP/Ag(111) 3.7 Å, CoTPP/Cu(111) 3.4 Å[240]. Although TPP on Cu(110) is expected to show strong adsorbate-substrate interaction, CoTPP on Cu(110) exhibits high diffusivity at room temperature which hampers STM imaging[89].

In particular, RuTPP is chosen for a system of this study. Initially, CoTPP on Cu(110) surface was studied, since its adsorption structure is already known[89], however CO does not binds onto CoTPP/Cu(110) at liquid nitrogen temperature. On the other hand, CO-RuTPP is known to show relatively strong CO-Ru bond, and available to purchase as a form of CO-RuTPP. CO-FeTPP can also be a candidate for this study, however FeTPP is stabilized as a form of Cl-FeTPP and removing chloride is experimentally difficult.

In this chapter, STM studies of the RuTPP adsorption structure on Cu(110) are described prior to SFG and STM-AS experiments in the following chapters. RuTPP in the gas phase shows a very similar structure to CoTPP[241,242], implying that adsorbed RuTPP may display similar structure and supramolecular assembly found for CoTPP[89]. The adsorption site of RuTPP is determined from the STM image showing that the ruthenium atom occupies the short bridge site. Upon CO exposure, a CO molecule adsorbs atop of a ruthenium atom to form a monocarbonyl complex which appears brighter in STM images. Two supramolecular structures have been observed with unit cells different by one copper atom in [1-10] direction. The detailed adsorption structure is investigated in collaboration with DFT.

4.2 Experimental

A low-temperature STM (Omicron GmbH, LT-STM, RIKEN, Japan) and a room-temperature STM (Specs STM 150 Aarhus instrument, RT-STM, University of Liverpool) were used for 4.7 K and 300 K imaging, respectively. All experiments were performed with an electrochemically etched tungsten tip. A Cu(110) single crystal surface was cleaned by several cycles of Ar^+ ion sputtering and annealing to 800 K. The CO-RuTPP is purchased from Sigma Aldrich (purity ~80 %) in the form of purple powder. This was transferred into a homemade molecular doser without further purification. The molecular doser was degassed over 12 h at ~100 °C in vacuum. Evaporation of CO-RuTPP onto the clean Cu(110) surface was performed by resistive heating of the molecular doser to ~150 °C holding the substrate at room temperature. After adsorption of RuTPP, the sample was left at room temperature over 12 h to form self-assembled island structures prior to transfer to the cryostat for LT-STM experiments. Acquired images were processed by WSxM[172] to tune image contrast and calibrate distance.

4.3 Results and discussion

4.3.1 Low temperature STM images

Deposition of CO-RuTPP by sublimation from its powder form onto the Cu(110) surface at room temperature led to the observation of bright protrusions across the surface as shown in the STM images of figure 4.2(a)-(b). These images were acquired at 4.7 K. Isolated molecules and self-assembled molecular islands have been observed as shown in figure 4.2(a). A monomer and dimer of RuTPP molecules are marked by circle and square in figure 4.2(b), respectively. Most monomers, dimers and larger molecular clusters are aligned to copper rows. Magnified STM images show each molecule consists of a four-lobe structure[89,215], which resembles the RuTPP molecular structure as shown in figure 4.1(b).

Previous studies of MTPP on metal surfaces also observed these features, which were assigned to TPP molecules. The angle and the size of STM images were calibrated by an atomically resolved STM image of a bare Cu(110) surface as shown in the inset of figure 4-2(b). After CO exposure at ~50 K, some ruthenium atoms show larger apparent height due to the formation of CO-RuTPP. This feature was not observed before CO exposure, thus it is concluded that CO-RuTPP decomposes to CO and RuTPP during the deposition process.

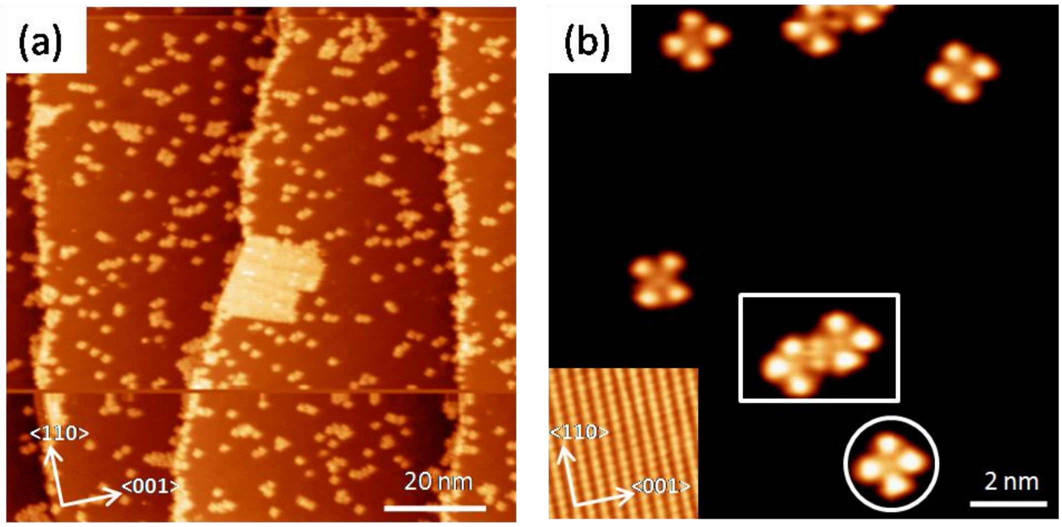

Figure 4.2 STM images of RuTPP on Cu (110) with increasing coverage, sample bias voltage V_s =500 mV and tunneling current I_t = 0.5 nA at measurement temperature T=4.7 K. (b) inset: atomic resolution of bare Cu(110). (b) A RuTPP monomer and dimer are marked by circle and square, respectively.

4.3.1.1 Adsorption site

The determination of the adsorption site is the first step to identify the adsorption structure. There are two methods to measure the adsorption site from an STM image. One is to obtain an atomic resolution image of the substrate simultaneously with molecules to enable direct calibration. Another is to use a marker molecule with known adsorption site. The former can be applied to any molecular system with better reliability, while the latter is experimentally easier and more commonly used. The adsorption site of RuTPP was investigated using coadsorbed CO in the STM image, as shown in figure 4.3. It is known that CO on Cu(110) occupies the atop site[78], which allowed us to draw the grid lines of the Cu(110) lattice superimposed on the STM image. The distances of Cu-Cu, CO-CO and Ru-Ru have been measured to confirm the accuracy of the overlay grid, showing a maximum error of 0.3 Å from their theoretical values. The STM image of figure 4.3 is acquired at 512 pixels over 13 nm × 13 nm with a resolution of 0.25 Å.

The ruthenium atom occupies a short bridge site, and a four-lobe structure is aligned with the copper rows, which is consistent with the previous results for other metalloporphyrins[89,240]. A free-base porphine (H_2P) adsorbed on the short bridge site by forming a chemisorption bond with the Cu(110) due to electron donation into unoccupied porphine π orbitals, accompanied by electron backdonation from molecular π orbitals. This hybridization induces shorter carbon-copper distances (2.20 Å for H_2P[239], and 2.50 Å for CoTPP[89]), which increase the stability of the adsorption to the short bridge site. From the STM image, it is hard to investigate the details of adsorption structure, e.g. the degree of phenyl rings deformation, which will be discussed based on the DFT calculations in later of this chapter. The calculated structural model of RuTPP is superimposed on figure 4.3.

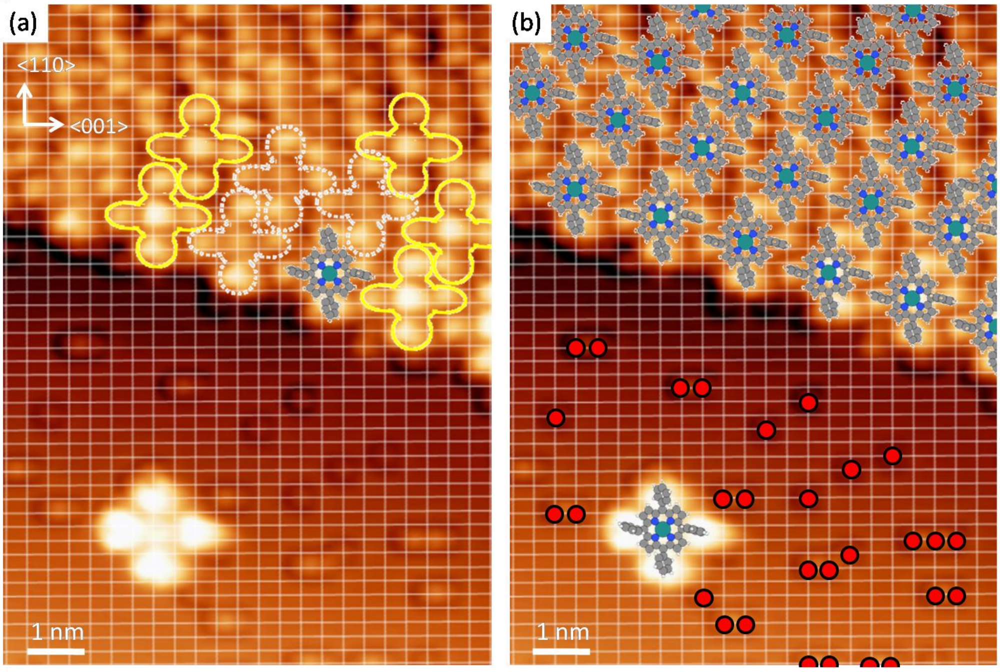

Figure 4.3 (a) STM images of RuTPP and CO-RuTPP on Cu(110), V_s = 500 mV and I_t = 0.5 nA at T=4.7 K. Cu lattice lines are calibrated by CO/Cu(110). (b) RuTPP and CO molecules are overlaid on (a). Structure model of RuTPP is adapted from calculated structure which is performed by Mr.Paolo Poli, and will be discussed later in this chapter, see figure 4.5 and 4.7.

4.3.1.2 CO adsorption onto RuTPP/Cu(110)

After CO exposure at ~50 K, the image contrast at the centre of RuTPP molecules became brighter, indicating attachment of CO on top of a ruthenium atom, as observed with CO adsorption onto metallophthalocyanines on metal surfaces[243,244]. The cross-sectional height profile demonstrated that CO-RuTPP had a larger apparent height than RuTPP, as shown in figure 4.4 which is consistent with CO-MnPc/Bi(110)[244], but different from CO-FePc/Au(111)[245] and CO-CoTPP/Ag(111)[246], where CO adsorption reduced the apparent heights of porphyrins by modifying the distributions of the local densities of states. The present observations and the previous report indicated that the contribution of CO to the STM image originates from its electronic structure. CO adsorption onto RuTPP did not alter the adsorption site of RuTPP.

For a deeper understanding of the surface geometrical structure of RuTPP/Cu(110) and CO-RuTPP/Cu(110), a DFT study was performed by Mr.Paolo Poli in the group of Prof.Mats Persson at the University of Liverpool. The periodic DFT calculations in this study were performed using the VASP code[247]. Plane waves were used as a basis set with an energy cut-off of 400 eV. Valence electron core interactions were included by using the projector-augmented wave method[248] and the generalized gradient approximation (optB86b) was used for the exchange-correlation functional. The calculations of RuTPP in a periodic structure were based on a unit cell that was derived directly from STM data and carried out on a 2×2×1 k-point grid. The copper surface was modelled by using a four-layer slab.

STM determined the adsorption site of RuTPP on Cu(110) as the short bridge site. Thus, the DFT calculation was only performed on the short bridge site. Here, the preliminary result of a supramolecular structure in the λ phase will be described and compared to CoTPP. Figure 4.5 shows the calculated structure of RuTPP and CO-RuTPP on Cu(110). Here, we focus on the position of CO and ruthenium. The displacement of phenyl rings and relevant intermolecular interaction is described in the next section. The shortest ruthenium-copper distance is 2.5 Å which is the same value as the cobalt-copper distance of CoTPP/Cu(110)[89], but this increases to 2.6 Å on adsorption of CO onto RuTPP/Cu(110). The distances between the uppermost copper layer and ruthenium are 2.2 Å and 2.1 Å for RuTPP and CO-RuTPP, respectively, indicating a weakening of the Ru-Cu interaction by adsorption of CO, as previously reported for CO-FePc/Au(111)[243]. The angle of C-O-Ru is 178.7 ° which means that CO adsorbs on the ruthenium atom almost perpendicularly to the surface. This is a similar value to the C-O-Ru angle of 175.8° obtained from X-ray crystallography[242]. No other local minimum of the CO position has been obtained. The distance of CO-Ru is 1.85 Å.

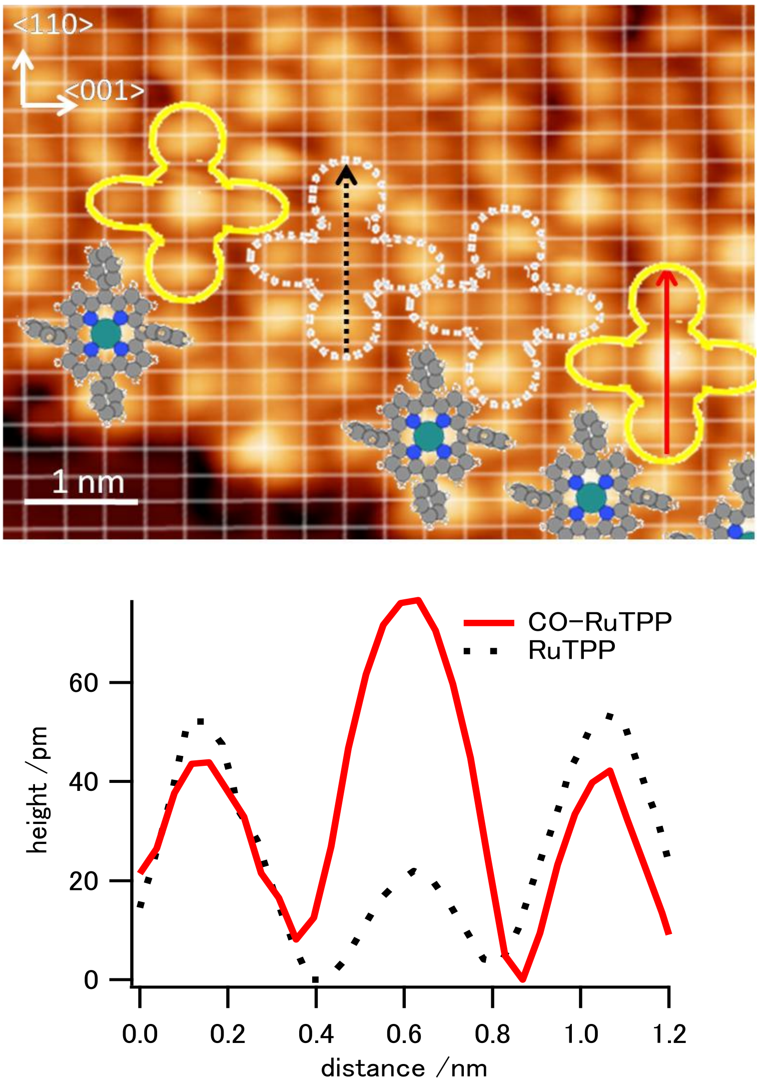

Figure 4.4 (top) STM images of RuTPP and CO-RuTPP adsorbed on Cu(110). The images were obtained at 4.7 K with V_s = 500 mV and I_t = 0.5 nA. The superimposed Cu(110) lattice lines are calibrated by CO/Cu(110). A ball and stick model of RuTPP is overlaid on the STM image. (bottom) Cross-sectional height profiles measured along the straight lines shown of RuTPP and CO-RuTPP on Cu(110). The corresponding solid and dotted lines are shown in the STM image.

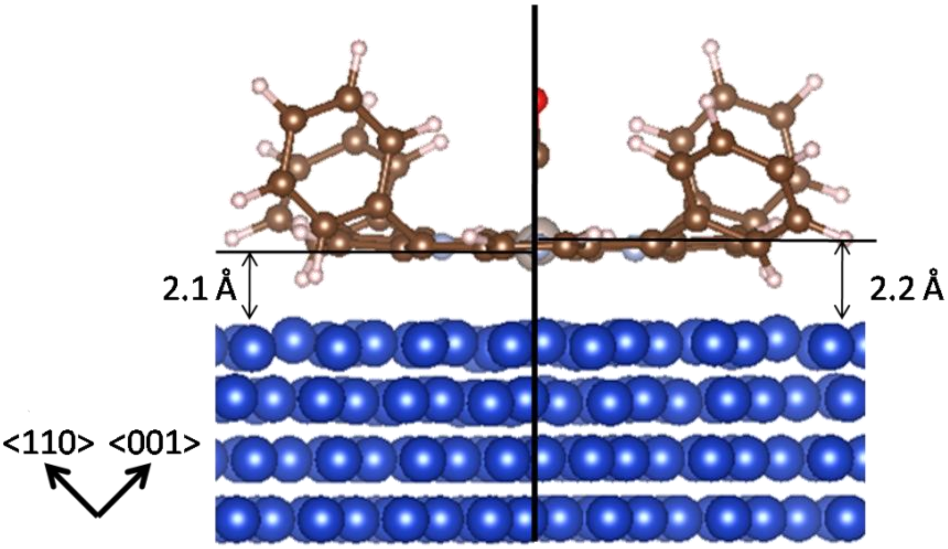

Figure 4.5 Calculated adsorption structures of (left) RuTPP and (right) CO-RuTPP on Cu(110) surfaces.

4.3.1.3 Supramolecular structure

Next, the morphology of the supramolecular structure is investigated. From the STM image and structure model of figure 4.6, the unit cell of the supramolecular structure is determined. Using standard convention[249], the unit cell can be described in matrix notation as,

$$G^{\lambda} = \begin{bmatrix} 2 & 4 \\ -6 & -2 \end{bmatrix}$$

Here, λ refers to a supramolecular structure observed in figure 4.6. This unit cell corresponds with the structure of CoTPP on Cu(110) structure[89]. These two molecules show almost identical adsorption structure, however there is a noticeable difference. The cobalt atom makes almost no contribution to the STM image, while ruthenium always appears as a protrusion. This difference can be interpreted as a different electronic hybridization of the centre metal and the copper substrate. The cobalt d_{z^2} orbital is broadened and becomes fully occupied resulting in a lower density of state, in contrast the ruthenium atom is weakly hybridized with the substrate as observed in the STM image.

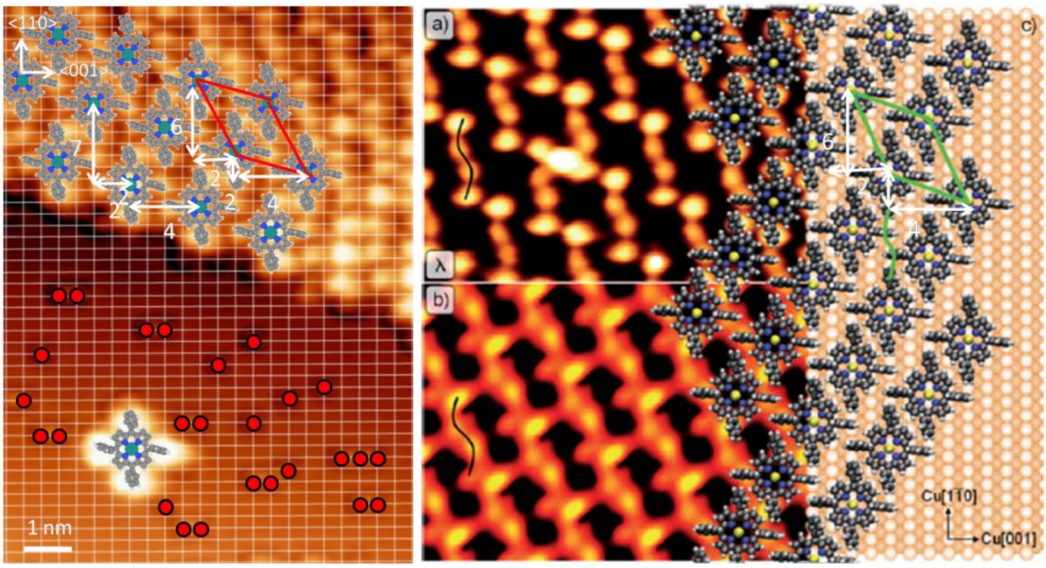

Figure 4.6 (left) STM image of RuTPP on Cu(110) with its unit cell vectors. (right) Experimental and simulated STM image of CoTPP on Cu(110), adopted from ref[89].

Next, the intermolecular interactions between RuTPP molecules are discussed. The key to understanding the surface self-assembly of TPP is the rotation of the phenyl rings. In the equilibrium crystal structure, phenyl rings are not coplanar[250,251], however, they rearrange to accommodate to the molecular island which is now discussed alongside the results of DFT. In the present system, the deformation of the phenyl groups is described by defining the tilt angle as θ: the angle between the plane of the tetrapyrrole macrocycle and the surface plane, and the twist (dihedral) angles as Φ: the angle between the phenyl ring plane and the surface plane as shown in calculated structure model of Figure 4.7. First, the isolated molecule in the vacuum is described for comparison. Tilting distortions are energetically unfavorable which leads to almost no change from Φ= 180°. In contrast, twist distortions are those which show a large twist angle of θ= 69°.

The deformations involved in accommodating the RuTPP supramolecular structure onto Cu(110) are shown in figure 4.7. The surface structure is governed by the interplay of two interactions: an attractive interaction between the RuTPP core and the copper surface and a repulsive interaction between the phenyl rings and the surface. The phenyl groups align to the copper rows to accommodate themselves by a combination of tilting and twisting. Two pairs of opposite phenyl rings exist which are clearly identified by their different twist angles both from experimental STM images and the calculated structure. A pair of phenyl rings which aligned with the [001] rows shows θ angles of 78° and Φ angles of 162°. The interaction between the second phenyl pair and the substrate is different. The second pair are the phenyl rings aligned onto the close-packed [1-10] rows and the calculated θ and Φ angles of 58° and 145° are obtained. CO adsorption changes the calculated angles by less than 1°, indicating that CO makes almost no contribution to the porphyrin-porphyrin interactions.

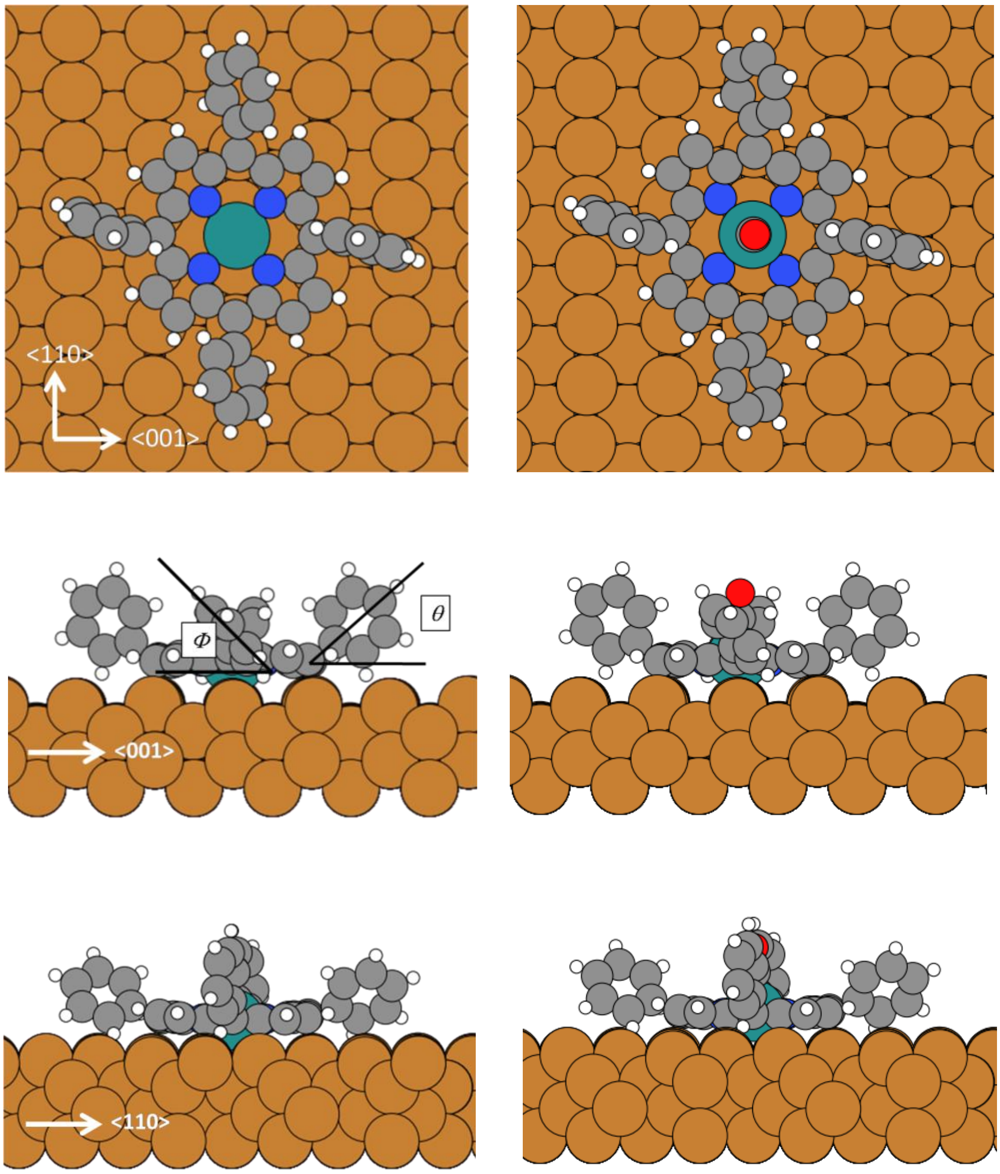

Figure 4.7 Calculated adsorption structures of (left) RuTPP and (right) CO-RuTPP on Cu(110) surfaces.

The deformation of phenyl rings has been observed in DFT which is consistent with previous work on CoTPP on Cu(110)[89]. The surface self-assembly of TPP is governed by the rotation of the phenyl rings. In the equilibrium crystal structure, the phenyl rings of TPP are not coplanar[250,251]. Self-assembly is driven by changing the angle of the phenyl rings to increase adsorbate-adsorbate interactions. It is common that more than two phases of self-assembled structures form for porphyrins on surfaces due to the interplay of adsorbate-adsorbate and adsorbate-substrate interactions[252]. It is important to know how phenyl rings interact with each other to understand the interplay of adsorbate-adsorbate interactions. Phenyl-phenyl interactions can be categorized into two types which are called T-type (T;figure 4-8) and parallel displaced type (PD; figure 4-8) interactions[253-259]. T-type interaction refers to the interaction of two perpendicularly aligned phenyl rings, while PD type is the interaction of phenyl rings which aligned in parallel. The major attractive force here is assigned as originating from long-range interactions such as electrostatic and dispersion forces, not short-range interactions such as charge transfer[257]. As a model system, several groups performed calculations for the benzene dimer, taking account of the dispersion interaction by using the second order Møller-Plesset perturbation theory (MP2)[257,259], or the coupled-cluster theory with single and double substitutions (CCSD) to incorporate the coupling between electron pairs[254,255,260]. These calculations have been expanded to the larger molecule[253,256] and the surface system[89]. In case of TPP on a surface, T and PD interactions coexist. The red square in figure 4.8 displays PD interaction with a neighboring molecule and the yellow square shows T interaction.

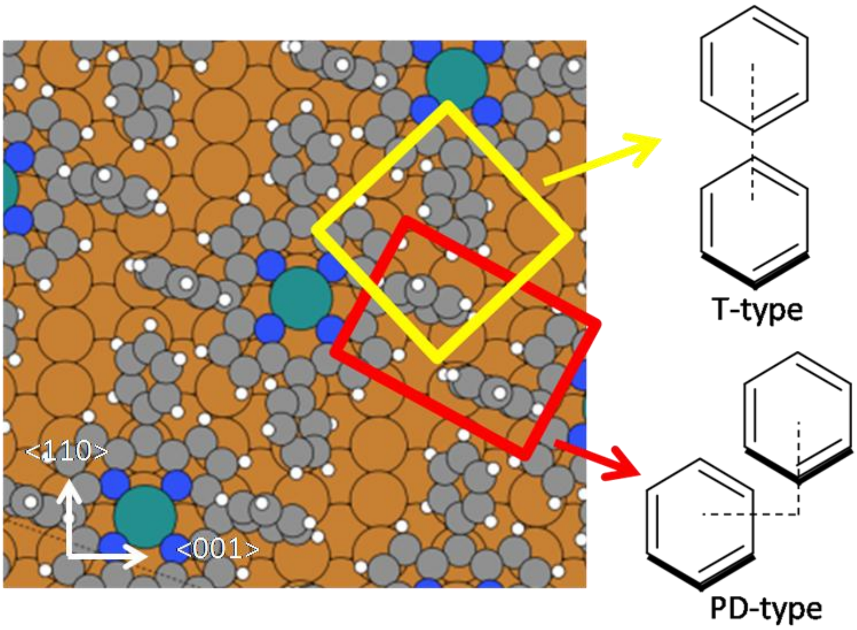

Figure 4.8 Schematic representation of intermolecular interaction of MTPP molecule via phenyl-phenyl interactions. T-type: the interaction of two perpendicularly aligned phenyl rings, PD type: interaction of phenyl rings which aligned in parallel.

4.3.1.4 Boundary structure

On closer inspection, there is a different unit cell at the edge of the molecular island in figure 4.4. The unit cell is larger than the one discussed in the last section, and can be written as,

$$G^{\lambda *} = \begin{bmatrix} 2 & 4 \\ -7 & -2 \end{bmatrix}.$$

This difference is noticeable from the STM image by focusing on the position of the phenyl rings. Molecules at the edge of an island exhibit two of their phenyl rings aligned along the [001] direction. Similar phenyl-phenyl locking has been observed inside the molecular island as marked by white lines in figure 4.9. These features are often observed regardless of the size of the molecular island and have been previously reported as antidomain boundaries in STM studies of 5,10,15,20-tetrakis (3,5-di-t-butylphenyl)porphyrin on Cu(111)[261] and CoTPP on Cu(110)[89] surfaces.

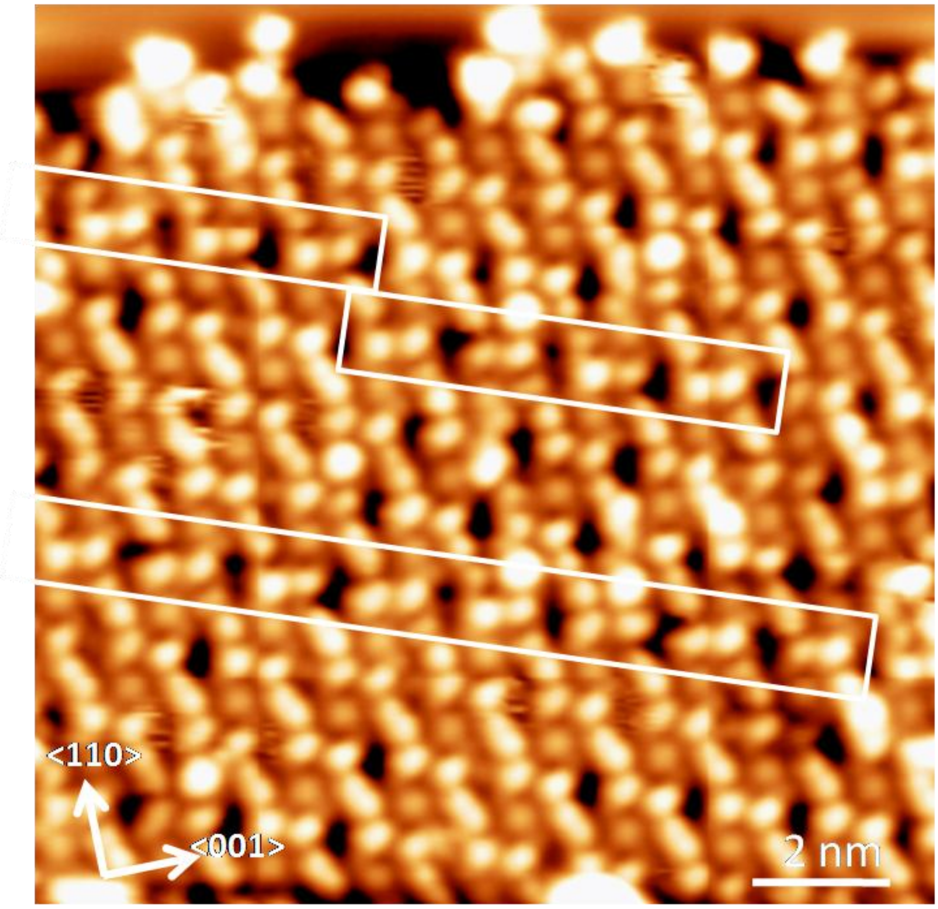

Figure 4.9 STM image of RuTPP on Cu(110) with different scales. V_s=500 mV, I_t=0.5 nA, T=4.7 K. Some molecules have brighter spots at the centre of RuTPP, which corresponds with CO adsorption.

4.3.2 Room temperature structures

4.3.2.1 Mixture of two phases

A large scale 50 nm × 50 nm STM image acquired at room temperature is shown in figure 4.10. Molecular island structures exhibit four domains. λ* and δ* phases are more frequently observed over a wide range of coverages, while λ and δ are observed only at high coverage. λ and δ are chiral to each other. To investigate the details of these phases, enlarged STM images are investigated.

Figure 4.11 shows an enlarged STM image of the boundary of λ and λ* phases. The top half of molecules are in the λ phases and the bottom half are in the λ* phase. The λ phase resembles the phase observed in STM images at 4.7 K. The λ* phase shows similarity with the boundary phase at 4.7 K. The structural model of these two phases is shown on the right side of figure 4.11. Two of four phenyl rings align to the [1-10] direction, the other two align to [001], resulting in a different local rearrangement, which alters their appearance in STM images. The two phenyl rings aligned to [1-10] appear brighter than the other two. This feature also appears for CoTPP on Cu(110) in where the combination of STM and DFT concludes that phenyl rings possess different heights and angles with respect to the surface[89].

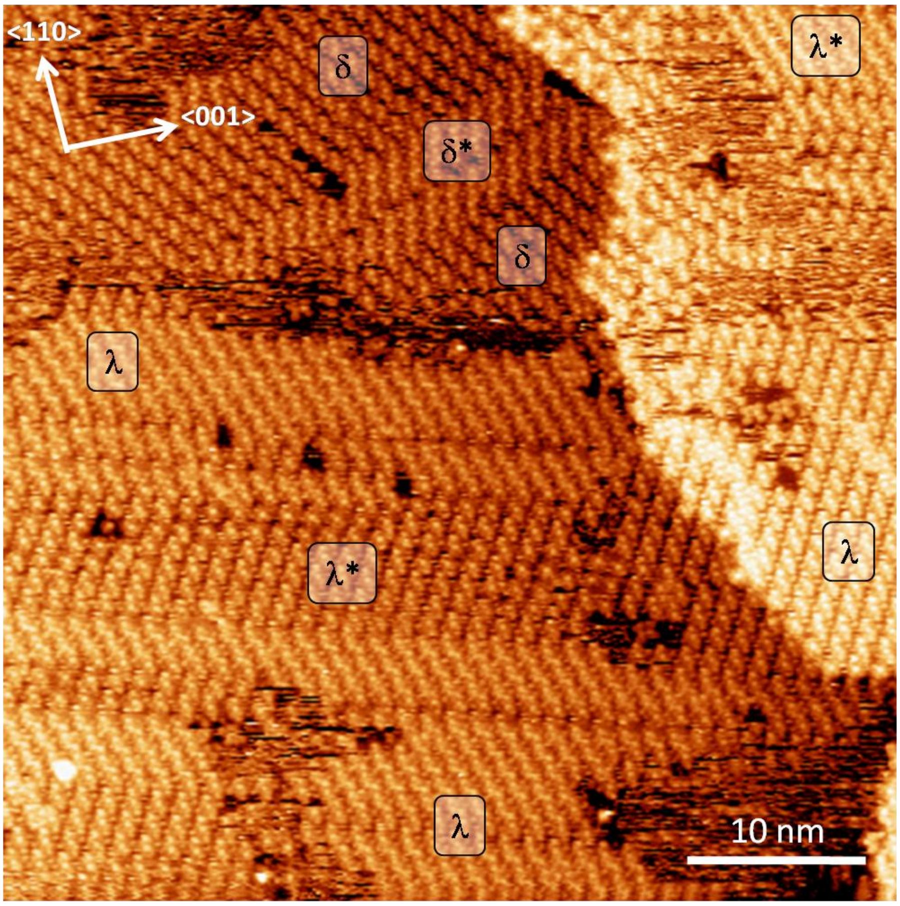

Figure 4.10 Large scale STM image of RuTPP on Cu(110). V_s=-524.3 mV, I_t=0.280 nA, T=RT.

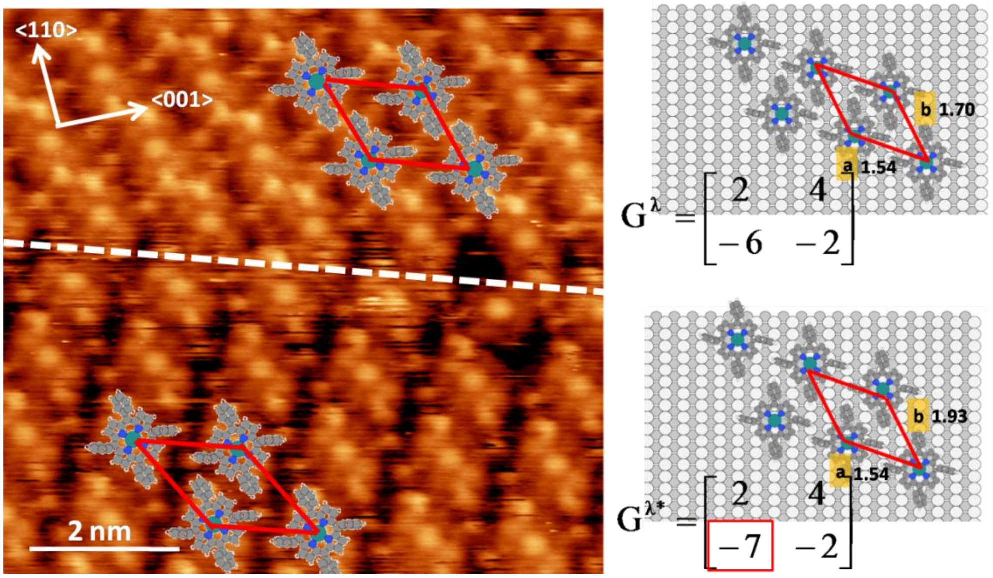

Figure 4.11 (left) STM images of the boundary of λ and λ* phases indicated by a dashed line. V_s=-524 mV, I_t=0.200 nA, T=RT. (right) schematic model of high coverage phase.

4.3.2.2 Low coverage phase

At lower coverage, where the molecules start to form islands but bare parts of copper still allows molecules to diffuse across the surface, a change in the organization of the supramolecular structure is seen. There are now only λ and δ phases, with some boundaries. Figure 4.10 shows two domains of molecular islands. These domain structures are chiral, even though RuTPP is an achiral molecule. Chirality arises either from chiral components or a combination of achiral components to create an overall chiral structure[249]. Specifically on surfaces, there are three types of chirality, global point chirality, local point chirality and organizational chirality[249]. A structure with global point chirality can be formed by a particular enantiomer, but not the other. This can be achieved by an intrinsically chiral molecule. Local point chirality is a single chiral molecular system on the surface. Even an achiral molecule can induce local point chirality upon adsorption. Finally, organizational chirality refers to the supramolecular chiral domain or arrangement.

In the case of RuTPP on Cu(110), the four fold symmetry of RuTPP is preserved after the adsorption onto Cu(110) as shown in the monomer structure of figure 4.2(b). In contrast, a supramolecular structure forms chiral domains as shown in figure 4.12. These domains have organizational chirality. This result indicates that intermolecular interaction is a key to induce chiral structure[89,249,262].

The STM images at RT exhibit two phases. The λ phase appeared as a minor phase at room temperature which was only observed at high coverage although the same phase is found for the majority at 4.7 K. This can be explained by a high local coverage inducing the λ phase at the low temperature. The two phases of molecules can interconvert during the cooling process. This hypothesis is supported by the high diffusivity at room temperature. Figure 4.13 shows the continuously acquired series of STM images at low RuTPP coverage at room temperature. The supramolecular island was observed in the first image, but the island shrinks in the second image, while the third image shows no island structure. Such thermally unstable supramolecular islands have been observed previously for a variety of adsorbates on metal surfaces[263-265]. It should be noted that the high diffusivity of the porphyrin on Cu(110) surface is unique for RuTPP, and not observed for 2HTPP, metal diphenyl porphyrins[234], and tetra(mesityl)porphyrin[235].

This diffusivity may affect further study by SFG and RAIRS, which were performed at liquid nitrogen temperatures. To confirm the structure in this temperature range, STM images at liquid nitrogen temperature have been recorded. Figure 4.14 shows the STM images of RuTPP/Cu(110) at 77 K (RIKEN) and ~200 K (Liverpool). These images resemble the STM image acquired at 4.7 K. Monomers and small molecular clusters of RuTPP on Cu(110) have been observed, indicating the suppression of surface diffusion.

An alternative interpretation of the two phases observed during the different experimental runs is a different flux from the molecular doser. Donovan proposed that the flux of CoTPP deposition affects the surface supramolecular structures[266]. The flux cannot be easily measured nor controlled. The differences between the two phases are the position of phenyl rings and the slight difference of the unit cell which is thought not to significantly affect the environment around ruthenium.

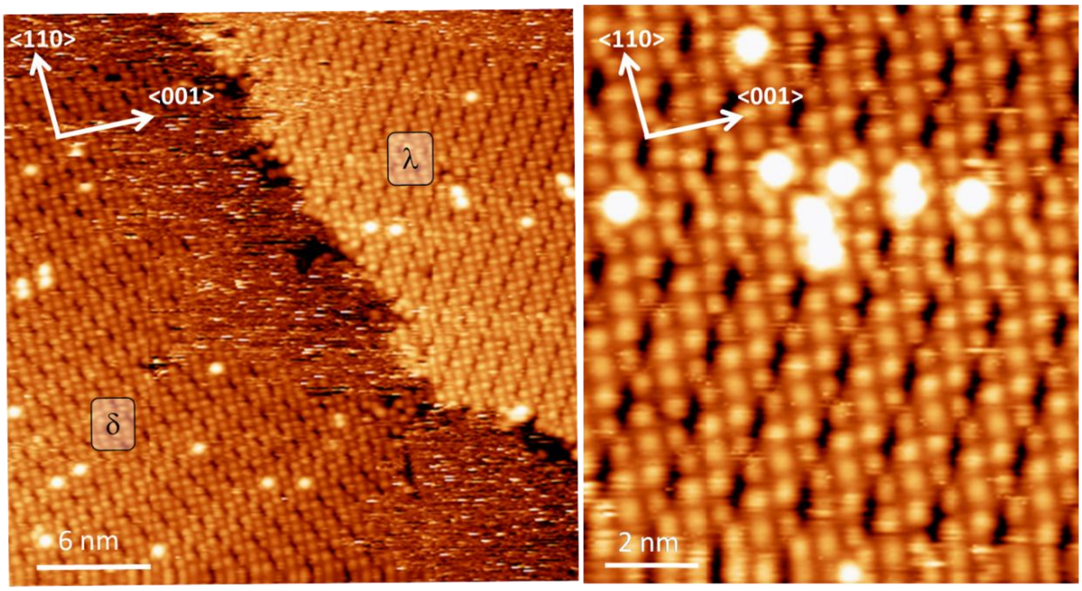

Figure 4.12 (left) Large scale and (right) enlarged STM images of RuTPP on Cu(110), V_s=-911.2 mV, I_t=0.130 nA, T=RT. The chirality of the two domains is denoted λ and δ.

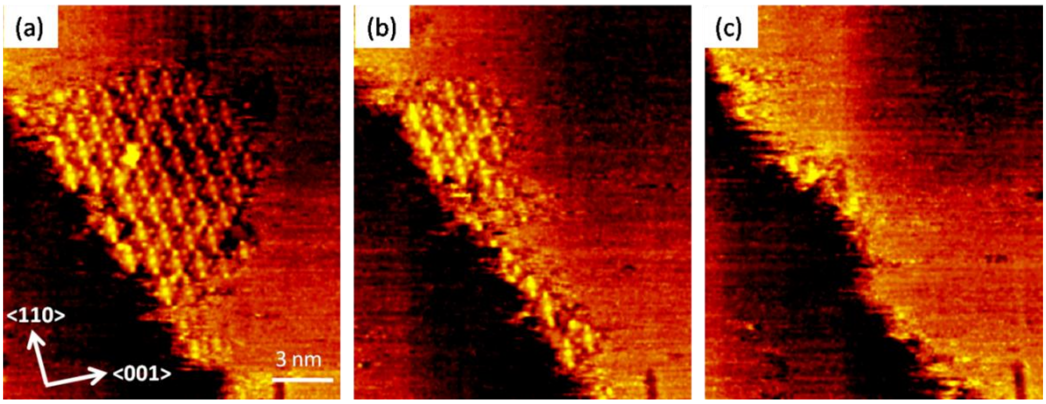

Figure 4.13 STM images of RuTPP on Cu(110) acquired at T=RT. Images were continuously recorded. An image acquisition requires 192 seconds. V_s = -1440 mV, I_t = 0.16 nA

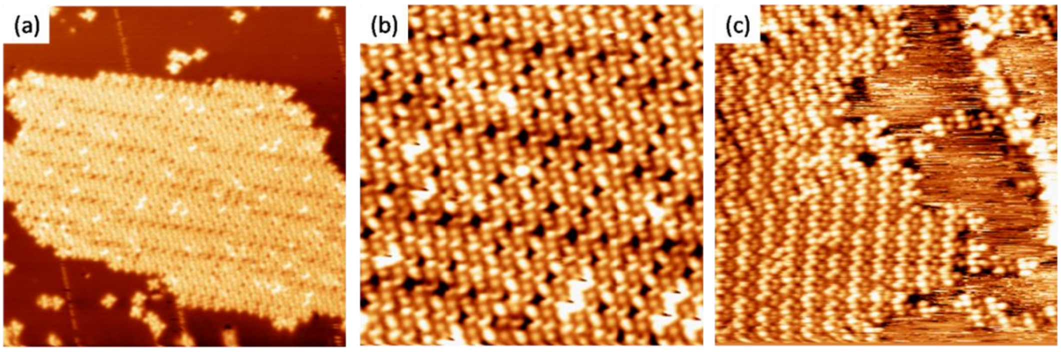

Figure 4.14 STM images of RuTPP on Cu(110). (a, b) V_s=-0.5 mV, I_t=0.5 nA, T=77 K (RIKEN) (c) V_s=-144.3 mV, I_t=0.20 nA, T=200 K±30 K (Liverpool). The distance and angle are not shown due to lack of a calibration image for measurements at these temperatures.

4.4 **Conclusion**

The adsorption structure and supramolecular formation of RuTPP on Cu(110) surface has been studied by STM. RuTPP adsorbs on the short bridge site, aligning phenyl rings to the copper rows. The STM images revealed a symmetry reduction of RuTPP arising from rearrangement of phenyl rings which may affects the potential energy surface of CO to facilitate dissociation of CO as will be discussed in chapter 5. Coexistence of two different supramolecular structures was observed. The unit cell of each supramolecular structure was determined to support a theoretical collaboration for further understanding of the desorption mechanism which will be discussed in chapters 6 and 7.

Chapter 5

Vibrational hot band of CO on bare and RuTPP covered Cu(110)

Vibrational hot band transitions of CO on a bare and a RuTPP covered Cu(110) surface have been studied by intense IR – visible SFG. The fundamental and first and second vibrational hot bands of CO on Cu(110) surfaces have been observed, which exhibit different frequency shifts with increasing coverage of CO, as the dipole-dipole coupling becomes stronger with increasing transition dipole moment. The excitation of the fundamental C-O stretch mode of CO-RuTPP on Cu(110) was observed at 1957 cm^{-1}, together with the first hot band transition at 1927 cm^{-1} showing a larger Morse anharmonicity χ_e and lower dissociation energy D_e than on bare copper. The frequency of the C-O stretch and the hot band population of CO-RuTPP/Cu(110) are independent of the coverage of CO, which indicates that dipole-dipole coupling among CO on neighboring RuTPP is negligibly small. The anharmonicity of the C-O stretch mode is compared on various surfaces, suggesting the importance of considering the effect of a local electric field in the form of vibrational Stark effect on the measured anharmonicity. The data also suggest that the Morse anharmonic potential does not perfectly describe the potential energy surface of CO on surfaces.

5.1 Introduction

It is highly desirable to achieve dissociation of specific chemical bonds to control chemical reactions. This can be achieved by vibrational excitation. For example, a reaction between a hydrogen atom and a H_2O (D_2O) molecule can be controlled by selectively exciting an O-H or O-D bond because the excited chemical bond preferentially reacts[267-269]. A higher degree of vibrational excitation increases the reactivity, and this is most easily achieved by vibrational ladder climbing. It has been proposed[270,271] and demonstrated[272] that chirped IR pulses can effectively populate higher vibrational states. The transition frequencies between vibrational states shift to the red due to the anharmonic potential energy surface (PES). For a Morse oscillator model[273], transitions between ν and $\nu + 1$ occur at

$$\omega(\nu\rightarrow\nu+1) = \omega_e(1-2\chi_e(1+\nu)) \qquad (5.1)$$

where ω_e is the equilibrium frequency and χ_e is the Morse anharmonicity constant. The anharmonic redshift between adjacent transitions ($0\rightarrow1$ to $1\rightarrow2$ etc) is constant in this model at $2\omega_e\chi_e$. For CO in the gas phase, $\chi_e = 0.0061$ which increases to 0.0065 and 0.0067 for CO/Ru(001)[142] and CO/Ir(111)[143], respectively. The dependence of the Morse anharmonicity χ_e on the character of the surfaces has not been discussed in detail yet.

From the Morse anharmonicity, the dissociation energy can be calculated as

$$D_e = \frac{\omega_e}{4\chi_e} \tag{5.2}$$

D_e is the dissociation energy measured from the potential minimum.

Higher vibrational states of organometallic-carbonyl complexes have been studied in solution. The C-O stretch mode of carboxyhemoglobin was investigated by pump-probe IR spectroscopy, revealing that the potential was well reproduced by the Morse PES with constant anharmonic shift of 25 $\mathrm{cm^{-1}}$ up to $\nu=7$. An interesting property was also reported regarding the anharmonicity of CO attached to a porphyrin complex. Nuernberger *et al.* observed a large anharmonic shift of 29 $\mathrm{cm^{-1}}$ of the C-O stretch mode bound to the heme domain FixLH from Bradyhizobium japonicum[274]. The authors speculate that this large anharmonicity is caused by a distortion of the potential energy surface by the protein environment. Chapter 4 described the structure of RuTPP on the Cu(110) surface, indicating distortion of the phenyl rings from the gas phase and lifting up the ruthenium atom towards vacuum. This could potentially have an effect on the PES of CO adsorbed on RuTPP.

In this chapter, the vibrational hot bands of the C-O stretch mode from CO on RuTPP covered Cu(110) are described. The hot band transition of CO on Cu(110) is first examined in detail as reference. The C-O stretch mode of CO-RuTPP/Cu(110) was investigated by RAIRS and SFG. The excitation of the $\nu = 0 \rightarrow 1$ C-O stretch mode of CO-RuTPP on Cu(110) is observed at 1957 $\mathrm{cm^{-1}}$ together with the $\nu = 1 \rightarrow 2$ hot band transition at 1927 $\mathrm{cm^{-1}}$ showing a larger Morse anharmonicity χ_e and lower dissociation energy D_e than for Cu(110). The $\nu = 2 \rightarrow 3$ hot band transition shows a larger anharmonic shift than the $\nu = 1 \rightarrow 2$ hot band transition for CO on both bare and RuTPP covered Cu(110) surfaces. The frequency of the C-O stretch and the hot band population of CO-RuTPP/Cu(110) are independent from the coverage of CO, which indicates that dipole-dipole coupling among CO on RuTPP is negligibly small.

5.2 Experimental

SFG experiments were performed with an amplified 10 Hz femtosecond laser system combined with a UHV chamber as described in Chapter 2. A TOPAS optical parametric amplifier generated 4-10 μJ, 200 fs mid-IR pulses. The remainder is passed through an etalon (SLS Optics) to produce an upconversion pulse of about 7 cm^{-1} spectral width, which is time-shifted by 1.3 ps to reduce the non-resonant sum frequency signal[133].

A Cu(110) single crystal was cleaned by Ar^+ bombardment at 1 keV, followed by annealing to 600 K. RuTPP (Sigma Aldrich) was used as purchased and sublimed at 500 K onto the Cu(110) surface, which was held at 300 K during deposition. The coverage is estimated from TPD and frequency of the C-O. CO is dosed from the background at a substrate temperature of 100 K. All sum frequency spectra shown were recorded at 100 K. Any indication of the instability of RuTPP to laser pulses has not been observed.

RAIRS experiments were carried out using a UHV chamber interfaced with a Nicolet 860 Magnon FTIR spectrometer via ancillary optics and KBr windows. A nitrogen cooled HgCdTe detector allowed the spectral range of 550- 4000 cm^{-1} to be accessed. The spectrometer was operated with a resolution of 4 cm^{-1}, with the addition of 256 scans to collect each spectrum. RuTPP was first deposited at room temperature, and subsequently cooled down to 87 K, where CO exposure and data acquisition was carried out. A reference background single beam spectrum representing the clean Cu(110) surface was subtracted from all subsequent spectra.

5.3 Results

5.3.1 Vibrational hot band of CO/Cu(110)

The SF spectra of CO on Cu(110) are first described in order to understand the behavior of vibrational hot bands of CO on metal surfaces. Figure 5.1 shows SF spectra of the C-O stretch mode from CO/Cu(110) as a function of IR power. With increasing IR power, the $\nu = 1 \rightarrow 2$ vibrational hot band of the C-O stretch mode becomes clearly visible at 2063.0 cm^{-1} in addition to the fundamental transition at 2088.6 cm^{-1}. Evidently, a significant fraction of the CO oscillators are excited into the first vibrational state. The third resonance at 2036.1 cm^{-1} is attributed to the $\nu = 2 \rightarrow 3$ hot band transition. The third vibrational hot band $\nu = 3 \rightarrow 4$ is also observed around 2009 cm^{-1}. The frequency of each transition is determined in the low coverage limit to minimize the effect of dipole-dipole coupling and chemical shift. The exact coverage of the low coverage limit was not measured, but estimated to be less than 0.01 ML from its SF intensity. The differences between the transitions of $\nu = 0 \rightarrow 1$, $\nu = 1 \rightarrow 2$ and $\nu = 2 \rightarrow 3$, the anharmonic frequency shift, equal 25.6 cm^{-1} and 26.9 cm^{-1}. For the accurate determination of the frequency, the contribution of $^{13}C^{16}O$ has to be considered.

The frequency of the ^{13}C-^{16}O stretch mode of 2042.2 cm^{-1} is estimated from the effective mass and the frequency of ^{12}C-^{16}O stretch mode[275]. This is close to the frequency of ν= 2→3, but should make a negligibly small contribution since the natural abundance of $^{13}C^{16}O$ is only 1 %.

At a coverage of 0.77 ML, a single peak is seen with a centre frequency of 2089.4 cm^{-1} at 10 μJ IR power, which is lower than the C-O stretch mode of the same sample measured with 4 μJ IR pulse (2093 cm^{-1}). The linewidth broadening from 4.7 cm^{-1} to 9.1 cm^{-1} and a tail of the spectra towards lower frequency were also observed. The lower frequency shift, the linewidth broadening and the tail structure can be explained by a transition from localized oscillator to delocalized oscillator. Here, the localized oscillator means a CO molecule isolated from others which independently oscillates, and the delocalized oscillator is a layer of CO molecules, which collectively oscillate. This delocalization can be caused by intermolecular energy exchange through dipole-dipole coupling. The transition from localized to delocalized oscillator has been observed by changing the coverage of CO on Ru(100) and Ir(111)[142,143]. Fundamental and hot band transitions merge with increasing CO coverage, as the Förster energy exchange rate gradually increases with decreasing distance between adsorbates.

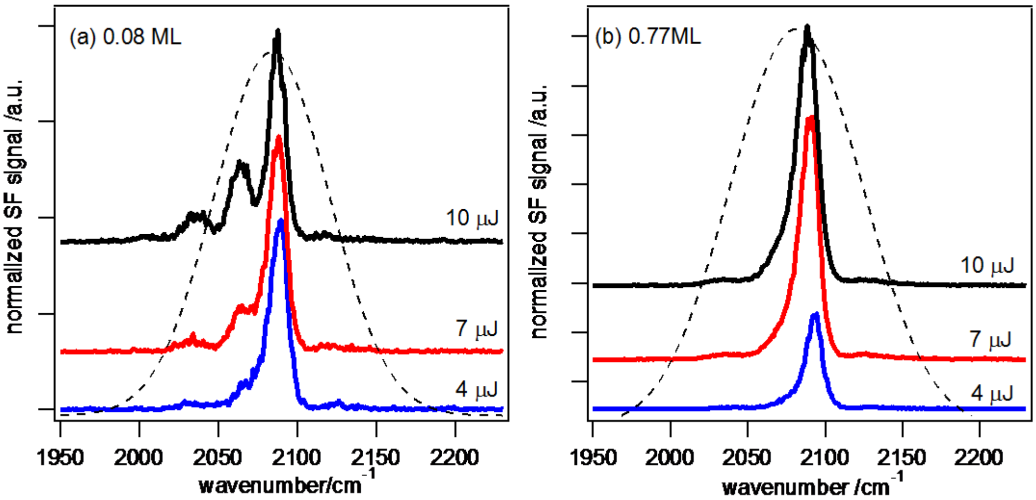

Figure 5.1 SFG spectra of (a) 0.08 ML and (b) 0.77 ML of CO/Cu(110) at 100 K as a function of the IR pulse energy. The fundamental (ν= 0→1) and the hot band (ν= 1→2) transitions are observed at low coverage. The dotted line indicates the spectral intensity of the non –resonant background which corresponds to the shape of the IR pulse.

Figure 5.2 shows SF spectra of the C-O stretch mode as a function of coverage. With increasing coverage from 0.01 ML to 0.08 ML, frequency shifts of the hot bands were observed which will be discussed later. At a coverage of 0.25 ML, the fundamental and hot band transitions have almost merged, and they are no longer distinguishable at saturation coverage. In the case of CO on Ru(001), the energy exchange occurs at a much lower coverage of 0.025 ML. This difference can be caused by a smaller transition dipole moment of CO on Cu(110) than on Ru(001). The energy exchange depends on the 4th power of the transition dipole moment μ because of the contribution from donor and accepter dipoles. The transition dipole moment of CO on copper is 0.25 D[39] while Bonn *et al.* proposed that CO on ruthenium has a dipole moment of 0.63 D[90,271]. This difference induces a 40× faster energy exchange for CO on Ru(001) compared with copper, while the difference in dipole-dipole coupling induced frequency shift is less than twice: ~45 cm^{-1} for CO on Cu(110)[82] and ~70 cm^{-1} for CO/Ru(001) at the saturated CO coverage[276].

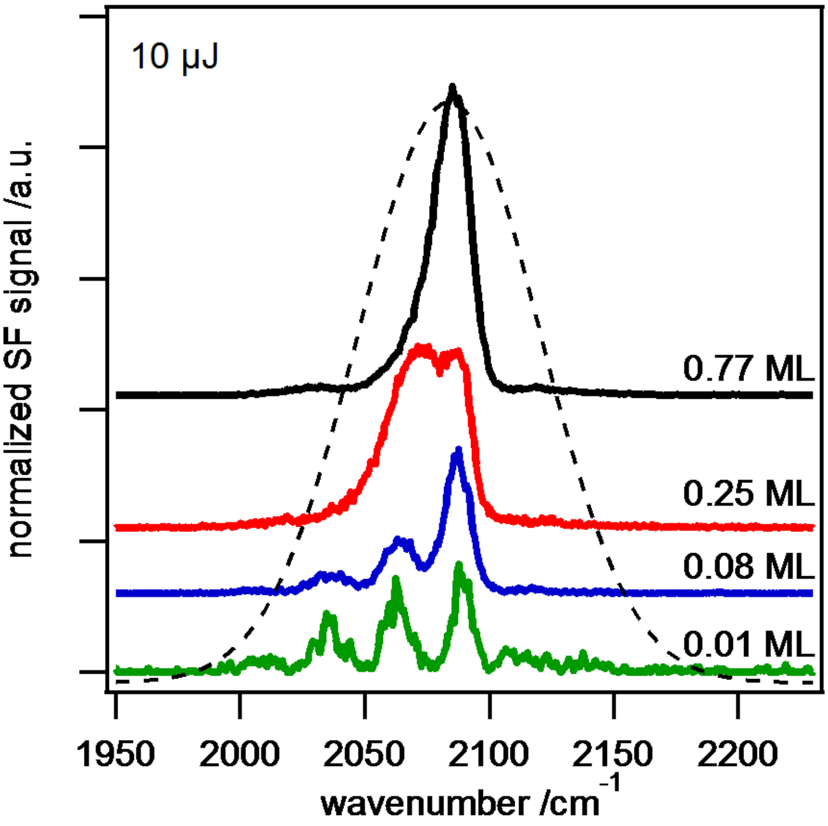

Figure 5.2 SFG spectra of CO/Cu(110) at 100 K as a function of CO coverage with incident 10 μJ IR pulse. The dotted line indicates the spectral intensity of the nonresonant background which corresponds to the spectra shape of the IR pulse.

The coverage dependent frequency shift is caused by both the dipole effect and chemical shift. The dipole effect results in a blueshift as a result of repulsive dipole-dipole interaction among CO molecules while chemical interactions induce a redshift in the case of CO on copper as discussed in chapter 3 and shown in the coverage dependent RAIR spectra in figure 2.5. Here, the dipole effect and chemical shift of the hot band transitions are described. Figure 5.3 shows a series of SF spectra at different coverages from 0.04 ML to 0.12 ML. At a coverage of 0.12 ML, the $\nu= 2\rightarrow3$ transition is hardly distinguishable. The frequency of each transition increases with increasing coverage, as shown in figure 5.3. A larger shift was observed for higher vibrational transitions. At 0.12 ML, the $\nu= 1\rightarrow2$ and $2\rightarrow3$ vibrational hot bands have shifted by +4 cm^{-1} and +10 cm^{-1}, respectively, while the frequency shift of the $\nu= 0\rightarrow1$ transition is less than 1 cm^{-1}. It is necessary to consider dipole-dipole coupling and chemical shift separately for a quantitative understanding of this coverage dependence. Persson and Ryberg derive a simplified equation for the coverage dependent frequency shift of an incomplete layer of single oscillators caused by dipole-dipole coupling[39,143],

$$\left(\frac{\nu}{\nu_s}\right)^2 = 1 + \frac{\alpha_\nu c_A \tilde{U}}{1+\alpha_e c_A \tilde{U}} \qquad (5.3)$$

where ν_s is the singleton frequency of the isolated oscillator, ν is the frequency at fractional coverage c_A, α_ν and α_e are the vibrational and electronic polarizability of CO, and $\tilde{U}$ is the dipole sum including image dipole terms for a given adsorbate structure at fractional coverage c_A=1. This model does not include the effect of the chemical shift. The polarizabilities α_e and α_υ are 3 Å^{-3} and 0.27 Å^{-3} for CO on Cu(100), respectively[39,143]. Transitions between higher vibrational states possess a larger transition dipole moment. The dipole moments of the $\nu= 1\rightarrow2$ and $2\rightarrow3$ transitions are 1.4 and 2 times larger than for the $\nu= 0\rightarrow1$ transition[277], respectively, in a harmonic oscillator. This trend was observed experimentally for the hot band of CO on Ir(111), indicating a 1.38 times larger dipole moment for the $\nu= 1\rightarrow2$ transition than the fundamental[143]. If we use the dipole sum of $\tilde{U}$=0.3 Å^{-3} for CO on Cu(100), then equation (5.3) results in dipole shift of 9.1, 12.8 and 17.8 cm^{-1} for $\nu= 0\rightarrow1$, $1\rightarrow2$ and $2\rightarrow3$ at 0.12 ML, respectively[13]. This theoretical prediction reproduces the experimental data if a chemical shift of -9 cm^{-1} is introduced, which is close to the value measured by mixed isotope experiments of ca. 10 cm^{-1} for 0.1 ML of CO on Cu(110)[82].

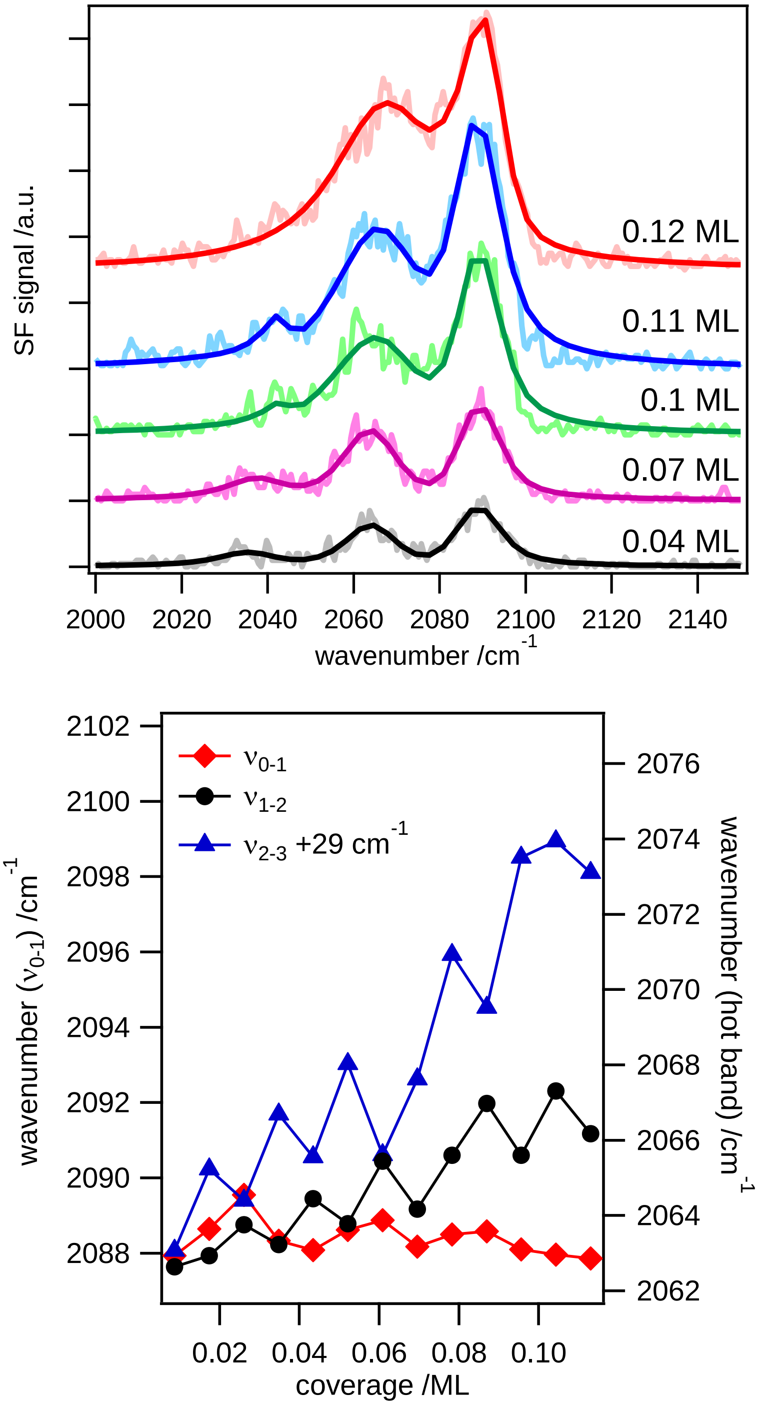

Figure 5.3 (top) SFG spectra of CO/Cu(110) at 100 K as a function of CO coverage with 10 μJ IR pulses. (bottom) The C-O frequency shift of the fundamental and the hot band transitions as a function of CO coverage.

5.3.2 RAIRS : CO-RuTPP/Cu(110)

As a first step to understand the vibrational properties of CO-RuTPP/Cu(110), RAIRS is used prior to the analysis of SFG spectra. Figure 5.4 shows the evolution of RAIR spectra from a RuTPP covered Cu(110) surface as a function of CO dosage. Two distinct peaks were observed in the C-O stretch region 1900-2200 cm^{-1}. The higher frequency peak above 2000 cm^{-1} was assigned to the C-O stretch mode of CO/Cu(110), as previously reported[82,278]. The other peak was observed around 1960 cm^{-1}. This frequency is similar to the reported value of the C-O stretch mode of CO-RuTPP in an argon matrix at 1951.1 cm^{-1} (8 K)[279] and in vacuum at 1944 cm^{-1} (293 K)[280] and we therefore assign this peak to the C-O stretch mode of CO-RuTPP/Cu(110). A prominent shoulder peak around 2030 cm^{-1} is also observed. This peak has not been observed from CO on Cu(110) without RuTPP deposition. It is tentatively assigned to arise from CO molecules in between the RuTPP array. A previous report with STM and XPS observed that NO molecules can intercalate in the CoTPP array on Ag(111)[281].

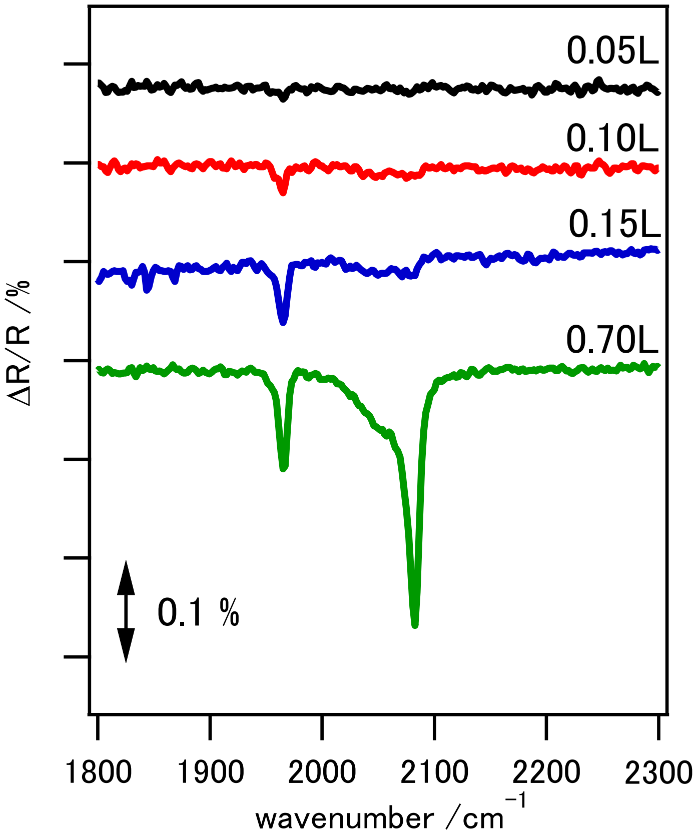

Figure 5.4 RAIR spectra of the C-O stretch region from the RuTPP covered Cu(110) surface as a function of CO dosage.

Next, RuTPP coverage dependence of the C-O stretch mode was monitored while dosing RuTPP at room temperature in under high CO background pressure of 1×10^{-7} torr. The deposition was performed at RT to form a self-assembled structure on the copper surface. A new peak appeared at 1967 cm^{-1} in addition to the C-O stretch mode of CO-RuTPP/Cu(110) at 1952 cm^{-1} as shown in figure 5.5. The redshift of the 1952 cm^{-1} peak compared with the measurement at 83 K can be explained by phonon coupling as discussed for CO on Cu(110) surface in chapter 3. There is no significant different in phonon coupling to CO-RuTPP/Cu(110) comparing to CO/Cu(110) (see chapter 7). The peak at 1967 cm^{-1} is observed after the peak at 1952 cm^{-1} is saturated. Neither increasing CO background pressure nor dosing RuTPP alone provides the peak at 1967 cm^{-1}. This peak is assigned to the C-O stretch mode of CO on multilayer RuTPP on Cu(110). CO adsorbed on multilayer RuTPP shows a higher frequency than CO adsorbed on monolayer RuTPP[279]. Multilayer RuTPP is expected to show weaker interaction with the copper substrate, which should create a stronger Ru-CO interaction inducing the increase of the backdonation from ruthenium d orbital to CO $2\pi^*$ orbital. This weakens the C-O bond and lowers the CO stretch frequency as proposed for mettalloporphyrin carbonyl complexes[282,283]. Thus, it cannot explain the observed blueshift. Another possibility is the creation of $(CO)_2$-metalloporphyrin which shows a higher C-O stretch frequency of 1990-2050 cm^{-1} than a monocarbonyl metalloporphyrin of 1920-1950 cm^{-1} by reduced backdonation due to two CO molecules competing for the centre metal d orbitals[284]. Dicarbonyl-RuTPP in Ar matrix[279] shows the C-O stretch mode at 2015 cm^{-1}. In surface confined porphyrins, CO-Fe protoporphyrin IX (CO-FePP) on gold electrode was studied by surface enhanced IR absorption spectroscopy, showing the frequency of ~1960 cm^{-1} for CO-FePP and a slightly higher frequency of $(CO)_2$-FePP[285]. Thus, formation of cis-dicarbonyl RuTPP can explain the higher frequency peak of multilayer RuTPP.

The transition dipole moment of CO on RuTPP compared to CO on Cu(110) surface can be estimated from RAIRS because infrared absorption provides a simple relationship between adsorbate coverage and signal intensity. The peak integral of 0.77 ML CO on Cu(110) is first obtained as reference. If the transition dipole moment of CO on RuTPP/Cu(110) is assumed to be same as CO on Cu(110), the coverage of saturated CO-RuTPP on Cu(110) is estimated as 0.031 ML from the RAIR spectra of monolayer CO-RuTPP. This assumption seems reasonable because the estimated saturated coverage is close to the expected value from the unit cell of the RuTPP supramolecular structure which suggests that dipole moment of CO-RuTPP/Cu(110) has similar value with CO/Cu(110). Since dipole-dipole coupling hardly affects the hot band frequencies of CO/Cu(110) at this coverage (figure 5.3b), we can be confident that the measured frequencies are the singleton frequencies.

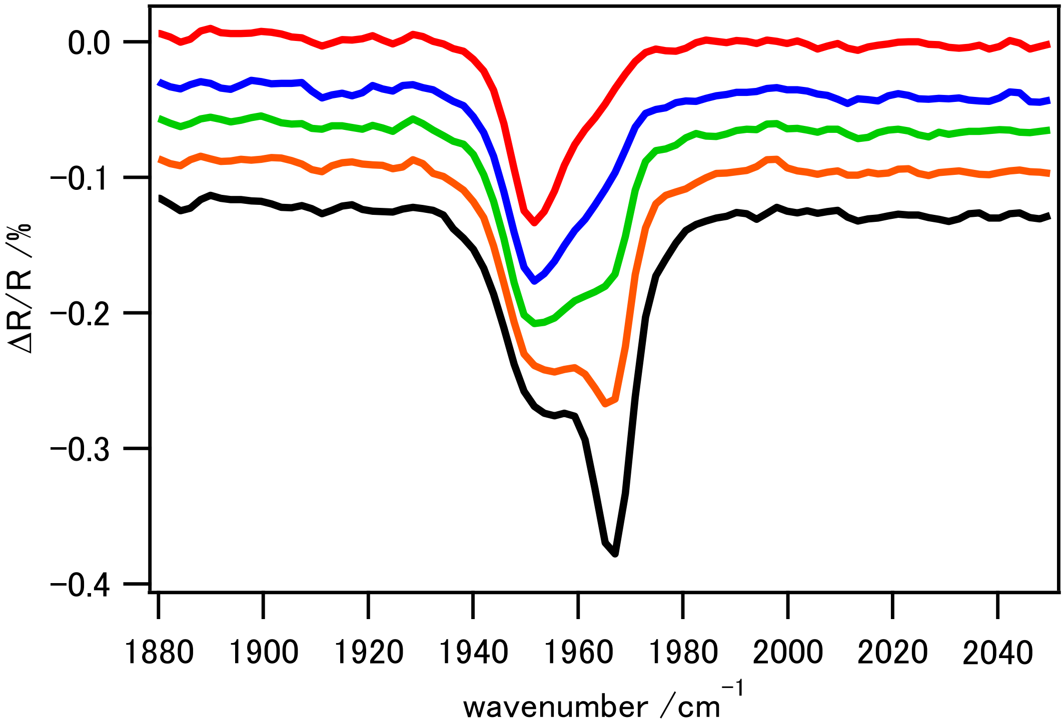

Figure 5.5 RAIR spectra of CO on RuTPP on Cu(110) as a function of RuTPP coverage. RuTPP coverage increases from top to bottom. Spectra were acquired every 3 minutes under continuous dosing of CO-RuTPP.

5.3.3 SFG : CO-RuTPP/Cu(110)

Figure 5.5 shows SF spectra of the C-O stretch mode from the CO-RuTPP/Cu(110) surface. A high frequency peak at 2093 cm^{-1} is observed, which is assigned to the C-O stretch mode of CO/Cu(110)[82,278]. The shoulder peak of RAIRS around 2030 cm^{-1} has not been observed in SF spectra. Generally, RAIRS and SFG should show resonant peaks at the same frequency, but the intensity ratio between peaks is not necessarily the same. The Raman tensor[286,287] and dipole-dipole coupling[288] affect SF intensity in addition to the transition dipole moment. Intercalated CO could conceivably have a different Raman tensor but we cannot exclude that differences are caused by the differences in sample preparation in the two chambers.

In addition, there are two lower frequency peaks at 1957.1 ±0.3 cm^{-1} and 1927.0 ±0.6 cm^{-1}. The peak at 1957.1 cm^{-1} is assigned to the C-O stretch mode of CO-RuTPP/Cu(110) as observed in RAIRS. A reasonable assignment of the peak at 1927.0 cm^{-1} is the ν= 1→2 hot band transition. To confirm this assumption, the power of the IR beam was decreased. Figure 5.6(a) shows the disappearance of 1927 cm^{-1} peak indicating that this peak is indeed the hot band transition. A third peak is observed around 1895 cm^{-1}, which can be assigned as the ν= 2→3 vibrational hot band transition. The anharmonic frequency shift between ν= 0→1 and ν= 1→2 is 30 cm^{-1} which is 10 % larger than for CO on metal surfaces.

Since dipole-dipole coupling can modify the frequency of a transition, we carefully examine the coverage dependence to evaluate its extent. The saturated CO-RuTPP coverage is estimated as 0.03 ML from the unit cell of RuTPP which was determined by STM images (chapter 4). The coverage of RuTPP is estimated from the temperature programmed desorption spectra which provide a coverage of 0.025 ML and 0.15 ML for CO-RuTPP and CO on Cu(110), respectively. The coverage of coadsorbed CO is higher than the Cu(110) area left bare by RuTPP molecules, which can be caused by the intercalation of CO into the RuTPP molecular islands. If the sticking coefficient is constant over the whole coverage range, then the lowest coverage of figure 5.6(b) is ~10 % of saturation from the amount of CO dosage, suggesting that the lowest coverage spectrum of CO on RuTPP/Cu(110) is recorded at 0.0025 ML. This corresponds to a distance of 8.9 nm between CO molecules which is much larger than the distance of 4.9 nm (0.006 ML) of CO on Ru(001)[142] where the energy exchange by dipole-dipole coupling was found to be negligible. Indeed, the intensity ratio of the ν= 1→2 hot band and ν= 0→1 transitions remains constant (32±2 %) while the coverage of CO increases. The frequency of vibrational excitation peaks is also independent from CO coverage and IR fluence, indicating that CO-CO interactions are negligibly small under these experimental conditions[82,142,271,289].

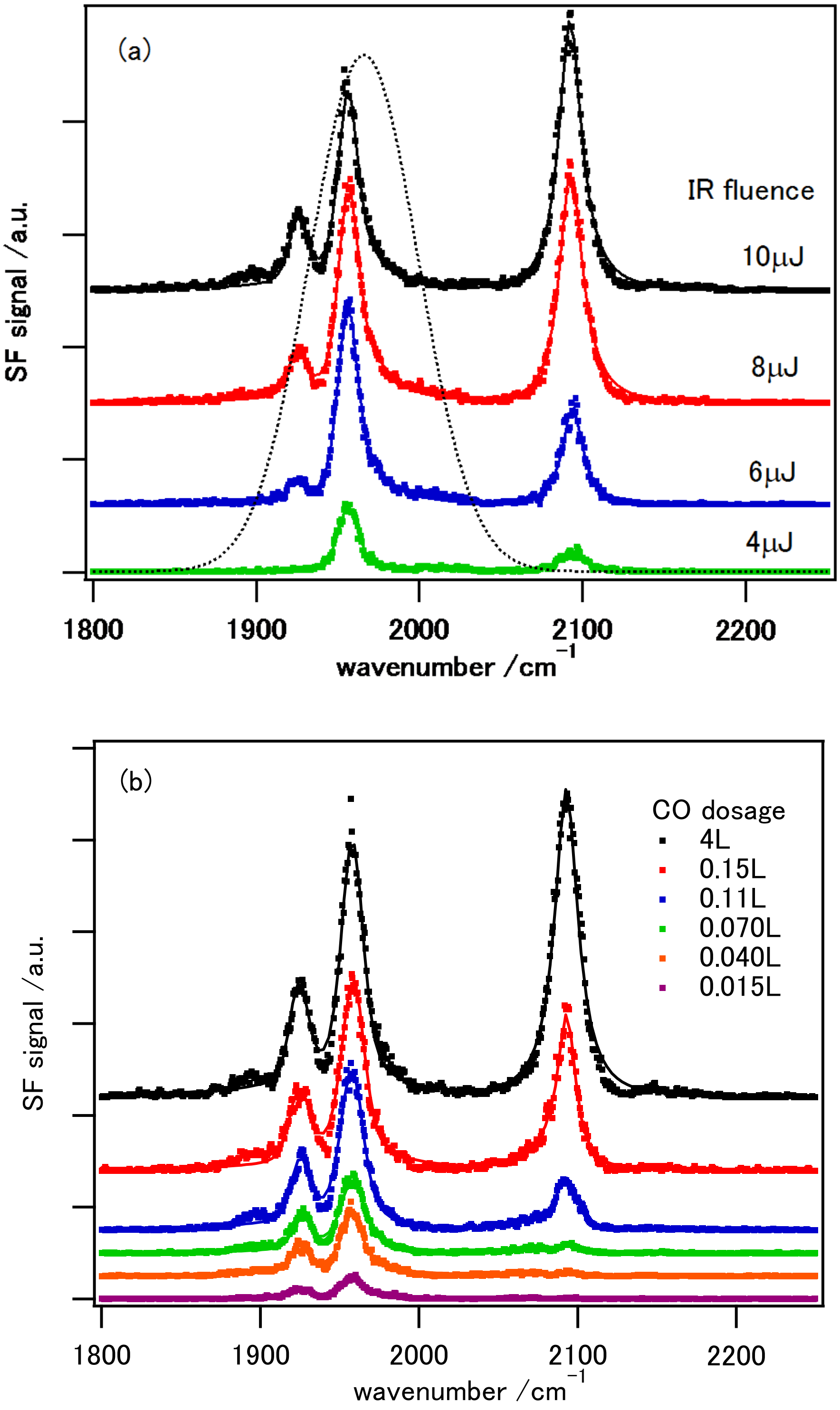

Figure 5.6 SFG spectra of the C-O stretch mode from CO-RuTPP/Cu(110) as a function of (a) IR fluence, (b) CO dosage. RuTPP coverage is estimated to be 80 % of saturation from the TPD spectra.

5.4 Discussion

Here we discuss the large anharmonicity of CO-RuTPP/Cu(110). Assuming a Morse potential, equation (5.1) gives 0.0076 for χ_e . This value is the highest value among the reported anharmonicities of the C-O stretch mode. We can exclude any artifacts caused by coverage and infrared probe power as shown above.

The C-O stretch of gas phase CO shows an anharmonic shift of 26.6 cm^{-1} which corresponds to χ_e=0.0061 [275]. Anharmonicity increases generally upon adsorption: 0.0066 (26.8 cm^{-1}), 0.0065 (26.8 cm^{-1}) and 0.0064 (25 cm^{-1}) have been reported for CO/Ru(001)[83], CO/Ir(111)[143] and carboxyl hemoglobin[272], respectively. A porphyrin carbonyl complex molecule, namely heme domain FixLH from Bradyhizobium japonicum, shows an even larger anharmonicity of 0.0069 (29 cm^{-1})[274]. The reported anharmonicities are summarized in table 5.1.

The anharmonicity of the C-O stretch mode has not been systematically investigated in detail. Here, CO on metal surfaces is first examined. The anharmonicity increases in the order of gas phase CO, and adsorbed on Cu(110), Ir(111) and Ru(001) surfaces. This trend indicates that the lower the stretch frequency, the higher the anharmonicity. A lower frequency of the C-O stretch mode generally corresponds to a weaker C-O bond and a stronger CO-metal bond[290-292] because donation from the metal d orbital to the CO $2\pi^*$ orbital weakens the C-O bond and decreases the frequency of the C-O stretch mode. A weaker C-O bond means a lower dissociation energy and therefore a larger anharmonicity. There is a good correlation between frequency and anharmonicity for gas phase CO and CO on metal surfaces as shown in figure 5.7.

Table 5.1 Anharmonicity of the C-O stretch mode in different systems

System	Fundamental [cm^{-1}]	Hot band [cm^{-1}]	Morse anharmonicity χ_e	D_e [eV]	Ref
CO-RuTPP/Cu(110)	1957.1	1927.0	0.0076	8.1	-
CO gas phase	2143.3	2116.6	0.0061	11	-
CO/Cu(110)	2088.6	2063.0	0.0061	10.7	-
CO/Cu(110)-(6×2)O	2112.1	2085.4	0.0063	10.5	-
CO/Ru(001)	1990.4	1961.4	0.0067	9.3	SFG[131]
CO/Ru(001)	1989.9	1963.1	0.0066	9.5	IR[83]
CO/O/Ru(001)	2069	2040	0.0070	9.3	SFG[131]
CO/Ir(111)	2041	2014.2	0.0065	9.9	SFG[143]
carboxy hemoglobin	1950	1925	0.0064	9.6	IR[272]
FiXLH-CO	2123	2094	0.0069	9.7	IR[274]

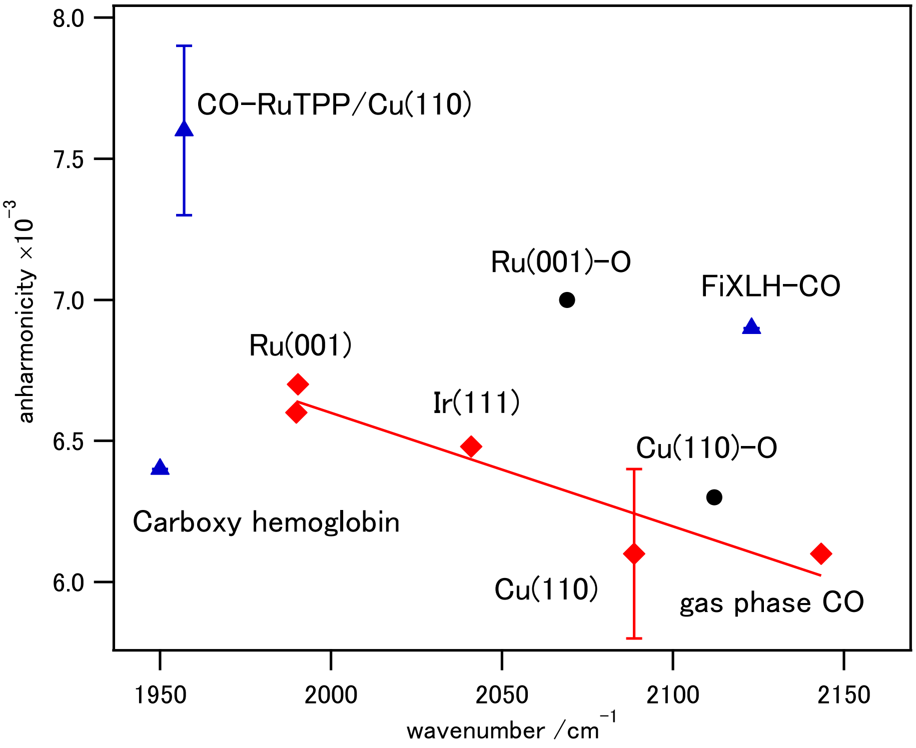

Figure 5.7 Morse anharmonicity of the C-O stretch mode as a function of the ν= 0→1 transition frequency. Red squares, black circles, and blue triangles represent CO on metals, oxidized metals and porphyrin complexes, respectively. The solid line is the result of a linear fit to the red squares.

Next, the anharmonicity of CO coadsorbed with oxygen is discussed which shows larger anharmonicity than expected. 0.0063 and 0.0070 are obtained from CO coadsorbed with oxygen on Cu(110) and Ru(001), respectively. Coadsorption of oxygen withdraws substrate electrons, which reduces backdonation (from copper d orbitals into the CO $2\pi^*$ orbital) increasing the frequency of the C-O stretch, as observed for CO on Cu(110)-(6×2)O. This reduction of backdonation also increases the dissociation energy, therefore the anharmonicity should decrease. This is clearly different from the observation. Oxygen coadsorption not only reduces the backdonation to CO, but also creates a static electric field around the CO molecules of 0.04 V/Å (=4 MV/cm) as calculated for O+CO on Pt(111)[198]. This static electric field can affect the vibrational properties of CO, also known as the vibrational Stark effect (VSE)[293].

The VSE was initially discussed in the context of adsorbates at electrochemical interfaces under potential control, where changes in frequency and intensity were observed as a function of applied potential[294-298]. The ground and vibrational excited states have different dipoles, thus they are influenced differently by an external field. For example, VSE of CO on Ru(001) surface has been studied by IR spectroscopy under potential control in an electrochemical cell, showing VSE is 37 $\mathrm{cm^{-1}/V}$ and 29 $\mathrm{cm^{-1}/V}$ for CO on (2×2)-O, and (3×1)-O oxide layers, respectively[299]. VSE is also often used to detect local electric fields in proteins observing frequency shifts, using reporter labels such as CN and CO[293]. For porphyrins and proteins, vibrational Stark tuning rates are measured to be around 0.5-2 $\mathrm{cm^{-1}/(MV/cm)}$.

The vibrational Stark tuning rate has two contributions from the mechanical anharmonicity ($\Delta\mu_{anh}$) and field dependent force constant ($\Delta\mu_{bond}$). The harmonic force constant of an oscillator is influenced by the external field interacting with partial charges in the CO which changes the frequency, but does not affect the anharmonicity of the oscillator. Mechanical anharmonicity means that the external field shifts the vibrational ground and excited states by different amounts, because these states possess different static dipole moments. This causes a frequency shift in the transition between vibrational ground and first excited states, but actually shifts the hot band transitions more, due to the increasing dipole moments, as shown in figure 5.8. It is known that $\Delta\mu_{anh}$ is almost equal to the Stark tuning rate for C-O stretch mode[294]. According to an estimate by Park and Boxer[294],

$$\Delta\mu_{anh}=3|M|\sqrt{\chi_e} \tag{5.4}$$

where |M| is the transition moment of the oscillator in units of Debye (D). Equation (5.4)gives $\Delta\mu_{anh}=0.07$ for the fundamental transition, which will increase by a factor 2 for the hot band due to the larger transition dipole moment. The Stark frequency shift is expressed by $\Delta\mu \times F$, where F is the external local field. The hot band transition therefore shows a frequency shift twice as large as for the fundamental, resulting in a Stark shift of -1 cm^{-1} for fundamental and -2 cm^{-1} for hot band per MV/cm. A field of 1 MV/cm^{-1} could then account for the apparent increase in anharmonicity of CO coadsorbed with oxygen to 0.0063 from 0.0061. Such a Stark shift may also bring the relatively large anharmonicity of CO-RuTPP back in line with the value expected from the C-O stretching frequency.

In our discussion, we also need to address whether a Morse potential is the best description for CO on surfaces. In the Morse potential, the anharmonic frequency shift must remain constant for higher vibrational transitions, however, the anharmonic shift between fundamental and first hot band, and first and second hot bands increases from 25.6 to 26.9 cm^{-1} for CO/Cu(110) and from 30.1 to 32.0 cm^{-1} for CO-RuTPP/Cu(110). The increase in anharmonic shifts cannot be due to a contribution of ^{13}CO, but there are no known cases in the literature where this assumption fails.

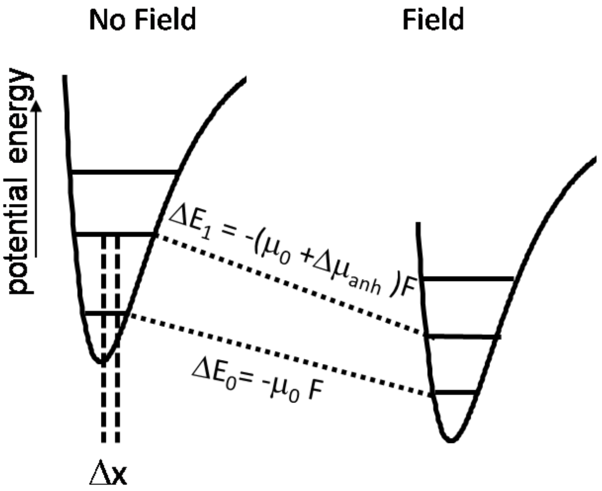

Figure 5.8 (adapted from ref[294]) Schematic illustration of the effect of an electric field on a vibrational transition energy leading to the observed VSE. Mechanical anharmonicity shifts vibrational levels depending on their dipole moment, which changes both the frequency of the transition and the anharmonic frequency shift between adjacent levels. q is the effective charge of the oscillator.

In order to elucidate oscillator anharmonicity, the simulation of the PES is currently in progress by Mr.Paolo Poli in collaboration with Prof. Mats Persson in Liverpool. Table 5.2 summarizes the preliminary results of the calculated frequency and anharmonicity. An increase of the Morse anharmonicity after adsorption of CO-RuTPP onto Cu(110) surface has been observed. However, the frequency of the C-O vibrational modes and absolute values of the anharmonicity are not reproduced by the simulation. Currently, a more accurate calculation of the dissociation energy, which accounts for more than just the PES near the potential minimum and a potential electric field caused by charge transfer between substrate and RuTPP (which was calculated to be $1.3e^-$ from substrate to adsorbate in the case CoTPP/Cu(110)[89]) are in progress.

Table 5.2 Calculated frequency and anharmonicity

System	Frequency of $\nu = 1 \rightarrow 2$ [cm^{-1}]		Morse anharmonicity χ_e		C-O equilibrium Distance [Å]
	Experimental	Simulation	Experimental	Simulation	-
CO gas phase	2143.3	2107	0.0061	0.0064	1.14
CO/Cu(110)	2088.6	2034	0.0061	0.0061	1.16
CO-RuTPP	1951.1	1935	-	0.0060	1.175
CO-RuTPP/ Cu(110)	1957.1	1912	0.0076	0.0064	1.174

5.5 Conclusion

Higher vibrational states of CO on a bare and a RuTPP covered Cu(110) surface have been studied by intense IR – visible SFG. The $\nu = 0 \rightarrow 1$ C-O stretch mode of CO-RuTPP on Cu(110) appeared at 1957 cm^{-1} with the $\nu = 1 \rightarrow 2$ hot band peak at 1927 cm^{-1} showing higher anharmonicity than for CO on metal surfaces. The frequency of the C-O stretch mode and the hot band population of CO-RuTPP/Cu(110) are independent from the coverage of CO, which indicates that dipole-dipole coupling among CO on RuTPP is negligibly small. A Morse anharmonicity of 0.0076 was obtained from CO-RuTPP/Cu(110) which is the largest value among reported C-O stretch modes. The anharmonic frequency shift is found to increase for higher vibrational transitions, which suggests that the Morse anharmonic potential is not a good description of the anharmonic potential at surfaces. Although the complexity of the surface anharmonic potential makes the design of ladder climbing reactions nontrivial, the porphyrin layer is shown to be a promising template for lowering the dissociation energy of CO.

Chapter 6

Desorption of CO from single ruthenium porphyrin on Cu(110) with STM

Magnetic, electronic and optical properties of metalloporphyrins have been controlled by adsorption/desorption of small molecules, such as CO, NO and NH_3, onto/from their centre metal atoms. Understanding the desorption mechanism is indispensable for describing how the energies are transferred and dissipated through the local electronic structure of the metalloporphyrins. In this work, the desorption of CO from a RuTPP on Cu(110) was investigated using an STM at a cryogenic temperature (4.7 K). Tunneling electrons between STM tip and CO-RuTPP/Cu(110) induce CO desorption. A desorption yield measurement with the STM exhibits a sudden increase at a sample bias voltage of -1.1 V, corresponding to electronic states observed in scanning tunneling spectra (STS). The desorption rate as a function of tunneling current was measured to be $I^{2.1}$, $I^{2.3}$ and $I^{1.8}$ at sample bias voltages of -1.25, -1.40, and -1.60 V, respectively, indicating that CO desorption is a two carrier process over a wide range of bias voltages. The mechanism of CO desorption is suggested to be the creation of a tentative positive ion.

6.1 Introduction

The formation and breakage of metal-carbonyl bonds have generated much interest because of their correlation with biological and catalytic properties such as the prevention of hemoglobin oxygen transport and CO poisoning in heterogeneous catalysis[300,301]. Thermal and photo-induced metal-carbonyl bond breaking provides information about the bond strength and energy transfer[302-304]. The formation/breakage of a metal-carbonyl bond also makes it possible to control the electronic structure and physical properties of organometallic compounds.

Metalloporphyrins attract profound interest because of their unique electronic structures and optical/magnetic properties as commonly used organic semiconductors. Introducing small molecules, such as CO[35,243-245,305,306], NO[243,307-310] and NH_3[311,312], onto the metal atom at the centre of the porphyrins provide additional flexibility to their electronic[35,305,307,311] and magnetic[243-245,306,308-310,312] properties for future applications in chemical sensing and molecular electronics[313-315]. For example, the coordination of CO onto RuTPP increases its electronic excitation lifetime by 1000 fold by switching the lowest excited state from a singlet (d,π^*) to a triplet the $^3(\pi,\pi^*)$ state, leading to phosphorescence[35].

A scanning tunneling microscope (STM) is a versatile tool for investigating the chemical reactions and motions of a single molecule by imaging and manipulating individual molecules. An important factor in chemical reactions when using the STM tip is the local density of states (LDOS) in which molecular orbitals of the adsorbate hybridize with the metal substrate. Tunneling electrons are trapped at the LDOS, which creates an electronically excited adsorbate, followed by the induction of motion or reaction before energy relaxation from the adsorbate into the metal substrate. This inelastic electron tunneling (IET) process induces vibrational excitation or direct electronic excitation, which leads to motions of the adsorbate. Various types of IET processes for carbon monoxide (CO) on metal surfaces have been studied. An important process of the vibrational excitation-induced bond breaking is resonant tunneling of electrons into the molecular orbitals (MOs) around the Fermi level, which lead to the excitation of an adsorbate vibration directly or indirectly along the reaction coordinate[28]. For example, the desorption and diffusion of a CO molecule on Cu(111) were observed, with a threshold sample bias voltage of V_s=2.4 V, which was explained by the fact that the motion of a CO molecule is caused by a single electronic transition through electron injection into the CO $2\pi^*$ state[58]. It should be noted that the excited electrons need to be localized at the target chemical bond for a sufficiently long period to induce motion. In contrast to CO on metal surfaces, only a few STM studies have been reported for CO desorption from organometallic complexes, which exhibits a much weaker interaction between CO and the metal substrate because of electronic decoupling by the organic molecular template.

The desorption of an attached CO, NO or NH_3 from a metalloporphyrins has been achieved either by heating the substrate[306-308,310-312] or by tunneling electron injection to the molecule[244,245,309,316] from the tip of an STM. Burema *et al.* reported controlled desorption of a NO molecule from cobalt tetraphenyl porphyrin (CoTPP) on Ag(111) by injecting electrons from the STM tip at a sample bias voltage (V_s) of 800 mV[316], which was explained by either electric field effect or substrate mediated electron propagation. The electron injection with the STM also induces CO desorption from manganese phthalocyanine[244]. The authors observed a sudden drop in the tunneling current (I_t) in a V_s range of 400–600 mV, depending on the tip-sample distance, implying that the CO desorption was caused by an electric field effect. Energy transfer to the Co-NO bond via inelastic electron tunneling was inferred from the desorption of NO from NO-CoTPP/Au(111)[317]. Desorption of NO was observed as a two-carrier process at 0.8 V, changing to a one-carrier process at 1.0 V. The proposed mechanism is vibrational ladder climbing of the Co-NO bond, where 1.0 V electrons are sufficient to lead to direct desorption, while two lower energy electrons need to arrive within the vibrational relaxation time to cause desorption[317].

This chapter presents a single molecule investigation of the desorption of CO from the ruthenium tetraphenyl porphyrin carbonyl complex (CO-RuTPP) on a Cu(110) surface using an STM. The CO desorption from a CO-RuTPP molecule was investigated in detail using a combination of scanning tunneling spectroscopy (STS) and reaction yield measurement with the STM (which corresponds to action spectroscopy in the electronic energy region), leading to the conclusion that CO desorption from CO-RuTPP/Cu(110) is driven by hole creation into occupied states of CO-RuTPP. Reaction yield measurements showed a sudden increase in the desorption yield at around V_s=-1.1 V. The current dependence of the reaction yield provided power law relationships of $I^{2.1}$, $I^{2.3}$, and $I^{1.8}$ at sample bias voltages of -1.25, -1.40, and -1.60 V, respectively, indicating a two-carrier process over a wide range of V_s.

6.2 Experimental

All of the experiments were performed using a low-temperature STM (Scienta Omicron Inc, LT-STM) at 4.7 K, with an electrochemically etched tungsten tip at a base pressure of 3×10^{-11} torr. A Cu(110) single crystal surface was cleaned using several cycles of Ar^+ ion sputtering and annealing at 800 K. The CO-RuTPP was purchased from Sigma Aldrich (purity ~80 %) and was transferred into the homemade molecular doser. The molecular doser was degassed over 12 h at ~150 °C in vacuum to remove residual solvent and other impurities. The purity of CO-RuTPP was monitored by mass spectroscopy, and also directly confirmed from STM image. The sublimation of the CO-RuTPP onto a clean Cu(110) surface was performed by resistive heating of the molecular doser to ~200 °C, holding the substrate at room temperature. After the adsorption of RuTPP, the sample was left at room temperature for 12 h prior to the transfer into the cryostat for LT-STM experiments, in order to form a self-assembled island structure. The deposition of CO molecules onto the Cu(110) surface was performed using a dosing tube at ~50 K. The acquired images were processed using the WSxM[172] software to adjust the image contrast and calibrate the distance.

6.3 Results

6.3.1 STM imaging

The deposition of CO-RuTPP onto the Cu(110) surface at room temperature led to the display of bright protrusions across the surface, as shown in the STM images of figure 6.1(a)–(b). The details of adsorption structure and supramolecular structures have been already described in chapter 4. Briefly, isolated molecules and self-assembled structures are observed. The STM images show a four-lobe structure that resembles the RuTPP molecular structure. The angle and size of the STM images were calibrated using an atomically resolved STM image of a bare Cu(110) surface, as shown in the inset of figure 6.1(a). With increasing molecular coverage, the RuTPP molecule forms a regular and ordered array structure. After CO exposure at ~50 K, the image contrast at the centre of RuTPP molecules becomes much brighter, indicating attachment of CO on top of a ruthenium atom, as observed with CO adsorption onto metallophtalocyanines on other metal surfaces[243,244]. This feature was not observed prior to CO exposure and was assigned to arise from CO adsorption onto a ruthenium atom, which leads to the conclusion that the CO-RuTPP decomposed into CO and RuTPP during the deposition process. The cross-sectional height profile demonstrates that CO-RuTPP has a larger apparent height than RuTPP, as shown in figure 6.1(d), which is consistent with CO-MnPc/Bi(110)[244], but different from CO-FePc/Au(111)[245] and CO-CoTPP/Ag(111)[246], where CO adsorption reduced the apparent heights of the porphyrins by modifying the local densities of states. This indicates that the contribution of CO to the STM image originates from the change in electronic structure rather than the height of the adsorbate.

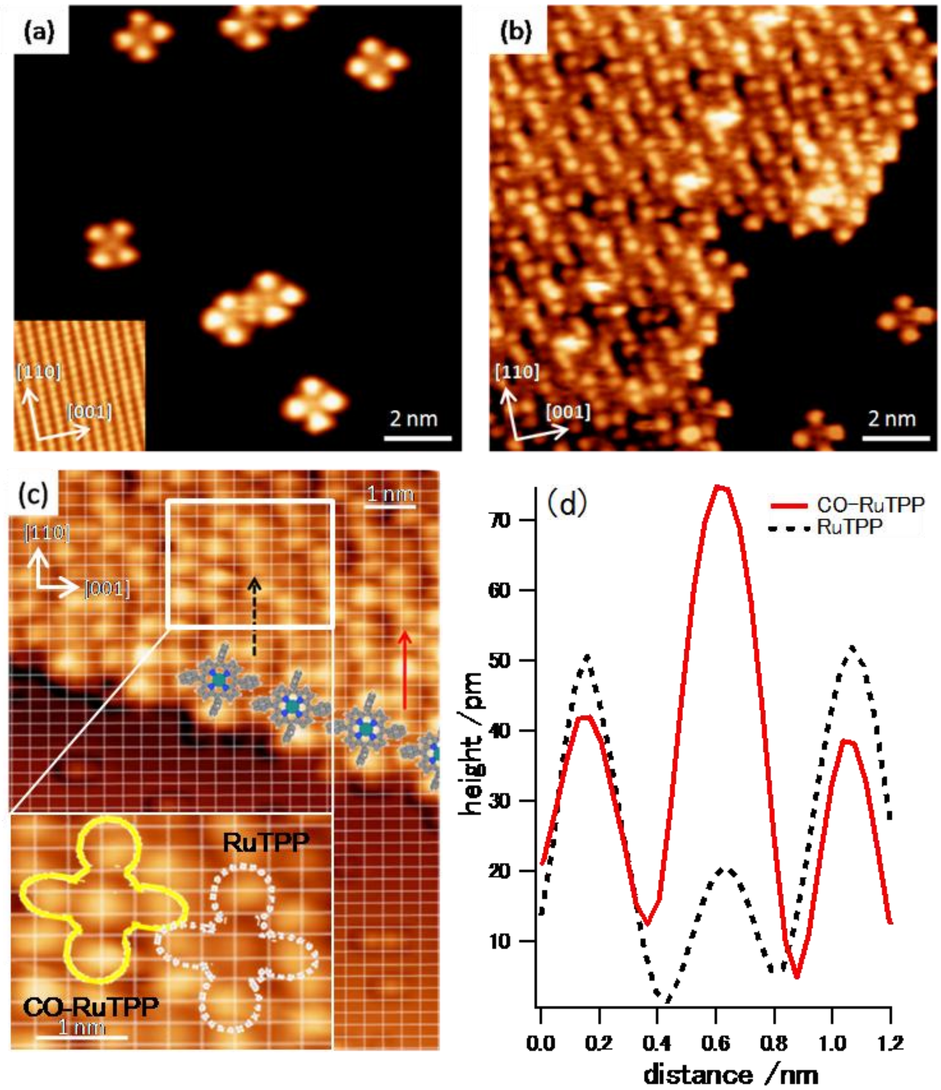

Figure 6.1 (a)–(c) STM images of RuTPP and CO-RuTPP adsorbed on Cu(110). The images were obtained at 4.7 K with V_s = 500 mV and I_t = 0.5 nA. (a) Inset: atomic resolution STM image of bare Cu(110) used to calibrate the distance and angle of the STM images. (c) STM image of RuTPP coadsorbed with CO, which is superimposed on the Cu(110) lattice lines calibrated by CO/Cu(110). A ball and stick model of RuTPP is overlaid on the STM image. Inset: enlarged image of RuTPP and CO-RuTPP, which are marked by dotted and solid lines, respectively. (d) Cross-sectional height profiles measured along the straight lines of RuTPP and CO-RuTPP on Cu(110). The corresponding solid and dotted lines are shown in (c).

6.3.2 Electronic structure

The electronic structure of RuTPP and CO-RuTPP on Cu(110) was studied using scanning tunneling spectroscopy (STS). Figure 6.2 shows STS spectra from the centre of RuTPP and CO-RuTPP after subtracting the reference signal from a bare Cu(110) surface. Due to the strongly nonlinear dependence of signal at high bias voltages, a reliable difference spectrum could only be obtained in the range of -1.3 to +0.9 V. RuTPP exhibits an increase in the LDOS at a negative V_s. A distinct peak at around V_s=-1.1 V (figure 6.2 (a) and (d)) was observed from both RuTPP and CO-RuTPP. Such occupied states have been widely observed for metalloporphyrins on metal surfaces[318,319] e.g. the STS spectrum of CoTPP on Cu(110) has been reported, and reveals a peak at a negative sample bias of -0.72 eV, which was assigned to the highest occupied molecular orbital (HOMO) of CoTPP[318]. We equally assign our peak at V_s=-1.1 V to the RuTPP HOMO and note that it is not shifted by subsequent CO adsorption. Two additional peaks were observed at V_s=-0.8 V (figure 6.2 (b)) and around the Fermi level (figure 6.2 (c)) for CO-RuTPP/Cu(110). The peak (b) of figure 6.2 can be assigned to the HOMO of CO-RuTPP. The origin of the peak (c) is currently unknown. Since CO-RuTPP exhibits a bright centre spot at V_s=0.5 V, the low energy states are likely localized to the centre of the CO-RuTPP. The assignment of each peak to molecular orbitals can be achieved by DFT calculation for partial DOS. It should be noted that CO adsorption onto CoTPP/Ag(111) did not produce any additional peaks in the range of -670 to +270 mV[246].

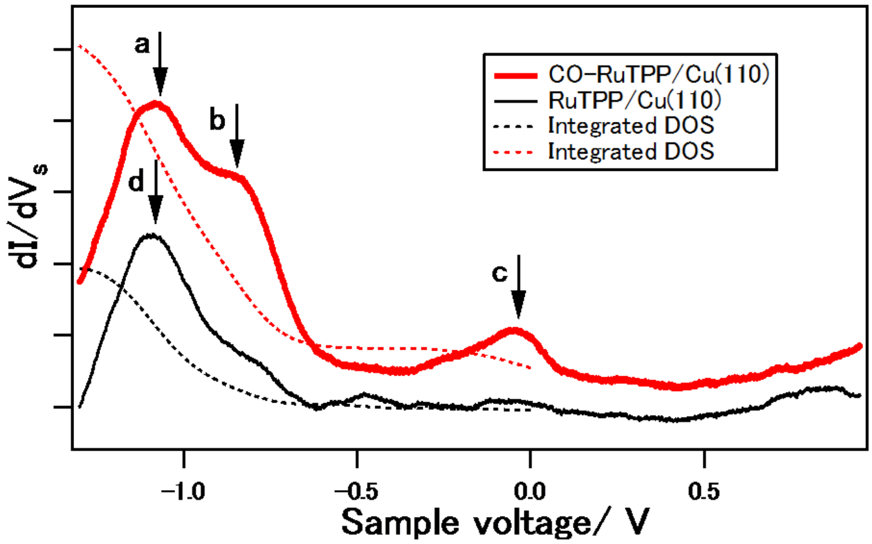

Figure. 6.2 STS spectra of CO-RuTPP and RuTPP on Cu(110). The STS spectrum of bare Cu(110) is subtracted to emphasize the change in dI/dV. Dotted lines show the integrated of STS signal from the Fermi level. For the assignment of each peak, see text.

6.3.3 Reaction yield measurement

We next studied the desorption of CO from CO-RuTPP/Cu(110) by tunneling electrons from the STM tip to the centre of CO-RuTPP. After recording an STM image (figure 6.3(a)) the tip was fixed over the centre of the CO-RuTPP and tunneling electrons injected into the molecule at a specific sample bias voltage with the feedback loop turned off. CO desorption appears as a sudden change in the tunneling current in the I_t plot, as shown in figure 6.3(c). This was confirmed by a subsequent STM image (figure 6.3(b)), where a loss of CO is seen as a loss of the bright protrusion in the RuTPP centre. CO-RuTPP and RuTPP molecules are indicated by solid and dotted lines in figure 6.3(a)-(b), respectively. The desorption yield Y was calculated from $Y = e/I\tau$, where e is the elementary charge, and τ is the average time required for desorption. The desorbed CO can transfer to the vacuum, tip or a neighboring molecule[58,244]. The averaged values of $Y(V_s)$ were obtained by repeating this experiment 10 times at each V_s.

The desorption yield was recorded in the range of V_s=-1.075 to -1.60 V, as shown in figure 6.4. No CO desorption was seen in the vibrational energy region below 400 mV at 4.7 K or 77 K. Instead, we observe an increase in the desorption probability at voltages below -1 V, followed by a plateau in the region of V_s=-1.15 to -1.45 V and an increase for higher bias voltages. Above about -1.2 V, signal levels allowed to measure the current dependence of the desorption yield Y (Figure 6.5). The slope of the double-log plot is the power n in the power-law dependence[320,321]: $Y=I^n$, where n=2.1±0.2, 2.3±0.3, and 1.8±0.1 for V_s=1.25, 1.40, and 1.60 V, respectively. This power-law dependence on the applied current means that the desorption process consists of a two-carrier process, regardless of the applied bias voltage, in the range of - 1.25 to -1.60 V. This is clearly different to NO desorption from CoTPP/Au(111) which shows a change from a single electron process at V_s=0.8 V to a two electron process at V_s=1.0 V.

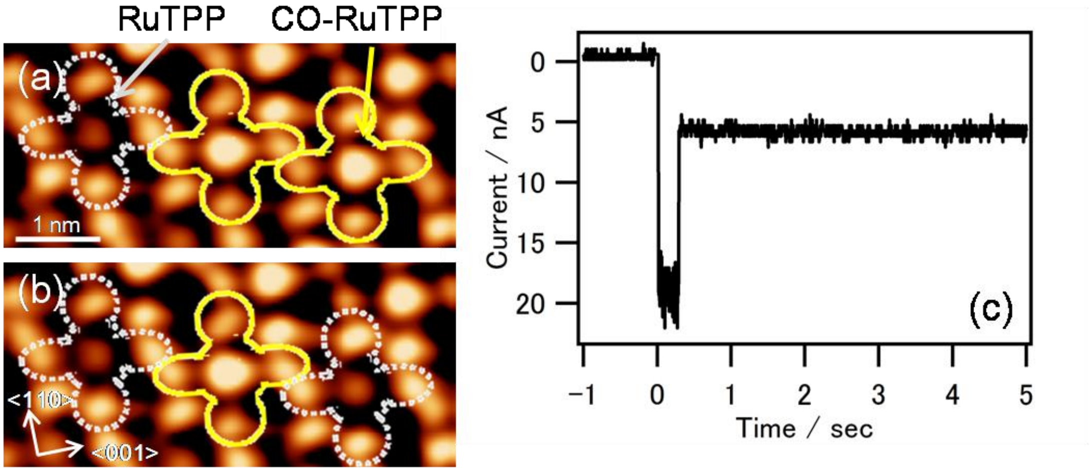

Figure. 6.3 (a)–(b) STM images of CO-RuTPP adsorbed on Cu(110) (V_s= 500 mV, I_t = 0.5 nA) before and after injection of tunneling electrons to the rightmost CO-RuTPP molecule. RuTPP and CO-RuTPP are marked by dotted and solid lines, respectively. (c) Tunneling current measured as a function of time under constant applied voltage (-1.5 V, 20 nA).

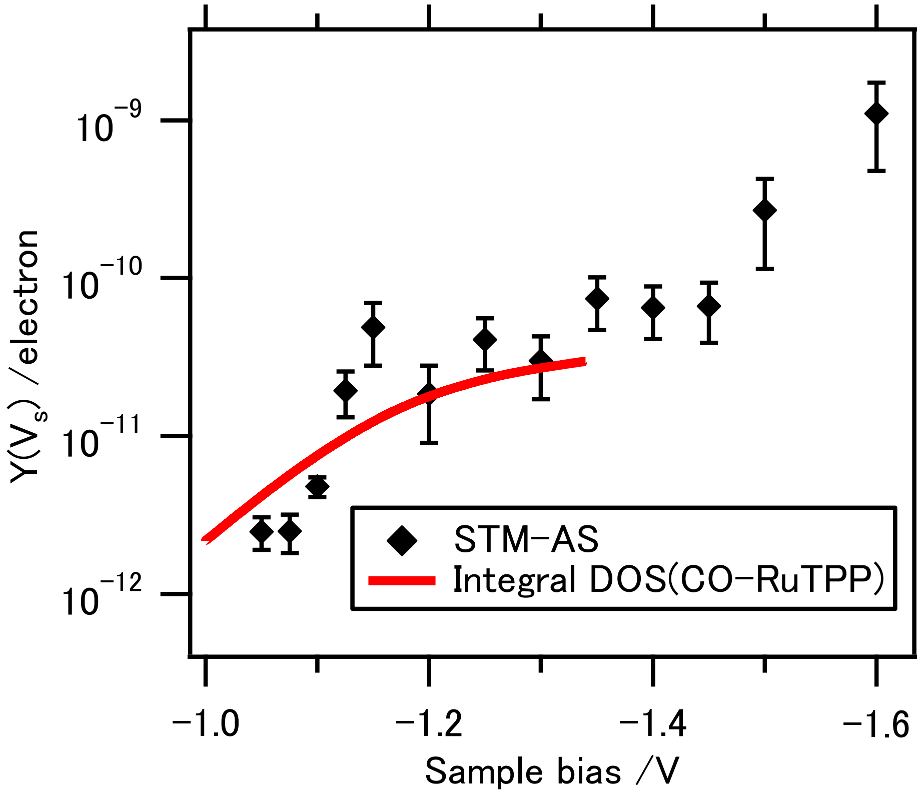

Figure. 6.4 Reaction yield per electron for desorption of CO from CO-RuTPP/Cu(110) as a function of the sample bias voltage of the injected electrons, I_t=20 nA. Solid line is the integrated DOS obtained from figure 6.2.

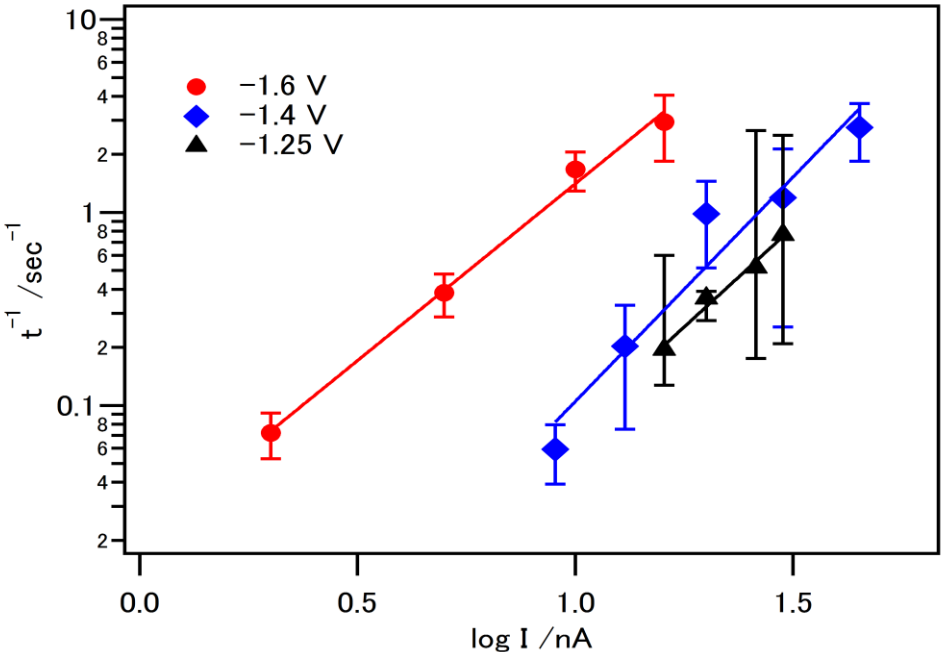

Figure 6.5 CO desorption rate as a function of tunneling current for V_s=-1.25, -1.40, and -1.60 V. The solid lines are the results of least squares fits to the data, whose slopes for the applied bias voltages correspond to powers (n) in the nonlinear power-law dependence. The error bars of (d) and (e) were determined from the standard deviation. The lower boundary of the error bar for -1.25 V in (e) is determined from the maximum desorption time.

6.4 Discussion

The driving force for CO desorption can be explained by either the electric field effect or inelastic scattering of the tunneling electrons. We can exclude an electric field effect, because it should result in a linear dependence of the desorption yield versus electric field (sample bias per tip-sample distance)[322], unlike the dependence shown in figure 6.4.

Next, we discuss the direct excitation of vibrational modes by IET as a possible origin of CO desorption. The desorption yield is too low at the sample voltage of below 1 V to measure the yield within a reasonable time scale. The desorption energy of CO from RuTPP/Cu(110) is ~0.75 eV which indicates that the C-O stretch mode with a vibrational energy of 250 meV is the most likely of all the vibrational modes to realize desorption. However, direct excitation of the C-O stretch mode is inefficient because of the lack of LDOS[28] at the vibrational energy range around 250 meV. We can explain the increase in the desorption yield observed below -1 V and the subsequent plateau by the peak observed by STS around V_s=-1.1 V: while STS detects the LDOS at a specific V_s, the reaction yield in action spectroscopy reflects the integral over the same LDOS. An overlaid plot of the LDOS integral for both bare RuTPP and CO-RuTPP shows the close correspondence between these two measurements in figure 6.4. The integral traces in figure 6.2 also show that we are not able to separate whether the process originates in a CO or a RuTPP-related peak. In either case, the IET process is enhanced by the CO-RuTPP HOMO or the pure RuTPP HOMO. A second threshold is observed at -1.5 V and corresponds again to a two electron process. We conclude that the IET process from the STM tip plays a dominant role in the desorption of CO between the V_s range of -1.075 and -1.5V. Since we are operating at negative bias voltages, the underlying process must be a hole injection into the occupied states, which then leads to desorption of CO.

Desorption induced by hole injection and other chemical reactions have been previously reported in studies of adsorbates on metal substrates[317,323-327]. Applying a positive bias voltage does not show desorption of CO within a reasonable time scale, which can be assigned to a low LDOS of unoccupied states as seen in figure 6.2. It should be noted that applying a high voltage (V_s>±1.5 V) can cause CO desorption non-locally which is assigned to the electric field effect as previously reported[244,245,316,317]. CO desorption from RuTPP on Cu(110) has been already observed to begin at V_s=-1.075 V of figure 6.4. In contrast, CO desorption from a copper surface requires a bias voltage higher than 2.4 V[58]. This difference cannot be explained by different desorption barriers, because the CO desorption temperature of CO-RuTPP is 80 K higher than that of CO/Cu(110) (as shown in figure 7.1 in next chapter). The desorption mechanism of CO from a copper surface is electron injection to the unoccupied $2\pi^*$ state, which occurs in a single-electron process[58]. A two-carrier process was not observed from CO on a copper surface, which can be explained by the short lifetime of the electronically excited state of around 0.8 to 5 fs[58]. We propose that the lower desorption threshold voltage of CO-RuTPP/Cu(110) is due to the two-carrier process as observed in figure 6.5.

The two-carrier induced IET process for a single molecule reaction in such a wide V_s range is unique and so far has not been reported. At this moment, it is unable to conclude the details of desorption mechanism. Here, a probable scenario is described. Since our reaction thresholds are in the energy range of electronic excitations, we propose that the first hole excites CO-RuTPP to an electronically excited (positive ion) state. The second electron then leads to desorption by injecting a further hole. A single hole in the CO-RuTPP HOMO at -0.8 V would unlikely result in desorption: the HOMO of CO-metalloporphyrins is governed by the d_{xy} orbital which has little overlap with the orbitals of CO[282] as shown in figure 6.6, while an efficient IET process would require the localization of the tunneling electrons at the target chemical bond[27]. However, once a hole is injected in the CO-RuTPP or RuTPP HOMO, lower occupied states might become energetically accessible to the second hole. For example, HOMO-1 and HOMO-2 originate from the hybridization between metal d_{xz}/d_{yz} and CO π^* orbitals[282], which contribute to the bond strength of the centre metal-CO. Since these states contain the target chemical bond, their excitation could lead to relatively efficient desorption via a vibrational excitation in analogy to desorption induced by electronic transition (DIET)[66] or by simply withdrawing electrons from bonding states to induce repulsive CO-Ru potential. Such a process would be aided by an increase in the lifetimes of electronically excited states, which could originate in an electronic decoupling of ruthenium from the copper substrate by CO adsorption, analogous to what has been observed for CO on FePc on Au(111)[243].

As an alternative mechanism, two holes could be created in two different orbitals. If one hole is created in the RuTPP derived occupied orbital at -1.1 V, and another is injected into the CO-RuTPP derived occupied orbital at -0.8 eV, and these orbitals show little spatial overlap, the ensuing repulsion between two positive ions could drive CO desorption.

The difference in desorption mechanism between CO from RuTPP and NO from CoTPP[317] could lie in the degree of hybridization between CO/NO and TPP orbitals. NO is adsorbed in a tilted geometry, which means stronger hybridization between orbitals, which could make desorption possible over a wider energy range through carrier injection into any molecular orbitals.

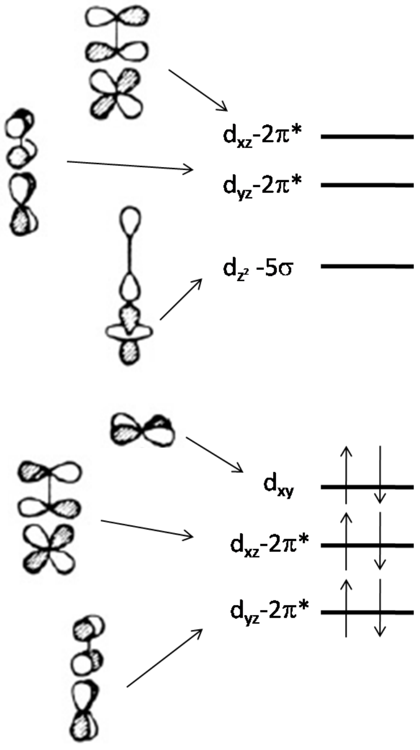

Figure 6.6 (adapted from ref[282,328]) Molecular orbital diagram of metalloporphyrin.

6.5 Conclusion

CO desorption by inelastic tunneling from CO-RuTPP on Cu(110) has been studied with a combination of STS and reaction yield measurements. Scanning tunneling spectroscopy shows different HOMO levels of both RuTPP and CO-RuTPP. CO desorption by inelastic tunneling has been observed by creating holes in the occupied states of CO-RuTPP/Cu(110). An efficient desorption compared to CO/Cu(110) is attributed to enhanced inelastic scattering through resonant tunneling. The two-carrier process is probably caused by tunneling of a second hole into an excited stated created by a hole tunneling into a RuTPP or CO-RuTPP HOMO. The desorption of CO from RuTPP/Cu(110) is further studied by femtosecond laser spectroscopy which is described in the next chapter.

Chapter 7

Photodesorption of CO from CO-RuTPP on Cu(110)

This chapter describes the femtosecond laser induced desorption of CO from CO-RuTPP/Cu(110) and associated electron-vibration coupling. Facile femtosecond laser desorption occurs from CO-RuTPP/Cu(110), but not from CO/Cu(110), although the thermal desorption spectra reveal that the desorption energy of CO from CO-RuTPP/Cu(110) is 0.75 eV, which is higher than the 0.54 eV found for CO/Cu(110). The origin of the facile laser desorption is suggested to be an enhancement of hot electron induced energy transfer via the LDOS around the Fermi level. Visible pump- SF probe spectroscopy revealed that the C-O stretch mode shows a blueshift in the first picosecond under photodesorption conditions, indicating that the CO-Ru bond weakens, which can be caused by either excitation of the CO-Ru stretch or bending of CO.

7.1 Introduction

7.1.1 Adsorbate dynamics and electron-vibration coupling

Understanding adsorbate dynamics at surfaces is crucial to design heterogeneous catalyst and sensing devices. Photodesorption can give rise to a new route for selective catalytic reactions, as demonstrated for CO oxidation to CO_2 on a ruthenium surface[173]. Due to the high absorption cross section of metal surfaces compared to most adsorbates, the photon energy is first deposited in the metal electrons followed by energy transfer to phonons and the adsorbate. The theoretical framework to describe energy transfer from electrons in the substrate to the adsorbate is provided by the Menzel, Gomer, Redhead (MGR) mechanism[72,329] in which transient electron attachment to the adsorbate causes vibrational excitation to overcome the desorption barrier. This is an electronically driven process, but surface phonons can also contribute to desorption. For further understanding of the energy transfer dynamics, it is required to distinguish thermally and electronically driven processes.

Ultrafast vibrational spectroscopy allows making this distinction by observing how quickly vibrations respond to photon excitation. Changes on a sub-picosecond timescale are generally attributed to be caused by hot electrons, changes over tens of picoseconds to hot phonons[19]. Ultrafast vibrational spectroscopy has been used to follow adsorbate dynamics such as desorption, diffusion and reaction[32,90]. The most well studied dynamics is desorption of CO which is now generally attributed to the excitation of the FR mode. This was demonstrated for CO on Ru(001)[21] and Pt(111)[20] which exhibit a large redshift of the C-O stretch while the surface electrons are hot. While the redshift itself is caused by excitation of the frustrated translational (FT) mode, which moves CO from the atop towards a higher coordination site, the fast response of the C-O stretch and high electron temperatures involved, suggest that the FT is indirectly heated via the frustrated rotation as modeled by Ueba and Persson[192,193]. The FR is then responsible for transferring the molecule into the transition state for diffusion[56] or desorption. This is further supported by a recent ultrafast photoelectron spectroscopy study, which revealed that the CO-Ru bond coordination increases in the first picosecond after pump excitation due to the excitation of the FR mode[65]. In addition to the redshift of the C-O stretch mode caused by the FR mode, Inoue *et al*. proposed that the CO-metal (M) mode may be also excited under desorption conditions from the observed blue shift of the C-O stretch mode in the first picosecond[191].

Despite this wealth of knowledge about CO on metal surfaces, little is known about how electron-vibration coupling occurs on other surfaces. In this chapter, the desorption of CO from a well-defined molecular substrate, namely metalloporphyrin covered Cu (110), is studied in the time domain. The closest related time-resolved studies were carried out on CO ligands at heme ligand in proteins. Upon absorption of photons by the heme, CO is photodissociated and transfers to a nearby docking site[274,330-332]. Ultrafast visible pump mid-IR probe measurements showed that CO rotates upon dissociation and moves to the new site in less than a picosecond[331].

Here, photodesorption of CO from CO-RuTPP/Cu(110) and its associated electron-vibration coupling is described. Thermal and laser desorption are compared, showing that the thermally more stable CO-RuTPP/Cu(110) exhibits facile laser desorption. Pump-probe SFG reveals that coupling to hot electrons is significantly altered by introducing the RuTPP monolayer to Cu(110). The frequency of the C-O stretch mode shows a blue shift during coupling to hot electrons under photodesorption conditions while phonon coupling at longer time scales causes the same redshift as on Cu(110). Before moving to the experimental and results section, optical and vibrational properties of CO-RuTPP are described for a reference of further discussion.

7.1.2 Optical and vibrational property of CO-RuTPP

For the study of adsorbate mediated process, it is important to know the optical property of the CO-RuTPP. Porphyrin molecules in general have unique light absorption properties, around 400-450 nm (Soret band) and 500-750 nm (Q band). In particular, (CO)(piperidine)RuTPP absorbs photons in the visible region with peaks at 412 nm, 531 nm and 567 nm in the ground state at 77 K and emits photons with a sharp peak at 652 nm as well as broadband 700-750 nm emission[333]. Excited state transition spectra reveal that CO(piperidine)RuTPP absorbs photons with a peak centre of 720 nm and 800 nm[35]. The lifetime of the excited state is 24-47 μs for CO(L)RuTPP while $(L)_2$RuTPP for 2 ns, 15 ns, 1.6 ps (L= piperidine, pyridine and dimethyl sulfoxide, respectively)[35]. A reduction of electronic excited state lifetime is observed at higher temperature, from 134 μs for 77 K to 35 μs for 295 K[334]. Recently, the details of excited state dynamics have been discusse by Iwakura *et al.* showing that initial excitation to $^1Q_{x(1,0)}(\pi, \pi^*)$ by 530 nm or $^1Q_{x(0,0)}(\pi, \pi^*)$ by 560 nm follows relaxation to $^3(d, \pi^*)$ in 1150 fs, then $^3(\pi, \pi^*)$ which emits the phosphorescence with >>4.8 ps lifetime[335].

Vibrational properties of CO-RuTPP have been studied as a model system to characterize CO-metalloporphyrin complex for vibrational dynamics[283,336], decarboxylation, and electronic excitation dynamics[335]. Dlott *et al.* reported a correlation of the frequency and the vibrational lifetime of the C-O stretch mode in metalloporphyrins, showing that the higher the frequency, the shorter the observed lifetime[283,336]. The authors conclude that vibrational deexcitation is caused by intramolecular energy relaxation and its rate depends on the extent of back-bonding from the metal d orbital to the CO 2π* orbital. In their study, the C-O stretch mode of CO-RuTPP is observed at ~1940 cm^{-1} and its lifetime is ~15-18 ps[336]. The C-O stretch mode of CO-RuTPP and $(CO)_2$RuTPP were investigated in a more isolated environment which shows the peaks at 1951.1 cm^{-1} and 2015.1 cm^{-1} (Ar matrix 8K)[279], 1944 cm^{-1} (293 K in vacuum) and 2009 cm^{-1} (200K in vacuum)[280], respectively. The Ru-CO external stretch mode is also observed as 590.1 cm^{-1} and 578.0 cm^{-1} for $Ru(CO)_2$TPP (in Ar matrix, 8K[279]) and $Ru(CO)_2$OEP (in solution[337]). The frequency of the external stretch mode of CO on Ru(001) is 446.5 cm^{-1} at 0.05ML[83].

7.2 Experimental

SFG experiments were performed with an amplified 10 Hz femtosecond laser system combined with an UHV chamber as described in chapter 2[145,278]. One TOPAS optical parametric amplifier generates 4 μJ, 200 fs mid-IR pulses, while second TOPAS creates a 150 fs pump beam with wavelength of 532 nm, 800 nm and 400 nm. The remainder is passed through an etalon (SLS Optics) to produce an upconversion pulse of about 7 cm^{-1} spectral width, time-shifted by 1.3 ps to reduce the non-resonant sum frequency signal[133].

A Cu(110) single crystal was cleaned by Ar^+ bombardment at 1 keV, followed by annealing to 600 K. RuTPP (Sigma Aldrich) was used as purchased and sublimed at 500 K onto the Cu(110) surface, which was held at 300 K during deposition. The RuTPP coverage is estimated from TPD. CO is dosed from background pressure at a substrate temperature of 100 K. All sum frequency spectra shown were recorded at 100 K substrate temperature. Unpumped sum frequency spectra were recorded every 4 delay points to confirm long term stability of the CO and RuTPP layer for the pulsed laser irradiation.

7.1. Results

7.3.1 Thermal and laser desorption

Thermal desorption of CO from CO-RuTPP/Cu(110) was studied by temperature programmed desorption. Figure 7.1 shows thermal desorption spectra of CO-RuTPP/Cu(110) and CO/Cu(110). The mass 28 signal appears around 200 K from 0.1 ML CO on Cu(110). The desorption temperature is lower for saturated CO on Cu(110). This lower desorption barrier at higher coverage can be explained by repulsive dipole-dipole interaction[82].

A similar desorption peak was observed around 190 K from the RuTPP pre-covered Cu(110) surface which is assigned to CO desorption from the bare parts of the Cu(110) surface. In addition, a new peak appears around 280 K as marked by an arrow. At this temperature the resonant SF signal of the C-O stretch mode from CO-RuTPP/Cu(110) disappears as shown in figure 7.2, therefore this peak is assigned to the CO desorption from the RuTPP molecules. From figure 7.1, desorption barriers of 0.54 eV and 0.75 eV are calculated by using the Redhead equation[71] for CO/Cu(110) and CO-RuTPP/Cu(110), respectively, with an assumption of frequency factor $\upsilon=10^{13}$ [s^{-1}] and the desorption is 1st order. The latter assumption should be reasonable because CO always adsorbs atop of Cu(110) and RuTPP down to 4.7K, as confirmed by STM and DFT. If the frequency factor is one order larger, desorption barrier increases to 0.04 eV, resulting in reduction of the accuracy of absolute value, however, the main conclusion here is that CO is more thermally stable on RuTPP/Cu(110) than on Cu(110). The dissociation energy of CO-RuTPP in the gas phase is unknown, but considered comparable[338] to the dissociation energy of CO-Fe porphyrins around 1.1-1.4 eV[339,340]. The thermal stability of CO-RuTPP is therefore reduced upon adsorption onto Cu(110). This can be explained by hybridization with the copper substrate, as previously reported for CoTPP/Cu(110)[89], where DFT deduced a charge transfer of $1.3e^-$ from the uppermost copper layer to the cobalt d_{z^2}, LUMO and LUMO+1 orbitals[89]. Adsorption of RuTPP onto copper could therefore also increase the occupation of the ruthenium $d\pi^*$ orbital, which would reduce the backdonation from the ruthenium d orbital to the CO 2π* orbital and as a result the CO-Ru bond would weaken. This in turn would strengthen the C-O stretch bond and increase its stretch frequency. Indeed, the C-O stretch frequency at 1957 cm^{-1}, as described in chapter 5 is higher than in an Ar matrix at 1951.1 cm^{-1} (8 K)[279] and in vacuum at 1944 cm^{-1} (293 K)[280]. The blueshift of 13 cm^{-1} corresponds to about 2% increase of 2π* occupation[341,342].

Since the electronic-vibration dynamics will be discussed in the next section, it is required to understand how the frequency of the C-O stretch mode for CO-RuTPP/Cu(110) responds to the substrate temperature. With increasing temperature, the frequency of the C-O stretch mode shifts to the red as shown in figure 7.2. Reference data from 0.1 ML of CO/Cu(110) are also shown. Both fundamental and hot band transitions exhibit redshift with increasing substrate temperature. It is known that the internal stretch and the frustrated translational (FT) mode anharmonically couple in case of CO on metal surfaces, which induces frequency redshift of the C-O stretch mode as described Equation (3.1)[19]. If the coupling mode is assumed to be the FT mode with the frequency of 28.8 cm^{-1}, the anharmonic constant of IS-FT (Γ_{14}) is in the range of 1.0± 0.4 cm^{-1} for all four transitions. Figure 7.2 includes the result of the linear fit.

This redshift is caused by the displacement of the CO molecule from the atop site to a high coordination sites on metal surfaces as described in chapter 3[19]. Ligand-metalloporphyrin-metal surface system contains similar low frequency modes to the FT mode of CO on metal surfaces. Burema *et al.* reported that the frustrated translational (FT) mode of NO on CoTPP/Ag(111) is around 10-13 meV[316], which is the typical energy range for the FT mode of a top CO and NO on metal surfaces. This FT mode can couple with surface phonons to displace the CO from the original position. In addition, there are many other low frequency modes in CO-RuTPP since this molecule contains 81 atoms, although we are unable to determine which particular low frequency modes of RuTPP contribute to the present observation. The observation suggests that low frequency modes in CO-RuTPP couple with phonons in a similar way to CO/Cu(110), and cause a redshift of the C-O stretch by displacement of CO from atop the ruthenium atom. A possible nearby high coordination site is the bridge site between the ruthenium atom and a nitrogen atom of an imine which was observed from CO-CoTPP/Ag(111)[305]. As an alternative mechanism, CO-Ru translate together with respect to the copper surface, i.e. the ruthenium atom moves away from the short bridge site, which can reduce the Ru-Cu hybridization, resulting in an increase of backdonation from Ru to CO. This would also induce the redshift of the C-O stretch mode.

Phonon coupling also causes linewidth broadening due to vibrational dephasing[343]. However, the linewidth of the C-O stretch mode of CO-RuTPP remains constant at 11±1

cm^{-1} over the observed temperature range. This result indicates that the dephasing contribution is smaller for CO on RuTPP/Cu(110) than for CO/Cu(110). The linewidth of the hot band is 10±2 cm^{-1} which is a similar value to the fundamental, while CO on metal surfaces often show a larger linewidth of the hot bands because the dephasing contribution is four times larger than the fundamental[83,344]. This observation on RuTPP is consistent with the hot band transition of hemoglobin, which shows the same linewidth of the C-O stretch mode from $v= 0\rightarrow1$ to $v= 6\rightarrow7$[272]. It should be noted that inhomogeneity of the CO layer also contributes to the linewidth broadening[101,345,346]. If the inhomogeneous contribution is larger than the dephasing contribution and if it is independent from the substrate temperature, there is no temperature dependent change in the linewidth.

The height of the resonant SF peak from CO-RuTPP/Cu(110) decreases after CO desorption from Cu(110), but remains constant from 190 K-250 K. The ratio of the hot band and the fundamental intensity is constant at ~31 % ±3 % over the measured temperature range.

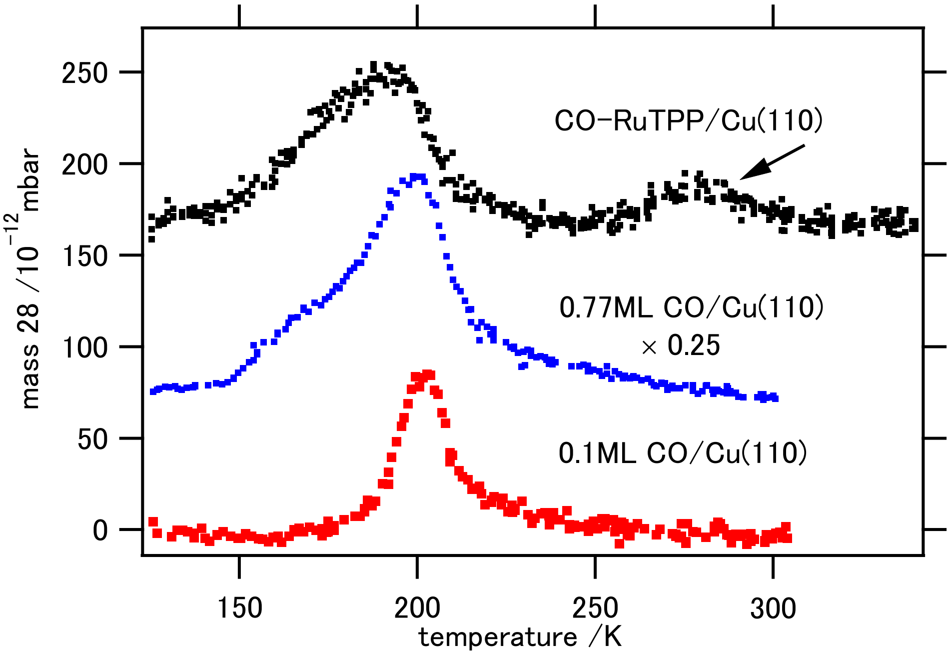

Figure 7.1 Thermal desorption spectra of CO (mass 28) acquired from CO/Cu(110) and CO-RuTPP/Cu(110), at a heating rate of 2 K/s. Spectra from 0.77 ML are scaled by 0.25. An arrow points to the peak around 280 K, which was assigned as CO desorption from RuTPP/Cu(110).

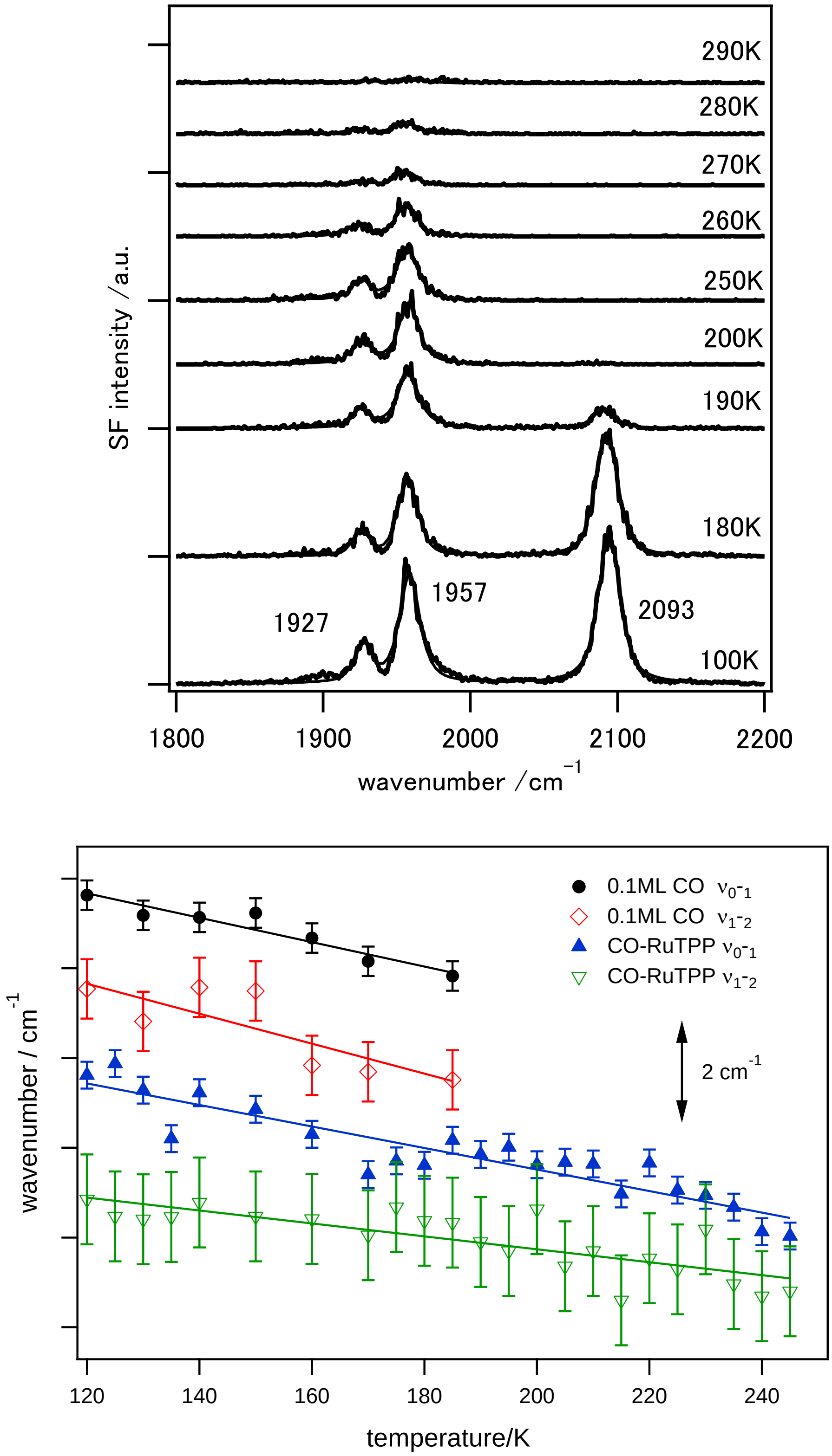

Figure 7.2 (top) SF spectra of the C-O stretch mode from CO-RuTPP/Cu(110) as a function of substrate temperature. (bottom) Substrate temperature-dependent frequency shift of the C-O stretch mode from 0.1 ML CO on Cu(110) and CO-RuTPP/Cu(110). Solid lines are the fitting results using equation (3.1).

Next, we look at the effect of a femtosecond laser beam. This leads to a SF signal reduction with time as shown in figure 7.3. The signal can be recovered by increasing CO partial pressure during irradiation, leading to the conclusion that the cause of SF signal reduction is CO desorption. The porphyrin layer was not damaged by the laser pulse since SF spectra at high CO pressure are stable for several hours. CO is only desorbed from RuTPP, not Cu(110), unless the fluence of the pump laser is increased more than 4 times. Such facile laser desorption was observed for all pump wavelengths used (400 nm, 532 nm and 800 nm). The lack of a wavelength dependence indicates that hot electrons or holes most likely induce laser desorption, not nascent electrons or resonant absorption by the adsorbates. Broadband CW light (from an ozone free Hg lamp, approximately 2 W incident power) was also used to attempt CO desorption, however, no desorption was observed confirming that this is not a simple photochemical effect. Changing the polarization of incident light can help to distinguish adsorbate-mediated from substrate-mediated processes if the transition dipole moment of the adsorbate is normal to the surface[347,348]. Figure 7.3 shows a four times faster desorption for p-polarized light than for s-polarized light. At the given incidence angle of 60° from the surface normal, using the bulk refractive incidence angles for copper, absorbances of 0.52 and 0.23 are obtained for p- and s- polarized light, respectively. Therefore, only a two times faster decay is expected for p-polarized light. This could indicate that the desorption is not purely substrate-mediated, although measurements at multiple incidence angles would be needed to confirm this assumption. It is worth noting that this method cannot ascertain the influence of surface parallel transition dipoles, such as the porphyrin Soret band, as this would show the same angular dependence as the substrate absorbance[348].

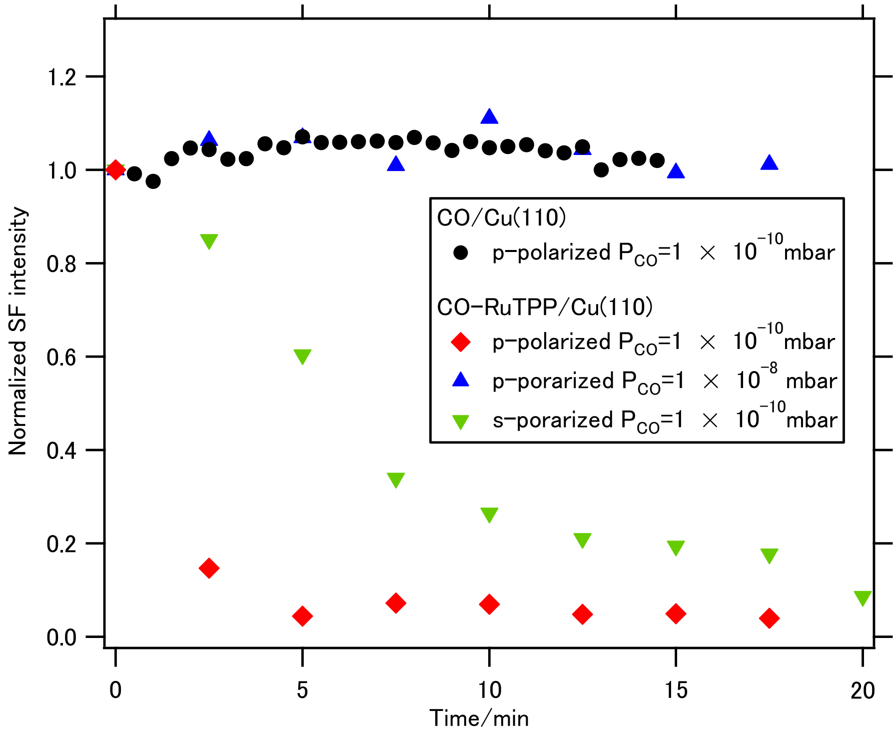

Figure 7.3 Time evolution of SF intensity under fs visible laser (150 fs, 532 nm, 10 J/m^2) irradiation. Black circles, red squares and green inverse triangles correspond to the integrated SF intensity of CO/Cu(110), CO-RuTPP at $P_{co}=1\times10^{-10}$ mbar, and CO-RuTPP at $P_{CO}=1\times10^{-8}$ mbar, respectively. Blue triangles show desorption from CO-RuTPP using an s-polarized beam.

7.3.2 Electron-vibration coupling

To gain further insight into the laser induced desorption, electron-vibration coupling was studied by visible pump- SF probe spectroscopy. The experiments were performed at high CO partial pressures of ~10^{-8} mbar to avoid any change in CO coverage by desorption. Figure 7.3(a) shows the frequency shift of the C-O stretch mode induced by 532 nm pump pulses at fluences of 9 and 13.5 J/m^2. The black circles in figure 7.4 show the corresponding data from CO adsorbed in between RuTPP molecules on Cu(110) together with the simulated frequency shift, derived from Carpene's modified two temperature model[186] as discussed in chapter 3. In the case of CO on the RuTPP copper surface Cu(110), the transient at delay times shorter than 1 ps reflects coupling via the FR mode to hot electrons, and the slower transient after 1 ps is caused by coupling to phonons via the FT mode[278]. The local coverage of CO adsorbed on sites not covered by RuTPP must be close to saturation, because the shape of the TPD peak in figure 7.1 is very similar to the TPD peak of a CO-saturated Cu(110) without RuTPP. The measured C-O frequency is moreover the same as for a saturated Cu(110) surface at 2093 cm^{-1}. The transient frequency shifts overlap at long delay times, where electrons, adsorbates and phonons have reached thermal equilibrium. This shows that the anharmonic coupling between the internal stretch and the

FT mode is very similar for CO on RuTPP and on Cu(110), which was confirmed by measuring the static temperature dependence of the C-O stretch in figure 7.2.

The transients are very different at short delay times < 5ps. At low fluence, the CO-RuTPP transient exhibits pure coupling to the phonon bath, which gradually heats up during the first few picoseconds. A fast transient, caused by coupling to hot electrons only appears with increasing fluence, as shown in figure 7.5. Unusually, the C-O frequency shifts to the blue now. The transients are independent of pump wavelength for 532 nm (2.33 eV) and 800nm (1.55 eV) as shown in figure 7.6. The absorbed fluences at the different wavelengths were adjusted to the same value by monitoring the effect on CO/Cu(110) at long delay times, where the effect is purely thermal. Transients with 400 nm (3.1 eV) pump were also recorded, but we could not achieve a high enough fluence to cause a clear blue shift around zero delay. Since widely different wavelengths produce similar transients, we can conclude that the copper d states starting at 2 eV below E_F are not involved in the transition. A direct contribution of CO-RuTPP can also be excluded as this shows an absorbance maximum around 530 nm (~2.3 eV)[333].

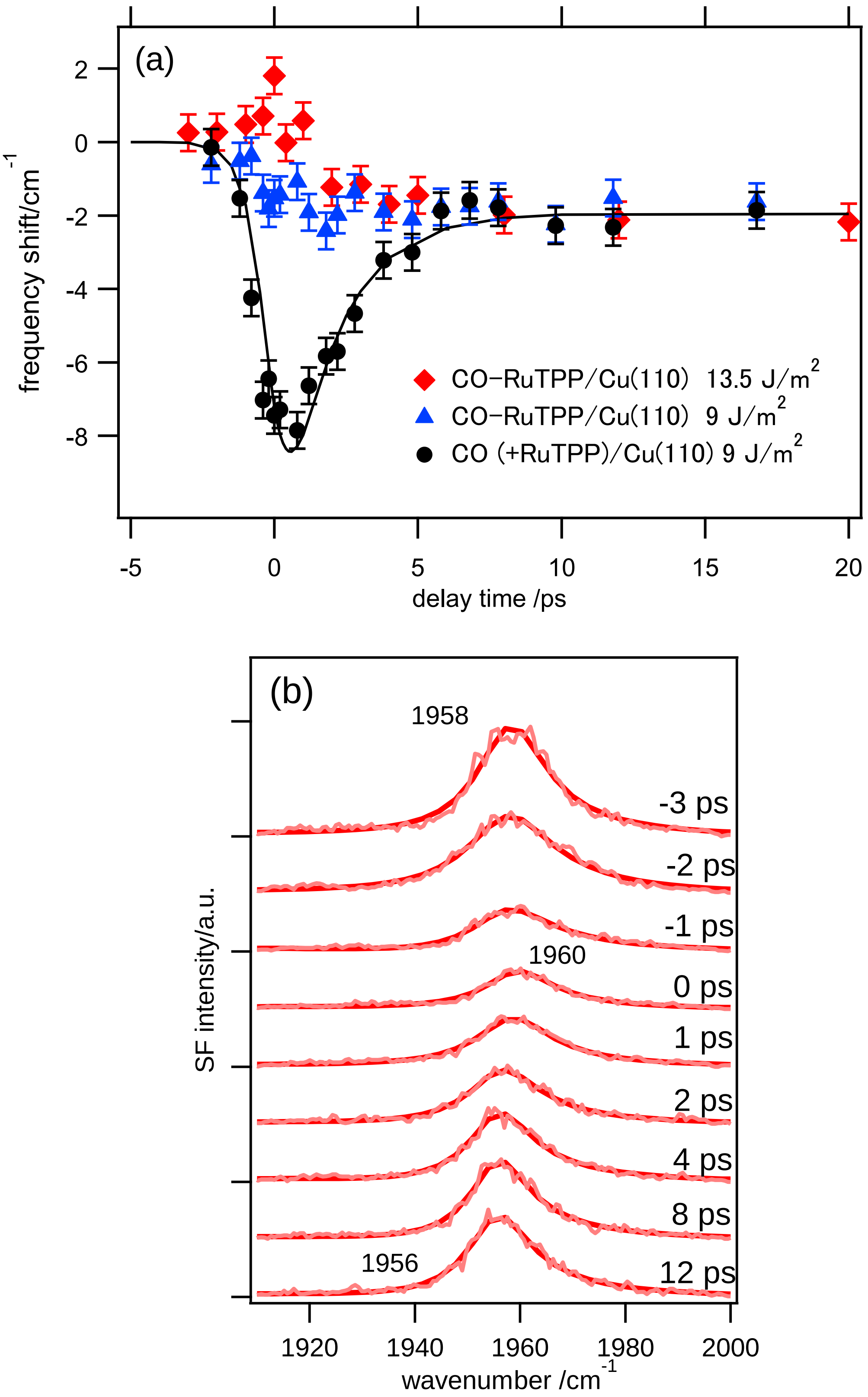

Figure 7.4 (a) Transient pump induced changes of the C-O stretch frequency of CO-RuTPP/Cu(110) and CO/Cu(110) as a function of the pump beam fluence. (b) SF spectra of CO-RuTPP as a function of pump delay time with 13.5 J/m^2 fluence.

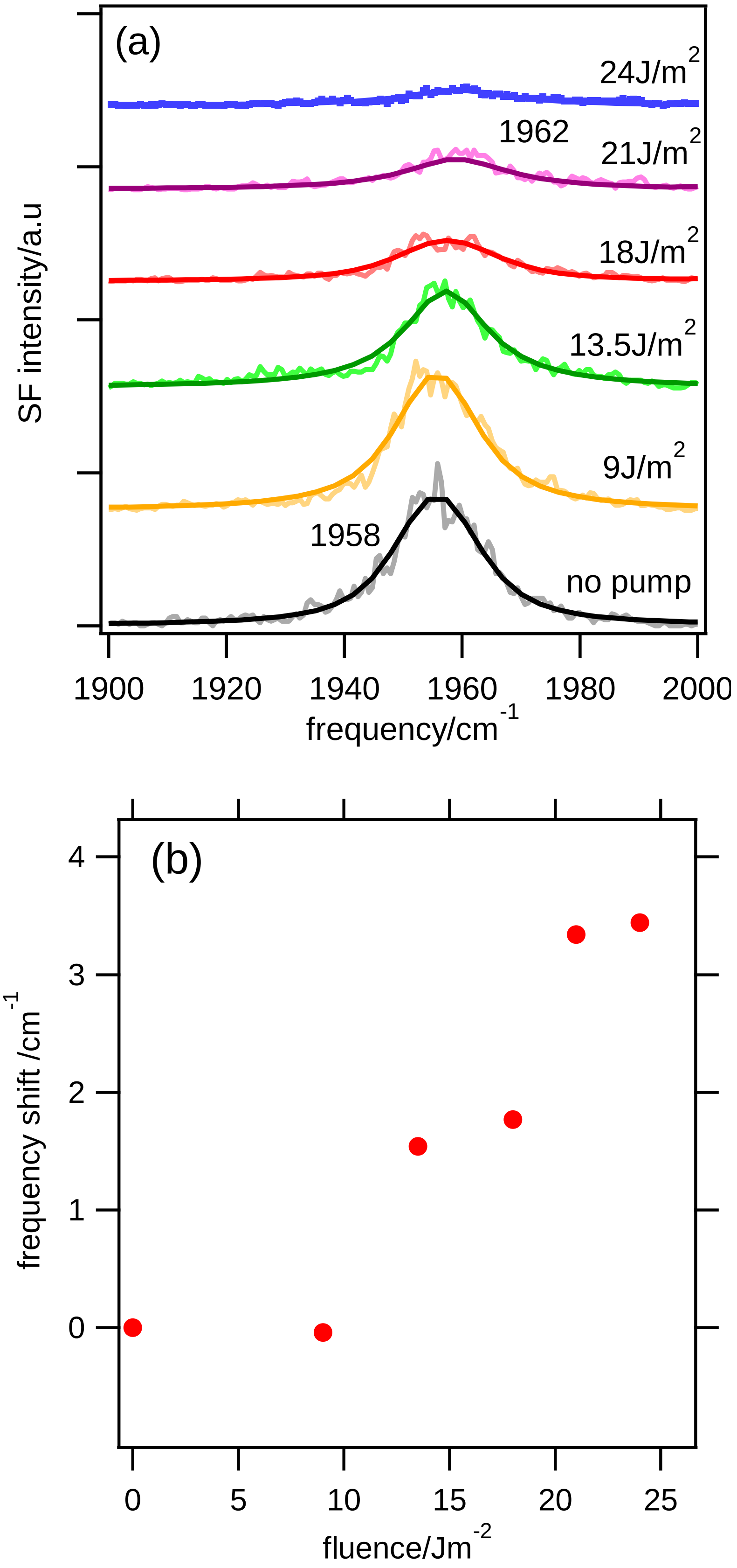

Figure 7.5 (a) SF spectra as a function of 532 nm pump fluence at delay time zero. (b) the frequency blue shift at time zero as a function of pump fluence.

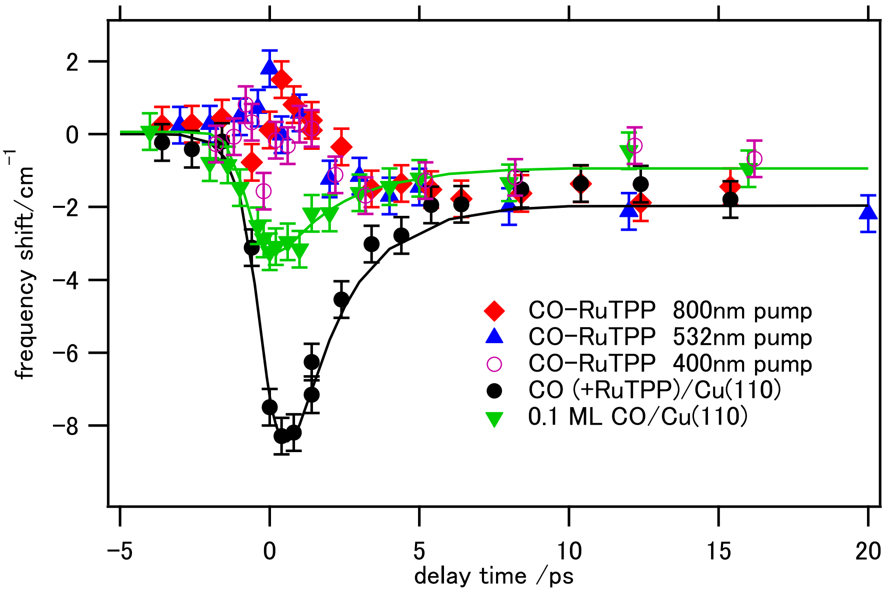

Figure 7.6 Transient pump induced changes in the C-O stretch frequency of CO-RuTPP and CO/Cu(110) as a function of wavelength of pump beams with the same fluence of ~14 J/m^2 for both pump wavelengths.

7.4 Discussion

First, the frequency-shift around time zero will be discussed as this is the relevant delay range for desorption. The redshift of the C-O stretch mode observed at long delay times is purely thermal and indicates a very small temperature increase (~40 K), which is too low to cause desorption. In order to understand the desorption mechanism, we look at possible origins of the frequency blueshift: change of adsorption site or anharmonic coupling with low frequency vibrational modes. Firstly, the possibility of CO moving to another adsorption site is discussed as seen in the decarboxylation of CO-protein complexes[274,330-332]. A possible intermediate site of CO on the RuTPP/Cu(110) surface could be a Ru-N (imine) bridge site, as observed for CoTPP/Ag(111) by STM and DFT[305]. However such a bridge site occupation by CO has not been observed by STM imaging at 4.7 K. Moreover, occupying such a bridge site is expected to show a frequency redshift. CO on ruthenium surfaces also shows an intermediate state prior to desorption on a picosecond time scale[64]. This precursor state would have a weaker Ru-CO bond and could thus show a C-O blueshift[21]. However, during pump-probe measurements, a large fraction of molecules are not in the precursor state to desorption and are instead just adsorbed on a hot surface, so the redshift caused by coupling to the FT mode dominates. Using phase-sensitive detection, the influence of a blue shift could however be discerned for CO/Pt(111)[191]. The excitation of the CO-Ru external stretch mode by the high electron temperatures is a possible explanation for the observed blueshift, however, it is difficult to model in detail, due to a lack of information about the degree of coupling between the C-O stretch mode and the

CO-metal stretch mode.

There is another explanation for the blue shift from a vibrational coupling view. Persson and Ryberg analyzed the temperature dependence of the C-O stretch mode of CO/Ni(111)[349,350], showing the redshift of atop CO and the blueshift of bridge site CO. With increasing temperature, the direction and magnitude of the shift can be explained by changes to the CO $2\pi^*$ occupation during the low frequency motion. The FT mode moves CO from an atop to a multiply coordinated site, which increases backdonation and reduces the frequency. The FR mode for CO on a bridge site, on the other hand, reduces the overlap between $2\pi^*$ and metal orbitals, which causes a blue shift.

In the case of CO on RuTPP, the excitation of the FT and FR modes always moves CO off the atop site, but not towards a higher coordination site as those are too far away. This can cause reduction of the backdonation to induce a blueshift of the C-O stretch mode. Indeed, bending of the C-O bond of heme proteins causes a frequency blue shift due to the reduction of the backdonation from the metal d orbital to the CO $2\pi^*$ orbital[282]. Changes in backdonation will also change the vibrational lifetime of the C-O stretch mode in a CO-porphyrin complex[336] which is dominated by π bonding. Bending of CO by as much as 25 ° can take place with an energy input of 2 kcal/mol (=0.087 eV =1000 K) or less[351]. Thus, it is suggested that hot electrons/holes induce bending of CO on RuTPP/Cu(110), which causes a transient blueshift.

This does not necessarily explain why the fast redshift disappears for CO-RuTPP/Cu(110). To better understand this, figure 7.6 includes a transient measured at low coverage on Cu(110) free from RuTPP. As explained in chapter 3, reducing the CO coverage reduces the degree of coupling to the hot electron bath. The lowest coverage for which we measured pump-probe transients on Cu(110) was 0.1 ML, while the coverage of CO on RuTPP is on the order of 0.03 ML. As figure 5.3 showed, hotband and fundamental are still separate at 0.1 ML, but the frequency starts shifting to the blue by dipole-dipole coupling, so the CO molecules are starting to interact slightly. It is therefore conceivable that a transient measured at 0.03 ML would have shown even less of a redshift at short delay times, although the change in coupling times with coverage (figure 3.6) suggests that the difference would not be large.

As explained in chapter 3, the cause of the redshift at all delay times is the anharmonic coupling between FT and internal stretch, but at short delay times, when the electrons are hot, the FR mode is able to heat the FT mode indirectly. The degree of coupling changes with coverage because the main effect of increasing CO coverage is an increased charge density around the carbon atom. This produces a stronger coupling between FR and hot electrons and the FT-FR intermode coupling then generates a stronger redshift. On RuTPP, this fast redshift disappears, even though the anharmonic coupling between internal stretch and FT does not change. It therefore seems likely that the intermode coupling between FT and FR is very different for CO on Cu(110) compared to CO on RuTPP. Helium atom scattering for CO on Cu(100) found a gradual increase in coupling between FT and FR modes with increasing CO coverage, as neighboring CO molecules led to a low-frequency motion that was more wagging- than translation-like[182]. Perhaps the opposite is true for CO adsorbed on RuTPP– because the macrocycle is relatively flat and the phenyl rings are relatively far away from CO adsorbed in the centre, the low frequency motions of CO might acquire a much more harmonic character than on a metal surface. This could drastically reduce FT-FR intermode coupling, explaining the lack of a fast response at lower fluences. As the fluence increases, direct coupling of the internal stretch to a different low frequency mode then becomes visible. Since both a bending of CO, as induced by FR excitation, or a lengthening of the Ru-CO bond, as induced by external stretch excitation, could lead to a blueshift, and since both external modes have relatively similar frequencies (see table 1.1) it is difficult to deduce which mode is involved from the transients alone.

Therefore, we next, consider which electronic states are responsible for the desorption and whether these can reveal the low frequency mode responsible for excitation or whether they could be the same as found by action spectroscopy described in the previous chapter. First, we need to clarify similarities and differences between desorption induced by tunneling electrons and hot electrons/holes created by femtosecond laser pulse. As described in Chapter 6, an inelastic tunneling electron process induces desorption of CO from CO-RuTPP/Cu(110) through the resonant tunneling to occupied states. In this case, electrons are transferred into/from LDOS at a set sample bias voltage. On the other hand, a femtosecond laser pulse creates electron-hole pairs in a substrate, which can play a similar role to tunneling electrons. For example, it is known that plasmon induced hot carriers can transfer from the metal substrate to the molecular state, causing desorption or reaction[175,352]. However, the IET process reflects the integral over the LDOS from E_F to the occupied bias voltage, while in femtosecond laser excitation we have to consider the overlap between either the nascent or thermalized hot carriers distribution and adsorbate electronic states. We can conclude from the lack of pump wavelength dependence that the relevant electronic states have to be relatively close to E_F, so that the thermalized electrons dominate the dynamics[353].

For example, STS revealed that occupied electronic states of CO-RuTPP/Cu(110) are found at 1.1 V and 0.8 V below the Fermi level. But even at 0.5 V below $E_{F,}$ heating the electron bath to 1500 K only reduces the probability of occupation *f*(E) to 0.98. A more likely candidate are the states around the Fermi level of CO-RuTPP/Cu(110) observed by STS, as shown in figure 7.7. It is known that a larger LDOS around the Fermi level enhances hot electron coupling[26,278], which increases desorption yields[26]. This CO-induced state is strongly affected by both hot electrons and holes in the present experimental condition and we suggest that it is responsible for the femtosecond induced desorption. How a change in occupation of this state causes a bending of CO or a lengthening of the Ru-CO bond is not clear at this point. In order to identify the nature of this state, DFT calculations are currently underway.

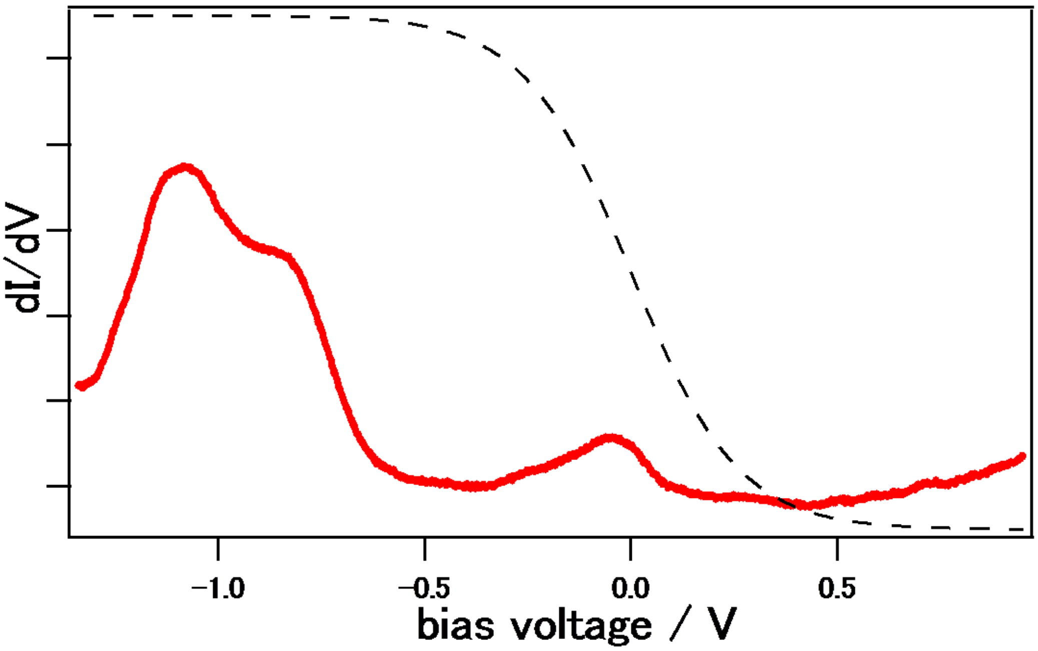

Figure 7.7 STS spectra of CO-RuTPP and RuTPP on Cu(110) surface. The STS spectrum of bare Cu(110) is subtracted to emphasis the change in dI/dV. The dotted line traces the Fermi distribution at a hot electron temperature of 1500K.

7.5 Conclusion

Femtosecond laser induced desorption and electron-vibration coupling of CO on the RuTPP covered Cu(110) surface have been studied by SFG. Thermally more stable CO-RuTPP/Cu(110) shows a more facile CO femtosecond laser induced desorption comparing with than CO/Cu(110). The origin of the facile laser desorption is suggested to be an enhancement of hot electron induced energy transfer via the LDOS around the Fermi level. Femtosecond visible pump- SF probe spectroscopy revealed that coupling with hot electrons is significantly altered by introducing the RuTPP monolayer, because the redshift characteristic for intermode coupling between FT and FR disappears. The C-O stretch mode of CO-RuTPP/Cu(110) instead shows a blueshift at short delay times under photodesorption conditions, which can be explained by direct anharmonic coupling of the internal stretch to either the frustrated rotation or Ru-CO stretching modes.

Chapter 8

Conclusion and Outlook

This thesis has focused on the vibrational and desorption dynamics of CO on RuTPP covered Cu(110) surface to obtain a deeper understanding of energy conversion at surfaces, in particular the importance of LDOS for the energy transfer between hot carriers and adsorbate. Vibrational dynamics have been studied by SFG, utilizing its sub-picosecond temporal resolution. In comparison, STM has a sub-molecular spatial resolution to enable transferring electrons into/from a specific part of the adsorbate and to observe their motion at a single molecule level. The combination of these two techniques provides a more comprehensive view of how electrons in metal substrate couple with adsorbates. Before summarizing the results, it is worth noting the differences of what can be observed by laser spectroscopy and STM.

- STM injects/removes electrons directly into/from the LDOS of the adsorbate and surface, while a femtosecond laser excites electrons in the copper substrate to create electron-hole pairs, which subsequently transfer to the adsorbates.
- STM controls the direction of electron flow i.e. injects or removes electrons, while photo-excitation creates electron-hole pairs and either can transfer to the adsorbate.
- STM based spectroscopies reflect LDOS, while the overlap between the excited electron distribution and adsorbate states is responsible for femtosecond pump-probe spectroscopy.

Summary

Coverage dependent non-adiabaticity was revealed for the first time in chapter 3. Electron-vibration coupling of CO on Cu(110) surface was characterized by visible pump-SF probe spectroscopy showing that the transient redshift increases from 3 cm^{-1} to 9 cm^{-1} with increasing coverage of CO from 0.1 ML to 0.77 ML which corresponds to the change in electron coupling constant τ_{el} from 6.7 ps to 4.6 ps. This study leads to two conclusions. Firstly, fast electron-vibration coupling cannot be explained by the FT mode alone, which suggests the importance of the FR mode for electron-vibration coupling even at low electron temperature. Secondly, coverage can adjust the non-adiabaticity of the adsorbate through both an increase in the adsorbate electronic density of states and an increasingly anharmonic potential energy surface caused by repulsive interactions between neighboring CO adsorbates.

The adsorption structure of RuTPP on Cu(110) surface was described in chapter 4. LT-STM images determine that the ruthenium atom occupies the short bridge site for both isolated molecules and any supramolecular structures. Two types of supramolecular structures have been observed. One shows a corresponding unit cell with CoTPP/Cu(110) which was reported by Donovan *et al.*[89]. Another phase shows a unit cell of one copper atom larger in the [1-10] direction. The latter phase has been observed at room temperature and at the boundary of the molecular island at 4.7 K. Adsorption of CO onto RuTPP does not change the supramolecular structure, but lifts up the ruthenium atom from the copper surface. Details of the supramolecular structure of RuTPP have been characterized in collaboration with DFT, suggesting that the phenyl rings of RuTPP molecules distort their structure upon adsorption onto Cu(110).

Vibrationally excited states of CO on bare and RuTPP covered Cu(110) surfaces have been studied by intense IR – visible SFG as discussed in chapter 5. The $\nu = 0 \rightarrow 1$ C-O stretch mode of CO-RuTPP on Cu(110) appeared at 1957 cm^{-1} with a $\nu = 1 \rightarrow 2$ hot band peak at 1927 cm^{-1}, which shows a higher anharmonic shift of 30 cm^{-1} than the 26 cm^{-1} found for CO on copper. The frequency of the C-O stretch and the hot band population of CO-RuTPP/Cu(110) are independent of the coverage of CO which indicates that dipole-dipole coupling among CO molecules on RuTPP is negligibly small. The Morse anharmonicity of 0.76 % was obtained for CO-RuTPP/Cu(110) which is the largest value among reported C-O stretch modes. A possible explanation is an increase in the apparent anharmonicity by the vibrational Stark effect. Charge transfer between copper and RuTPP could lead to a local electric field which affects the vibrational transitions differently due to their different dipole moments. It was also found that a Morse potential might not correctly describe the PES of CO-RuTPP because the anharmonic shifts increase for higher transitions.

Desorption of CO from CO-RuTPP/Cu(110) was studied in detail in chapters 6 and 7. The inelastic tunneling electron process can induce the desorption of CO from CO-RuTPP/Cu(110) with a two-carrier process. The desorption threshold of V_s=-1.1 V can be explained by the increase of LDOS as observed from STS. The lower desorption threshold compared with CO on copper surfaces has been attributed to resonant electron tunneling into occupied molecular orbitals. The two carrier process is likely caused by tunneling of a second hole into an excited state created by a hole tunneling into a RuTPP or CO-RuTPP HOMO. Facile femtosecond laser desorption was also observed from CO-RuTPP/Cu(110), but not from CO/Cu(110), although the thermal desorption spectra revealed that the desorption energy of 0.75 eV for CO from the CO-RuTPP/Cu(110) is higher than the 0.54 eV for CO/Cu(110). The C-O stretch mode of CO-RuTPP/Cu(110) shows a transient blueshift at short decay time under photodesorption conditions indicating that the CO-Ru bond weakens prior to desorption, which can be explained either by excitation of the CO-Ru external stretch or bending of CO on RuTPP. The origin of this facile laser desorption is suggested to be an enhancement of hot carrier transfer via the LDOS around the Fermi level.

This thesis provides a first example to study energy transfer between CO and porphyrins on surfaces by ultrafast vibrational spectroscopy and STM based single molecule spectroscopy. STM provides a good support to interpret SFG results as it provides details of the geometric and electronic structure of the adsorbate. This thesis aimed to study the same surface dynamics by SFG and STM i.e. desorption of CO from CO-RuTPP/Cu(110), to build a more comprehensive picture, however it obtained a somewhat different conclusion: CO desorption with STM shows a clear dependence on sample bias voltage while femtosecond laser induced desorption does not depend on pump frequency. Femtosecond laser induced desorprion involves only states close to the Fermi level, while STM-AS finds no reactively for the same states. This could be due to the vastly different number of excited carriers involved in each spectroscopy. In STM, a tunneling current of 20 nA corresponds to 1.25×10^{11} electrons per seconds over an area of a few nm^2. By comparison, an adsorbed fluence of 14 J/m^2 of a 532 nm femtosecond beam consists of 4×10^{19} photons per m^2 in 200 fs, corresponding to 1×10^{14} photon absorbance per nm^2 per second, which all create electron-hole pairs. The 1000 fold difference could explain why femtosecond laser induced desorption could originate from a comparatively low LDOS around E_F. On the other hand, STS showed that hole-induced processes dominate. It is difficult to create holes in the same energy range with laser irradiation because the majority of photons are absorbed by copper and the copper density of states is very low at 1 eV below E_F.

As described in chapter 1, two hypotheses of how LDOS affects energy conversion at surfaces were proposed;

1. Direct absorption of visible light by CO-RuTPP may induce photolysis if an adsorbate mediated photochemical reaction occurs.
2. Hot electron transfer and/or inelastic tunneling electron process may be enhanced through the LDOS of CO-RuTPP/Cu(110).

The first hypothesis is clearly not true in the present study, since we have seen frequency independent laser-induced-desorption of CO for CO-RuTPP/Cu(110). The lack of an adsorbate-mediated process can be explained by the reduction of excited state lifetime upon adsorption to the copper surface. On the other hand, the second hypothesis has been proven, as observed for enhanced desorption probability via inelastic tunneling electrons and hot electron processes. This thesis shows that modification of LDOS through introduction of another molecule (i.e. RuTPP), or simply by increasing coverage, cause a considerable effect on the energy conversion between electrons and adsorbate vibration, which influences the surface dynamics.

Outlook

This thesis not only provides new insights into energy conversion at surfaces, in particular focused on the role of adsorbate LDOS at the surface, but also inspires further studies.

This work guides collaboration with theorists in the field of surface physics. The coexistence of two phases of RuTPP supramolecular structures can be elucidated by DFT, which requires an accurate modeling of vdW interactions. STM images provide solid information for adsorption site and structure which helps to improve the accuracy of the simulation. The experimentally observed vibrational hot bands in different systems provide a reference for calculation of potential energy surfaces. The spectral distribution of the projected density of states helps to understand facile laser desorption of CO and associated blue shift, by correlating surface electronic states and ease of photodesorption.

This work can be extended to investigate electron-vibration coupling at electrochemical interface. Chapter 3 and 7 revealed that the DOS of adsorbate and surface are responsible for electron-vibration coupling. The importance of DOS around E_F for electron-vibration coupling has been suggested by experimental results[26,278], however, its relationship with the transient redshift is still under debate[56]. It can be argued that the degree of tilt and coupling to the FR mode can be the dominant reason for the frequency shift, and that the electronic structure at the surface only has a minor effect. This assumption could be verified by adjusting the position of the Fermi level to vary DOS, which can be achieved by applying a potential to the CO-electrode interface which has been already demonstrated to change the vibrational lifetime[354-356]. It is expected that moving the Fermi level to increase DOS induces larger redshift of the C-O stretch mode by hot electron coupling, if surface electronic states plays a dominant role in the transients.

This work might in future also address an unsolved issue in organometallic chemistry. Chapter 4 and 6 focused on the geometric and electronic structure of RuTPP on Cu(110). RuTPP can change its electronic structure by attaching CO. This strongly changes its optical properties because the coordination of CO onto RuTPP increases its luminescence lifetime 10^3 times[35,333], however, this mechanism is not well understood. The correlation of electronic structure and optical properties can be investigated by adding a photon detection system to the STM, which allows injecting electrons into target molecular orbitals and obtaining luminescence spectra triggered by inelastic electron tunneling[357,358]. A proposed mechanism for the increased luminescence lifetime of CO-RuTPP is the switch of the lowest excited state from (d,π^*) to $^3(\pi,\pi^*)$[35] which could be proven by spatial mapping of dI/dV spectra and luminescence spectra to investigate orbital specific luminescence.

The work presented here, was exclusively performed in UHV. The electron source is a femtosecond laser or tip of STM, which are difficult to apply to real world problems. Alternatively, plasmon-excitation of metal nanostructures have attracted interest as potential materials for hot electron chemistry[10], which can be also used for catalytic reaction and photovoltaic applications[359]. Porphyrin-nanoparticle hybrid materials may open new strategies for the design of plasmonic materials by utilizing or avoiding electronic hybridization between adsorbates and metal surfaces. This thesis has shown that manipulating the electronic structures is the key to controlling energy transfer.

Appendix.A

The dynamics of hot band transitions

A.1 Visible pump SF probe spectroscopy of hot band transition

Chapter 3 revealed that visible pump pulses likely induce the excitation of the FR mode by hot electrons, although it was believed that only the FT mode contributes to the transient redshift at low electron temperatures. This led us to reconsider the possibility that a visible femtosecond laser pulse could excite other vibrational modes. Bandara *et al.* reported SFG spectra of CO on Ni(111) and NiO(111) showing that new shoulder peaks appeared at the lower frequency side of the C-O stretch mode under irradiation of UV light, leading to the conclusion that vibrational hot bands are excited[287,360]. Pump-probe spectroscopy can follow the intensity ratio of the fundamental and vibrational hot bands, which allows to monitor how the vibrational population evolves, which can be a direct proof of whether the C-O stretch mode is directly excited by a femtosecond visible pulse. Here, visible pump-SF probe spectroscopy are described to study the dynamics of hot band transitions.

Visible pump- SF probe spectroscopy is presented to investigate the possibility that hot electrons directly excite the C-O stretch mode. Femtosecond visible pump pulses cause a frequency shift, linewidth broadening and intensity reduction of the C-O stretch mode as shown in figures A.1 and A.2.

The frequency transients depend on the infrared probe power. When the vibrational hot band is not excited at a probe power of 4 μJ, the fundamental transition of CO on Cu(110) show a redshift of around 3 cm^{-1}. When the IR power is increased to 10 μJ, we find that the fundamental transition now shows a smaller frequency shift than the hot band. The hot band transition is a higher in the potential energy surface than the fundamental, which may induce stronger anharmonic coupling with FT or FR modes. The dependence on probe power is nevertheless surprising, as it suggests that energy is transferred differently when there are vibrationally excited molecules on the surface. There are no drastic differences in the linewidths, although the fundamental broaden more than the hot band transition. This is also reflected in the signal intensities, since a larger linewidth means faster decay of the vibrational polarization means lower SF intensity. The fundamental and hot band transitions show signal reductions of 65 % and 30 %, roughly in line with the linewidth changes. Nevertheless, the ratio of hot band to fundamental intensities increases at short delay times, as shown in figure A.3.

CO-RuTPP/Cu(110) displays different transient. The fundamental transition of the C-O stretch mode of CO on Cu(110) surface can be simultaneously recorded from coadsorbed CO. This C-O stretch mode shows very similar transient as observed for 0.77ML CO on Cu(110)[278] as explained in chapter 7. The fundamental transitions now shows much larger change in FWHM than the hot band, but is comparable to the change seen in coadsorbed CO on Cu(110). Fundamental and hot band transitions both show a signal reduction of 65 %, where the hot band recovers on a slightly faster timescale than the fundamental transition.

In the following discussion, changes in SF intensity in the pump-probe transient are discussed to evaluate the possibility of a direct excitation of the C-O stretch mode by femtosecond visible pulses. If the C-O stretch mode is excited by the pump beam, the population ratio of the fundamental and hot band should change, however, two main aspects have to be taken account.

Firstly, the anharmonic coupling with the FT and/or FR modes causes the linewidth broadening, which in turn reduces peak height. To evaluate this effect, the Bloch equation can be solved by the procedure described in chapter 3. A functional dependence of the FWHM on adsorbate temperature has to be guessed and adapted until the widths and frequencies extracted from the calculated spectra match the measured transients. Then the intensity ratio can be calculated from the theoretical spectra and compared against the experimental values. Given the noise apparent in the plotted intensity ratio in figure A.3, this comparison is difficult.

Secondly, the displacement of CO from the atop site causes signal reduction. It was previously suggested that excitation of the FT and FR modes move CO away from atop site, resulting the SF intensity reduction[20,21], although this is largely captured in a larger linewidth expected for a multiply coordinated sites. Moreover, the tilt of CO decreases SF intensity by the reduced dipole moment perpendicular to the surface, therefore the intensity ratio might change not because the C-O stretch is directly excited, but for example fundamental and hot band couple different to low frequency modes, as it appears from figure A.1(a).

Simulated SF spectra were generated from the Bloch equation to obtain a predicted ratio of the fundamental and hot band SF intensity. Figure A.3 shows both the experimental and simulated change in intensity ratio of the fundamental and the hot band as a function of pump-probe delay for CO/Cu(110). The measured intensity ratio becomes over 1.6 times larger compared to non-pumped spectra. The simulated ratio does not quite reproduce this large change, so it is possible that direct excitation of the C-O stretch mode or tilting of molecules may play a role, but much higher quality spectra would be needed to confirm this effect.

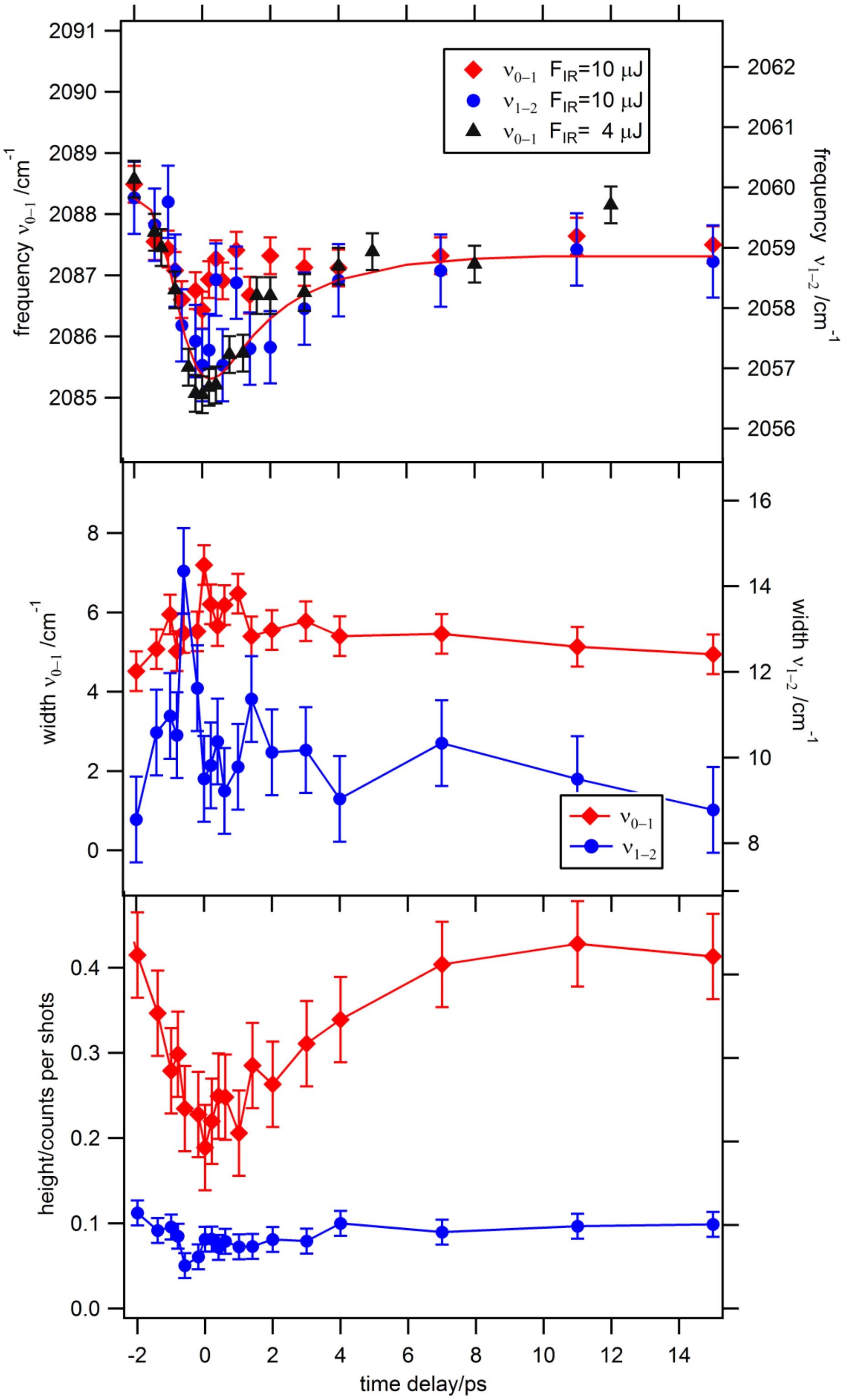

Figure A.1 (from top to bottom) Frequency, FWHM and SF signal of the C-O stretch of CO on bare Cu(110) as a function of pump-probe(IR) time delay.

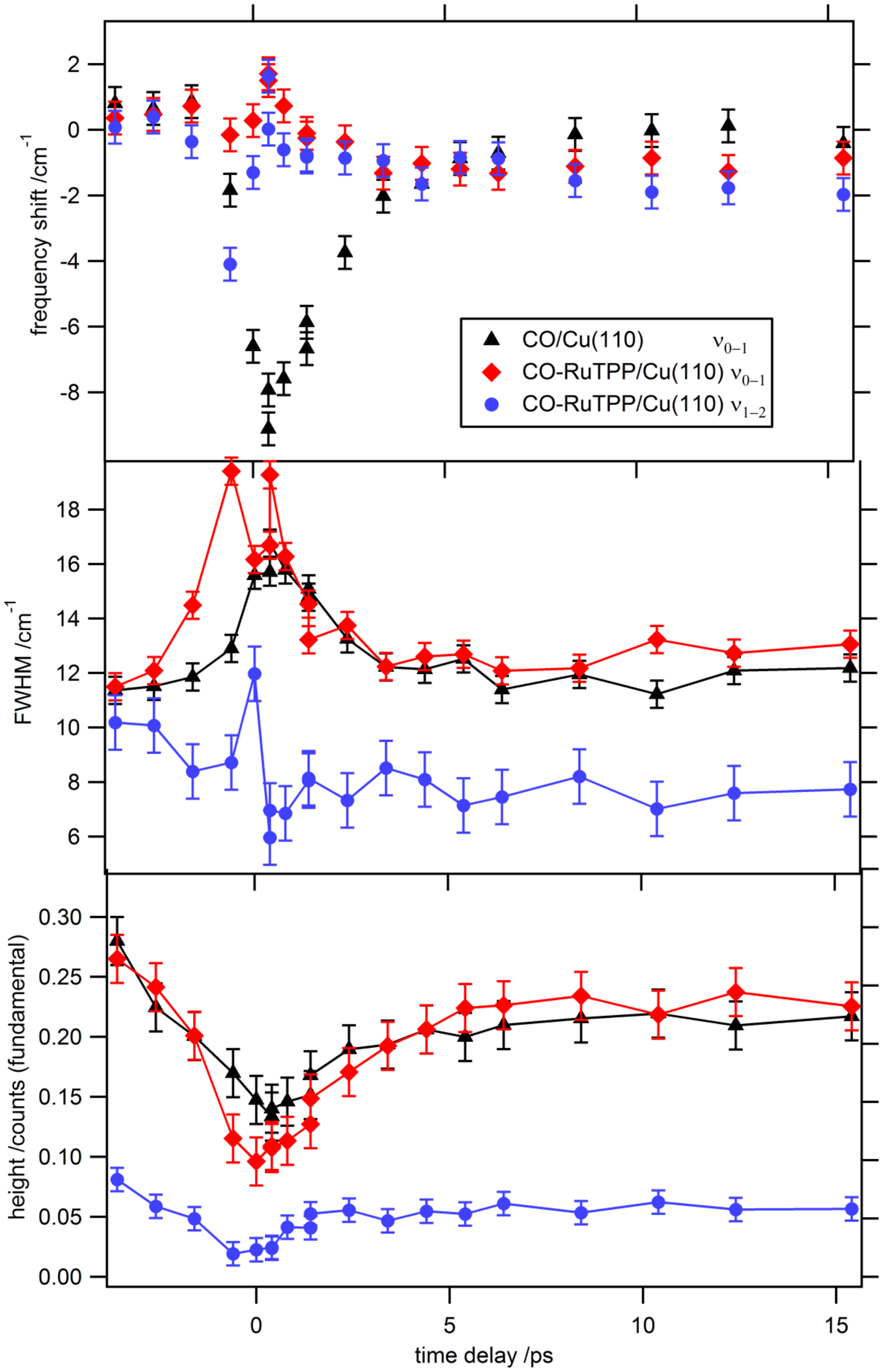

Figure A.2 (from top to bottom) Frequency, FWHM and SF signal of the C-O stretch of CO on bare Cu(110) as a function of pump-probe(IR) time delay

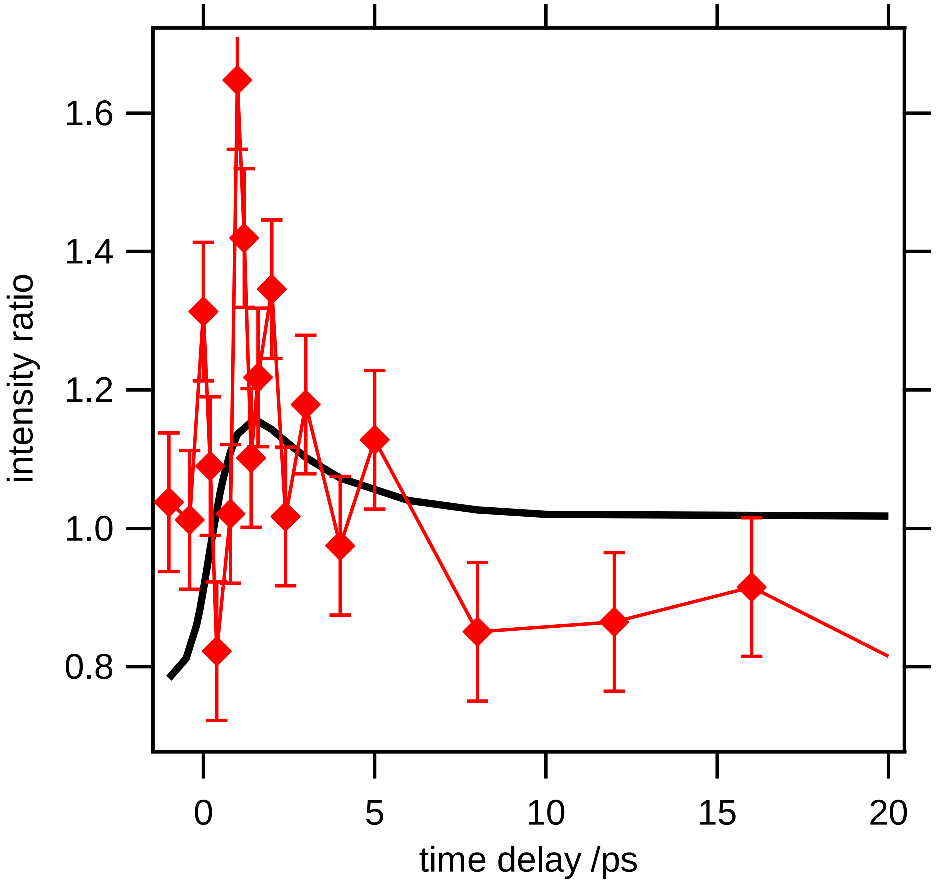

Figure A.3 SF intensity ratio of the hot band and fundamental of CO/Cu(110) as a function of pump-probe time delay.

A.2 Pump-probe spectra of 0.77 ML CO on CU(110) with 10μJ IR pulse

An intense IR pulse excites not only the fundamental ν =0 → 1 transition, but also the ν =1 → 2 transition, as discussed in chapter 5. The hot band transition peak merges with the fundamental at high coverage, due to the transition from localized to delocalized oscillator in a dipole-dipole coupled layer[142]. IR fluence does not affect the static temperature dependence as shown in figure A.4. Figure A.5 shows SF spectra of saturated CO on Cu(110) as a function of infrared power. The frequency redshift from 2093.9 cm^{-1} to 2089.4 cm^{-1} and linewidth broadening from 4.7 cm^{-1} to 9.1 cm^{-1} are observed as the IR power increase from 4 μJ to 10 μJ. This is due to the excitation of the higher vibrational states and merging with the fundamental transition due to strong dipole-dipole coupling as reported for different metal substrates[142,143]. The temperature dependent frequency shift and the linewidth broadening were also observed. The frequency shift shows identical values regardless of IR power, while the linewidth broadening is larger with a 10 μJ IR pulse, which can be explained by a larger dephasing contribution to the linewidth in hot bands. Pump-probe spectra also show the indication of vibrationally excited coupled oscillator state. The peak shape changes visibly when the pump-probe delay is 0-2 ps. The frequency transients are similar for both probe powers, although the linewidth changes back to the unpumped value more slowly, which can be explained by saturating the vibrational transition with the probe pulse.

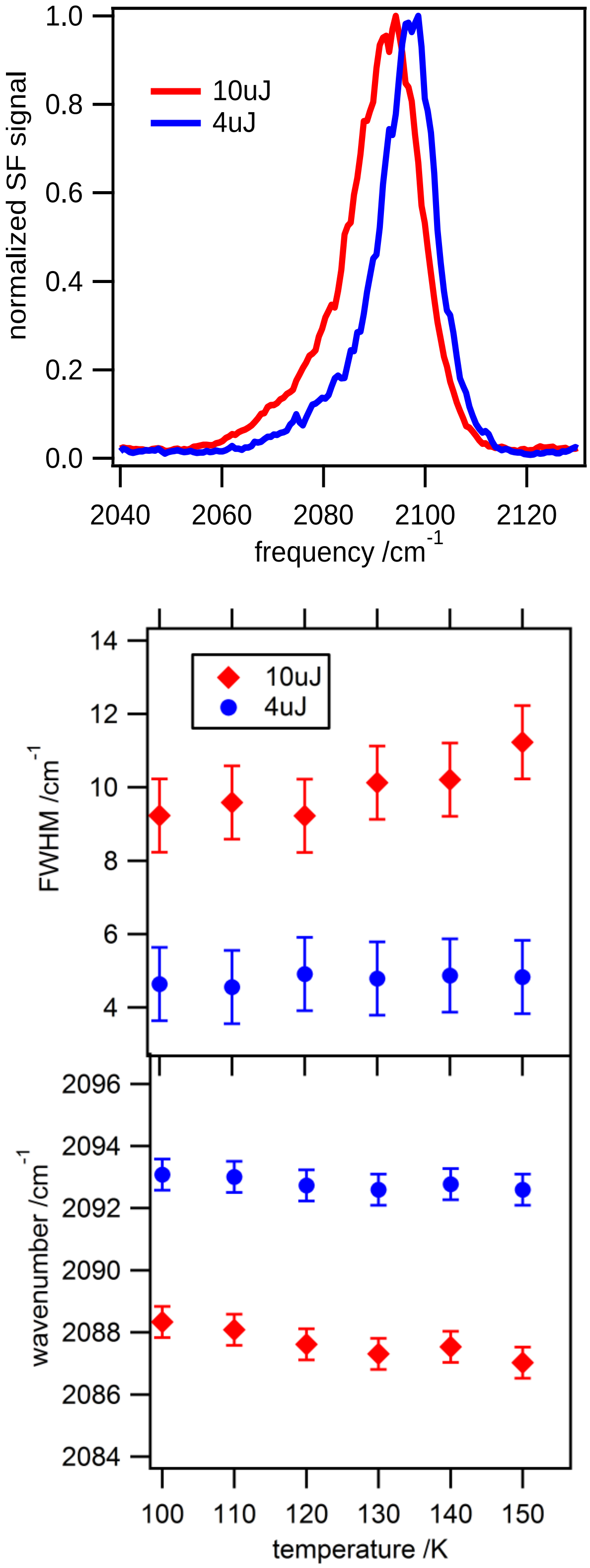

Figure A.4 (top) SF spectra of 0.77 ML CO as a function of IR fluence. (bottom) temperature dependent frequency shift and linewidth broadening.

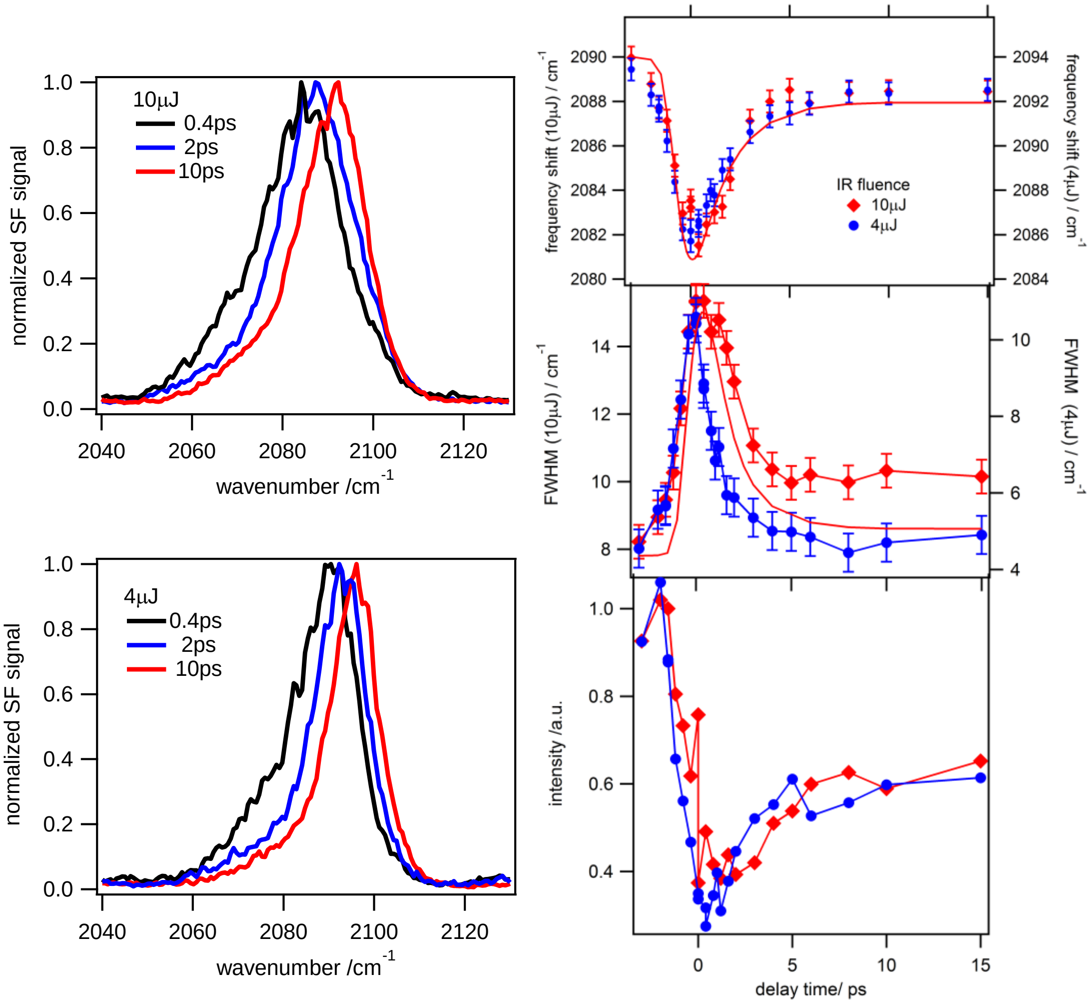

Figure A.5 (left) SF spectra of 0.77 ML CO as a function of IR power and pump-probe(IR) time delay. (right) Frequency shift, linewidth broadening and intensity reduction as a function of pump-probe(IR) time delay.

Appendix.B

Simulation of SFG spectra

The time evolution of SF spectra can be simulated by solving the optical Bloch equations. The temperature dependence of the frequency shift and the linewidth broadening can be obtained from the static temperature dependent SF spectra. These parameters allow an initial estimate of the SF spectra after the pump beam arrives based on the results of the two temperature model calculation. The numerical simulation is iterated for different values of τ_{el} and τ_{lat}, until minimum χ^2 is obtained. The intensity of SF spectra I_{SFG} is obtained by the Fourier transform of the IR polarization $P_{IR}(t,\tau)$ convoluted with the picosecond visible field $E_{vis}(t)$. The visible pulse is modeled as an etalon shape with a certain IR-Vis time delay, which affects the linewidth broadening and intensity reduction. The following equation gives I_{SFG},

$$I_{SFG}(\nu,\tau) \propto [\, E_{vis}(t) \otimes \int dt\, P_{IR}(t,\tau) e^{2\pi i\nu t}]^2 \qquad \text{(B.1)}$$

$P_{IR}(t,\tau)$ can be modeled by solving the optical Bloch equations, which describe the temporal evolution of the density matrix. The solution approach of two and three-level systems for SFG pump-probe experiments has been discussed previously[23,90,361,362]. Here, a brief summary of how to solve the two level Bloch equation, i.e. *a*(ground) and *b*(excited) levels, is described. This two level system contains four matrix elements, ρ_{aa}, ρ_{bb} (populations) and ρ_{ab}, ρ_{ba} (coherences/transitions). The rotating wave approximation is used; off diagonal elements are only driven close to their resonance $\omega_{ab}=2\pi\nu_{ab}$. This approximation means that the rapid oscillation of the electric field can be neglected[90]. Thus, the equations can be solved for the off-diagonal elements $\sigma_{ba}(t)$, which is $\rho_{ba},= \sigma_{ba}(t)e^{-2\pi i\nu t}$, then $\sigma_{ba}(t)$ can be rewritten by separating real and imaginary parts,

$$\sigma_{ba}(t)\equiv \frac{1}{2}\ (A(t)\text{-}iB(t))\ e^{-2\pi i\nu t} \qquad \text{(B.2)}$$

The population difference between the vibrational excited and ground states can be written as $C=\rho_{bb}\text{-}\rho_{aa}$, and the optical Bloch equations are then given by,

$$\frac{d}{dt}A = \left(\nu - \nu_{ab}(t)\right)B - \frac{A}{T_2(t)}$$

$$\frac{d}{dt}B = -\left(\nu - \nu_{ab}(t)\right)A - \frac{B}{T_2(t)} + \kappa E_{IR}C$$

$$\frac{d}{dt}C = -\frac{C - C^{eq}}{T_1} - \kappa E_{IR} B$$

where C_{eq} is the population difference of ground and excited states in thermal equilibrium. C_{eq}= -1 is assumed because most of the vibration is in the ground state at typical experimental tempertatures. κ is the molecule-field coupling which affects the amplitude of the spectrum. T_1 is the population decay time from the excited state b to the ground state a. T_2 is the dephasing time. $\nu_{ad}(t)$ is the instantaneous time dependence of pump-induced changes in frequency. Their temperature dependence can be obtained from separate experiments. The above equation is solved by using the Runge-Kutta method[21,23].

Bibliography

[1]A. H. Zewail, http://www.nobelprize.org/nobel_prizes/chemistry/laureates/1999/press.html, **1999**.

[2]A. H. Zewail, Laser Femtochemistry, *Science* **1988**, *242*, 1645

[3]J. C. Polanyi, A. H. Zewail, Direct Observation of the Transition State, *Accounts of Chemical Research* **1995**, *28*, 119

[4]S. Pedersen, L. Bañares, A. H. Zewail, Femtosecond vibrational transition‐state dynamics in a chemical reaction, *The Journal of Chemical Physics* **1992**, *97*, 8801

[5]S. Takeuchi, S. Ruhman, T. Tsuneda, M. Chiba, T. Taketsugu, T. Tahara, Spectroscopic Tracking of Structural Evolution in Ultrafast Stilbene Photoisomerization, *Science* **2008**, *322*, 1073

[6]C. Frischkorn, M. Wolf, Femtochemistry at metal surfaces: nonadiabatic reaction dynamics, *Chemical Reviews* **2006**, *106*, 4207

[7]M. J. Comstock *et al.*, Reversible Photomechanical Switching of Individual Engineered Molecules at a Metallic Surface, *Physical Review Letters* **2007**, *99*, 038301

[8]S. Hagen, F. Leyssner, D. Nandi, M. Wolf, P. Tegeder, Reversible switching of tetra-tert-butyl-azobenzene on a Au(1 1 1) surface induced by light and thermal activation, *Chemical Physics Letters* **2007**, *444*, 85

[9]S. Hagen, P. Kate, F. Leyssner, D. Nandi, M. Wolf, P. Tegeder, Excitation mechanism in the photoisomerization of a surface-bound azobenzene derivative: Role of the metallic substrate, *The Journal of Chemical Physics* **2008**, *129*, 164102

[10]M. L. Brongersma, N. J. Halas, P. Nordlander, Plasmon-induced hot carrier science and technology, *Nat Nano* **2015**, *10*, 25

[11]M. Moskovits, The case for plasmon-derived hot carrier devices, *Nat Nano* **2015**, *10*, 6

[12]M. Bonn, D. N. Denzler, S. Funk, M. Wolf, S. S. Wellershoff, J. Hohlfeld, Ultrafast electron dynamics at metal surfaces: Competition between electron-phonon coupling and hot-electron transport, *Physical Review B* **2000**, *61*, 1101

[13]M. Bauer, A. Marienfeld, M. Aeschlimann, Hot electron lifetimes in metals probed by time-resolved two-photon photoemission, *Progress in Surface Science* **2015**, *90*, 319

[14]H. Nienhaus, Electronic excitations by chemical reactions on metal surfaces, *Surface Science Reports* **2002**, *45*, 1

[15]H. Inouye, K. Tanaka, I. Tanahashi, K. Hirao, Ultrafast dynamics of nonequilibrium electrons in a gold nanoparticle system, *Physical Review B* **1998**, *57*, 11334

[16]T. Germer, J. Stephenson, E. Heilweil, R. Cavanagh, Hot carrier excitation of adlayers: Time-resolved measurement of adsorbate-lattice coupling, *Physical Review Letters* **1993**, *71*, 3327

[17]T. A. Germer, J. C. Stephenson, E. J. Heilweil, R. R. Cavanagh, Picosecond measurement of substrate-to-adsorbate energy transfer: The frustrated translation of CO/Pt(111), *The Journal of Chemical Physics* **1993**, *98*, 9986

[18]J. P. Culver, M. Li, L. G. Jahn, R. M. Hochstrasser, A. G. Yodh, Vibrational response of surface adsorbates to femtosecond substrate heating, *Chemical Physics Letters* **1993**, *214*, 431

[19]T. A. Germer, J. C. Stephenson, E. J. Heilweil, R. R. Cavanagh, Picosecond time‐resolved adsorbate response to substrate heating: Spectroscopy and dynamics of CO/Cu(100), *The Journal of Chemical Physics* **1994**, *101*, 1704

[20]F. Fournier, W. Zheng, S. Carrez, H. Dubost, B. Bourguignon, Vibrational dynamics of adsorbed molecules under conditions of photodesorption: Pump-probe SFG spectra of CO/Pt(111), *The Journal of Chemical Physics* **2004**, *121*, 4839

[21]M. Bonn, C. Hess, S. Funk, J. H. Miners, B. N. J. Persson, M. Wolf, G. Ertl, Femtosecond surface vibrational spectroscopy of CO adsorbed on Ru(001) during desorption, *Physical Review Letters* **2000**, *84*, 4653

[22]J. P. R. Symonds, Femtosecond sum-frequency spectroscopy of metal-adsorbate systems, *PhD thesis, University of Cambridge* **2003**,

[23]J. P. R. Symonds, H. Arnolds, D. A. King, Femtosecond pump/probe spectroscopy of CO on Ru{10$\bar{1}$0} from experimental and theoretical perspectives, *The Journal of Physical Chemistry B* **2004**, *108*, 14311

[24]I. M. Lane, Z. P. Liu, D. A. King, H. Arnolds, Ultrafast vibrational dynamics of NO and CO adsorbed on an iridium surface, *Journal of Physical Chemistry C* **2007**, *111*, 14198

[25]I. M. Lane, D. A. King, Z.-P. Liu, H. Arnolds, Real-time observation of nonadiabatic surface dynamics: the first picosecond in the dissociation of NO on iridium, *Physical Review Letters* **2006**, *97*, 186105

[26]E. H. G. Backus, M. Forsblom, M. Persson, M. Bonn, Highly efficient ultrafast energy transfer into molecules at surface step sites, *The Journal of Physical Chemistry C* **2007**, *111*, 6149

[27]Y. Sainoo, Y. Kim, T. Okawa, T. Komeda, H. Shigekawa, M. Kawai, Excitation of molecular vibrational modes with inelastic scanning tunneling microscopy processes: examination through action spectra of cis-2-butene on Pd(110), *Physical Review Letters* **2005**, *95*, 246102

[28]M. Ohara, Y. Kim, S. Yanagisawa, Y. Morikawa, M. Kawai, Role of molecular orbitals near the Fermi level in the excitation of vibrational modes of a single molecule at a scanning tunneling microscope junction, *Physical Review Letters* **2008**, *100*, 136104

[29]Y. Kim, T. Komeda, M. Kawai, Single-molecule reaction and characterization by vibrational excitation, *Physical Review Letters* **2002**, *89*, 126104

[30]S. Katano, Y. Kim, M. Trenary, M. Kawai, Orbital-selective single molecule reactions on a metal surface studied using low-temperature scanning tunneling microscopy, *Chemical Communications* **2013**, *49*, 4679

[31]F. Bisio, A. Winkelmann, W. C. Lin, C. T. Chiang, M. Nývlt, H. Petek, J. Kirschner, Band structure effects in surface second harmonic generation: The case of Cu(001), *Physical Review B* **2009**, *80*, 125432

[32]H. Arnolds, Vibrational dynamics of adsorbates – Quo vadis?, *Progress in Surface Science* **2011**, *86*, 1

[33]Z. Wang, J. A. Carter, A. Lagutchev, Y. K. Koh, N.-H. Seong, D. G. Cahill, D. D. Dlott, Ultrafast Flash Thermal Conductance of Molecular Chains, *Science* **2007**, *317*, 787

[34]K. C. Chou, S. Westerberg, Y. R. Shen, P. N. Ross, G. A. Somorjai, Probing the charge-transfer state of CO on Pt(111) by two-dimensional infrared-visible sum frequency generation spectroscopy, *Physical Review B* **2004**, *69*, 153413

[35]L. M. A. Levine, D. Holten, Axial-ligand control of the photophysical behavior of ruthenium(II) tetraphenyl- and octaethylporphyrin: contrasting properties of metalloporphyrin (π,.π*) and (d,π*) excited states, *The Journal of Physical Chemistry* **1988**, *92*, 714

[36]G. Blyholder, Molecular orbital view of chemisorbed carbon monoxide, *The Journal of Physical Chemistry* **1964**, *68*, 2772

[37]J. Dewar, A review of the pi-complex theory, *Bulletin de la Societe Chimique de France* **1951**, *18*, C71

[38]J. Chatt, L. A. Duncanson, L. M. Venanzi, Directing effects in inorganic substitution reactions. Part I. A hypothesis to explain the trans-effect, *Journal of the Chemical Society* **1955**, 4456

[39]B. N. J. Persson, R. Ryberg, Vibrational interaction between molecules adsorbed on a metal surface: The dipole-dipole interaction, *Physical Review B* **1981**, *24*, 6954

[40]R. Ryberg, Vibrational line shape of chemisorbed CO, *Physical Review B* **1985**, *32*, 2671

[41]C. Hirschmugl, G. Williams, F. Hoffmann, Y. Chabal, Adsorbate-substrate resonant interactions observed for CO on Cu(100) in the far infrared, *Physical Review Letters* **1990**, *65*, 480

[42]J. Braun, J. Weckesser, J. Ahner, D. Mocuta, J. T. Yates, C. Wöll, The frustrated translational mode of CO on Cu(110): Azimuthal anisotropy studied by helium atom

scattering—A comparison with time-of-flight electron stimulated desorption of ion angular distribution measurements, *The Journal of Chemical Physics* **1998**, *108*, 5161

[43]L. J. Lauhon, W. Ho, Single-molecule vibrational spectroscopy and microscopy: CO on Cu(001) and Cu(110), *Physical Review B* **1999**, *60*, R8525

[44]J. T. Yates, J. Ahner, D. Mocuta, Tracking the motion of chemisorbed molecules on their adsorption sites, *Proceedings of the National Academy of Sciences* **1998**, *95*, 443

[45]N. Lorente, H. Ueba, CO dynamics induced by tunneling electrons: differences on Cu(110) and Ag(110), *The European Physical Journal D* **2005**, *35*, 341

[46]C. Bartels, R. Cooper, D. J. Auerbach, A. M. Wodtke, Energy transfer at metal surfaces: the need to go beyond the electronic friction picture, *Chemical Science* **2011**, *2*, 1647

[47]M. Head-Gordon, J. Tully, Molecular-orbital calculations of the lifetimes of the vibrational modes of CO on Cu(100), *Physical Review B* **1992**, *46*, 1853

[48]M. Head-Gordon, J. C. Tully, Electric field effects on chemisorption and vibrational relaxation of CO on Cu(100), *Chemical Physics* **1993**, *175*, 37

[49]M. Head - Gordon, J. C. Tully, Molecular dynamics with electronic frictions, *The Journal of Chemical Physics* **1995**, *103*, 10137

[50]B. Hellsing, M. Persson, Electronic damping of atomic and molecular vibrations at metal surfaces, *Physica Scripta* **1984**, *29*, 360

[51]A. M. Wodtke, J. C. Tully, D. J. Auerbach, Electronically non-adiabatic interactions of molecules at metal surfaces: Can we trust the Born–Oppenheimer approximation for surface chemistry?, *International Reviews in Physical Chemistry* **2004**, *23*, 513

[52]E. Hasselbrink, How non-adiabatic are surface dynamical processes?, *Current Opinion in Solid State and Materials Science* **2006**, *10*, 192

[53]B. N. J. Persson, M. Persson, Vibrational lifetime for CO adsorbed on Cu(100), *Solid State Communications* **1980**, *36*, 175

[54]M. Morin, N. J. Levinos, A. L. Harris, Vibrational energy transfer of CO/Cu(100): Nonadiabatic vibration/electron coupling, *The Journal of Chemical Physics* **1992**, *96*, 3950

[55]V. Krishna, J. C. Tully, Vibrational lifetimes of molecular adsorbates on metal surfaces, *The Journal of Chemical Physics* **2006**, *125*, 054706

[56]E. H. Backus, A. Eichler, A. W. Kleyn, M. Bonn, Real-time observation of molecular motion on a surface, *Science* **2005**, *310*, 1790

[57]T. Komeda, Y. Kim, M. Kawai, B. N. Persson, H. Ueba, Lateral hopping of molecules induced by excitation of internal vibration mode, *Science* **2002**, *295*, 2055

[58]L. Bartels, G. Meyer, K. H. Rieder, D. Velic, E. Knoesel, A. Hotzel, M. Wolf, G. Ertl, Dynamics of electron-induced manipulation of individual CO molecules on Cu(111), *Physical Review Letters* **1998**, *80*, 2004

[59]H. Ueba, Y. Ootsuka, Lateral hopping and desorption of a single CO molecule on a Cu(110) surface induced by femtosecond laser pulses, *Physical Review B* **2013**, *87*, 205403

[60]D. Menzel, R. Gomer, Desorption from metal surfaces by low energy electrons, *The Journal of Chemical Physics* **1964**, *41*, 3311

[61]J. A. Misewich, T. F. Heinz, D. M. Newns, Desorption induced by multiple electronic transitions, *Physical Review Letters* **1992**, *68*, 3737

[62]P. A. Redhead, Interaction of slow electrons with chemisorbed oxygen *Canadian Journal of Physics* **1964**, *42*, 886

[63]M. Brandbyge, P. Hedegård, T. F. Heinz, J. A. Misewich, D. M. Newns, Electronically driven adsorbate excitation mechanism in femtosecond-pulse laser desorption, *Physical Review B* **1995**, *52*, 6042

[64]M. Dell'Angela *et al.*, Real-time observation of surface bond breaking with an x-ray laser, *Science* **2013**, *339*, 1302

[65]M. Beye *et al.*, Selective ultrafast probing of transient hot chemisorbed and

precursor states of CO on Ru(0001), *Physical Review Letters* **2013**, *110*, 186101

[66]V. N. Ageev, Desorption induced by electronic transitions, *Progress in Surface Science* **1994**, *47*, 55

[67]G. Attard, C. Barnes, Surfaces (Oxford Chemistry Primers), *Oxford University Press, USA* **1998**, *No.59*,

[68]H. E. Elsayed-Ali, T. B. Norris, M. A. Pessot, G. A. Mourou, Time-resolved observation of electron-phonon relaxation in copper, *Physical Review Letters* **1987**, *58*, 1212

[69]L. R. Apker, Surface phenemona useful in vacuum technique, *Industrial & Engineering Chemistry* **1948**, *40*, 846

[70]D. A. King, Thermal desorption from metal surfaces: A review, *Surface Science* **1975**, *47*, 384

[71]P. A. Redhead, Thermal desorption of gases, *Vacuum* **1962**, *12*, 203

[72]P. A. Redhead, The first 50 years of electron stimulated desorption (1918–1968), *Vacuum* **1997**, *48*, 585

[73]D. A. King, T. E. Madey, J. T. Yates, Interaction of oxygen with polycrystalline tungsten. I. Sticking probabilities and desorption spectra, *The Journal of Chemical Physics* **1971**, *55*, 3236

[74]F. M. Lord, J. S. Kittelberger, On the determination of activation energies in thermal desorption experiments, *Surface Science* **1974**, *43*, 173

[75]L. Zhu, A scanning tunneling microscopy study on atomic carbon and nitrogen on Pt(111), *PhD thesis, University of Illinois at Chicago* **2014**,

[76]R. Raval, Probing the nature of molecular chemisorption using RAIRS, *Surface Science* **1995**, *331–333, Part A*, 1

[77]N. Sheppard and T.T. Nguyen, Advances in infrared and raman spectroscopy, *Eds. R.J.H. Clark and R.E. Hester (Heyden, London)* **1978**, *Vol. 5,*, 67

[78]B. G. Briner, M. Doering, H.-P. Rust, A. M. Bradshaw, Microscopic molecular diffusion enhanced by adsorbate interactions, *Science* **1997**, *278*, 257

[79]B. Gumhalter, 2π Resonance shapes and relaxation shifts in inverse photoemission from CO/Cu(110), *Surface Science Letters* **1985**, *157*, L355

[80]J. Rogozik, H. Scheidt, V. Dose, K. C. Prince, A. M. Bradshaw, The 2π-derived level in the adsorption system CO/Cu(110), *Surface Science Letters* **1984**, *145*, L481

[81]H. Ueba, Chemical effects on vibrational properties of adsorbed molecules on metal surfaces: Coverage dependence, *Surface Science* **1987**, *188*, 421

[82]D. P. Woodruff, B. E. Hayden, K. Prince, A. M. Bradshaw, Dipole coupling and chemical shifts in IRAS of CO adsorbed on Cu(110), *Surface Science* **1982**, *123*, 397

[83]P. Jakob, B. N. J. Persson, Infrared spectroscopy of overtones and combination bands, *The Journal of Chemical Physics* **1998**, *109*, 8641

[84]P. Jakob, B. N. J. Persson, Dephasing of localized and delocalized vibrational modes: CO adsorbed on Ru(001), *Physical Review B* **1997**, *56*, 10644

[85]C. Lamberti, A. Zecchina, E. Groppo, S. Bordiga, Probing the surfaces of heterogeneous catalysts by in situ IR spectroscopy, *Chem Soc Rev* **2010**, *39*, 4951

[86]M. Peter, J. M. Flores Camacho, S. Adamovski, L. K. Ono, K. H. Dostert, C. P. O'Brien, B. Roldan Cuenya, S. Schauermann, H. J. Freund, Trends in the binding strength of surface species on nanoparticles: how does the adsorption energy scale with the particle size?, *Angewandte Chemie International Edition* **2013**, *52*, 5175

[87]F. Zaera, Infrared absorption spectroscopy of adsorbed CO: new applications in nanocatalysis for an old approach, *ChemCatChem* **2012**, *4*, 1525

[88]H. Noei *et al.*, Vibrational spectroscopic studies on pure and metal-covered metal oxide surfaces, *physica status solidi (b)* **2013**, *250*, 1204

[89]P. Donovan, A. Robin, M. S. Dyer, M. Persson, R. Raval, Unexpected deformations induced by surface interaction and chiral self-assembly of Co(II)-tetraphenylporphyrin

(Co-TPP) adsorbed on Cu(110): a combined STM and periodic DFT study, *Chemistry – A European Journal* **2010**, *16*, 11641

[90]H. Arnolds, M. Bonn, Ultrafast surface vibrational dynamics, *Surface Science Reports* **2010**, *65*, 45

[91]A. H. Zewail, Femtochemistry: Atomic-scale dynamics of the chemical bond, *The Journal of Physical Chemistry A* **2000**, *104*, 5660

[92]C. Zhou, Z. Ma, Z. Ren, A. M. Wodtke, X. Yang, Surface photochemistry probed by two-photon photoemission spectroscopy, *Energy & Environmental Science* **2012**, *5*, 6833

[93]X. Y. Zhu, Electronic structure and electron dynamics at molecule–metal interfaces: implications for molecule-based electronics, *Surface Science Reports* **2004**, *56*, 1

[94]H. Petek, S. Ogawa, Surface femtochemistry: Observation and quantum control of frustrated desorption of alkali atoms from noble metals, *Annual Review of Physical Chemistry* **2002**, *53*, 507

[95]H. Petek, M. J. Weida, H. Nagano, S. Ogawa, Real-time observation of adsorbate atom motion above a metal surface, *Science* **2000**, *288*, 1402

[96]X.-Y. Zhu, Electron transfer at molecule-metal interfaces : A two-photon photoemission study, *Annual Review of Physical Chemistry* **2002**, *53*, 221

[97]T. Katayama *et al.*, Ultrafast soft X-ray emission spectroscopy of surface adsorbates using an X-ray free electron laser, *Journal of Electron Spectroscopy and Related Phenomena* **2013**, *187*, 9

[98]M. Mehlhorn, H. Gawronski, L. Nedelmann, A. Grujic, K. Morgenstern, An instrument to investigate femtochemistry on metal surfaces in real space, *Review of Scientific Instruments* **2007**, *78*, 033905

[99]Y. Terada, S. Yoshida, O. Takeuchi, H. Shigekawa, Laser-combined scanning tunnelling microscopy for probing ultrafast transient dynamics, *Journal of Physics: Condensed Matter* **2010**, *22*, 264008

[100]I. Katayama, S. Koga, K.-i. Shudo, J. Takeda, T. Shimada, A. Kubo, S. Hishita, D.

Fujita, M. Kitajima, Ultrafast dynamics of surface-enhanced Raman scattering due to Au nanostructures, *Nano Letters* **2011**, *11*, 2648

[101]I. M. Lane, D. A. King, H. Arnolds, The determination of an inhomogeneous linewidth for a strongly coupled adsorbate system, *The Journal of Chemical Physics* **2007**, *126*, 024707

[102]N. Bloembergen, P. S. Pershan, Light waves at the boundary of nonlinear media, *Physical Review* **1962**, *128*, 606

[103]X. D. Zhu, H. Suhr, Y. R. Shen, Surface vibrational spectroscopy by infrared-visible sum frequency generation, *Physical Review B* **1987**, *35*, 3047

[104]J. H. Hunt, P. Guyot-Sionnest, Y. R. Shen, Observation of C-H stretch vibrations of monolayers of molecules optical sum-frequency generation, *Chemical Physics Letters* **1987**, *133*, 189

[105]A. L. Harris, C. E. D. Chidsey, N. J. Levinos, D. N. Loiacono, Monolayer vibrational spectroscopy by infrared-visible sum generation at metal and semiconductor surfaces, *Chemical Physics Letters* **1987**, *141*, 350

[106]A. G. Lambert, P. B. Davies, D. J. Neivandt, Implementing the theory of sum frequency generation vibrational spectroscopy: A tutorial review, *Applied Spectroscopy Reviews* **2005**, *40*, 103

[107]Y. R. Shen, Basic theory of surface sum-frequency generation, *The Journal of Physical Chemistry C* **2012**, *116*, 15505

[108]M. Hayashi, Y.-J. Shiu, K. K. Liang, S. H. Lin, Y. R. Shen, Theory of time-resolved sum-frequency generation and its applications to vibrational dynamics of water, *The Journal of Physical Chemistry A* **2007**, *111*, 9062

[109]S. Yamaguchi, T. Tahara, Development of electronic sum frequency generation spectroscopies and their application to liquid interfaces, *The Journal of Physical Chemistry C* **2015**, 150522132639005

[110]Z. Chen, Y. R. Shen, G. A. Somorjai, Studies of polymer surfaces by sum frequency generation vibrational spectroscopy, *Annual Review of Physical Chemistry* **2002**, *53*, 437

[111]C. S. Tian, Y. R. Shen, Recent progress on sum-frequency spectroscopy, *Surface Science Reports* **2014**, *69*, 105

[112]E. C. Y. Yan, L. Fu, Z. Wang, W. Liu, Biological macromolecules at interfaces probed by chiral vibrational sum frequency generation spectroscopy, *Chemical Reviews* **2014**, *114*, 8471

[113]Y. R. Shen, The principles of nonlinear optics, *John Wiley and Sons, New York,* **1984**,

[114]R. W. Boyd., Nonlinear optics, *Nonlinear Optics, Academic Press, San Diego, 2nd edition,* **2003**,

[115]L. J. Richter, T. P. Petralli-Mallow, J. C. Stephenson, Vibrationally resolved sum-frequency generation with broad-bandwidth infrared pulses, *Optics Letters* **1998**, *23*, 1594

[116]E. W. M. van der Ham, Q. H. F. Vrehen, E. R. Eliel, Self-dispersive sum-frequency generation at interfaces, *Optics Letters* **1996**, *21*, 1448

[117]R. Superfine, J. Y. Huang, Y. R. Shen, Phase measurement for surface infrared–visible sum-frequency generation, *Optics Letters* **1990**, *15*, 1276

[118]N. Ji, V. Ostroverkhov, C.-Y. Chen, Y.-R. Shen, Phase-sensitive sum-frequency vibrational spectroscopy and its application to studies of interfacial alkyl chains, *Journal of the American Chemical Society* **2007**, *129*, 10056

[119]S. Yamaguchi, T. Tahara, Heterodyne-detected electronic sum frequency generation: “Up” versus “down” alignment of interfacial molecules, *The Journal of Chemical Physics* **2008**, *129*, 101102

[120]S. Nihonyanagi, S. Yamaguchi, T. Tahara, Direct evidence for orientational flip-flop of water molecules at charged interfaces: A heterodyne-detected vibrational sum frequency generation study, *The Journal of Chemical Physics* **2009**, *130*, 204704

[121]I. V. Stiopkin, H. D. Jayathilake, A. N. Bordenyuk, A. V. Benderskii, Heterodyne-detected vibrational sum frequency generation spectroscopy, *Journal of the*

American Chemical Society **2008**, *130*, 2271

[122]P. Guyot-Sionnest, Y. R. Shen, Local and nonlocal surface nonlinearities for surface optical second-harmonic generation, *Physical Review B* **1987**, *35*, 4420

[123]S. Yamaguchi, K. Shiratori, A. Morita, T. Tahara, Electric quadrupole contribution to the nonresonant background of sum frequency generation at air/liquid interfaces, *The Journal of Chemical Physics* **2011**, *134*, 184705

[124]L. Dreesen, C. Humbert, M. Celebi, J. J. Lemaire, A. A. Mani, P. A. Thiry, A. Peremans, Influence of the metal electronic properties on the sum-frequency generation spectra of dodecanethiol self-assembled monolayers on Pt (111), Ag (111) and Au (111) single crystals, *Applied Physics B* **2002**, *74*, 621

[125]U. Schröder, P. Guyot-Sionnest, Optical sum frequency studies of adsorption and laser-induced desorption of CO on W(110), *Surface Science* **1999**, *421*, 53

[126]S. Westerberg, C. Wang, K. Chou, G. A. Somorjai, High-pressure ammonia adsorption and dissociation on clean Fe(111) and oxygen-precovered Fe(111) studied by sum frequency generation vibrational spectroscopy, *The Journal of Physical Chemistry B* **2004**, *108*, 6374

[127]S. Lin, A. Oldfield, D. Klenerman, In-situ studies of polycrystalline copper during methanol synthesis at high pressure using sum frequency generation at surfaces, *Surface Science* **2000**, *464*, 1

[128]S. Hosseinpour, J. Hedberg, S. Baldelli, C. Leygraf, M. Johnson, Initial oxidation of alkanethiol-covered copper studied by vibrational sum frequency spectroscopy, *The Journal of Physical Chemistry C* **2011**, *115*, 23871

[129]S. Hosseinpour, M. Schwind, B. Kasemo, C. Leygraf, C. M. Johnson, Integration of quartz crystal microbalance with vibrational sum frequency spectroscopy–quantification of the initial oxidation of alkanethiol-covered copper, *The Journal of Physical Chemistry C* **2012**, *116*, 24549

[130]G. M. Santos, S. Baldelli, Monitoring localized initial atmospheric corrosion of alkanethiol-covered copper using sum frequency generation imaging microscopy: Relation between monolayer properties and Cu2O formation, *The Journal of Physical*

Chemistry C **2013**, *117*, 17591

[131]C. Hess, M. Bonn, S. Funk, M. Wolf, Hot-band excitation of CO chemisorbed on Ru(001) studied with broadband-IR sum-frequency generation, *Chemical Physics Letters* **2000**, *325*, 139

[132]A. Lagutchev, A. Lozano, P. Mukherjee, S. A. Hambir, D. D. Dlott, Compact broadband vibrational sum-frequency generation spectrometer with nonresonant suppression, *Spectrochim Acta A Mol Biomol Spectrosc* **2010**, *75*, 1289

[133]A. Lagutchev, S. A. Hambir, D. D. Dlott, Nonresonant background suppression in broadband vibrational sum-frequency generation spectroscopy, *The Journal of Physical Chemistry C* **2007**, *111*, 13645

[134]T. Ishibashi, H. Onishi, Vibrationally resonant sum-frequency generation spectral shape dependent on the interval between picosecond-visible and femtosecond-infrared laser pulses, *Chemical Physics Letters* **2001**, *346*, 413

[135]I. V. Stiopkin, H. D. Jayathilake, C. Weeraman, A. V. Benderskii, Temporal effects on spectroscopic line shapes, resolution, and sensitivity of the broad-band sum frequency generation, *The Journal of Chemical Physics* **2010**, *132*, 234503

[136]C. Weeraman, S. A. Mitchell, R. Lausten, L. J. Johnston, A. Stolow, Vibrational sum frequency generation spectroscopy using inverted visible pulses, *Opt Express* **2010**, *18*, 11483

[137]M. Born, E. Wolf, Principles of optics, *Principles of Optics, Cambridge University Press, 7th edition edition* **1999**,

[138]N. Garcia Rey, Interaction of a copper surface with light: Plasmons, electrons & molecular vibrations, *PhD thesis, University of Liverpool* **2011**,

[139]P. Hollins, J. Pritchard, Interactions of CO molecules adsorbed on oxidised Cu(111) and Cu(110), *Surface Science* **1983**, *134*, 91

[140]P. Guyot-Sionnest, Two-phonon bound state for the hydrogen vibration on the H/Si(111) surface, *Physical Review Letters* **1991**, *67*, 2323

[141]P. Guyot - Sionnest, P. H. Lin, E. M. Hiller, Vibrational dynamics of the Si-H stretching modes of the Si(100)/H:2×1 surface, *The Journal of Chemical Physics* **1995**, *102*, 4269

[142]C. Hess, M. Wolf, M. Bonn, Direct observation of vibrational energy delocalization on surfaces: CO on Ru(001), *Physical Review Letters* **2000**, *85*, 4341

[143]V. L. Zhang, H. Arnolds, D. A. King, Hot band excitation of CO/Ir(111) studied by broadband sum frequency generation, *Surface Science* **2005**, *587*, 102

[144]R. Trebino., Frequency resolved optical gating: The measurement of ultrashort laser pulses, *Kluwer Academic Publishers, Norwell, MA,* **2000**,

[145]H. Arnolds, J. P. R. Symonds, V. L. Zhang, D. A. King, In situ characterization of ultrafast laser pulses for sum frequency surface studies, *Review of Scientific Instruments* **2003**, *74*, 3943

[146]G. Binnig, H. Rohrer, C. Gerber, E. Weibel, Tunneling through a controllable vacuum gap, *Applied Physics Letters* **1982**, *40*, 178

[147]G. Binnig, H. Rohrer, Scanning tunneling microscopy, *Surface Science* **1983**, *126*, 236

[148]J. A. Stroscio, W. J. Kaiser, Scanning tunneling microscopy, *Volume 27 (Academic Press)* **1993**,

[149]C. J. Chen, Introduction to scanning tunneling microscopy,, *Oxford Scholarship Online* **2007**, 1

[150]R. Wiesendanger, Scanning probe microscopy and spectroscopy methods and applications,, *Cambridge University Press* **1994**, 1

[151]W. M. Haynes, Boca Raton, CRC Handbook of chemistry and physics. , *CRC Press* **2011**, *92th ed*,

[152]J. Tersoff, D. R. Hamann, Theory and application for the scanning tunneling microscope, *Physical Review Letters* **1983**, *50*, 1998

[153]J. Tersoff, D. R. Hamann, Theory of the scanning tunneling microscope, *Physical Review B* **1985**, *31*, 805

[154]J. Bardeen, Tunnelling from a many-particle point of view, *Physical Review Letters* **1961**, *6*, 57

[155]G. Binnig, K. H. Frank, H. Fuchs, N. Garcia, B. Reihl, H. Rohrer, F. Salvan, A. R. Williams, Tunneling spectroscopy and inverse photoemission: image and field states, *Physical Review Letters* **1985**, *55*, 991

[156]G. Binnig, N. Garcia, H. Rohrer, Conductivity sensitivity of inelastic scanning tunneling microscopy, *Physical Review B* **1985**, *32*, 1336

[157]H. J. Lee, W. Ho, Single-bond formation and characterization with a scanning tunneling microscope, *Science* **1999**, *286*, 1719

[158]B. N. J. Persson, A. Baratoff, Inelastic electron tunneling from a metal tip: The contribution from resonant processes, *Physical Review Letters* **1987**, *59*, 339

[159]J. R. Hahn, H. J. Lee, W. Ho, Electronic resonance and symmetry in single-molecule inelastic electron tunneling, *Physical Review Letters* **2000**, *85*, 1914

[160]B. C. Stipe, M. A. Rezaei, W. Ho, Inducing and viewing the rotational motion of a single molecule, *Science* **1998**, *279*, 1907

[161]B. C. Stipe, M. A. Rezaei, W. Ho, Coupling of vibrational excitation to the rotational motion of a single adsorbed molecule, *Physical Review Letters* **1998**, *81*, 1263

[162]M. Kawai, T. Komeda, Y. Kim, Y. Sainoo, S. Katano, Single-molecule reactions and spectroscopy via vibrational excitation, *Philos.Trans. R. Soc. London Ser.A* **2004**, *362*, 1163

[163]K. Motobayashi, Y. Kim, H. Ueba, M. Kawai, Insight into action spectroscopy for single molecule motion and reactions through inelastic electron tunneling, *Physical Review Letters* **2010**, *105*,

[164]Y. Kim, K. Motobayashi, T. Frederiksen, H. Ueba, M. Kawai, Action spectroscopy for single-molecule reactions – Experiments and theory, *Progress in Surface Science*

2015, *90*, 85

[165]S. Katano, Y. Kim, M. Hori, M. Trenary, M. Kawai, Reversible control of hydrogenation of a single molecule, *Science* **2007**, *316*, 1883

[166]J. Henzl, K. Morgenstern, An electron induced two-dimensional switch made of azobenzene derivatives anchored in supramolecular assemblies, *Phys Chem Chem Phys* **2010**, *12*, 6035

[167]B. C. Stipe, M. A. Rezaei, W. Ho, Single-molecule vibrational spectroscopy and microscopy, *Science* **1998**, *280*, 1732

[168]N. Lorente, M. Persson, Theory of single molecule vibrational spectroscopy and microscopy, *Physical Review Letters* **2000**, *85*, 2997

[169]H. Ueba, B. N. J. Persson, Action spectroscopy for single-molecule motion induced by vibrational excitation with a scanning tunneling microscope, *Physical Review B* **2007**, *75*, 041403

[170]W. Ho, Single-molecule chemistry, *The Journal of Chemical Physics* **2002**, *117*, 11033

[171]G. Binnig, D. P. E. Smith, Single tube three - dimensional scanner for scanning tunneling microscopy, *Review of Scientific Instruments* **1986**, *57*, 1688

[172]I. Horcas, R. Fernández, J. M. Gómez-Rodríguez, J. Colchero, J. Gómez-Herrero, A. M. Baro, WSXM: A software for scanning probe microscopy and a tool for nanotechnology, *Review of Scientific Instruments* **2007**, *78*, 013705

[173]M. Bonn, S. Funk, C. Hess, D. N. Denzler, C. Stampfl, M. Scheffler, M. Wolf, G. Ertl, Phonon- versus electron-mediated desorption and oxidation of CO on Ru(0001), *Science* **1999**, *285*, 1042

[174]L. Bartels, F. Wang, D. Moller, E. Knoesel, T. F. Heinz, Real-space observation of molecular motion induced by femtosecond laser pulses, *Science* **2004**, *305*, 648

[175]S. Mukherjee *et al.*, Hot electrons do the impossible: Plasmon-induced dissociation of H2 on Au, *Nano Letters* **2013**, *13*, 240

[176]H. Arnolds, Vibrational dynamics of adsorbates - Quo vadis?, *Progress in Surface Science* **2011**, *86*, 1

[177]T. Olsen, J. Schiøtz, Origin of power laws for reactions at metal surfaces mediated by hot electrons, *Physical Review Letters* **2009**, *103*, 238301

[178]P. Szymanski, A. L. Harris, N. Camillone, Adsorption-state-dependent subpicosecond photoinduced desorption dynamics, *The Journal of Chemical Physics* **2007**, *126*, 214709

[179]S. T. Marshall, J. W. Medlin, Surface-level mechanistic studies of adsorbate–adsorbate interactions in heterogeneous catalysis by metals, *Surface Science Reports* **2011**, *66*, 173

[180]A. P. Graham, The low energy dynamics of adsorbates on metal surfaces investigated with helium atom scattering, *Surface Science Reports* **2003**, *49*, 115

[181]A. P. Graham, F. Hofmann, J. P. Toennies, J. R. Manson, Helium atom scattering from isolated CO molecules on copper (001), *The Journal of Chemical Physics* **1996**, *105*, 2093

[182]A. P. Graham, F. Hofmann, J. P. Toennies, G. P. Williams, C. J. Hirschmugl, J. Ellis, A high resolution helium atom scattering and far infrared study of the dynamics and the lateral potential energy surface of CO molecules chemisorbed on Cu(001), *The Journal of Chemical Physics* **1998**, *108*, 7825

[183]C. Harendt, J. Goschnick, W. Hirschwald, The interaction of CO with copper (110) studied by TDS and LEED, *Surface Science* **1985**, *152–153, Part 1*, 453

[184]J. C. Cook, E. M. McCash, Vibrational energy-transfer processes in the CO/Cu(100) system, *Surface Science* **1997**, *371*, 213

[185]B. Persson, F. Hoffmann, R. Ryberg, Influence of exciton motion on the shape of optical absorption lines: Applications to vibrations at surfaces, *Physical Review B* **1986**, *34*, 2266

[186]E. Carpene, Ultrafast laser irradiation of metals: Beyond the two-temperature

model, *Physical Review B* **2006**, *74*, 024301

[187]J. Garduño-Mejía, M. P. Higlett, S. R. Meech, Modelling the influence of nonthermal electron dynamics in thin and ultrathin gold films, *Chemical Physics* **2007**, *341*, 276

[188]S. I. Anisimov, B. L. Kapeliovich, T. L. Perel'man, Electron emission from metal surfaces exposed to ultrashort laser pulses *Sov. Phys.-JET* **1974**, *39*, 375

[189]S. I. Anisimov, B. Rethfeld, Theory of ultrashort laser pulse interaction with a metal, *Proc. SPIE* **1997**, *3093*, 192

[190]L. M. Struck, L. J. Richter, S. A. Buntin, R. R. Cavanagh, J. C. Stephenson, Femtosecond laser-induced desorption of CO from Cu(100): Comparison of theory and experiment, *Physical Review Letters* **1996**, *77*, 4576

[191]K.-i. Inoue, K. Watanabe, Y. Matsumoto, Instantaneous vibrational frequencies of diffusing and desorbing adsorbates: CO/Pt(111), *The Journal of Chemical Physics* **2012**, *137*, 024704

[192]H. Ueba, B. N. J. Persson, Heat transfer between adsorbate and laser-heated hot electrons, *Journal of Physics: Condensed Matter* **2008**, *20*, 224016

[193]H. Ueba, B. Persson, Heating of adsorbate by vibrational-mode coupling, *Physical Review B* **2008**, *77*, 035413

[194]L. G. M. Pettersson, A. Nilsson, A molecular perspective on the d-band model: Synergy between experiment and theory, *Topics in Catalysis* **2014**, *57*, 2

[195]P. R. Kole, H. Hedgeland, A. P. Jardine, W. Allison, J. Ellis, G. Alexandrowicz, Probing the non-pairwise interactions between CO molecules moving on a Cu(111) surface, *Journal of Physics-Condensed Matter* **2012**, *24*, 104016

[196]E. Borguet, H. L. Dai, Probing surface short range order and inter-adsorbate interactions through IR vibrational spectroscopy: CO on Cu(100), *The Journal of Physical Chemistry B* **2005**, *109*, 8509

[197]M. Mehlhorn, V. Simic-Milosevic, S. Jaksch, P. Scheier, K. Morgenstern, The

influence of the surface state onto the distance distribution of single molecules and small molecular clusters, *Surface Science* **2010**, *604*, 1698

[198]P. Deshlahra, J. Conway, E. E. Wolf, W. F. Schneider, Influence of dipole-dipole interactions on coverage-dependent adsorption: CO and NO on Pt(111), *Langmuir* **2012**, *28*, 8408

[199]J. C. Tremblay, G. Füchsel, P. Saalfrank, Excitation, relaxation, and quantum diffusion of CO on copper, *Physical Review B* **2012**, *86*, 045438

[200]J. Ahner, D. Mocuta, R. D. Ramsier, J. T. Yates, Adsorbate-adsorbate repulsions—the coverage dependence of the adsorption structure of CO on Cu(110) as studied by electron-stimulated desorption ion angular distribution, *The Journal of Chemical Physics* **1996**, *105*, 6553

[201]J. T. Kindt, J. C. Tully, M. Head-Gordon, M. A. Gomez, Electron-hole pair contributions to scattering, sticking, and surface diffusion: CO on Cu(100), *The Journal of Chemical Physics* **1998**, *109*, 3629

[202]H. Arnolds, D. A. King, I. M. Lane, Inducing non-adiabatic effects through coadsorption: CO+NO on iridium, *Chemical Physics* **2008**, *350*, 94

[203]A. Rezaeifard, M. Jafarpour, The catalytic efficiency of Fe-porphyrins supported on multi-walled carbon nanotubes in the heterogeneous oxidation of hydrocarbons and sulfides in water, *Catalysis Science & Technology* **2014**, *4*, 1960

[204]I. Mochida, K. Suetsugu, H. Fujitsu, K. Takeshita, K. Tsuji, Y. Sagara, A. Ohyoshi, A kinetic study on reduction of nitric oxide over cobalt tetraphenylporphyrin supported on titanium dioxide, *Journal of Catalysis* **1982**, *77*, 519

[205]N. A. Rakow, K. S. Suslick, A colorimetric sensor array for odour visualization, *Nature* **2000**, *406*, 710

[206]S. Mathew *et al.*, Dye-sensitized solar cells with 13% efficiency achieved through the molecular engineering of porphyrin sensitizers, *Nat Chem* **2014**, *6*, 242

[207]A. Yella *et al.*, Porphyrin-sensitized solar cells with cobalt (II/III)–based redox electrolyte exceed 12 percent efficiency, *Science* **2011**, *334*, 629

[208]F. Moresco, G. Meyer, K.-H. Rieder, H. Tang, A. Gourdon, C. Joachim, Conformational changes of single molecules induced by scanning tunneling microscopy manipulation: A route to molecular switching, *Physical Review Letters* **2001**, *86*, 672

[209]X. H. Qiu, G. V. Nazin, W. Ho, Mechanisms of reversible conformational transitions in a single molecule, *Physical Review Letters* **2004**, *93*, 196806

[210]C. B. Winkelmann, I. Ionica, X. Chevalier, G. Royal, C. Bucher, V. Bouchiat, Optical switching of porphyrin-coated silicon nanowire field effect transistors, *Nano Letters* **2007**, *7*, 1454

[211]C. Li, J. Ly, B. Lei, W. Fan, D. Zhang, J. Han, M. Meyyappan, M. Thompson, C. Zhou, Data storage studies on nanowire transistors with self-assembled porphyrin molecules, *The Journal of Physical Chemistry B* **2004**, *108*, 9646

[212]S. Yoshimoto, K. Itaya, Advances in supramolecularly assembled nanostructures of fullerenes and porphyrins at surfaces, *Journal of Porphyrins and Phthalocyanines* **2007**, *11*, 313

[213]C. M. Drain, A. Varotto, I. Radivojevic, Self-organized porphyrinic materials, *Chemical Reviews* **2009**, *109*, 1630

[214]T. Niu, A. Li, Exploring single molecules by scanning probe microscopy: porphyrin and phthalocyanine, *The Journal of Physical Chemistry Letters* **2013**, *4*, 4095

[215]W. Auwärter, D. Ecija, F. Klappenberger, J. V. Barth, Porphyrins at interfaces, *Nat Chem* **2015**, *7*, 105

[216]J. Otsuki, STM studies on porphyrins, *Coordination Chemistry Reviews* **2010**, *254*, 2311

[217]S. Mohnani, D. Bonifazi, Supramolecular architectures of porphyrins on surfaces: The structural evolution from 1D to 2D to 3D to devices, *Coordination Chemistry Reviews* **2010**, *254*, 2342

[218]M. Jurow, A. E. Schuckman, J. D. Batteas, C. M. Drain, Porphyrins as molecular electronic components of functional devices, *Coordination Chemistry Reviews* **2010**, *254*,

2297

[219]J. V. Barth, Molecular architectonic on metal surfaces, *Annual Review of Physical Chemistry* **2007**, *58*, 375

[220]J. M. Gottfried, Surface chemistry of porphyrins and phthalocyanines, *Surface Science Reports* **2015**, *70*, 259

[221]T. A. Jung, R. R. Schlittler, J. K. Gimzewski, Conformational identification of individual adsorbed molecules with the STM, *Nature* **1997**, *386*, 696

[222]T. Yokoyama, S. Yokoyama, T. Kamikado, Y. Okuno, S. Mashiko, Selective assembly on a surface of supramolecular aggregates with controlled size and shape, *Nature* **2001**, *413*, 619

[223]W. Auwärter *et al.*, Site-specific electronic and geometric interface structure of Co-tetraphenyl-porphyrin layers on Ag(111), *Physical Review B* **2010**, *81*, 245403

[224]V. Iancu, A. Deshpande, S.-W. Hla, Manipulating Kondo temperature via single molecule switching, *Nano Letters* **2006**, *6*, 820

[225]G. Rojas *et al.*, Self-assembly and properties of nonmetalated tetraphenyl-porphyrin on metal substrates, *The Journal of Physical Chemistry C* **2010**, *114*, 9408

[226]D. Stefanie, R. Michael, B. Florian, Z. Elisabeth, S. Michael, S. Hans-Peter, M. Hubertus, Towards the engineering of molecular nanostructures: local anchoring and functionalization of porphyrins on model-templates, *Nanotechnology* **2013**, *24*, 115305

[227]F. Buchner, E. Zillner, M. Röckert, S. Gläßel, H.-P. Steinrück, H. Marbach, Substrate-mediated phase separation of two porphyrin derivatives on Cu(111), *Chemistry – A European Journal* **2011**, *17*, 10226

[228]F. Buchner, I. Kellner, W. Hieringer, A. Gorling, H.-P. Steinruck, H. Marbach, Ordering aspects and intramolecular conformation of tetraphenylporphyrins on Ag(111), *Physical Chemistry Chemical Physics* **2010**, *12*, 13082

[229]G. Di Santo, C. Sfiligoj, C. Castellarin-Cudia, A. Verdini, A. Cossaro, A. Morgante,

L. Floreano, A. Goldoni, Changes of the molecule–substrate interaction upon metal inclusion into a porphyrin, *Chemistry – A European Journal* **2012**, *18*, 12619

[230]W. Auwärter, A. Weber-Bargioni, S. Brink, A. Riemann, A. Schiffrin, M. Ruben, J. V. Barth, Controlled metalation of self-assembled porphyrin nanoarrays in two dimensions, *ChemPhysChem* **2007**, *8*, 250

[231]C. Humbert, L. Dreesen, Y. Sartenaer, A. Peremans, P. A. Thiry, C. Volcke, On the Protoporphyrin Monolayers Conformation, *ChemPhysChem* **2006**, *7*, 569

[232]M. Kanai, T. Kawai, K. Motai, X. D. Wang, T. Hashizume, T. Sakura, Scanning tunneling microscopy observation of copper-phthalocyanine molecules on Si(100) and Si(111) surfaces, *Surface Science* **1995**, *329*, L619

[233]F. Rochet, G. Dufour, H. Roulet, N. Motta, A. Sgarlata, M. N. Piancastelli, M. De Crescenzi, Copper phthalocyanine on Si(111)-7 × 7 and Si(001)-2 × 1: an XPS/AES and STM study, *Surface Science* **1994**, *319*, 10

[234]S. Haq, F. Hanke, M. S. Dyer, M. Persson, P. Iavicoli, D. B. Amabilino, R. Raval, Clean coupling of unfunctionalized porphyrins at surfaces to give highly oriented organometallic oligomers, *Journal of the American Chemical Society* **2011**, *133*, 12031

[235]M. In't Veld, P. Iavicoli, S. Haq, D. B. Amabilino, R. Raval, Unique intermolecular reaction of simple porphyrins at a metal surface gives covalent nanostructures, *Chemical Communications* **2008**, 1536

[236]S. Haq *et al.*, A small molecule walks along a surface between porphyrin fences that are assembled in situ, *Angewandte Chemie International Edition* **2015**, *54*, 7101

[237]S. Haq, F. Hanke, J. Sharp, M. Persson, D. B. Amabilino, R. Raval, Versatile bottom-up construction of diverse macromolecules on a surface observed by scanning tunneling microscopy, *ACS Nano* **2014**, *8*, 8856

[238]F. Hanke, S. Haq, R. Raval, M. Persson, Heat-to-connect: surface commensurability directs organometallic one-dimensional self-assembly, *ACS Nano* **2011**, *5*, 9093

[239]M. S. Dyer, A. Robin, S. Haq, R. Raval, M. Persson, J. Klimeš, Understanding the

interaction of the porphyrin macrocycle to reactive metal substrates: Structure, bonding, and adatom capture, *ACS Nano* **2011**, *5*, 1831

[240]T. Houwaart, T. Le Bahers, P. Sautet, W. Auwärter, K. Seufert, J. V. Barth, M.-L. Bocquet, Scrutinizing individual CoTPP molecule adsorbed on coinage metal surfaces from the interplay of STM experiment and theory, *Surface Science* **2015**, *635*, 108

[241]T. Wolfle, A. Gorling, W. Hieringer, Conformational flexibility of metalloporphyrins studied by density-functional calculations, *Physical Chemistry Chemical Physics* **2008**, *10*, 5739

[242]J. J. Bonnet, S. S. Eaton, G. R. Eaton, R. H. Holm, J. A. Ibers, Spectroscopic and structural characterization of ruthenium(II) carbonyl-porphine complexes, *Journal of the American Chemical Society* **1973**, *95*, 2141

[243]C. Isvoranu, B. Wang, E. Ataman, J. Knudsen, K. Schulte, J. N. Andersen, M.-L. Bocquet, J. Schnadt, Comparison of the carbonyl and nitrosyl complexes formed by adsorption of CO and NO on monolayers of iron phthalocyanine on Au(111), *The Journal of Physical Chemistry C* **2011**, *115*, 24718

[244]A. Stróżecka, M. Soriano, J. I. Pascual, J. J. Palacios, Reversible change of the spin state in a manganese phthalocyanine by coordination of CO molecule, *Physical Review Letters* **2012**, *109*,

[245]N. Tsukahara, E. Minamitani, Y. Kim, M. Kawai, N. Takagi, Controlling orbital-selective Kondo effects in a single molecule through coordination chemistry, *The Journal of Chemical Physics* **2014**, *141*, 054702

[246]K. Seufert, W. Auwärter, J. V. Barth, Discriminative response of surface-confined metalloporphyrin molecules to carbon and nitrogen monoxide, *Journal of the American Chemical Society* **2010**, *132*, 18141

[247]G. Kresse, J. Furthmüller, Efficiency of ab-initio total energy calculations for metals and semiconductors using a plane-wave basis set, *Computational Materials Science* **1996**, *6*, 15

[248]G. Kresse, D. Joubert, From ultrasoft pseudopotentials to the projector augmented-wave method, *Physical Review B* **1999**, *59*, 1758

[249]S. M. Barlow, R. Raval, Complex organic molecules at metal surfaces: bonding, organisation and chirality, *Surface Science Reports* **2003**, *50*, 201

[250]E. B. Fleischer, C. K. Miller, L. E. Webb, Crystal and molecular structures of some metal tetraphenylporphines, *Journal of the American Chemical Society* **1964**, *86*, 2342

[251]S. J. Silvers, A. Tulinsky, The crystal and molecular structure of triclinic tetraphenylporphyrin, *Journal of the American Chemical Society* **1967**, *89*, 3331

[252]L. G. Teugels, L. G. Avila-Bront, S. J. Sibener, Chiral domains achieved by surface adsorption of achiral nickel tetraphenyl- or octaethylporphyrin on smooth and locally kinked Au(111), *The Journal of Physical Chemistry C* **2011**, *115*, 2826

[253]S. Grimme, C. Muck-Lichtenfeld, J. Antony, Analysis of non-covalent interactions in (bio)organic molecules using orbital-partitioned localized MP2, *Physical Chemistry Chemical Physics* **2008**, *10*, 3327

[254]A. Puzder, M. Dion, D. C. Langreth, Binding energies in benzene dimers: Nonlocal density functional calculations, *The Journal of Chemical Physics* **2006**, *124*, 164105

[255]M. O. Sinnokrot, C. D. Sherrill, High-accuracy quantum mechanical studies of π−π interactions in benzene dimers, *The Journal of Physical Chemistry A* **2006**, *110*, 10656

[256]T. Thonhauser, A. Puzder, D. C. Langreth, Interaction energies of monosubstituted benzene dimers via nonlocal density functional theory, *The Journal of Chemical Physics* **2006**, *124*, 164106

[257]S. Tsuzuki, K. Honda, T. Uchimaru, M. Mikami, K. Tanabe, Origin of attraction and directionality of the π/π interaction: Model chemistry calculations of benzene dimer interaction, *Journal of the American Chemical Society* **2002**, *124*, 104

[258]H. Yildirim, A. Kara, S. Durukanoglu, T. S. Rahman, Calculated pre-exponential factors and energetics for adatom hopping on terraces and steps of Cu(100) and Cu(110), *Surface Science* **2006**, *600*, 484

[259]P. Hobza, H. L. Selzle, E. W. Schlag, Potential energy surface for the benzene dimer. Results of ab initio CCSD(T) calculations show two nearly isoenergetic structures:

T-shaped and parallel-displaced, *The Journal of Physical Chemistry* **1996**, *100*, 18790

[260]G. D. Purvis, R. J. Bartlett, A full coupled cluster singles and doubles model: The inclusion of disconnected triples, *The Journal of Chemical Physics* **1982**, *76*, 1910

[261]J. P. Hill, Y. Wakayama, K. Ariga, How molecules accommodate a 2D crystal lattice mismatch: an unusual 'mixed' conformation of tetraphenylporphyrin, *Physical Chemistry Chemical Physics* **2006**, *8*, 5034

[262]A. G. Mark, M. Forster, R. Raval, Direct visualization of chirality in two dimensions, *Tetrahedron: Asymmetry* **2010**, *21*, 1125

[263]M. Eichberger *et al.*, Dimerization boosts one-dimensional mobility of conformationally adapted porphyrins on a hexagonal surface atomic lattice, *Nano Letters* **2008**, *8*, 4608

[264]F. Buchner *et al.*, Diffusion, rotation, and surface chemical bond of individual 2H-tetraphenylporphyrin molecules on Cu(111), *The Journal of Physical Chemistry C* **2011**, *115*, 24172

[265]F. Rosei, M. Schunack, Y. Naitoh, P. Jiang, A. Gourdon, E. Laegsgaard, I. Stensgaard, C. Joachim, F. Besenbacher, Properties of large organic molecules on metal surfaces, *Progress in Surface Science* **2003**, *71*, 95

[266]P. Donovan, Adsorption and self-assembly of cobalt(II)-tetraphenylporphyrin on Cu(110), *PhD thesis, University of Liverpool* **2010**,

[267]A. Sinha, M. C. Hsiao, F. F. Crim, Bond selected bimolecular chemistry: H+HOD(4 ν OH)→OD+H2, *The Journal of Chemical Physics* **1990**, *92*, 6333

[268]M. C. Hsiao, A. Sinha, F. F. Crim, Energy disposal in the vibrational-state- and bond-selected reaction of water with hydrogen atoms, *The Journal of Physical Chemistry* **1991**, *95*, 8263

[269]M. J. Bronikowski, W. R. Simpson, B. Girard, R. N. Zare, Bond specific chemistry: OD:OH product ratios for the reactions H+HOD(100) and H+HOD(001), *The Journal of Chemical Physics* **1991**, *95*, 8647

[270]S. Chelkowski, A. D. Bandrauk, P. B. Corkum, Efficient molecular dissociation by a chirped ultrashort infrared laser pulse, *Physical Review Letters* **1990**, *65*, 2355

[271]M. Bonn, C. Hess, M. Wolf, The dynamics of vibrational excitations on surfaces: CO on Ru(001), *The Journal of Chemical Physics* **2001**, *115*, 7725

[272]C. Ventalon, J. M. Fraser, M. H. Vos, A. Alexandrou, J. L. Martin, M. Joffre, Coherent vibrational climbing in carboxyhemoglobin, *Proceedings of the National Academy of Sciences* **2004**, *101*, 13216

[273]P. M. Morse, Diatomic molecules according to the wave mechanics. II. Vibrational levels, *Physical Review* **1929**, *34*, 57

[274]P. Nuernberger, K. F. Lee, A. Bonvalet, L. Bouzhir-Sima, J. C. Lambry, U. Liebl, M. Joffre, M. H. Vos, Strong ligand-protein interactions revealed by ultrafast infrared spectroscopy of CO in the heme pocket of the oxygen sensor FixL, *Journal of the American Chemical Society* **2011**, *133*, 17110

[275]P. Atkins, Physical chemistry, *Oxford University Press, USA* **2014**,

[276]H. Pfnür, D. Menzel, F. M. Hoffmann, A. Ortega, A. M. Bradshaw, High resolution vibrational spectroscopy of CO on Ru(001): The importance of lateral interactions, *Surface Science* **1980**, *93*, 431

[277]E. B. Wilson, J. C. Decius, P. C. Cross, *Molecular vibrations: the theory of infrared and Raman vibrational spectra*. Editor, Courier Corporation, **2012**.

[278]T. Omiya, H. Arnolds, Coverage dependent non-adiabaticity of CO on a copper surface, *The Journal of Chemical Physics* **2014**, *141*, 214705

[279]L. Krim, S. Sorgues, B. Soep, N. Shafizadeh, Infrared spectra of RuTPP, RuCOTPP, and Ru(CO)2TPP isolated in solid argon, *The Journal of Physical Chemistry A* **2005**, *109*, 8268

[280]A. S. Azizyan, T. S. Kurtikyan, G. G. Martirosyan, P. C. Ford, Tracking reactive intermediates by FTIR monitoring of reactions in low-temperature sublimed solids: nitric oxide disproportionation mediated by ruthenium(II) carbonyl porphyrin Ru(TPP)(CO), *Inorganic Chemistry* **2013**, *52*, 5201

[281]F. Buchner, K. Seufert, W. Auwärter, D. Heim, J. V. Barth, K. Flechtner, J. M. Gottfried, H.-P. Steinrück, H. Marbach, NO-induced reorganization of porphyrin arrays, *ACS Nano* **2009**, *3*, 1789

[282]X. Y. Li, T. G. Spiro, Is bound carbonyl linear or bent in heme proteins? Evidence from resonance Raman and infrared spectroscopic data, *Journal of the American Chemical Society* **1988**, *110*, 6024

[283]D. D. Dlott, M. D. Fayer, J. R. Hill, C. W. Rella, K. S. Suslick, C. J. Ziegler, Vibrational relaxation in metalloporphyrin CO complexes, *Journal of the American Chemical Society* **1996**, *118*, 7853

[284]J. Yu, S. Mathew, B. S. Flavel, M. R. Johnston, J. G. Shapter, Ruthenium porphyrin functionalized single-walled carbon nanotube arrays—A step toward light harvesting antenna and multibit information storage, *Journal of the American Chemical Society* **2008**, *130*, 8788

[285]M. Ma, Yan, S.-J. Huo, Q.-J. Xu, W.-B. Cai, In situ surface-enhanced IR absorption spectroscopy on CO adducts of iron protoporphyrin IX self-assembled on a Au electrode, *The Journal of Physical Chemistry B* **2006**, *110*, 14911

[286]S. Katano, A. Bandara, J. Kubota, K. Onda, A. Wada, K. Domen, C. Hirose, Screening of SFG signals from bridged CO on Ni(111) by the coexistence of linear CO, *Surface Science* **1999**, *427–428*, 337

[287]A. Bandara, S. Katano, J. Kubota, K. Onda, A. Wada, K. Domen, C. Hirose, The effect of co-adsorption of on-top CO on the sum-frequency generation signal of bridge CO on the Ni(111) surface, *Chemical Physics Letters* **1998**, *290*, 261

[288]E. H. G. Backus, M. Bonn, A quantitative comparison between reflection absorption infrared and sum-frequency generation spectroscopy, *Chemical Physics Letters* **2005**, *412*, 152

[289]J. C. Kimball, C. Y. Fong, Y. R. Shen, Anharmonicity, phonon localization, two-phonon bound states, and vibrational spectra, *Physical Review B* **1981**, *23*, 4946

[290]S. A. Wasileski, M. J. Weaver, Vibrational spectroscopy as a probe of

potential-dependent electrode-chemisorbate bonding: an assessment using finite-cluster density functional theory, *Journal of Electroanalytical Chemistry* **2002**, *524–525*, 219

[291]I. Dabo, Resilience of gas-phase anharmonicity in the vibrational response of adsorbed carbon monoxide and breakdown under electrical conditions, *Physical Review B* **2012**, *86*, 035139

[292]G. Marek, E. Andreas, H. Jürgen, CO adsorption on close-packed transition and noble metal surfaces: trends from ab initio calculations, *Journal of Physics: Condensed Matter* **2004**, *16*, 1141

[293]S. D. Fried, S. G. Boxer, Measuring electric fields and noncovalent interactions using the vibrational stark effect, *Accounts of Chemical Research* **2015**, *48*, 998

[294]E. S. Park, S. G. Boxer, Origins of the sensitivity of molecular vibrations to electric fields: Carbonyl and nitrosyl stretches in model compounds and proteins, *The Journal of Physical Chemistry B* **2002**, *106*, 5800

[295]E. S. Park, S. S. Andrews, R. B. Hu, S. G. Boxer, Vibrational Stark spectroscopy in proteins: A probe and calibration for electrostatic fields, *The Journal of Physical Chemistry B* **1999**, *103*, 9813

[296]J. M. Kriegl, K. Nienhaus, P. Deng, J. Fuchs, G. U. Nienhaus, Ligand dynamics in a protein internal cavity, *Proceedings of the National Academy of Sciences* **2003**, *100*, 7069

[297]H. Lehle, J. M. Kriegl, K. Nienhaus, P. Deng, S. Fengler, G. U. Nienhaus, Probing electric fields in protein cavities by using the vibrational Stark rffect of carbon monoxide, *Biophysical Journal* **2005**, *88*, 1978

[298]I. T. Suydam, C. D. Snow, V. S. Pande, S. G. Boxer, Electric fields at the active site of an enzyme: Direct comparison of experiment with theory, *Science* **2006**, *313*, 200

[299]W. F. Lin, P. A. Christensen, A. Hamnett, M. S. Zei, G. Ertl, The electro-oxidation of CO at the Ru(0001) single-crystal electrode surface, *The Journal of Physical Chemistry B* **2000**, *104*, 6642

[300]R. M. Ziff, E. Gulari, Y. Barshad, Kinetic phase transitions in an irreversible

surface-reaction model, *Physical Review Letters* **1986**, *56*, 2553

[301]J. P. Collman, J. I. Brauman, T. R. Halbert, K. S. Suslick, Nature of O2 and CO binding to metalloporphyrins and heme proteins, *Proceedings of the National Academy of Sciences* **1976**, *73*, 3333

[302]T. P. M. Goumans, A. W. Ehlers, M. C. van Hemert, A. Rosa, E.-J. Baerends, K. Lammertsma, Photodissociation of the phosphine-substituted transition metal carbonyl complexes Cr(CO)5L and Fe(CO)4L: A theoretical study, *Journal of the American Chemical Society* **2003**, *125*, 3558

[303]K. Ishii, S.-i. Hoshino, N. Kobayashi, Photodecarbonylation of ruthenium carbonyl octaethylporphyrin via stepwise two-photon absorption of visible light, *Inorganic Chemistry* **2004**, *43*, 7969

[304]C. R. Child, S. Kealey, H. Jones, P. W. Miller, A. J. P. White, A. D. Gee, N. J. Long, Binding and photodissociation of CO in iron(ii) complexes for application in positron emission tomography (PET) radiolabelling, *Dalton Transactions* **2011**, *40*, 6210

[305]K. Seufert, M.-L. Bocquet, W. Auwärter, A. Weber-Bargioni, J. Reichert, N. Lorente, J. V. Barth, Cis-dicarbonyl binding at cobalt and iron porphyrins with saddle-shape conformation, *Nat Chem* **2011**, *3*, 114

[306]C. F. Hermanns, M. Bernien, A. Krüger, W. Walter, Y.-M. Chang, E. Weschke, W. Kuch, Huge magnetically coupled orbital moments of Co porphyrin molecules and their control by CO adsorption, *Physical Review B* **2013**, *88*, 104420

[307]K. Flechtner, A. Kretschmann, H.-P. Steinrück, J. M. Gottfried, NO-induced reversible switching of the electronic interaction between a porphyrin-coordinated cobalt ion and a silver surface, *Journal of the American Chemical Society* **2007**, *129*, 12110

[308]C. Wäckerlin, D. Chylarecka, A. Kleibert, K. Muller, C. Iacovita, F. Nolting, T. A. Jung, N. Ballav, Controlling spins in adsorbed molecules by a chemical switch, *Nat Commun* **2010**, *1*, 61

[309]H. Kim, Y. H. Chang, S.-H. Lee, Y.-H. Kim, S.-J. Kahng, Switching and sensing spin states of Co–porphyrin in bimolecular reactions on Au(111) using scanning

tunneling microscopy, *ACS Nano* **2013**, *7*, 9312

[310]J. Miguel, C. F. Hermanns, M. Bernien, A. Krüger, W. Kuch, Reversible manipulation of the magnetic coupling of single molecular spins in Fe-porphyrins to a ferromagnetic substrate, *The Journal of Physical Chemistry Letters* **2011**, *2*, 1455

[311]K. Flechtner, A. Kretschmann, L. R. Bradshaw, M.-M. Walz, H.-P. Steinrück, J. M. Gottfried, Surface-confined two-step synthesis of the complex (ammine)(meso-tetraphenylporphyrinato)-zinc(II) on Ag(111), *The Journal of Physical Chemistry C* **2007**, *111*, 5821

[312]C. Isvoranu, B. Wang, E. Ataman, K. Schulte, J. Knudsen, J. N. Andersen, M. L. Bocquet, J. Schnadt, Ammonia adsorption on iron phthalocyanine on Au(111): influence on adsorbate-substrate coupling and molecular spin, *The Journal of Chemical Physics* **2011**, *134*, 114710

[313]R. Purrello, S. Gurrieri, R. Lauceri, Porphyrin assemblies as chemical sensors, *Coordination Chemistry Reviews* **1999**, *190–192*, 683

[314]M. Biesaga, K. Pyrzyńska, M. Trojanowicz, Porphyrins in analytical chemistry. A review, *Talanta* **2000**, *51*, 209

[315]J. S. Rebouças, B. R. James, Molecular recognition using ruthenium(II) porphyrin thiol complexes as probes, *Inorganic Chemistry* **2013**, *52*, 1084

[316]S. R. Burema, K. Seufert, W. Auwärter, J. V. Barth, M.-L. Bocquet, Probing nitrosyl ligation of surface-confined metalloporphyrins by inelastic electron tunneling spectroscopy, *ACS Nano* **2013**, *7*, 5273

[317]H. Kim, Y. H. Chang, W.-J. Jang, E.-S. Lee, Y.-H. Kim, S.-J. Kahng, Probing single-molecule dissociations from a bimolecular complex NO–Co-porphyrin, *ACS Nano* **2015**, *9*, 7722

[318]V. C. Zoldan, R. Faccio, C. Gao, A. A. Pasa, Coupling of cobalt–tetraphenylporphyrin molecules to a copper nitride layer, *The Journal of Physical Chemistry C* **2013**, *117*, 15984

[319]T. G. Gopakumar, H. Tang, J. Morillo, R. Berndt, Transfer of Cl ligands between

adsorbed iron tetraphenylporphyrin molecules, *Journal of the American Chemical Society* **2012**, *134*, 11844

[320]B. C. Stipe, M. A. Rezaei, W. Ho, S. Gao, M. Persson, B. I. Lundqvist, Single-Molecule Dissociation by Tunneling Electrons, *Physical Review Letters* **1997**, *78*, 4410

[321]D. M. Eigler, C. P. Lutz, W. E. Rudge, An atomic switch realized with the scanning tunnelling microscope, *Nature* **1991**, *352*, 600

[322]M. Alemani, M. V. Peters, S. Hecht, K.-H. Rieder, F. Moresco, L. Grill, Electric field-induced isomerization of azobenzene by STM, *Journal of the American Chemical Society* **2006**, *128*, 14446

[323]S. Alavi, R. Rousseau, S. N. Patitsas, G. P. Lopinski, R. A. Wolkow, T. Seideman, Inducing desorption of organic molecules with a scanning tunneling microscope: Theory and experiments, *Physical Review Letters* **2000**, *85*, 5372

[324]M. Nakaya, Y. Kuwahara, M. Aono, T. Nakayama, Reversibility-controlled single molecular level chemical reaction in a C60 monolayer via ionization induced by scanning transmission microscopy, *Small* **2008**, *4*, 538

[325]K. Stokbro, C. Thirstrup, M. Sakurai, U. Quaade, B. Y.-K. Hu, F. Perez-Murano, F. Grey, STM-induced hydrogen desorption via a hole resonance, *Physical Review Letters* **1998**, *80*, 2618

[326]P. A. Sloan, M. F. G. Hedouin, R. E. Palmer, M. Persson, Mechanisms of molecular manipulation with the scanning tunneling microscope at room temperature: chlorobenzene Si(111) 7x7, *Physical Review Letters* **2003**, *91*, 118301

[327]N. L. Yoder, N. P. Guisinger, M. C. Hersam, R. Jorn, C. C. Kaun, T. Seideman, Quantifying desorption of saturated hydrocarbons from silicon with quantum calculations and scanning tunneling microscopy, *Physical Review Letters* **2006**, *97*, 187601

[328]R. Hoffmann, M. M. L. Chen, D. L. Thorn, Qualitative discussion of alternative coordination modes of diatomic ligands in transition metal complexes, *Inorganic Chemistry* **1977**, *16*, 503

[329]D. Menzel, Thirty years of MGR: How it came about, and what came of it, *Nuclear Instruments and Methods in Physics Research Section B: Beam Interactions with Materials and Atoms* **1995**, *101*, 1

[330]P. Nuernberger, K. F. Lee, A. Bonvalet, M. H. Vos, M. Joffre, Multiply excited vibration of carbon monoxide in the primary docking site of hemoglobin following photolysis from the heme, *The Journal of Physical Chemistry Letters* **2010**, *1*, 2077

[331]M. Lim, T. A. Jackson, P. A. Anfinrud, Ultrafast rotation and trapping of carbon monoxide dissociated from myoglobin, *Nat Struct Mol Biol* **1997**, *4*, 209

[332]L. J. G. W. van Wilderen, J. M. Key, I. H. M. Van Stokkum, R. van Grondelle, M. L. Groot, Dynamics of carbon monoxide photodissociation in bradyrhizobium japonicum FixL probed by picosecond midinfrared spectroscopy, *The Journal of Physical Chemistry B* **2009**, *113*, 3292

[333]A. Vogler, H. Kunkely, Photochemistry of biologically important transition metal complexes. II. carbonylpiperidinetetraphenylporphine complexes of iron(II) and ruthenium(II), *Berichte der Bunsengesellschaft für physikalische Chemie* **1976**, *80*, 425

[334]J. Rodriguez, L. McDowell, D. Holten, Elucidation of the role of metal-to-ring charge-transfer excited states in the deactivation of photoexcited ruthenium porphyrin carbonyl complexes, *Chemical Physics Letters* **1988**, *147*, 235

[335]I. Iwakura, T. Kobayashi, A. Yabushita, Direct observation of molecular structural change during intersystem crossing by real-time spectroscopy with a few optical cycle laser, *Inorganic Chemistry* **2009**, *48*, 3523

[336]J. R. Hill, C. J. Ziegler, K. S. Suslick, D. D. Dlott, C. W. Rella, M. D. Fayer, Tuning the vibrational relaxation of CO bound to heme and metalloporphyrin complexes, *The Journal of Physical Chemistry* **1996**, *100*, 18023

[337]D. Kim, Y. O. Su, T. G. Spiro, Back-bonding in ruthenium porphyrins as monitored by resonance Raman spectroscopy, *Inorganic Chemistry* **1986**, *25*, 3993

[338]N. Shafizadeh, L. Krim, S. Sorgues, B. Soep, Observation and decay of free and ligated metalloporphyrins in the gas phase, *Chemical Physics Letters* **2002**, *357*, 37

[339]C. Rovira, K. Kunc, J. Hutter, P. Ballone, M. Parrinello, Equilibrium geometries and electronic structure of iron−porphyrin complexes: A density functional study, *The Journal of Physical Chemistry A* **1997**, *101*, 8914

[340]T. Bollwein, P. J. Brothers, H. L. Hermann, P. Schwerdtfeger, Theoretical investigations into transition metal−group 13 element bonding: comparison between ruthenium porphyrin and ruthenium carbonyl diyl compounds, *Organometallics* **2002**, *21*, 5236

[341]E. J. Baerends, P. Ros, Evaluation of the LCAO Hartree—Fock—Slater method: Applications to transition-metal complexes, *International Journal of Quantum Chemistry* **1978**, *14*, 169

[342]F. M. Hoffmann, Infrared reflection-absorption spectroscopy of adsorbed molecules, *Surface Science Reports* **1983**, *3*, 107

[343]M. Trenary, K. J. Uram, F. Bozso, J. T. Yates Jr, Temperature dependence of the vibrational lineshape of CO chemisorbed on the Ni(111) surface, *Surface Science* **1984**, *146*, 269

[344]M. Bonn, C. Hess, W. G. Roeterdink, H. Ueba, M. Wolf, Dephasing of vibrationally excited molecules at surfaces: CO/Ru(001), *Chemical Physics Letters* **2004**, *388*, 269

[345]J. W. Gadzuk, A. C. Luntz, On vibrational lineshapes of adsorbed molecules, *Surface Science* **1984**, *144*, 429

[346]R. G. Tobin, Vibrational linewidths of adsorbed molecules: Experimental considerations and results, *Surface Science* **1987**, *183*, 226

[347]X. L. Zhou, X. Y. Zhu, J. M. White, Photochemistry at adsorbate/metal interfaces, *Surface Science Reports* **1991**, *13*, 73

[348]L. J. Richter, S. A. Buntin, D. S. King, R. R. Cavanagh, Constraints on the use of polarization and angle-of-incidence to characterize surface photoreactions, *Chemical Physics Letters* **1991**, *186*, 423

[349]B. N. J. Persson, R. Ryberg, Brownian motion and vibrational phase relaxation at

surfaces: CO on Ni(111), *Physical Review B* **1985**, *32*, 3586

[350]B. N. J. Persson, R. Ryberg, Vibrational phase relaxation at surfaces: CO on Ni(111), *Physical Review Letters* **1985**, *54*, 2119

[351]A. Ghosh, D. F. Bocian, Carbonyl tilting and bending potential energy surface of carbon monoxyhemes, *The Journal of Physical Chemistry* **1996**, *100*, 6363

[352]M. J. Kale, T. Avanesian, H. Xin, J. Yan, P. Christopher, Controlling catalytic selectivity on metal nanoparticles by direct photoexcitation of adsorbate-metal bonds, *Nano Letters* **2014**, *14*, 5405

[353]T. Avanesian, P. Christopher, Adsorbate specificity in hot electron driven photochemistry on catalytic metal surfaces, *The Journal of Physical Chemistry C* **2014**, *118*, 28017

[354]C. Matranga, P. Guyot-Sionnest, Vibrational relaxation of cyanide at the metal/electrolyte interface, *The Journal of Chemical Physics* **2000**, *112*, 7615

[355]C. Matranga, B. L. Wehrenberg, P. Guyot-Sionnest, Vibrational relaxation of cyanide on copper surfaces: Can metal d-bands influence vibrational energy transfer?, *The Journal of Physical Chemistry B* **2002**, *106*, 8172

[356]M. Forsblom, M. Persson, Vibrational lifetimes of cyanide and carbon monoxide on noble and transition metal surfaces, *The Journal of Chemical Physics* **2007**, *127*, 154303

[357]C. Chen, P. Chu, C. A. Bobisch, D. L. Mills, W. Ho, Viewing the interior of a single molecule: vibronically resolved photon imaging at submolecular resolution, *Physical Review Letters* **2010**, *105*, 217402

[358]H. Imada, K. Miwa, J. Jung, K. T. Shimizu, N. Yamamoto, Y. Kim, Atomic-scale luminescence measurement and theoretical analysis unveiling electron energy dissipation at a p -type GaAs(110) surface, *Nanotechnology* **2015**, *26*, 365402

[359]C. Clavero, Plasmon-induced hot-electron generation at nanoparticle/metal-oxide interfaces for photovoltaic and photocatalytic devices, *Nat Photon* **2014**, *8*, 95

[360]A. Bandara, S. S. Kano, K. Onda, S. Katano, J. Kubota, K. Domen, C. Hirose, A.

Wada, SFG spectroscopy of CO/Ni(111): UV pumping and the transient hot band transition of adsorbed CO, *Bulletin of the Chemical Society of Japan* **2002**, *75*, 1125

[361]M. Bonn, H. Ueba, M. Wolf, Theory of sum-frequency generation spectroscopy of adsorbed molecules using the density matrix method—broadband vibrational sum-frequency generation and applications, *Journal of Physics: Condensed Matter* **2005**, *17*, S201

[362]S. Roke, A. W. Kleyn, M. Bonn, Ultrafast surface dynamics studied with femtosecond sum frequency generation, *The Journal of Physical Chemistry A* **2001**, *105*, 1683